JAERI-Conf
95-016

INDC(JPN)-174/U

Circulaten
1. A.J. Koning
2. H. Gruppelaar

PROCEEDINGS OF THE SECOND SPECIALISTS' MEETING ON HIGH ENERGY NUCLEAR DATA

January 26-27, 1995, JAERI, Tokai, Japan

July 1995

(Eds.) Tokio FUKAHORI and Norio KISHIDA

日本原子力研究所
Japan Atomic Energy Research Institute

JAERI－Conf 95－016

Proceedings of the Second Specialists' Meeting on High Energy Nuclear Data January 26-27, 1995, JAERI, Tokai, Japan

(Eds.) Tokio FUKAHORI and Norio KISHIDA

Japanese Nuclear Data Committee and Nuclear Data Center
Japan Atomic Energy Research Institute
Tokai-mura, Naka-gun, Ibaraki-ken

(Received June 16, 1995)

This report is the Proceedings of the Second Specialists' Meeting on High Energy Nuclear Data. The meeting was held on January 26-27, 1995, at the Tokai Research Establishment of Japan Atomic Energy Research Institute with the participation of sixty-odd specialists, who were the evaluators, theorists, experimentalists and users of high energy nuclear data including the members of the Japanese Nuclear Data Committee.

The need of the nuclear data up to a few GeV has been stressed in the meeting for many applications, such as spallation neutron sources for radioactive waste treatment, accelerator shielding design, medical isotope production, radiation therapy, the effects of space radiation on astronauts and their equipments, and the cosmic history of the meteorites and other galactic substances. After the first Specialists' Meeting in 1991, such an evaluation activity in Japan has been grown and the results are accumulated. Foreign activities of high energy nuclear data evaluation are also being increased.

According to the above situation, with the view of producing an evaluated high energy nuclear data file, theoretical models and codes, available and necessary measurements, needs on nuclear data, various applications, and status of evaluated file were reviewed and discussed.

Keywords: Proceedings, Nuclear Data, High Energy, Evaluation, Experiment, Applicative Review, Theoretical Review

JAERI－Conf 95－016

第２回高エネルギー核データ専門家会議報文集

1995年１月26～27日，日本原子力研究所，東海村

日本原子力研究所東海研究所
シグマ研究委員会・核データセンター
（編）深堀　智生・岸田　則生

（1995年６月16日受理）

本報文集は，第２回高エネルギー核データ専門家会議の報文を収録したものである。専門家会議は，1995年１月26日と27日の両日，日本原子力研究所東海研究所において，60数名の専門家の出席のもとに開催された。出席した専門家は，高エネルギー核データの評価者，理論的研究者，実験者，利用者及びシグマ委員会委員であった。

数GeV までの入射エネルギーにおける高エネルギー核データは，放射性廃棄物処理のためのスポレーション中性子源，加速器の遮蔽設計，医療用放射性同位元素製造，放射線治療，宇宙空間での宇宙飛行士や装置への宇宙線の影響の研究，宇宙物理学などの多岐にわたる分野から必要とされている。第１回専門家会議の後，わが国では評価及び理論的研究の進展及びその結果の集積があり，諸外国での高エネルギー核データ評価活動も盛んになってきた。

このような状況を受け，本専門家会議では，高エネルギー核データの評価済ファイルを整備するという視点に立って，理論モデルや理論計算コード，既存もしくは必要な実験データ，利用者からの核データの要求及び応用分野の紹介，評価済ファイルの現状などが報告・討議された。

東海研究所：〒319-11茨城県那珂郡東海村白方白根2-4

Program Committee

Norio KISHIDA (Chairman)	(Japan Atomic Energy Research Institute)
Satoshi CHIBA	(Japan Atomic Energy Research Institute)
Tokio FUKAHORI	(Japan Atomic Energy Research Institute)
Yukio OYAMA	(Japan Atomic Energy Research Institute)
Hiroshi TAKADA	(Japan Atomic Energy Research Institute)
Naoki YAMANO	(Sumitomo Atomic Energy Industries, Ltd.)
Nobuaki YOSHIZAWA	(Mitsubishi Research Institute, Inc.)

プログラム委員会

岸田　則生（委員長）	（日本原子力研究所）
千葉　　敏	（日本原子力研究所）
深堀　智生	（日本原子力研究所）
大山　幸夫	（日本原子力研究所）
高田　　弘	（日本原子力研究所）
山野　直樹	（住友原子力工業（株））
義澤　宣明	（（株）三菱総合研究所）

Contents

目　　次

1. Theory

1.1 Semiclassical Approach to Statistical Multistep Direct Reactions - Recent progress in Semiclassical Distorted Wave Model -

Yukinobu Watanabe, Hiroyuki Shinohara+ and Mitsuji Kawai*

Department of Energy Conversion Engineering, Graduate school of Engineering and Sciences, Kyushu University, Kasuga, Fukuoka 816, Japan

**Department of Physics, Faculty of Science, Kyushu University, Fukuoka 812, Japan*

ABSTRACT

We report recent progress in the semiclassical distorted wave (SCDW) model in which some semiclassical assumptions and approximations are made in MSD theories based on the distorted wave Born approximation method and a simple closed-form formula is derived. The SCDW calculations including the one- and two-step processes are compared with the experimental data of (p,xp) and (p,xn) reactions for incident energies from 65 to 200 MeV.

I. INTRODUCTION

Preequilibrium process in nuclear reactions has been studied extensively [1] as a nonequilibrium phenomenon in a nucleus consisting of a quantum many-body system. One of recent trends in the theoretical work is the quantum-mechanical (QM) approach, such as the FKK[2], the TUL[3], and the NWY theories[4] which have proposed in 1980's. In these days, some practical efforts are being made to apply those theories to intermediate energy nuclear data evaluation work[5].

According to the QM theories[1,2-4], preequilibrium particle emission occurs via statistical multistep reactions which can be distinguished into multistep direct (MSD) and multistep compound (MSC) processes. In the MSD process, the reaction occurs in the P space configuration which at least one particle is unbound. Consequently, the emitted particles show smoothly forward-peaked angular distributions. On the other hand, the MSC process is involved with the Q space where all particles are bound. Particle emission via the MSC process takes place after a nucleon or a complex particle happens to get the energy enough to escape from the compound nucleus during a series of two-body interaction. The MSC angular distribution is symmetry against 90° in the c.m. system. As the incident energy increases, the MSD process becomes predominant. In particular, the high energy portion of preequilibrium emission spectra can be explained by the one- and two-step MSD processes.

+ Present address: Hitachi Works, Hitachi, Ltd., Hitachi, Ibaraki, 317, Japan

Any MSD theories which have so far proposed can be regarded basically as an extended version of the distorted wave Born approximation (DWBA) method to direct transition into continuum. Within the same framework, we have proposed the semiclassical distorted wave (SCDW) model[6-8], in which several semiclassical approximations and assumptions are introduced into the MSD formulas based on the DWBA. In this model, the double differential MSD cross section can be expressed in such a simple closed-form given by eqs.(2.1) and (2.2) in Sec.II as to allow us a straightforward intuitive interpretation. The SCDW model has been applied to analyses of several experimental data of (p,xp) and (p,xn) reactions for incident energies with several tens of MeV to 200 MeV. In this report, we summarize recent progress in the SCDW model calculation with particular attention to the two-step calculation.

II. SEMICLASSICAL DISTORTED WAVE MODEL FORMULA

The double differential one- and two-step cross sections derived finally in terms of the SCDW model are given in the following closed form expression:

$$\left(\frac{\partial^2\sigma}{\partial\varepsilon_f\partial\Omega_f}\right)^{1step} = \left(\frac{A}{A+1}\right)^2 \int d\mathbf{r}_1 \left|\chi_i^{(+)}(\mathbf{r}_1)\right|^2 \left|\chi_f^{(-)}(\mathbf{r}_1)\right|^2 \frac{k_f/k_f(\mathbf{r}_1)}{k_i/k_i(\mathbf{r}_1)} \left(\frac{\partial^2\sigma}{\partial\varepsilon_f\partial\Omega_f}\right)_{\mathbf{r}_1} \rho(\mathbf{r}_1), \tag{2.1}$$

for the one-step process, and

$$\left(\frac{\partial^2\sigma}{\partial\varepsilon_f\partial\Omega_f}\right)_{\nu}^{2step} = \left(\frac{A}{A+1}\right)^4 \int dE_m \int d\mathbf{r}_1 \int d\mathbf{r}_2 \frac{k_f/k_f(\mathbf{r}_2)}{k_i/k_i(\mathbf{r}_1)} \left|\chi_f^{(-)}(\mathbf{r}_2)\right|^2 \left[\left(\frac{\partial^2\sigma}{\partial\varepsilon_f\partial\Omega_f}\right)_{\mathbf{r}_2} \rho(\mathbf{r}_2)\right]_{\nu}$$
$$\times \frac{\exp\left[-2\gamma_\nu|\mathbf{r}_2-\mathbf{r}_1|\right]}{|\mathbf{r}_2-\mathbf{r}_1|^2} \left[\left(\frac{\partial^2\sigma}{\partial\varepsilon_m\partial\Omega_m}\right)_{\mathbf{r}_1} \rho(\mathbf{r}_1)\right]_{\nu} \left|\chi_i^{(+)}(\mathbf{r}_1)\right|^2 \tag{2.2}$$

for the two-step process, respectively.

The details for the derivation and the approximations used in the SCDW model have been described in refs.[6-8]. For the following explanation, we show schematically a picture of the two-step process which can be drawn by the SCDW model in Fig.1.

Now let us consider the two-step process in (p,p'x) reactions. There are two types of intermediate paths; (p,p'') (p'',p') and (p,n)(n,p'). The two-step cross section is given by the incoherent sum with eq. (2.2):

$$\left(\frac{\partial^2\sigma}{\partial\varepsilon_f\partial\Omega_f}\right)^{2step} = \left(\frac{\partial^2\sigma}{\partial\varepsilon_f\partial\Omega_f}\right)_p + \left(\frac{\partial^2\sigma}{\partial\varepsilon_f\partial\Omega_f}\right)_n, \tag{2.3}$$

where the subscripts, p and n, denote the kind of the intermediate fast particle. The physical quantities in eq. (2.2) are as follows: the subscript ν denotes p or n, A is the target mass. $\mathbf{r}_1(\mathbf{r}_2)$ is the point of the first (second) collision of the fast particle with a target nucleon, $k_i(\mathbf{r}_1)$ ($k_f(\mathbf{r}_2)$) is the local wave number of the incident (outgoing) particle at $\mathbf{r}_1(\mathbf{r}_2)$, and the χ are the distorted waves normalized to a δ-function of the wave number vector. $\left[\left(\partial^2\sigma/\partial\varepsilon\partial\Omega\right)_r\rho(\mathbf{r})\right]_\nu$ is the local average nucleon-nucleon scattering cross section at $\mathbf{r}$ defined by

$$\left[\left(\frac{\partial^2\sigma}{\partial\varepsilon\partial\Omega}\right)_r\rho(\mathbf{r})\right]_p=\left(\frac{\partial^2\sigma_{pp}}{\partial\varepsilon\partial\Omega}\right)_r\rho_p(\mathbf{r})+\left(\frac{\partial^2\sigma_{pn}}{\partial\varepsilon\partial\Omega}\right)_r\rho_n(\mathbf{r}) \tag{2.4a}$$

for $\mathbf{r}=\mathbf{r}_1$ and $\mathbf{r}_2$, and

$$\left[\left(\frac{\partial^2\sigma}{\partial\varepsilon\partial\Omega}\right)_r\rho(\mathbf{r})\right]_n=\left(\frac{\partial^2\sigma_{pn}}{\partial\varepsilon\partial\Omega}\right)_r\times\begin{cases}\rho_n(\mathbf{r}) & \text{at } \mathbf{r}=\mathbf{r}_1\\ \rho_p(\mathbf{r}) & \text{at } \mathbf{r}=\mathbf{r}_2\end{cases}, \tag{2.4b}$$

where $\left(\partial^2\sigma_{pp}/\partial\varepsilon\partial\Omega\right)_r\left(\left(\partial^2\sigma_{pn}/\partial\varepsilon\partial\Omega\right)_r\right)$ is the local average cross section of the pp (pn) scattering inside the nucleus, averaged over the Fermi momentum distribution of the target nucleon with the local Fermi momentum $k_F(\mathbf{r})$ based on the local Fermi-gas model , with the Pauli principle taken into account[9]. $\rho_p(\mathbf{r})$ ($\rho_n(\mathbf{r})$) is the proton (neutron) density at $\mathbf{r}$. E_m is the energy and γ_ν is the imaginary part of the wave number of the intermediate fast particle of kind ν. k_i (k_f) is the asymptotic wave number of the incident (outgoing) nucleon. Since the sudden approximation is made for intermediate steps in the SCDW model, there are four different intermediate nuclear states leading to one final state. The scattering amplitude is given by a sum of those of the four processes. The interference terms of those amplitudes in the cross section are neglected since they are small compared with the cross sections of the individual processes[7].

The main ingredients in eqs. (2.1) and (2.2) are as follows: (i) the incoming and outgoing distorted waves, and the Green function describing the propagation of the fast particle in intermediate states, (ii) the nucleon-nucleon (N-N) scattering cross section inside the nucleus, and (iii) the nuclear density. The distorting potentials for the fast nucleon in the initial, the intermediate and the final states are taken to be the global optical potentials whose parameters are given in ref.[10] for energies less than 80 MeV and in ref.[11] for energies above 80 MeV. As for (ii), two types of the N-N scattering cross sections are compared for investigation of nuclear medium effect on the N-N scattering. One is a free N-N empirical formula[12] used in the same way as in ref.[8]. Another is a parameterized formula[13] of the density-dependent N-N cross section (which is called the in-medium N-N cross section)

derived from the G-matrix theory. For the nuclear density, the Wood-Saxson shape with the geometrical parameter given by Negel[14] is used.

Furthermore, the nonlocality correction of the distorting potentials is made using the Perey factor defined in ref. [15] as in the previous calculations[8] of the one-step SCDW cross section. Similarly, the nonlocality correction for the Green function $G(\mathbf{r}_2,\mathbf{r}_1)$ describing the propagation in the two-step process is made by multiplication of two Perey factors $F(\mathbf{r})$ as follows:

$$G_{NL}(\mathbf{r}_2,\mathbf{r}_1) = F(\mathbf{r}_2)G_L(\mathbf{r}_2,\mathbf{r}_1)F(\mathbf{r}_1), \tag{2.5}$$

where the subscripts *NL* and *L* mean the nonlocal and the local Green functions, respectively, and the nonlocality range β is taken to be 0.85 fm[8,15].

As mentioned above, all physical quantities necessary for the calculation of eqs.(2.1) and (2.2) are determined on the basis of experiments and/or theoretical models without any adjustable parameters. Thus our SCDW model calculation has no free parameter, which is different from the other QM models, such as the FKK model including an adjustable parameter (e.g., the strength V_0 of effective interaction) to determine the magnitude of the MSD cross section.

III. RESULTS AND DISCUSSIONS

Using Monte Carlo numerical integration with quasi-random numbers [16], we have developed a code[17] to calculate the double differential one- and two-step MSD cross sections for nucleon emission in nucleon-induced reactions.

In Fig.2, the results calculated with (a) the free N-N cross sections and (b) the in-medium N-N cross sections are compared with the experimental data[18] for the ^{58}Ni(p,xp) reaction at 120 MeV. The case of (a) shows remarkable overprediction at low ejectile proton energies of 40 and 60 MeV, in particular, for the two-step cross sections at forward angles. By use of the in-medium N-N cross section, the overprediction of two-step cross sections is improved and reasonably good agreement is obtained at 100 MeV of the ejectile energy, except at small angles around 20°. This improvement seen in (b) may indicate the importance of nuclear medium effects in the MSD calculations, although the overprediction at low ejectile energies still remains to the extent of a factor of three.

In the above calculations, the nonlocality correction for a nucleon inside the nucleus was neglected. Therefore, we took into account the correction using the Perey factor as well. In the SCDW model, the nuclear state at a give $\mathbf{r}$ is described as a plane wave with the momentum $\mathbf{k}_2(\mathbf{r})$ in terms of the local Fermi-gas model. Here we regard the local equivalent potential influencing a nucleon in the momentum with $\mathbf{k}_2(\mathbf{r})$ as $U(\mathbf{r})= -(S+E_F(\mathbf{r}))$, where S is

the separation energy and $E_F(\mathbf{r})$ is the local Fermi energy calculated from the nuclear density $\rho(\mathbf{r})$. For the bound states, the Perey factor should be equal to unity, that is, no Perey effect exists. On the other hand, in the case where the struck nucleon is in an unbound state, we should multiply the plane wave with the momentum $\mathbf{k'}_2(\mathbf{r})$ for the struck nucleon by the Perey factor. To calculate the Perey factor, in practice, we assume that the local equivalent potential for a nucleon with $\mathbf{k'}_2(\mathbf{r})$ is same as the global optical potential used in the calculation of incoming and outgoing distorted waves.

The result calculated by taking this correction into account is shown in Fig.2 (c). The one-step cross sections reduce slightly compared with the case of (b). However, much larger reduction is seen for the two-step cross sections at small angles. As a result, the agreement with the experimental data[18] is found to be improved as the energy transfer becomes large. This reduction may be because it is more likely that both nucleons after collision (the fast nucleon and the struck nucleon) are excited into unbound final states with increasing the energy transfer and the Perey factor for the struck nucleon becomes less than unity. The underprediction seen at backward angles is possibly responsible for exclusion of the three-step SCDW calculation.

In addition, SCDW results for the ^{58}Ni(p,p'x) reactions at incident energies of 200 MeV and 65 MeV are shown together with the experimental data in Figs.3 and 4, respectively. The former result gives quite good agreement with the experimental data over the wide outgoing energy range, except at backward angles larger than 100°. The disagreement may be because the higher step MSD processes are not included in the present SCDW calculation. As shown in Fig.4, the SCDW model reproduce satisfactorily the experimental data at small angles less than 90° even at such a low incident energy as the semiclassical approximations are supposed to become worse.

Figure 5 shows comparisons of the SCDW calculation with the experimental data[20] for the ^{90}Zr(p,p'x) reaction at 120 MeV. The SCDW calculation with all corrections (the solid line) is in better agreement with the experimental data than that with the free N-N cross section (the dotted line), especially at 20 MeV of the low outgoing energy. The intranuclear cascade (INC) model calculation[21] is also compared with the SCDW. A remarkable underprediction seen at large angles in the INC calculation, especially for 100 MeV of the high outgoing energy, is improved obviously by the SCDW calculation. The major reason may be because the refraction effect is taken into account explicitly by using the distorting potentials. Some underestimation at backward angles still remains for 20 MeV. This may be because the SCDW components of more than three-step are not included in the present calculation.

The SCDW model is applicable to (p,xn) reactions as well. We show the angular distribution of the ^{90}Zr(p,xn) reaction at 120 MeV as one of the examples in Fig. 6. The

calculation is in reasonably good agreement with the experimental data[22] to the same extent as the ^{90}Zr(p,p'x) reaction.

In Figs. 2 to 6, we find that the calculated angular distribution of the one-step process has a broad peak structure. The peak position is nearly equal to that of the quasi-free scattering(e.g., 45° for the case of the outgoing energy of 60 MeV for the incident energy of 120 MeV in Fig.1). In such cases, it was found that the collision between an incident nucleon and a target nucleon occurs primarily in the peripheral region of the nucleus . The target nucleon in the peripheral region has the small momentum because the Fermi momentum in the peripheral region is much smaller than that in the center according to the local Fermi-gas model. Thus it is expected that the collision process with the incident nucleon resembles the quasi-free scattering process. However, the peak has a broad shape owing to the Fermi motion of target nucleons and the distortion effect of incoming and outgoing waves.

Finally, we remark on a comparison of our SCDW calculations with the other calculations based on the FKK theory[23] or microscopic simulation methods such as QMD[24] and AMD[25]. Those models can reproduce the experimental data to similar extent. When comparing those step-wise components, however, we notice that the two-step SCDW component is larger compared with the other models, especially, for low ejectile energies. Such larger two-step cross section is also seen in a calculation made by Koning and Akkermans[26] in terms of the NWY theory in which the same sudden approximation is made for intermediate steps as in the SCDW model. For further discussions about the difference in the two-step cross section among the models, it would be necessary to extend the present SCDW model dealing with only the one- and two-step processes so that the three-step process can be calculated.

IV. SUMMARY

We have proposed the semiclassical distorted wave (SCDW) model which is derived as a semiclassical approach to the DWBA method of describing multistep direct process into continuum. The SCDW model has no adjustable parameter such as the interaction strength V_0 in the FKK model. Using the SCDW code which has been extended so that both of the one- and two-step MSD cross sections are calculated with Monte Carlo integration, we have analyzed several (p,p'x) and(p,xn) reactions in the incident energy range from 65 MeV to 200 MeV. Through the analyses, we have found it essential to use the in-medium N-N cross sections instead of the free N-N cross sections and to take account of the nonlocality correction for the mean nuclear field in order to improve the overprediction of the two-step cross sections. As a result, overall good agreement with the experimental data was obtained.

From comparisons of the SCDW calculation with the other model calculations (QMD, AMD, and FKK), it was found that the two-step SCDW cross section is larger than the others.

The reason is not clear at present, and it would be necessary to continue the comparisons from various viewpoints. Since, in particular, the present SCDW model does not include the three-step component, the SCDW model should be extended along the direction and the preliminary calculation is now in progress. In addition, we plan to make further investigation about the g-matrix used in the calculation of in-medium N-N cross section and the effect of the target nucleons with high momentum for which the local Fermi-gas model with zero-temperature cannot account.

Acknowledgements

The authors wish to express their thanks to Dr. M. Kono (Kyushu Dental College) for helpful comments about the G-matrix theory and the nonlocality correction. They also acknowledge Dr. S. Chiba (JAERI), Dr. M.B. Chadwick (LLNL), Prof. H. Horiuchi and Dr. E.I. Tanaka (Kyoto University) for valuable discussions. We are indebted to Research Center for Nuclear Physics, Osaka University, for use of the computer FACOM M1800 and financial support for computation at the Computer Center of Kyushu University with the computer FACOM M1800/VP2600.

References

[1] E. Gadioli and P.E. Hodgson, *Pre-Equilibrium Nuclear Reactions*, (Oxford University Press, 1992).

[2] H. Feshbach, A.K. Kerman, and S. Koonin, Ann. of Phys. **125**, 429 (1980).

[3] T. Tamura, T. Udagawa, and H. Lenske, Phys. Rev. C **26**, 379 (1982).

[4] N. Nishioka, H.A. Weidenmüller, and S. Yoshida, Ann. of Phys. **183**, 166 (1988); **193**, 195 (1989).

[5] See for instance, P.E. Hodgson and M.B. Chadwick, *Proc. of Int. Conf. on Nuclear Data for Science and Technology,* Gatlinburg, Tennessee, U.S.A, May 9-13, 1994, Ed. by J.K. Dickens, (American Nuclear Society, Inc., 1994), p. 519.

[6] Y. Luo and M. Kawai, Phys. Rev. C **43**, 2367 (1991).

[7] M. Kawai and H.A. Weidenmüller, Phys. Rev. C **45**, 1856 (1992).

[8] Y. Watanabe and M. Kawai, Nucl. Phys. **A 560**, 43 (1993).

[9] K.Kikuchi and M. Kawai, *Nuclear Matter and Nuclear Reactions,* (North-Holland, Amsterdam, 1968).

[10] R.L. Walter and P.P. Guss, *Proc. Int. Conf. Nucl. Data for Basic and Applied Science*, Santa Fe, 1985, p. 1075.

[11] P. Schwandt et al., Phys. Rev. C **26**, 55 (1982).

[12] N. Metropolis et al., Phys. Rev. **110** (1958).

[13] G. Q. Li and R. Machleidt, Phys. Rev. C **48**, 1702 (1993); **49**, 566 (1994).

[14] J. W. Negel, Phys. Rev. C **1**, 1260 (1970).

[15] F.G. Perey and B. Buck, Nucl. Phys. **32**, 353 (1962).

[16] C.B. Haselgrove, Math. Comp. **15**, 323 (1961); Y. Akaishi, private communication (1993).

[17] H. Shinohara, Master Thesis, Kyushu University (1993); H. Shinohara et al., preprint KU-ECE(NS)-94-01 (1994).

[18] S.V. Förtsch et al., Phys. Rev. C **43**, 691 (1991).

[19] H. Sakai et al., Nucl. Phys. **A344**, 41 (1980).

[20] A.A. Cowley et al., Phys. Rev. C **43**, 678 (1991).

[21] H. Takada, private communication (1993); the INC calculation was performed with a HETC code.

[22] W. Scobel et al., Phys. Rev. C **41**, 2010 (1990).

[23] M. B. Chadwick et al., Phys. Rev. C **50**, 996 (1994).

[24] S. Chiba et al., *Proc. of Int. Conf. on Nuclear Data for Science and Technology,* Gatlinburg, Tennessee, U.S.A, May 9-13, 1994, Ed. by J.K. Dickens, (American Nuclear Society, Inc., 1994), p. 505; To be published in *Proc. of the Second Symposium on Simulation of Hadronic Many-body Sytem*, Tokai, JAERI, Nov.30 - Dec.2, 1994.

[25] E. I. Tanaka et al., preprint KUNS 1319 (1995).

[26] A.J. Koning and J.M. Akkermans, Phys. Rev. C **47**, 724 (1993).

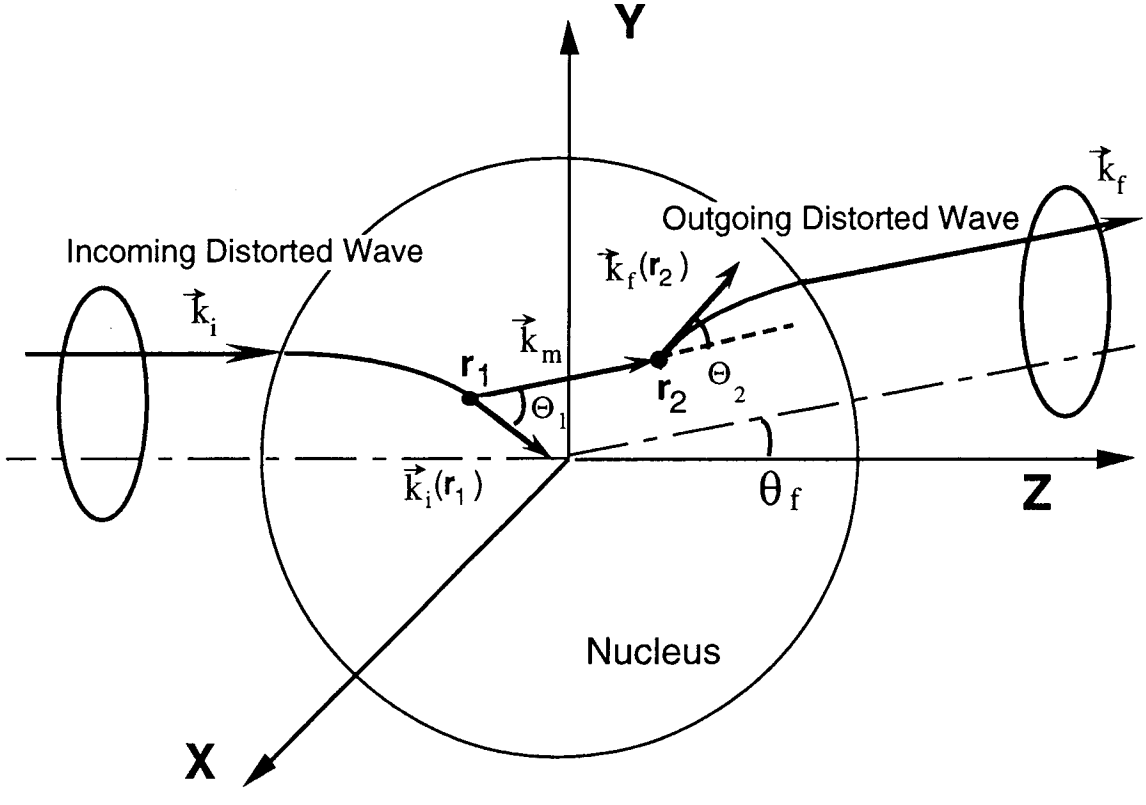

Fig.1 Schematic picture of two-step process based on the SCDW model.

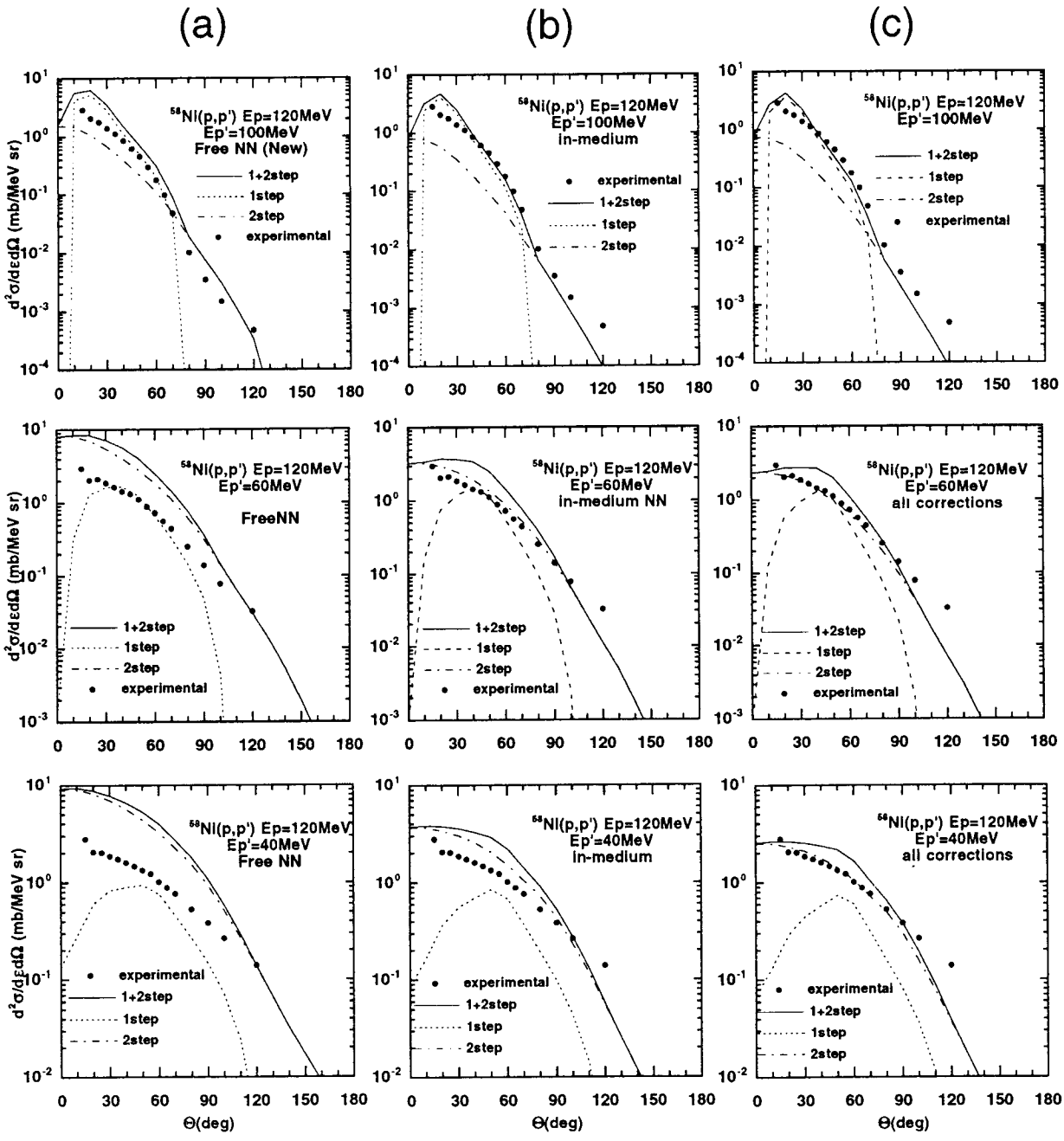

Fig.2 Comparisons of the SCDW calculation and the experimental data for ^{58}Ni(p,p'x) at 120 MeV. The dotted and the dash-dotted lines present the one-step and the two-step SCDW calculations, respectively, and the solid line is their sum. (a) The case with the free NN cross section. (b) The case with the in-medium NN cross section and (c) The case where the nonlocality correction is taken into account for the struck nucleon in addition to the calculation of (b). See the details in text. The experimental data are taken from ref. [18].

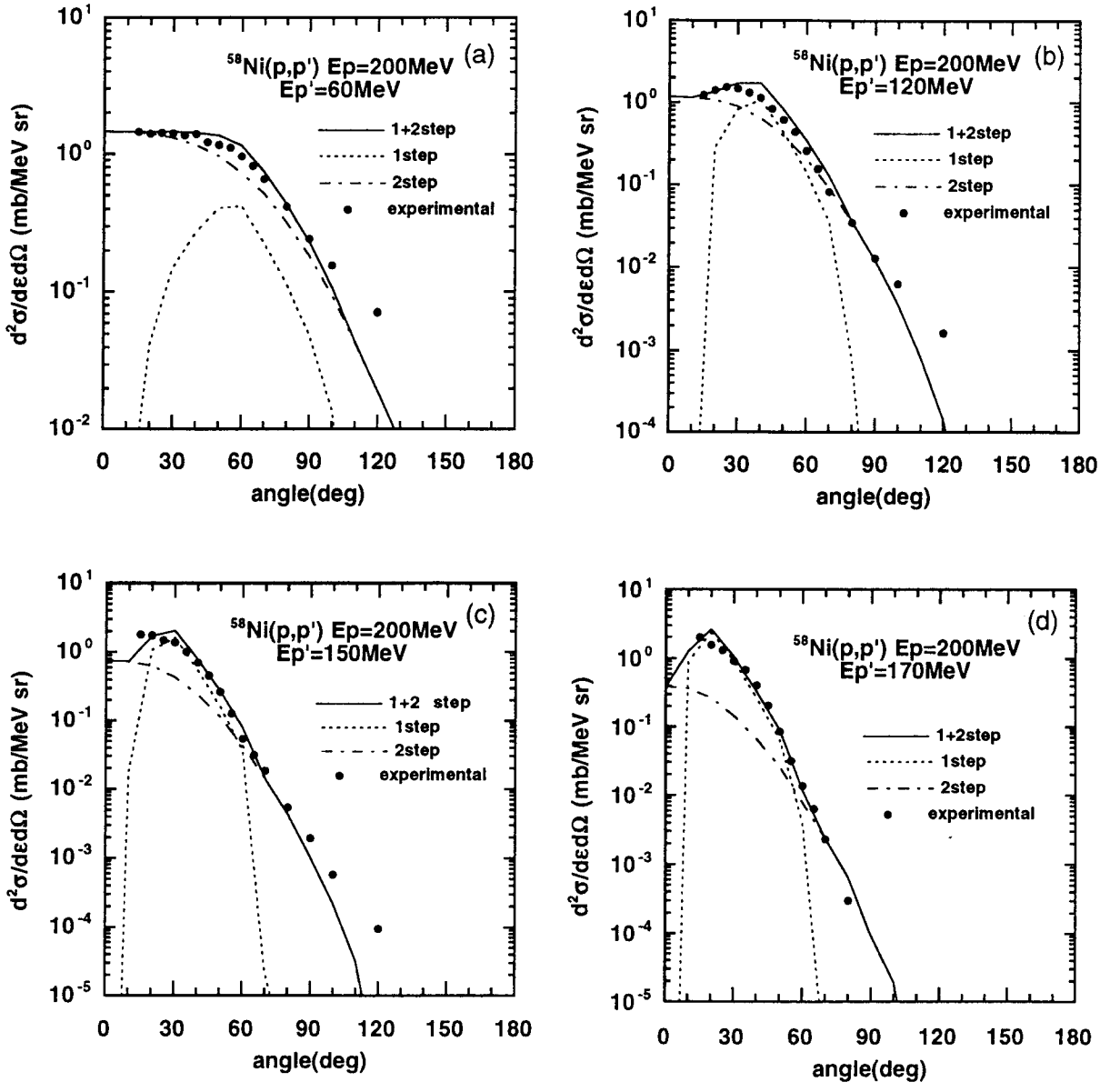

Fig. 3 Angular distribution of ^{58}Ni(p,p'x) at 200 MeV for outgoing energies of (a) 60, (b) 120, (c) 150, and (d) 170 MeV. The dotted and the dash-dotted lines present the one-step and the two-step SCDW calculations with all corrections, respectively. The solid line is their sum. The experimental data are taken from [18].

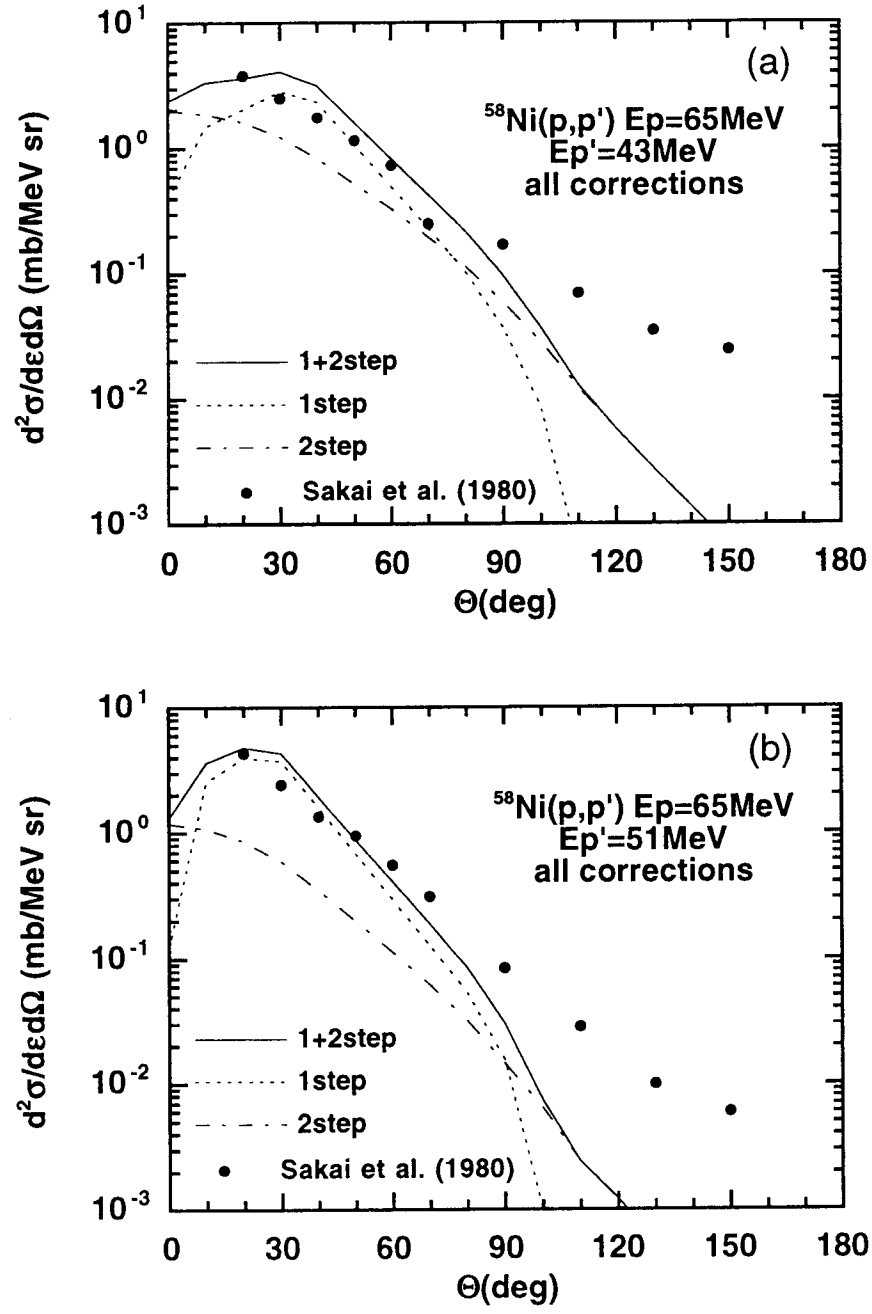

Fig.4 Angular distribution of ^{58}Ni(p,p'x) at 65 MeV for outgoing energies of (a) 43 MeV and (b) 51 MeV. The closed circles are experimental data taken from ref. [19]. Also, see Fig.3 for the explanation of each line.

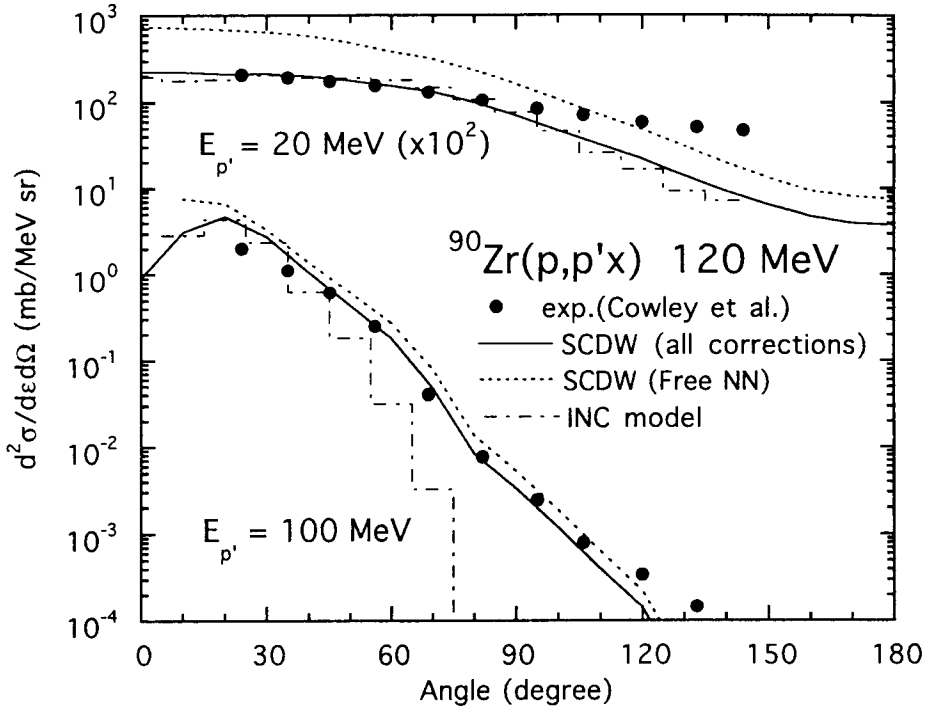

Fig.5 Angular distribution of ^{90}Zr(p,p'x) at 120 MeV for outgoing energies of $E_{p'}$=20 MeV and 100 MeV. The solid and dotted lines present the SCDW calculations with all corrections (see in Fig.1(c)) and with the Free N-N cross section (see in Fig.1(a)), respectively. The dash-dotted histogram denotes the INC model calculation.The data are taken from ref. [20].

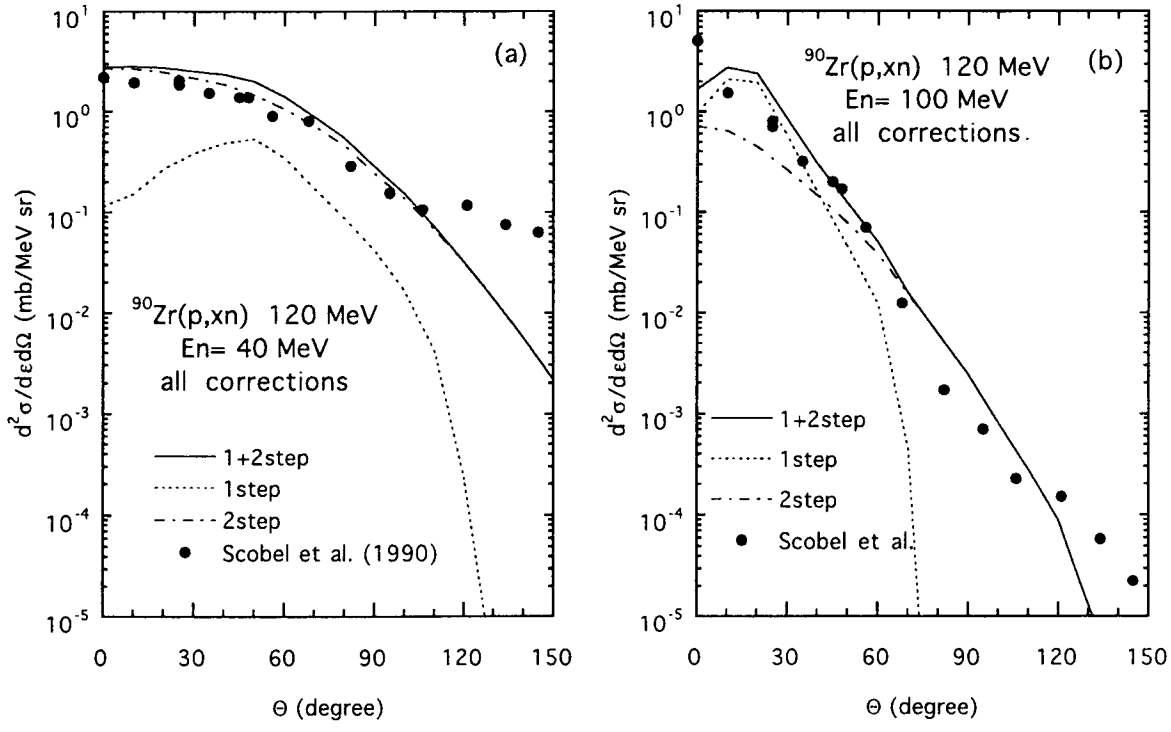

Fig.6 Angular distribution of ^{90}Zr(p,xn) at 120 MeV for outgoing energies of (a) E_n=40 MeV and (b) 100 MeV. The dotted and dash-dotted lines present the one-step and the two-step SCDW calculations, respectively. The solid line is their sum. The experimental data are taken from ref. [22].

1.2 Progress in Quantum Molecular Dynamics

Toshiki Maruyama
Advanced Science Research Center, JAERI,
Tokai, Naka, Ibaraki, 319-11 Japan

1. Introduction

Nuclear reactions from several MeV/u to several GeV/u show much variety in reaction mechanisms. In the low energy region below about ten MeV/u, such process dominate as fusion, fission, elastic scattering, deep inelastic scattering, and so on. Above 100 MeV/u, there occur the fragmentation of the total system for central collisions or the fragmentation of the participant region for non-central collisions. In medium energies, there appear more complex mechanisms such as incomplete fusion, deep inelastic scattering with the many nucleon transfer and the pre-equilibrium nucleon emission. If the time evolution of reaction is discussed, low-energy phenomena, such as evaporation of nucleons from the excited fragments, occur after the high-energy phenomena, e.g., fragmentation. In the traditional theoretical study of nuclear reactions, a specific model is made for the corresponding reaction mechanism. However, such a model is valid only for one phenomenon but can not be used for others.

With the progress of computers, microscopic simulation methods have become popular. In the simulations, one calculates the time evolution of the system based on the nucleon-nucleon interactions or mean-field potentials. The benefit of microscopic simulation method is that one can investigate nuclear reactions without making any specific assumption on the reaction mechanism. There are many kinds of microscopic simulations such as the time-dependent Hartree Fock (TDHF)[1] which is a mean-field theory, Vlasov equation which is the semiclassical approximation of TDHF, Vlasov-Uehling-Uhlenbeck (VUU) equation or Boltzmann-Uehling-Uhlenbeck (BUU) equation[2] in the other name, which are similar to Vlasov but including the two-body collision term, the Cascade model[3] which includes only two-body collision term, and so on. Especially, VUU/BUU equation, which includes both of mean-field and two-body collision term, is available from the low or intermediate energy to the high energy region and has become a standard framework for the heavy-ion reaction study. However, VUU equation, which is basically one-body theory, has a difficulty in dealing with the phenomena of fluctuation such as the fragment formation.

Molecular dynamics approaches like quantum molecular dynamics (QMD)[4] have been developed in order to calculate the fragmentation process. In QMD, we

assume a single-particle distribution function of a nucleon as the Gaussian wave packet, and calculate the time evolution of the system according to the classical Newtonian equation of motion and to the two-body collision term. It contains both effects of the mean-field and two-body collisions, and is available in the wide energy-region. Furthermore, QMD can deal with the fragment formation since it is a many-body framework which traces the motion of each nucleon. In this paper, the author would like to discuss on the framework of QMD method, especially mainly on two improvements of QMD in which the group of the author is concerned, such as the extensions of QMD for the relativistic energy region and for the low energy region.

2. Formulation of QMD

QMD deals with the time-evolution of the many-body system of Gaussian wave packets. The time-evolution is described by two elements: the classical Hamilton equation of motion and the two-body collision term with the Pauli-blocking factor.

We assume the total wave function of the system to be a direct product of nucleon wave packets:

$$\Psi = \prod_i \phi_i(\mathbf{r}_i) \ , \tag{2.1}$$

$$\phi_i(\mathbf{r}_i) = (\nu\pi)^{3/4} \exp\left[-\frac{\nu}{2}(\mathbf{r}_i - \mathbf{R}_i)^2 + \frac{i}{\hbar}\mathbf{P}_i \cdot \mathbf{r}_i\right] \ . \tag{2.2}$$

Here $\mathbf{R}_i$ and $\mathbf{P}_i$ are centers of the space- and the momentum-coordinate, and ν is the width parameter of wave packets, the value of which we take as $0.25 \sim 0.5$ fm^{-2}. To obtain the equation of motion which is the smooth part to define the time evolution of the system, we start from the time-dependent variational principle

$$\delta \int_{t_1}^{t_2} \mathcal{L} dt = 0 \ , \tag{2.3}$$

$$\mathcal{L}(\{\mathbf{R}_i, \mathbf{P}_i, \dot{\mathbf{R}}_i, \dot{\mathbf{P}}_i\}) = \langle\Psi|i\hbar\frac{d}{dt} - \hat{H}|\Psi\rangle \ . \tag{2.4}$$

and finally we get

$$\dot{\mathbf{R}}_i = \frac{\partial H}{\partial \mathbf{P}_i} \ , \quad \dot{\mathbf{P}}_i = -\frac{\partial H}{\partial \mathbf{R}_i} \ , \tag{2.5}$$

$$H = \langle \Psi | \hat{H} | \Psi \rangle \ . \tag{2.6}$$

In the Hamiltonian, the term from the variance of momentum of each wave packet is subtracted, since it is a constant spurious term.

$$H = \langle \Psi | \sum_i -\frac{\hbar^2}{2m} \nabla_i^2 + \hat{H}_{\rm int} | \Psi \rangle \tag{2.7}$$

$$= \sum_i \frac{\mathbf{P}_i^2}{2m} + H_{\rm int} \ . \tag{2.8}$$

As effective interactions, we adopt the Skyrme force, the symmetry energy and the Coulomb force,

$$H_{\rm int}(\{\mathbf{R}_{ij}\}) = H_{\rm Skyrme} + H_{\rm Coulomb} + H_{\rm Symmetry} \ . \tag{2.9}$$

Another part of the time-evolution is the stochastic two-body collision term with Pauli-blocking factor. In QMD, two-body collisions are introduced in a phenomenological way (Fig. 1). If two nucleons come within the distance corresponding to the nucleon-nucleon cross section, the final state of the collision is decided by sampling the scattering angle according to the double differential cross section. The total energy and momentum conservation is also considered. If the final state is breaking the Pauli principle, this collision is canceled with the probability of

$$P_{\rm block} = 1 - (1 - f_1')(1 - f_2'), \tag{2.10}$$

where f_1' and f_2' are the final phase-space occupations of the colliding particles 1 and 2. This prescription is analogous to the numerical treatment of the two-body collision term in the VUU/BUU equation and the cascade model.

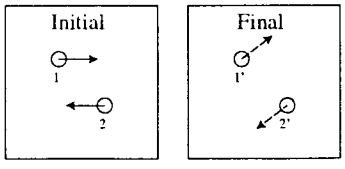

FIG. 1. Two-body collision in QMD. The final state is decided by sampling the scattering angle according to $d\sigma/d\Omega$ and considering the energy and momentum conservation. If the final state is Pauli-blocked, this scattering is canceled.

In the QMD simulation, many events are calculated to get good statistics. For all the produced fragments, their statistical decay processes into the final products are calculated[5]. In general, within a time-scale of about 100 fm/c the dynamical parts of nuclear reaction are completed, and the statistical decay process takes place afterward in a time-scale of several-order longer. Since it is not practical nor reliable to treat this statistical process in a framework of simulation, we adopt this hybrid model. If the dynamical parts of reaction are completed and while the produced fragments are excited enough, we stop the QMD calculation to switch to the statistical decay calculation.

$t = 0$	$t = t_c$	$t = \infty$
Dynamical process	Equilibrated process	
QMD calc.	Stat. Decay calc.	

With this hybrid model of QMD plus statistical decay calculation, we can well reproduce observables such as the mass distribution and the energy spectra of fragments.

3. Extension of QMD to Relativistic Energy Region ("QMDrel")

With the QMD plus statistical decay model, precise analysis of the nuclear reaction from several tens MeV/u to several hundreds MeV/u has become possible. For more common use of it, however, extension of the QMD model to the higher energy region is required. Even in the high energy region, where two-body collision process is regarded as the dominant part, effect of the mean-field is still important especially in the spectators or the residual nuclei. Therefore the framework like the QMD plus statistical decay model is much more reliable to calculate observables other than the high-energy part of spectra.

To apply QMD to the energy region above about 1 GeV/u, non-relativistic kinematics does not work. Relativistic QMD (RQMD)[6] is a fully Lorentz-covariant framework which is available even in the super-relativistic region. This model needs, however, much CPU time proportional to the third power of particle number, while the CPU time needed in the standard QMD is proportional to the second power. To resolve this point, we make an extension of QMD with the relativistic kinematics and interaction with a covariant form of nucleon-nucleon distance.[7]

$$H = \sum_i \frac{\mathbf{P}_i^2}{2m} + H_{\rm int}$$

$$\Downarrow$$

$$H = \sum_i E_i + H_{\rm int} \tag{3.1}$$

$$= \sum_i \sqrt{\mathbf{P}_i^2 + m_i^2} + H_{\rm int} \tag{3.2}$$

$$H_{\rm int}(\mathbf{R}_{ij}) \Rightarrow H_{\rm int}(\tilde{\mathbf{R}}_{ij}) \tag{3.3}$$

$$\tilde{\mathbf{R}}_{ij}^2 = \mathbf{R}_{ij}^2 + \gamma_{ij}^2 \left(\mathbf{R}_{ij} \cdot \beta_{ij}\right)^2 , \tag{3.4}$$

$$\beta_{ij} = \frac{\mathbf{P}_i + \mathbf{P}_j}{E_i + E_j}, \qquad \gamma_{ij} = \frac{1}{\sqrt{1 - \beta_{ij}^2}} \lambda \tag{3.5}$$

With this extension of QMD, the Lorentz-boosted initial nuclei keep their stability until they collide with each other. We call this extension of QMD code "QMDrel". QMDrel agrees with the standard QMD in the low energy region and it can be employed in the energy region of several GeV/u. This model is however different from the fully covariant RQMD and the result slightly depends on the reference frame of calculation.

Above about 1 GeV/u, not only elastic collisions but also inelastic channels of nucleon-nucleon into excited states of baryons and their pion-decays should be considered. We include in our code channels listed below:

$$\begin{array}{lllllllll}
1. & B_i & + & B_j & \longrightarrow & B_i & + & B_j & \text{(elastic)} \\
2. & N & + & N & \longrightarrow & N & + & \Delta & \\
3. & N & + & \Delta & \longrightarrow & N & + & N & \\
4. & N & + & N & \longrightarrow & N & + & N^* & \\
5. & N & + & N^* & \longrightarrow & N & + & N & \\
6. & N & + & \pi & \longrightarrow & \Delta & & & \\
7. & N & + & \pi & \longrightarrow & N^* & & & \\
8. & \Delta & + & \pi & \longrightarrow & N^* & & & \\
9. & & \Delta & & \longrightarrow & N & + & \pi & \\
10. & & N^* & & \longrightarrow & N & + & \pi & \\
11. & & N^* & & \longrightarrow & \Delta & + & \pi &
\end{array} \tag{3.6}$$

$N(938),\ \Delta(1232),\ N^*(1440),\ \pi(138)$

As elastic cross sections below 1 GeV we employ the Cugnon parameterization[8], and above 1 GeV a fitting from experimental data:

$$\sigma = \frac{C_1}{1 + 100(\sqrt{s} - M_i - M_j - C_3)} + C_2 \ [\text{mb}]$$

$$(E_{\rm lab}(N\!-\!N) < 1 \text{ GeV} : \text{Cugnon parameterization}) \qquad (3.7)$$

$$\sigma = C_4 \left[1 - \frac{2}{\pi}\tan^{-1}\left(1.5(\sqrt{s} - M_i - M_j - C_3) - 0.8\right)\right] + 7 \text{ [mb]}$$

$$(E_{\rm lab}(N\!-\!N) \geq 1 \text{ GeV} : \text{parameterization from exp.}) \qquad (3.8)$$

Cross sections of the inelastic channels and their decay are determined by the experimental cross sections of pion production (Fig. 2) and the parameterization of VerWest-Arndt[9] (Fig. 3).

$$\begin{aligned}
p + p &\longrightarrow n + \Delta^{++} : \sigma_{10} + \tfrac{1}{2}\sigma_{11} \\
p + p &\longrightarrow p + \Delta^{+} : \tfrac{3}{2}\sigma_{11} \\
n + p &\longrightarrow p + \Delta^{0} : \tfrac{1}{2}\sigma_{11} + \tfrac{1}{4}\sigma_{10} \\
n + p &\longrightarrow n + \Delta^{+} : \tfrac{1}{2}\sigma_{11} + \tfrac{1}{4}\sigma_{10} \\
n + n &\longrightarrow p + \Delta^{-} : \sigma_{10} + \tfrac{1}{2}\sigma_{11} \\
n + n &\longrightarrow n + \Delta^{0} : \tfrac{3}{2}\sigma_{11} \\
p + p &\longrightarrow p + N^{*+} : \tfrac{3}{2}\sigma_{01} \\
n + p &\longrightarrow p + N^{*0} : \tfrac{3}{4}\sigma_{01} \\
n + p &\longrightarrow n + N^{*+} : \tfrac{3}{4}\sigma_{01} \\
n + n &\longrightarrow n + N^{*0} : \tfrac{3}{2}\sigma_{01}
\end{aligned} \qquad (3.9)$$

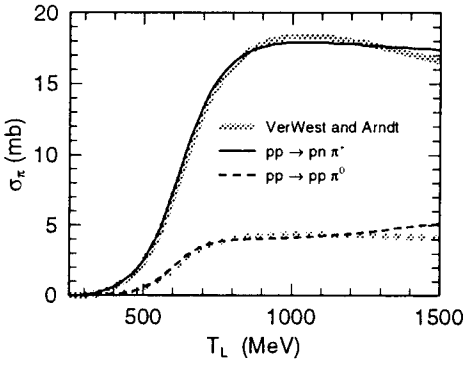

FIG. 2. Pion production cross section.

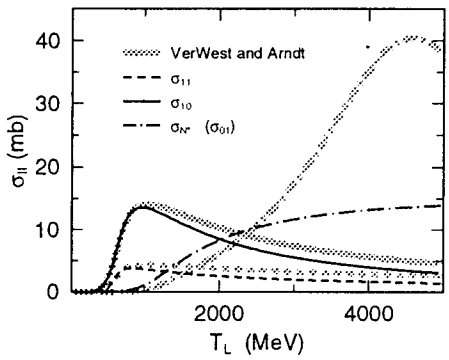

FIG. 3. Cross sections of inelastic channels.

Next, we show some results of the QMDrel calculation on nucleon-induced reactions. Figures 4∼7 show energy spectra of neutrons, protons and pions in the proton-induced collisions on ^{27}Al, ^{56}Fe and ^{208}Pb targets. The incident energies are from 113 MeV to 3.17 GeV. Experimental data are taken from Refs.[10 ∼ 12]. Though there are some deviation from experiments for the lower incident energies

at the forward-angle high-energy peak (quasi elastic peak), our calculations show overall good agreements with data. Especially at backward angles, our model fits the data better than the conventional model where the effect of the mean-field is omitted. We can describe proton-induced reactions of compound, pre-equilibrium and fragmentation processes in the unified framework of QMD plus statistical decay model with a fixed parameter set.

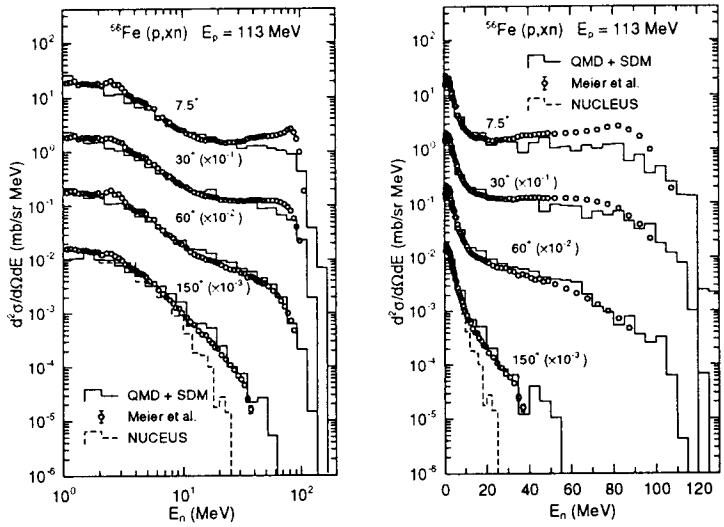

FIG. 4. Neutron spectra in p (113 MeV) + ^{56}Fe reaction. In the left hand side, the energy axis is plotted in logarithmic scale while in the right hand side shown is the same in linear scale. Open circles with error bar denote experimental data, and solid histograms denote results of the QMD plus statistical decay model. Dashed histogram at 150° is the result of NUCLEUS code[13].

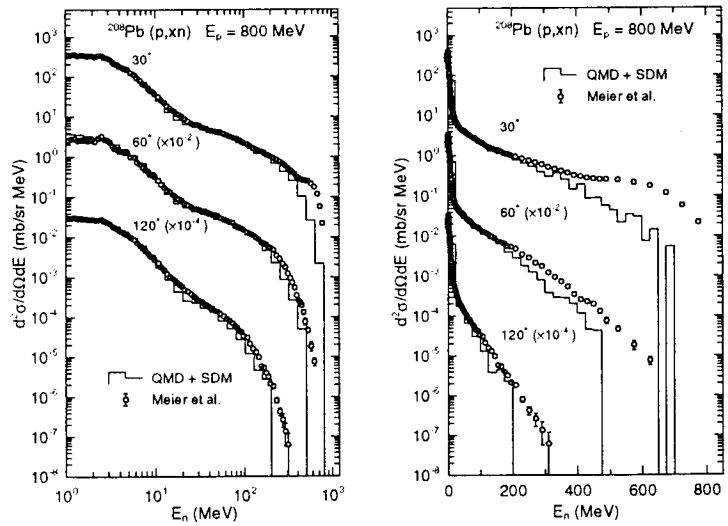

FIG. 5. Neutron spectra in p(800 MeV)+^{208}Pb reaction.

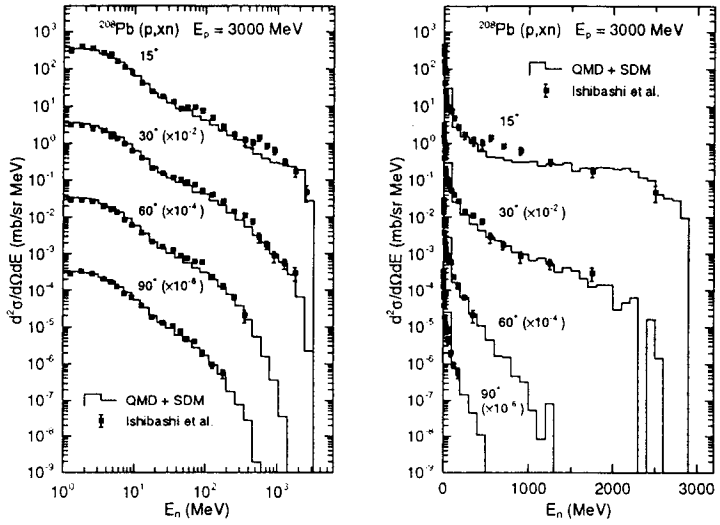

FIG. 6. Neutron spectra in p(3 GeV)+^{208}Pb reaction.

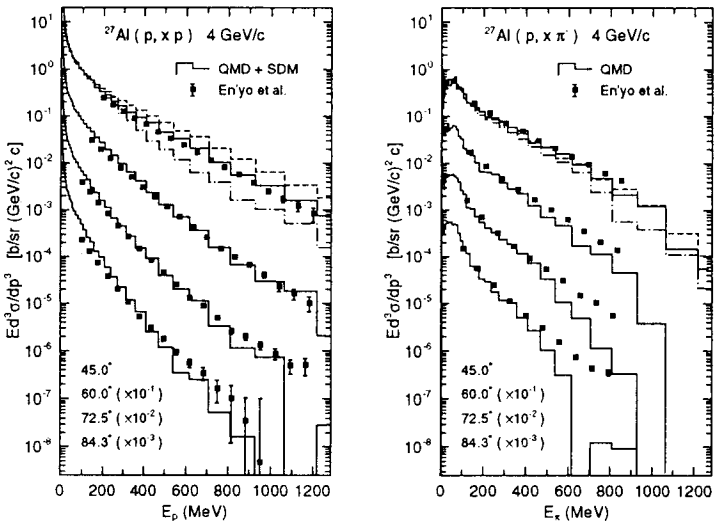

FIG. 7. Proton (left hand side) and pion (right hand side) spectra in p (4 GeV/c = 3.17 GeV) + ^{27}Al reaction.

We should check how the results depend on the time when the calculation is switched from QMD to the statistical decay model. If the fragments are already equilibrated and still are excited enough, it is desirable that there appear no switching-time dependence. Figure 8 shows the results of three cases, namely, the switching time t_{sw} of 50, 100 and 150 fm/c. The difference between t_{sw} = 100 and 150 fm/c cases is small, while the result of t_{sw}=50 fm/c obviously deviates from others. This means that the dynamical parts of reaction are completed before 100 fm/c but not before 50 fm/c. We can take, in this case, the switching time t_{sw} after around 100 fm/c.

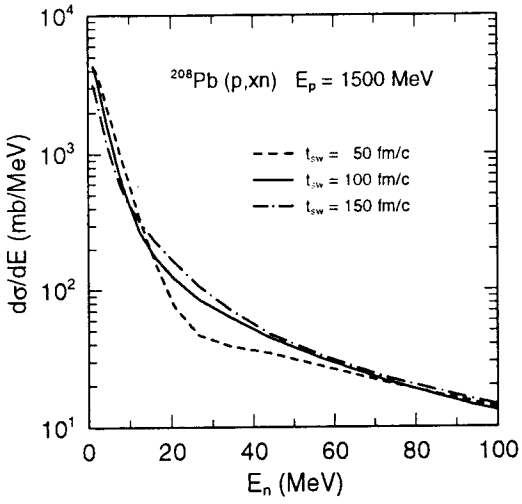

FIG. 8. Neutron spectra in p (1.5 GeV) + ^{208}Pb reaction, comparing the results for switching time t_{sw} at 50, 100 and 150 fm/c.

4. Extension of QMD to Low Energy Region ("EQMD")

Next we consider how to apply QMD to the low energy region. For the simulation of low-energy nuclear reactions, frameworks with anti-symmetrization of the total wave function like FMD[14] and AMD[15] are powerful for their fine description of ground states and reaction processes. In spite of their success specially in light heavy-ion reactions, the CPU time they consume is approximately proportional to the fourth power of the particle number. For calculations of heavy systems, application of the QMD framework (without anti-symmetrization) is still necessary.

The fusion reaction is already analyzed also using QMD.[16] It was reported that several nucleons are excessively emitted. This is due to the insufficient stability of initial ground nuclei. We have to settle this problem to study low-energy collisions of heavy systems using the molecular dynamics.

The insufficient stability of the QMD ground state is mainly due to the fact that they are not at their energy-minimum states. If we take the energy-minimum states, they break the Pauli-principle and become over-bound. The subtracted spurious energy term of momentum variance of wave packets also causes excessive binding.

Then we make an extension of QMD in two points and take energy-minimum states as the initial ground nuclei: First, we include the so-called Pauli potential into effective interactions[17] in order to approximate the nature of Fermion many-body system. Second, we make the width of each wave packet a dynamical variable[18] to add the kinetic-energy term of the momentum variance to the Hamiltonian. We call here this extension of QMD "EQMD".

In EQMD, we take as a total wave function the direct product of Gaussian wave packets:

$$\Psi = \prod_i \phi_i(\mathbf{r}_i) \ , \tag{4.1}$$

$$\phi_i(\mathbf{r}_i) = \left(\frac{\nu_i + \nu_i^*}{2\pi}\right)^{3/4} \exp\left[-\frac{\nu_i}{2}(\mathbf{r}_i - \mathbf{R}_i)^2 + \frac{i}{\hbar}\mathbf{P}_i \cdot \mathbf{r}_i\right] \ , \tag{4.2}$$

$$\nu_i = \frac{1}{\lambda_i} + i\delta_i \tag{4.3}$$

where $\mathbf{R}_i$, $\mathbf{P}_i$ and ν_i denote the centers of space and momentum coordinates and the complex width of the wave packet i. The Hamiltonian includes the kinetic energy term of wave-packet momentum variance while in the standard QMD it was subtracted as a spurious constant.

$$H = \langle\Psi|\sum_i -\frac{\hbar^2}{2m}\nabla_i^2 + \hat{H}_{\rm int}|\Psi\rangle \tag{4.4}$$

$$= \sum_i \left[\frac{\mathbf{P}_i^2}{2m} + \frac{3\hbar^2(1+\lambda_i^2\delta_i^2)}{4m\lambda_i}\right] + H_{\rm int} \ . \tag{4.5}$$

Equations of motion are derived from the time-dependent variational principle as

$$\delta\int_{t_1}^{t_2} \mathcal{L}dt = 0 \ , \tag{4.6}$$

$$\mathcal{L}(\{\mathbf{R}_i, \mathbf{P}_i, \lambda_i, \delta_i, \dot{\mathbf{R}}_i, \dot{\mathbf{P}}_i, \dot{\lambda}_i, \dot{\delta}_i\}) = \langle\Psi|i\hbar\frac{d}{dt} - \hat{H}|\Psi\rangle \tag{4.7}$$

and we get Newtonian equations for $\mathbf{R}_i, \mathbf{P}_i$ and for the real- and imaginary-parts λ_i, δ_i of wave packet width.

$$\begin{aligned} \dot{\mathbf{R}}_i &= \frac{\partial H}{\partial \mathbf{P}_i} \ , \quad \dot{\mathbf{P}}_i = -\frac{\partial H}{\partial \mathbf{R}_i} \ , \\ \frac{3\hbar}{4}\dot{\lambda}_i &= -\frac{\partial H}{\partial \delta_i} \ , \quad \frac{3\hbar}{4}\dot{\delta}_i = \frac{\partial H}{\partial \lambda_i} \ . \end{aligned} \tag{4.8}$$

The interaction term includes ordinary effective interactions and the so-called Pauli potential which is introduced to approximate the nature of Fermion many-body system,

$$H_{\rm int} = H_{\rm Skyrme} + H_{\rm Yukawa} + H_{\rm Coulomb} + H_{\rm Symmetry} + H_{\rm Pauli} \ . \tag{4.9}$$

$$H_{\rm Pauli} = \frac{c_P}{2}\sum_i (f_i - f_0)^2\theta(f_i - f_0) \ , \tag{4.10}$$

$$f_i \equiv \sum_j \delta(S_i, S_j)\delta(T_i, T_j)\,|\langle\phi_i|\phi_j\rangle|^2 \ , \tag{4.11}$$

where f_i is the overlap with same kinds of particles (including itself). If f_i exceeds the threshold value f_0 (≈ 1), the repulsive force suppresses their large overlapping. The values of f_0 and c_P are adjustable parameters.

To simulate nuclear reactions, one have to prepare energy-minimum states as initial ground nuclei. They are obtained by starting from a random configuration and by solving the damping equations of motion as

$$\begin{aligned} \dot{\mathbf{R}}_i &= \frac{\partial H}{\partial \mathbf{P}_i} + \mu_{\rm R}\frac{\partial H}{\partial \mathbf{R}_i} \ , \quad \dot{\mathbf{P}}_i = -\frac{\partial H}{\partial \mathbf{R}_i} + \mu_{\rm P}\frac{\partial H}{\partial \mathbf{P}_i} \ , \\ \frac{3\hbar}{4}\dot{\lambda}_i &= -\frac{\partial H}{\partial \delta_i} + \mu_\lambda\frac{\partial H}{\partial \lambda_i} \ , \quad \frac{3\hbar}{4}\dot{\delta}_i = \frac{\partial H}{\partial \lambda_i} + \mu_\delta\frac{\partial H}{\partial \delta_i} \ . \end{aligned} \tag{4.12}$$

Here $\mu_{\rm R}$, $\mu_{\rm P}$, μ_λ and μ_δ are damping coefficients with negative values. As shown in Fig. 9, the ground-state binding energies of our model well agree to observed values from light to very heavy nuclei.

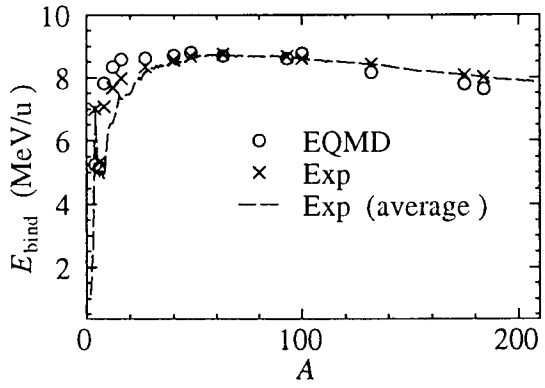

FIG. 9. Binding energies per nucleon of ground state nuclei. Open circles denote our model, crosses denote corresponding experimental values, and dashed line average of stable isotopes.

As for the shapes (density distribution) of ground states we show some results. In the case of light nuclei, e.g., ^{12}C, we can describe the α-clustering structures as displayed in Fig. 10. For heavy nuclei, the density profiles (upper parts of Fig. 11) are also well reproduced with reasonable density and reasonable surface thickness. The lower parts of Fig. 11 shows the distribution of the real parts of nucleon wave-packet widths. The horizontal axes represent the distance of the wave packet from the center. Wave packets near the center are spatially wide-spread more than those near the surface. Please note that this fact does not mean the kinetic-energy density is higher at the surface since the imaginary part of the width also contributes to

kinetic energy and the overall density distribution is flat or a little higher near the center.

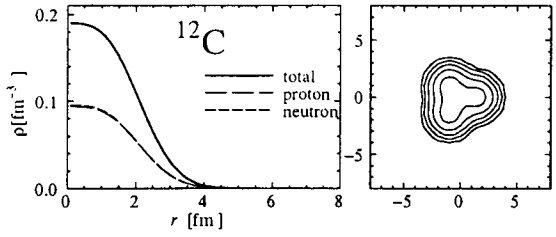

FIG. 10. Radial distribution (left hand side) and the contour plot (right hand side) of density in ^{12}C.

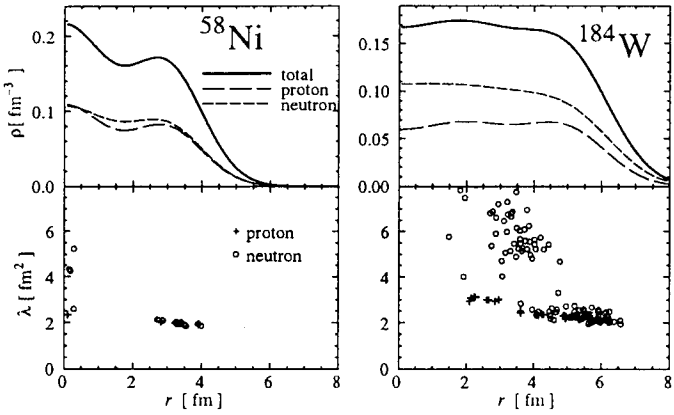

FIG. 11. Density distribution (upper parts) and Gaussian widths (lower parts) of ^{58}Ni and ^{184}W nuclei. Horizontal axes for both denote the distance from the center.

Next, we apply our model to nucleus-nucleus collisions. In the calculation of nucleus reaction we boost two initial nuclei according to the incident energy and then solve the EQMD equation of motion together with the two-body collision term as in the usual QMD. Before applying to very low energy collisions, we test out model in light heavy-ion collisions at Fermi-energies. Figure 12 shows our calculation of fragment production cross sections in the ^{12}C+^{12}C(29 MeV/u) reaction compared with other models such as the standard QMD (QMDstd) and AMD[15] which agrees to the experimental data especially for light fragments. Solid lines show the final fragment distribution after the statistical decay calculation while dashed lines show fragments at finite time (before the statistical decay). Though the final results of three models are quite similar, there are some differences between them before the statistical decay. Especially, AMD and QMDstd obviously differ with each other: In the AMD result, enhancement of $A_f = 4$ and 8 (N alpha fragments) is seen while there is no peak at $4N$ in the QMDstd result. This is mainly because AMD can describe three-α structure in ^{12}C while QMDstd can not. Present result of EQMD shows some enhancement of $4N$ fragments like AMD. Dynamical emissions of α clusters are, to some degree, described due to the improvement of ground states in our model.

To see the effect of dynamical treatment of wave-packet width, we also com-

pare the result of constrained calculation with fixed width (lower-right part of Fig. 12). In this calculation we solve the equation of motion only for $\mathbf{R}_i$ and $\mathbf{P}_i$ ($6N$-dimensional calculation), however, exactly the same interactions and initial conditions as the full EQMD are used. (In this sense this calculation is not of QMDstd.) With fixed wave-packet widths, the distribution of dynamically produced fragments has strong peaks at $A_f = 4N$. Productions of other fragments and nucleons are extremely hindered. In full EQMD calculations, contrarily, nucleons can be emitted from fragments by changing widths and releasing their internal kinetic-energies.

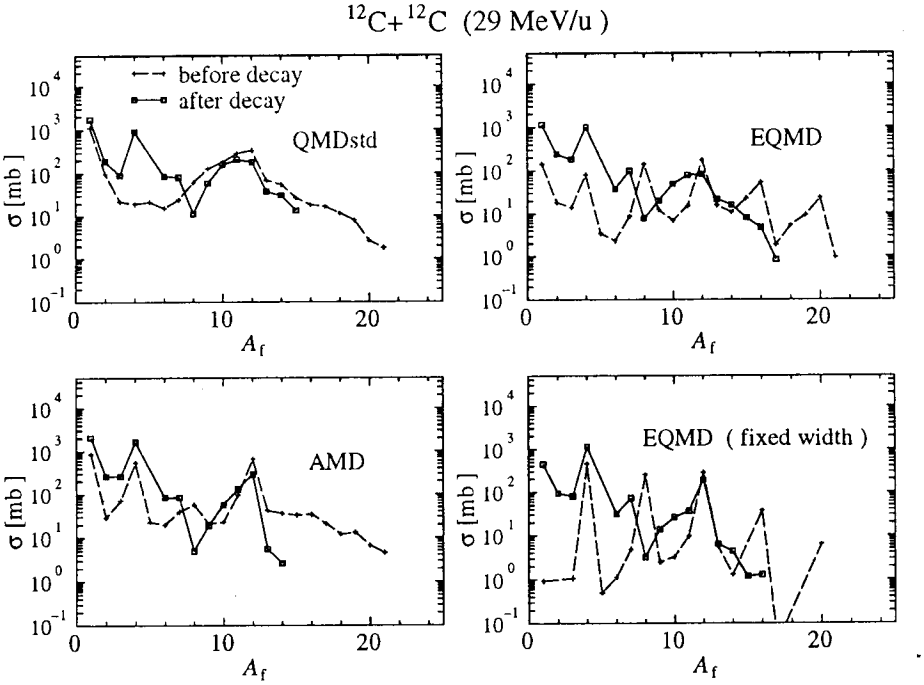

FIG. 12. Fragment mass distribution in ^{12}C+^{12}C(29 MeV/u) reaction. Dashed lines denote fragments at finite time (before statistical decay calculation), while solid lines denote final fragments after statistical decay.

Tough we have not carried out any quantitative analysis on very low energy reactions, which is our main aim of this extension of QMD, we show in Fig. 13 a preliminary result of ^{63}Cu+^{63}Cu (5 MeV/u) comparing the full EQMD calculation with the constrained fixed-width calculation. In the case of full calculation the fusion of two nuclei occurs, while they are scattered with each other in the fixed-width case. This comparison indicates the insufficiency of the model space where the total wave-function is only a direct product of wave packets with fixed widths. We expect the dynamical treatment of wave-packet width is, to a certain extent, an improvement on this point.

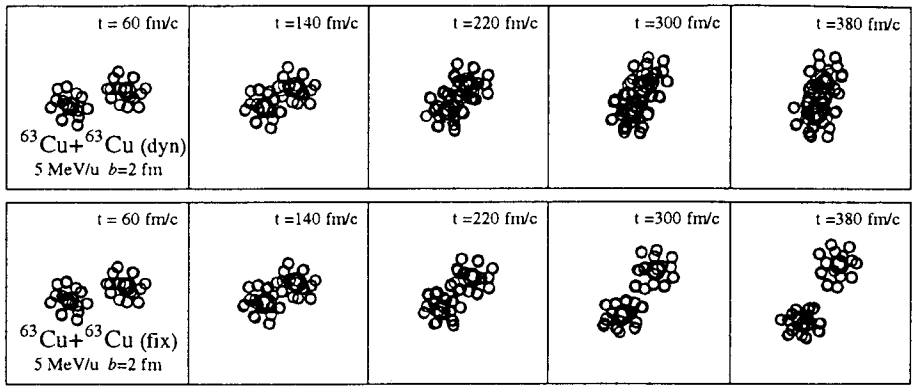

FIG. 13. An example of ^{63}Cu+^{63}Cu (5 MeV/u) reaction. Upper part shows full EQMD calculation of $8N$-dimensional equation of motion, while the lower part shows $6N$-dimensional constrained calculation with fixed width.

5. Summary

In this paper a microscopic simulation method of the quantum molecular dynamics (QMD) and its extensions to high- and low-energy regions are reported. Combined with the statistical decay calculation, QMD can reproduce experimental data with fixed and very few parameters.

First, we have made an extension of the QMD model to the relativistic energy region by employing the relativistic kinematics together with the relativistic expression of interactions and introducing baryon-baryon inelastic channels. This model can reproduce particle spectra in nucleon induced reactions from several hundreds MeV to several GeV. According to the success of our model, nucleon-induced reactions are well described as the two-nucleon collisions in the nuclear potential and the following statistical decays.

Second, we have introduced a phenomenological Pauli potential into effective interactions and have made the width of each wave packet a dynamical variable. With this extension of QMD, we can make a fine description of the ground states such as α-clustering structure in light nuclei and good density profiles in heavy nuclei. In the calculation of nucleus-nucleus collisions, this model has an ability to describe such processes as dynamical emission of alpha clusters or fusion at low energies. We are planning to apply this model for very low energy collisions of heavy systems.

These studies reported here have been made in collaboration of Research Group for Hadron Transport Theory, Advanced Science Research Center, JAERI. Support

of Institute of Physics and Chemical Research (RIKEN) for the use of VPP-500 super-computer is acknowledged.

REFERENCES

1. For example, J. W. Negele, Rev. Mod. Phys. **54** (1982) 913.
2. For example, G. F. Bertsch and S. Das Gupta, Phys. Rep. **160** (1988) 189; and references therein.
3. For example, Y. Yariv and Z. Fraenkel, Phys. Rev. C **20** (1979) 2227.
4. For example, J. Aichelin, Phys. Rep. **202** (1991) 233; and references therein.
5. T. Maruyama, A. Ono, A. Ohnishi and H. Horiuchi, Prog. Theor. Phys. **87** (1992) 1367.
6. For example, H. Sorge, H. Stöcker, and W. Greiner, Ann. of Phys. **192** (1989) 266; T. Maruyama, S.W. Huang, N. Ohtsuka, G.Q. Li, and A. Faessler, Nucl. Phys. **A534** (1991) 720.
7. K. Niita, S. Chiba, T. Maruyama, H. Takada, T. Fukahori, Y. Nakahara and A. Iwamoto, submitted to Phys. Rev. C.
8. J. Cugnon, Phys. Rev. C **22** (1980) 1885.
9. B. J. VerWest and R. A. Arndt, Phys. Rev. C **25** (1982) 1979.
10. W. B. Amian, B. C. Byrd, C. A. Goulding, M. M. Meier, G. L. Morgan, C. E. Moss and D. A. Clark, Nucl. Sci. and Eng. **112** (1992) 78; and private communication.
11. K. Ishibashi et al., to be published in J. Nucl. Sci. Technol; and private communication.
12. H. En'yo, S. Sasaki, T. Nagae, K. Tokushuku, M. Sano, M. Sekimoto, J. Chiba, K. Ichimura, T. Mori, T. Katsumi, H. Yokota, R. Chiba and K. Nakai, Phys. Lett. B **159** (1985) 1.
13. T. Nishida et al., JAERI-M 86-116 (1986); and private communication.
14. H. Feldmeier, Nucl. Phys. **A515** (1990) 147.
15. A. Ono, H. Horiuchi, T. Maruyama and A. Ohnishi, Prog. Theor. Phys. **87** (1992) 1185.
16. T. Maruyama, A. Ohnishi and H. Horiuchi, Phys. Rev. **C42** (1990) 386.
17. Similar way to A. Ohnishi, T. Maruyama and H. Horiuchi, Prog. Theor. Phys. **87** (1992) 417.
18. P. Valta, J. Konopka, A. Bohnet, J. Jaenicke, S. Huber, C. Hartnack, G. Peilert, L. W. Neise, J. Aichelin, H. Stöcker and W. Greiner, Nucl. Phys. **A538** (1992) 417c.

2. Evaluation

2.1 Discussions on the Computer Simulation Scheme for the Intermediate Energy Hadron Nucleus Interactions

Yasuaki Nakahara
Advanced Science Research Center
Japan Atomic Energy Research Institute
Tokai-mura, Naka-gun, Ibaraki-ken 319-11, Japan

Discussions are made on the present status of the hadron transport simulation studies. Nucleon - nucleus and pion - nucleus cross section data required in the intermediate energy region are listed at the begin -ning. Next, the 3 - step simulation scheme, i.e., the intranuclear cas-cades,the preequilibrium decay and the fission-evaporation competitions, are described briefly, as well as the nuclear structure modelling, nucle -on - nucleon and nucleon-meson inelastic scattering processes, medium effects on the hadron properties and the mass formula.

A brief summary is given also on the problems unchecked yet.

1. Introduction

The hadron transport simulation codes have been developed and improved strenuously for use in the design studies of the intense and more intense spallation neutron sources. [1] On the other hand, the technical possibilities of introducing the intermediate energy intense proton beam linear accelerator in the nuclear fuel cycle have been recognized gradually in the nuclear energy societies [2],[3] ever since the President Carter's initiative in the more proliferation resistent Alternative Systems Assessment Program.

In 1990 International Atomic Energy Agency organized the Advisory Group meeting on the Intermediate Nuclear Data for Applications.[4] The Group made the recommendation to IAEA to conduct the international bench -mark test of the hadron transport simulation codes. The aim was to make clear the predictive power of nuclear reaction models and codes in the energy range from 20MeV to 1,600MeV. The results of the test were expect -ed to make clear also the needs for improvements of the codes and the data bases which would be used in the assessment studies of the varoius concepts of tramsmuting the long life radioactive nuclear wastes.

But difficulties arose in the procedual and practical ways to perform the test. In the meanwhile NEA OECD took over the responsibility. The owners of the codes were requested to perform the benchmark calcul-

ations with their codes and send the results to NEA. From Japan, JAERI and Kyushu University group took part in the exercise. The final report was published from OECD [5] and the summary was made public recently. [6]

2. Nuclear Data in the Intermediate Energy Region

Since there is no clear definition of the intermediate energy region, let us understand here that it means the energy range from 20MeV up to 2GeV.

In this energy region various kinds of and huge amount of nuclear data are required in the design studies of proton beam target, blanket and shielding systems. For the proton incident nuclear reactions, we need the nuclear data sets of the kinds listed below.

(p, elastic),
(p, nonelastic),
(p, injpk π^+ l π^- m π^0),
where i, j, k, l and m = 0, 1, 2, ------.
(p, γ),
(p, d),
(p, t),
(p, α),
(p, complex),
where 'complex' means particles more complex than α, nuclear fragmentation and fission products.
(p, injpk π^+ l π^- m π^0 , complex).

Even if the primary incident particle is a proton, other kinds of energetic hadrons are knocked out from the nucleus and they play the role of incident particles in the sequential reactions. They are protons with energies different from the incident energy, neutrons and pions (π^+ , π^- , π^0) . In the late 1980s pioneering work in making the intermediate energy nuclear data libraries started both in USA[7] and USSR[8] . Entering 1990s, activities in this field spread over the inter-national scope.[9],[10] The ENDF/B-VI High Energy library for ^{56}Fe prepared by NNDC BNL is a complete library covering the energy range from 1 to 1,000MeV. [7] On the other hand, the Barashenkov's work is a compilation of the total and inelastic scattering cross sections in the energy from 14MeV to 1,000MeV for incident particles p, n, π^+ and π^- , and for the target nuclei He, Be, C, N, O, Na, Al, Si, Ca, Fe, Cu,Mo, Cd , Sn, W, Pb and U.

3. Computer Simulation Scheme of the Hadron Transport Processes

At present we have no nuclear data file available for the systematic analyses of hadron transport processes in the intermediate energy region. In these circumstances the strenuous efforts have been devoted to develop the computer simulation codes employing the algorithms not using the so-called nuclear data files.

The nuclear reaction induced by the hadrons with the intermediate energy is called the nuclear spallation. The currently used simulation method is based on the algorithms modelling the spallation as the three step processes, as shown in Fig.1, i.e., the intra-nuclear hadron cascade process, the preequilibrium nuclear decay process and the compound nucleus decay process(fission - evaporation competitions). This three step modelling has been employed in the most advanced simulation codes, although there are some differences in the practical algorithms. These codes are HETC-3STEP[11], HERMES [12], LAHET-TM [13] and CEM92 [14].

4. Data Base used in the Simulation Codes

The data base used in the codes are very simple. It consists of the nuclear structure data, the nucleon - nucleon and pion - nucleon scattering data and the mass formulas.

4.1 Nuclear Structure Data

Values of the nuclear radii r_E, determined approximately from the definition:

$$\rho(r_E) = 0.01\rho(0), \qquad (1)$$

are stored in the table, where $\rho(r)$ is the nucleon density distribution in the nucleus, obtained from the electron scattring. From r_E the geometrical cross sections $\sigma_E = \pi (r_E)^2$ are calculated in the codes to be used as the total nuclear cross sections. The inadequancy of this crude definition has become noticed recently. Nakahara pointed out that there are great discrepancies between σ_E and the experimental cross sections compiled by Pearlstein [7]. [15] Discrepancies are greater for heavier and lighter nuclei. Brown et al. have shown also that in the description of proton nucleus data the radii slightly smaller than those obtained from the electron scattering must be used to get good fits for Pb-208, Ni-58 and Co-40.[16] In the attempts to define r_E, Ageli proposed the following expression:[17]

$$r_g = [\, r_T(A) + a_s (I - I_{ST})], \qquad (2)$$

where $r_T(A) = r_0 + r_1 A^{-2/3} + r_2 A^{-4/3} + \cdots$

$I = (N - Z)/A$,

I_{ST} = the line of stability,

$a_s, r_0, r_1, r_2, \cdots$ = constants.

Neutron and proton density distributions in the nucleus are given as

$$\rho^n(r) = \rho(r) * (A - Z), \qquad (3a)$$

$$\rho^p(r) = \rho(r) * Z \qquad (3b)$$

by distributing simply the $\rho(r)$ with the weights of neutron and proton numbers. No systematic evaluations of these definitions of r_g have not been tried yet. Problems we have at present can be summarized as listed below.

Problem 1: How to define the nuclear radius?

Problem 2: Do neutrons and protons have the density distributions of the same shape as given by Eq.(3)?
How about the effects of the surface diffuseness, such as given in Eq.(2)?

Problem 3: As for the shapes of lighter nuclei such as Li, Be, F, is it permissible to treat them as spherical nuclei?
Again, how to define the nuclear radius of the light, small nucleus?

4.2 Nucleon - Nucleon and Meson - Nucleon Scattering Data

The most important hadron inelastic scattering events in the intermediate energy region are the meson production processes. In the hadron transport simulation codes of the NMTC and HETC series only the pion production processes are taken into cosideration and the data libraries used in them contain the data only for the one pion production and the two pion production via the Δ excitation as listed below.

$n\,p \rightarrow n\,p\pi^0$, $\quad p\,p \rightarrow p\,p\pi^0$,

$\rightarrow p\,p\pi^-$, $\quad \rightarrow p\,n\pi^+$,

$\rightarrow n\,n\pi^+$,

$N\,N \rightarrow \Delta\,\Delta$, $\quad \pi\,N \rightarrow \pi\,\Delta$,

$\Delta \rightarrow N\,\pi$, $\quad \Delta \rightarrow N\,\pi$.

$\pi\,p \rightarrow$ charge exchange, $\quad \pi\,n \rightarrow$ absorption,

$\rightarrow$ absorption,

where π stands for π^0 or π^- or π^+ and N for p or n.

The n n scattering events are taken as the same as the p p scattering events on the assumption that the Coulomb scattering has little effects in the intermediate energy region.[18]

A question arises here if this scheme is adequate enough, because there are other heavier mesons known to exist nowadays. The mesons with the mass below 1 GeV are in increasing order of the mass, [19]

$m = 138.03$ MeV
$\eta = 548.8$
$\sigma = 550$
$\rho = 769$
$\omega = 782.6$
$\delta = 983.$

In the phase shift analysis of the NN scattering in the energy region below 1 GeV, Elster, et al. have shown that the inclusion of $\pi\rho$ and $\rho\rho$ exchange contributions gives successful results. [20] A ques-tion arises naturally why π and ρ are important. The answer lies in their quark(q) and anti-quark($\bar{q}$) structures.

The particles which give important contributions in the hadron trans-port processes in the intermediate energy region are made from the up-quark(u),the down-quark(d), and their anti-quarks($\bar{u}$ and $\bar{d}$). Their essen-tial differences are charges and spins, as described below. [21]

p = uud spin = 1/2
n = udd
Δ : resonance states of uuu, uud, udd and ddd, spin = 3/2
$\pi^+ = \bar{d}u$ spin = 0 $\rho^+ = \bar{d}u$ spin = 1
$\pi^- = \bar{u}d$ $\rho^- = \bar{u}d$

The roles and effects of ρ mesons in the hadron transport processes, however, have not been examined yet.

4.3 Medium Effects on the Hadron Transport Processes in the Nucleus

The medium effects incorporated in the simulation codes are
(a) neutron and proton density distributions,
(b) Fermi energy distributions for neutrons and protons,
(c) potential energy distribution,
(d) Pauli blocking for fermions.

Entering the 1990s, active controversies arose about the medium effects on the masses and the sizes of hadrons in the nucleus, i.e., if they would become heavier or lighter and larger or smaller. The results published recently are as summarized below. The quantities with the asterisk * indicate the values in the nucleus and those with out it are the values in the free space.

(1) Nucleon mass [22),(23),(24)

$$m_N^* < m_N.$$

(2) Δ (1232) resonance [25]

$$m\Delta^{*} < m\Delta .$$

(3) Pion mass

$$m\pi^{*} \fallingdotseq m\pi , \quad [17],[26]$$

$$m\pi^{*} < m\pi . \quad [27]$$

Recently, Arima, et al. have shown that the mass of N(1520) is larger in the nuclear medium than in the free spsce. [28] The N resonance, however, is not taken into consideration in the currently used simulation codes.

(4) Nucleon size, nucleon - nucleon scattering cross sections.

According to the arguments by Li and Machleidt, based on the Dirac - Brueckner approach for nuclear matter,

$$\sigma^{*} < \sigma ,$$

which is mainly due to the Pauli blocking. [29] On the other hand, Mao , et al. made analysis of the medium effects on the nucleon - nucleon inelastic scattering cross section in the relativistic heavy ion collisions, using the relativistic Boltzmann - Uehling - Uhlenbeck approach. [30] Their result is

$$\sigma^{*} > \sigma ,$$

where no Pauli blocking is taken into consideration.

These results indicate that one should be careful in defining the in-medium hadron cross sections and using them in the intra-nuclear hadron transport simulations, in conjunction with the computational scheme how to take into consideration of the Pauli brocking.

4.4 Mass Formula

The mass formula is one of the most important relations to give physical quantities to be used in the simulation calculations. The mass formula is used to obtain the binding energies of nucleons and other particles in the nucleus. The binding energy is, in its turn, a crucial quantity in determining

(a) particle emission probabilities,
(b) fission probabilities,
(c) excitation energy of the residual nucleus,

and also for use in

(d) half-life estimation, especially for the exotic nuclei, half lives of which are not known yet.

The mass formulas employed in the currently used simulation codes are compilations [31] of the contributions of Wapstra(1955) [32], Huizenga(1955)[33], Cameron(1957) [34] and Mattauch, et al.(1965) [35].

No revision work of the mass formula has been tried ever since, although the various kinds of them have been proposed, as reviewed by M. Yamada, et al. [36]

5. Summary

There are several other problems remaining unchecked up to now, as listed below.

(1) Effects of the Δ propagation and the Δ N interaction in the nucleus.
(2) Are there cluster effects during the intranuclear cascade process? Especially, how about the deuteron effects?
(3) What is the difference between the complex particle evaporation and the nuclear multifragmentation?

References:

(1) M. Misawa, M. Furusaka, H. Ikeda and N. Watanabe(Ed.), Proc. the 11-th Meeting of International Collaboration on Advanced Neutron Sources, ICANS-XI, KEK Report 90-25(1991).
(2) H. J. Kouts and M. Steinberg(Ed.), Proc. an Information Meeting on Accelerator Breeding, BNL, 1977, Conf-770107(1977).
(3) P. Grand, H. J. Kouts, J. R. Powell, M. Steinberg and H.Takahashi, Conceptual Design Analysis of a Light Water Reactor Fuel Enricher/ Regenerator, BNL-50838(1979).
(4) N. Kocherov(Ed.), Intermediate Energy Nuclear Data for Applications, INDC(NDS)-245 Distr.L(1991).
Y. Nakahara, Computer codes and nuclear data needs for the simulation of intermediate energy nuclear reactions, pp.77-92.
(5) M. Blann, H. Gruppelaar, P. Nagel and J. Rodens(Ed.), International Code Comparison for Intermediate Energy Nuclear Data, OECD(1994).
(6) P. Nagel, J. Rodens, M. Blann and H. Gruppelaar, Nucl.Sci.Eng. 119 , 97-107(1995).
(7) S. Pearlstein, Astrophys J., 346, 1049-1060(1989).
(8) V. S. Barashenkov, Nucleon-Nucleus Cross Sections, P2-89-770, Dubna (1989)(in Russian).
V. S. Barashenkov, Pion-Nucleus Cross Sections, P2-90-158, Dubna (1990)(in Russian).
(9) S. M. Qaim(Ed.), Proc. Nuclear Data for Science and Technology, Jülich, 1991, Springer Verlag(1992).

Y. Nakahara, Nuclear and nucleon data needs for incineration of the radioactive wastes from fission reactors with a proton accelerator, pp.23-28.
(10)T. Fukahori(Ed.), Proc. the Specialists Meeting on High Energy Nuclear Data, Tokai, 1991, JAERI-M 92-039(1992).
(11)H. Takada, K. Ishibashi, N. Yoshizawa and Y. Nakahara, J. Nucl. Sci. Technol., 31, 80-82(1994).
(12)P. Cloth, D. Filges, G. Sterzenbach, T. W. Armstrong and B. L. Colborn, The KFA-Version of the High Energy Transport Code HETC and the generalized Evaluation Code SIMPEL, Jül-Spez-196(1983).
(13)R. E. Prail, A Review of Physics Models in LAHET-TM Code, LA-UR-94-1817(1994).
(14)V. Konshin, private communication.
(15)Y. Nakahara, JAERI internal memo(1992).
(16)G. E. Brown, A. Sethi and N. M. Hintz, Phys. Rev. C, 44, 2653-2662 (1991).
(17)I. Ageli, Role of nucleonic promiscuity in charge radii: comparison of radius formulae, Inst. Phys. Conf. Ser. No.132, 93-95(1992).
(18)H. W. Bertini, Monte Carlo Calculations on Intranuclear Cascades, ORNL-3383(1963).
(19)R. Machleidt, The Meson Theory of Nuclear Forces and Nuclear Structure, Adv. Nucl. Phys., vol.19, 189-363(1989), Prenum Press.
(20)Ch. Elster, K. Holinde, D. Schütte and R. Machleidt, Phys. Rev. C, 38, 1828-1842(1988).
(21)H. Frizsch, Quarks the Stuff of Matter, Penguin Books(1983).
(22)B. ter Haar and R. Machleidt, Phys. Rev. C, 36, 1611-1620(1987).
(23)R. J. Furnstal, D. K. Griegel and T. D. Cohen, Phys. Rev. C, 46, 1507-1527(1992).
(24)Guangjun Mao, Zhuxia Li, Yizhong Zhuo and Yinlu Han, Phys. Rev. C, 49, 3137-3146(1994).
(25)T. Udagawa, P. Oltmanns F. Osterfeld and S. W. Hong, Phys. Rev. C, 49, 3162-3181(1994).
(26)M. C. Ruivo, C. A. de Sousa, B. Hiller and A. H. Blin, Nucl. Phys., A575, 460-476(1994).
(27)W. Weise, Nucl. Phys., A574, 347c-363c(1994).
(28)M. Arima, K. Masutani and R. Seki, Phys. Rev. C, 51, 285-298(1995).
(29)G. Q. Li and R. Machleidt, Phys. Rev. C, 48, 1702-1712(1993).
(30)Guangjun Mao, Zhuxia Li, Yizhong Zhuo and Zigiang Yu, Phys. Lett., B327, 183-186(1994).
(31)W. A. Coleman and T. W. Armstrong, NMTC Monte Carlo Nucleon Meson

Transport Code, ORNL-4606(1970).
Y. Nakahara and T. Tsutsui, NMTC/JAERI:a Simulation Code System for High Energy Nuclear Reactions and Nucleon-Meson Transport Processes, JAERI-M 82-198(1982)(in Japanese).
(32)A. M. Wapstra, Physica, 21, 367(1955).
(33)J. R. Huizenga, Physica,21, 410(1955).
(34)A. G. W. Cameron, Canad. J. Phys., 35, 1021(1957).
(35)J. H. E. Mattauch, W. Thiele and A. H. Wapstra, Nucl. Phys., 17, 1(1965).
(36)M. Yamada, T. Tachibana and H. Nakata, Inst. Phys. Conf. Ser. No.132, 121-123(1992).

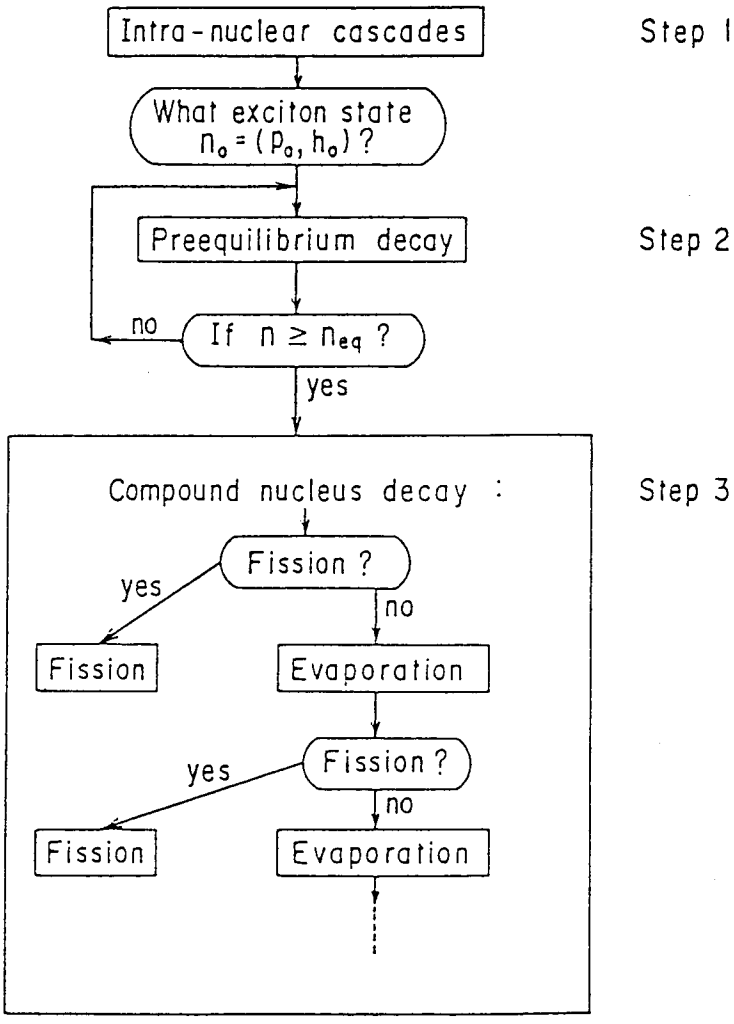

Fig.1 Three-step simulation scheme of the hadron induced nuclear reactions in the intermediate energy region

2. 2 NEA/NSC International Code Comparison for Intermediate Energy Nuclear Data

Hiroshi Takada

Department of Reactor Engineering
Japan Atomic Energy Research Institute
Tokai-mura, Naka-gun, Ibaraki-ken, 319-11
JAPAN

Abstract

In order to evaluate the current predictive power of various nuclear reaction models and radiation transport codes for intermediate energy region, benchmark calculations for thin and thick targets were organized by OECD/NEA. It has been found through the benchmark calculations that nuclear reaction models employed in the preequilibrium calculation codes could predict the differential cross sections with good accuracy below 160 MeV. It has also been confirmed that the intranuclear cascade evaporation model could give reasonable agreement with experimental results of the double differential cross sections at higher incident energy above 256 MeV.

1.Introduction

Interests are growing for the application of high energy proton accelerators to medical usage and to nuclear engineering for the transmutation of long-lived transuranic nuclides and/or fission products. In these applications, intermediate energy nuclear data covering energies between 20 and 1600 MeV are required for the radiation therapy dosimetry and the development of radiation transport codes to design accelerator-based transmutation systems.

Several models are thought to be applicable to the evaluation of intermediate energy nuclear data. One is deterministic methods taken in the preequilibrium reaction calculation using exciton model[1], geometry dependent hybrid (GDH) model[2], multistep direct and compound models based on FKK-theory[3] and so on. Some attempts are made to extend their available energy range up to 250 MeV for the estimation of radiation therapy dosimetry. Another is the Monte Carlo method used in the intranuclear cascade evaporation (INCE) model[4,5] including high energy fission process. Inclusion of preequilibrium process in terms of the exciton model have been studied to improve its validity in the energy region below 200 MeV. Furthermore, an investigation of the Quantum Molecular Dynamics[6,7] for the analysis of nucleon-nucleus reaction is also made because the model has mainly been employed to analyze heavy ion reactions so far.

As for the radiation transport calculation in a thick medium, nuclear reactions and particle transport process have been simulated using the INCE model based transport code in combination with the conventional neutron transport code such as MCNP. Many versions of such code systems have been developed and employed for the design study of the spallation neutron source facility.

It is important to comprehend the current predictive power of these models and code systems to get some hints for further improvements. From this point of view, OECD/NEA organized benchmark problems for thin and thick target calculations. A large number of contributions have been made to these benchmark calculations. At present, comparisons of the

calculated results for the thin target benchmark have been finished and the results have already been published[8,9]. On the other hand, comparisons of the thick target benchmark are still in progress. This paper summarizes the benchmark problems and gives a brief explanation of the results obtained in the thin target benchmark.

2. Benchmark Problems

2.1 Thin Target Problem (Phase-I)

For the check of the physical model for nuclear reaction analysis, neutron and proton reactions on ^{90}Zr and ^{208}Pb have been chosen as targets because some experimental data have been obtained at several incident energies. As for the incident energy, the following 6 points of 25, 45, 80, 160, 256 and 800 MeV were selected. 1600 MeV was also chosen to get further information of the model for higher incident energy. The quantities for comparison in the benchmark calculation were total reaction cross section, neutron/proton yield, single differential cross section and double differential cross section.

2.2 Thick Target Problem (Phase-II)

In order to know the predictive power of various radiation transport calculation codes, a thick target problem was set up for 800 MeV proton incidence on cylindrical targets. For simplicity, the target is composed of monochromatic nuclide of ^{208}Pb or ^{186}W. The size of the target is 20 cm in diameter and 60 cm in length. The profile of the proton beam is a pencil beam which is injected on the center axis of the target. The following quantities were selected for comparison i.e. neutron yield, leakage neutron energy spectrum, neutron spectra in various regions in the target and nuclide production rate.

3. Calculation Codes

The calculation codes contributed to the thin target benchmark are listed in Tables 1 and 2. The codes are classified into two groups. One is the codes such as ALICE-92[10] and GNASH[11] which consist of the preequilibrium calculation part and the statistical decay calculation part. They are based on the exciton model using Kalbach systematics[12] and have been widely used in nuclear reaction analysis in tens of MeV region. The reaction cross section and the inverse cross section are determined using global optical model parameters.

In ALICE-92, Fermi energy obtained by Thomas Fermi local density approximation is employed to estimate the nuclear density in a nucleus and represents geometric dependence of the nucleus in the hybrid model for the analysis of the preequilibrium reaction. Here, the central density radius is given by the droplet model of Myers[13], i.e. $1.18A^{1/3}\{1.- (1/1.18A^{1/3})2\}$. Partial state densities in the preequilibrium process are Ericson-Williams exciton densities. Angular distributions of the emitted particles are calculated from N-N scattering kinematics or Kalbach systematics. In this benchmark calculation, cluster emission are not treated in the preequilibrium process.

In GNASH code, Kalbach systematics is employed for the calculation of the angular distribution of the particles emitted from the preequilibrium process. For the equilibrium decay calculation, Ignatyuk level density model[14] is adopted. As for the optical model parameters, Bechetti-Greenlees parameters[15] and coupled channel ones are employed for proton and for neutrons, respectively.

FKK-GNASH[16] and MINGUS are in development for the extension of the existing preequilibrium calculation code GNASH to 200 MeV. In these codes, the exciton model are replaced into the multistep direct and compound models based on FKK theory which analyzes

the nuclear reaction by the formula derived quantum mechanically. The effective interaction strength factor is treated as an adjustable parameter in this model.

As for INCE model, NUCLEUS[17] and HETC-PSI[18] are close to the original code although the treatment of the fission process is somewhat different in each code. The preequilibrium process is taken into account in HETC-3STEP[19], LAHET[20], CEM92M[21] and FLUKA/MILANO[22]. Three of them adopted the exciton model for the preequilibrium calculation but FLUKA employed the GDH model. In HETC-3STEP, the preequilibrium calculation is applied only to the nucleus with high excitation energy. In other codes, however, the preequilibrium calculation is applied when 2p1h state is created in the cascade process.

4. Results and Discussions

The calculated total proton reaction cross sections calculated by ALICE-92, GNASH, LAHET and NUCLEUS for ^{90}Zr and ^{208}Pb are compared with experimental data in Fig. 1. It is observed that the results of LAHET and NUCLEUS quite differ from those of ALICE-92 and GNASH below 100 MeV for ^{208}Pb. It seems that GNASH has the best predictive power on the reaction cross section among those codes below 100 MeV. The difference between ALICE-92 and GNASH comes from the optical model parameter employed in the codes. In the INCE model, strong dependence of the nuclear reaction on the incident energy is not treated correctly in tens of MeV region.

Total cross section of ^{56}Fe and ^{208}Pb for neutron incidence is shown in Fig. 2. In the INCE model, the geometric cross section is employed so that the model might underestimate the evaluated total cross section. The use of the geometric cross section causes the INCE model to gives different reaction cross sections from ALICE-92 and GNASH as is seen in Fig. 1. Since the geometric cross section is used in radiation transport code NMTC/JAERI[23] and HETC/KFA2[24], the mean free path of a travelling neutron in a matter is overestimated especially in tens of MeV region. In order to take into account energy dependent total reaction cross section, an option to include elastic cross section is implemented in HETC-KFA2. On the other hand, the author modified NMTC/JAERI by replacing the geometric cross section into the values estimated by Pearlstein[25],which is devoted as in Fig. 2, to treat the total cross section as correct as possible.

In Fig. 3, calculated neutron energy spectra in tungsten target installed lead assembly bombarded with 500 MeV protons are compared between the case of the geometric cross section and the one of Pearlstein systematics. The size of the assembly is 60 cm in diameter and 100 cm in length. The tungsten target of 16 cm in diameter and 30 cm in length are installed at the depth of 20 cm from the surface. The range of the incident proton is about 12 cm in tungsten target. It is easily observed that the overestimation of the neutron spectra between 20 and 50 MeV by the use of the geometric cross section is getting more significant as the distance from the incident point to the detection point increases.

In Fig. 4, calculated yield of ^{56}Co in ^{nat}Ni samples inserted in various positions in the assembly are compared with the measured ones. It is clear that the calculated results gives reasonable agreement with the measured ones by taking into account the energy dependent cross sections correctly. The calculated results still overestimate the experimental results by 40% at worst. The reason of the discrepancy seems to be due to the ambiguity of the predictive power of the INCE model in the calculation of the nuclide production cross section.

In Figs. 5 and 6, the proton double differential cross sections (DDXs) calculated with GNASH, FKK-GNASH, NUCLEUS and HETC-3STEP are compared with the experimental data[26] for 80 MeV proton incidence on ^{90}Zr. In Figs. 7 to 12, comparisons are made between

the calculated neutron DDXs of ALICE-92, GNASH, FKK-GNASH, NUCLEUS and HETC-3STEP and the experimental data[27-31] for Pb target at incident proton energies 80 to 800 MeV. At incident energies up to 160 MeV, it is observed in common that NUCLEUS underestimates the experimental neutron DDX above 10 MeV at the backward angles greater that 90°. On the contrary, good agreements are obtained between NUCLEUS and the experiment at the intermediate angles of 25° to 60°. At very forward angles at 11°, NUCLEUS overestimates the highest energy component of the neutron spectra by a factor of 5 or more which comes from the quasi-elastic reaction. However, the code underestimates the continuum part following the quasi-elastic part.

HETC-3STEP successfully improves the outstanding underestimation of NUCLEUS for the neutron emission to backward angles and achieves excellent agreements with the experimental data for both ^{208}Pb and ^{90}Zr below 160 MeV. This means that the inclusion of preequilibrium process improves the accuracy of INCE model in the energy region below 160 MeV.

The calculations with GNASH code give satisfactory agreement with the experimental data at all angles for incident proton energy up to 160 MeV. The models and parameters chosen for calculation seems to be reliable enough to predict nuclear reactions with good accuracy. In comparison with the results of GNASH, on the other hand, the results obtained using FKK theory fall off too rapidly relative to the experimental data at backward angles. It is necessary to study multistep direct calculation part in detail to improve this discrepancy.

As for the calculated results with ALICE-92, those are in good agreement with the experimental data at all angles as well as the results with GNASH for incident energy up to 160 MeV. For 160 MeV incidence, it is observed in Figs. 9 and 10 that the neutron yield in the energy range from 20 to 30 MeV is considerably different among the calculation codes. The neutron emission in this energy region comes from the preequilibrium process. It is necessary to investigate the reason of this discrepancy.although there are not any experimental results in this energy region in this benchmark calculation.

For the incident energy above 256 MeV, there is little difference between the calculated results of NUCLEUS and HETC-3STEP even at the backward angles. Consequently, the INCE model predicts the backward neutron emission fairly well. On the very forward neutron spectrum at 7.5°, the calculation codes cannot reproduce the quasi-elastic peak and the following continuum part as well as the case of 160 MeV incidence. This may indicate the limit of the approximation of two-body collision of free particles in the intranuclear cascade process. As a whole, however, it is considered that the INCE model has good accuracy enough to evaluate the neutron DDX at incident energies above 256 MeV.

5. Summary

It has been found through the thin target benchmark that GNASH and ALICE-92 have good predictive power for the nuclear reactions up to 160 MeV. HETC-3STEP also improves the outstanding underestimation of NUCLEUS and gives reasonable agreement with the experimental data. For incident energies above 256 MeV, INCE-model can predict nuclear reactions fairly well although it remains some discrepancies in neutron emission at very forward angles. Judging from the results of the benchmark calculations, these code can predict neutron double differential cross sections within a factor of two at present.

Since there is some discrepancies in reaction cross sections, further improvements are required in INCE model. Further investigation of the optical model parameter are also required. In the thick target calculation with the code NMTC/JAERI, it has been confirmed that the use of

the geometric cross section leads to overestimate the neutron energy spectra between 20 and 50 MeV. Therefore, it is important to pay attention on the total cross sections employed in the high energy particle transport code such as NMTC/JAERI and HETC/KFA2.

References

1) C.Kalbach, *Z. Phys.* **A283**, 401 (1977).
2) M.Blann and H.K.Vonach, *Phys. Rev. Lett.* **28**, 757 (1972).
3) H.Feshbach, A.Kerman and S.Koonin, *Ann. Phys.* **125**, 429 (1980).
4) H.W.Bertini, *Phys. Rev.* **188**, 1711 (1969).
5) L. Dresner, *ORNL-TM*-196 (1962).
6) J.Aichelin and H.Stocker, *Phys. Lett.* **176B**, 14 (1986).
7) J. Aichelin, G.Peilert, A.Bohnet, A.Rosenhauser, H.Stocker and W.Greiner, *Phys. Rev.* **C37**, 2451 (1988).
8) M.Blann, H.Gruppelaar, P.Nagel and J.Rodens, "International Code Comparison for Intermediate Energy Nuclear Data", (OECD/NEA), (1994).
9) "Intermediate Energy Nuclear Data: Models and Codes", Proc. of A Specialists' Mtg., Issy-les-moulineaux, FRANCE, 30 May- 1 June, 1994. (OECD/NEA), (1994).
10) M.Blann and H.K.Vonach, *Phys. Rev.* **C28**, 1475 (1983).
11) P.G.Young, E.D.Arthur and M.B.Chadwick, *LA-12343-MS* (1992).
12) C.Kalbach, *Phys. Rev.* **C37**, 2350 (1988), C.Kalbach and F.M.Mann, *Phys. Rev.* **C23**, 112 (1981).
13) R.D.Myers, *Droplet Model of Atomic Nuclei,* (Plenum, New York, 1977).
14) A.V.Ignatyuk, G.N.Smirenkin and A.S. Tishin, *Sov. J. Nucl. Phys.* **21**, 255 (1975).
15) F.D.Bechetti Jr. and G.W.Greenlees, *Phys. Rev.* **182**, 1190 (1969).
16) M.B.Chadwick and P.G.Young, *LA-UR*-93-104 (1993).
17) T.Nishida, Y.Nakahara and T.Tsutsui, *JAERI-M* 86-119 (1986), (in Japanese).
18) F.Atchison, "Spallation and Fission in Heavy Metal Nuclei under Medium Energy Proton Bombardment", Proc. of Mtg. on Targets for Neutron Beam Spallation Source, KFA-Jülich, Germany, June 11-12, 1979, *Jül-Conf* 34 (1980).
19) K.Ishibashi, N.Yoshizawa, H.Takada, and Y Nakahara, "High Energy Transport Code HETC-3STEP Applicable to Incident Energies Below 100 MeV", Proc. of Int. Conf. on Nucl. Data for Sci. and Technol. Gatlinburg, Tennessee, May 9-13, 1994, to be published.
20) R.Prael and H.Lichtenstein, *LA-UR* 89-3014 (1989).
21) K.K.Gudima, S.G.Mashnik and V.D. Toneev, *Nucl. Phys.* **A401**, 329 (1983).
22) A. Fasso, A.Ferrari, J.Ranft, P.R.Sala, G.R.Stevenson and J.M.Zazula, "FLUKA92", Proc.of the Workshop on "Simulating Accelerator Radiation Environments", Santa Fe, January 11-15, 1993, (in press).
23) Y.Nakahara and T.Tsutsui, *JAERI-M 82-198* (1982), (in Japanese).
24) P.Cloth, D.Filges, R.D.Neef, G.Sterzenbach, Ch. Reul, T.W.Armstrong, B.L.Colborn B.Anders and H.Brückmann, *Jül-2203*, (1988).
25) S.Pearlstein, *Astrophys. J.*, **346**, 1049 (1989).
26) A.A.Cowley, A.van Kent, J.J.Lawlie, S.V.Förtsch, D.W.Whitthal, J.V.Plcher, F.D.Smit, W.A.Richter, R.Lindsay, I.J.van Heerden, R.Bonetti and P.E.Hodgson, *Phys. Rev.* **C43**, 678 (1991).
27) M.Trabandt, W.Scobel, M.Blann, B.A.Pohl, R.C.Byrd, C.C.Foster and R.Bonetti, *Phys.*

Rev. **C39**, 452 (1989).
28) W.Scobel, M.Trabandt, M.Blann, B.A.Pohl, B.R.Remington, R.C.Byrd, C.C.Foster, R.Bonetti, C.Chiesa and S.M.Grimes, *Phys. Rev.* **C41**, 2010 (1992).
29) M.M.Meier, C.A.Goulding, G.L.Morgan and J.Ullmann, *Nucl. Sci. Eng.* **104**, 339 (1990).
30) S.Stamer, W.Scobel, W.B.Amian, R.C.Byrd, R.C.Haight, J.L.Ullmann, R.W.Bauer, M.Blann, B.A.Pohl, J.Bisplinghoff and R.Bonetti, *Phys. Rev.* **C47**, 1647 (1993).
31) W.B.Amian, B.C.Byrd, C.A.Goulding, M.M.Meier, G.L.Morgan, C.E.Moss and D.A.Clark, *Nucl. Sci. Eng.* **112**, 78 (1992).

Table 1. Codes and models employed in the nuclear reaction calculation codes using optical model parameters

Code/Organization	Direct Process	Preequilibrium	Equilibrium
ALICE92/LLNL		GDH-Model	Weisskopf-Ewing
GNASH/LANL		Exciton Model	Hauser Feshbach
FKK-GNASH/LLNL	DWUCK	FKK-MSD/MSC	Hauser-Feshbach
MINGUS/ECN	ECIS88	FKK-MSD/MSC	Hauser-Feshbach

Table 2. Codes and models employed in the calculation codes based on the intranuclear cascade evaporation model.

Code/Organization	Cascade	Evaporation	Fission	Preequilibrium
NUCLEUS/JAERI	MECC-4	EVAP-4	Nakahara	
HETC-PSI/PSI	MECC-RL	EVAP-5	Atchison	
HETC-3STEP/ Kyushu	MECC-RL	EVAP-5	Atchison	Exciton Model
LAHET/LANL	MECC-7 ISABEL	EVAP-5	Atchison ORNL-Model	Exciton Model
FLUKA/Milano /CERN	MECC-7 HADRIN NUCLIN	EVAP-5	Atchison	GDH-Model
CEM92M	MECC-Dubna	Hauser Feshbach		Exciton Model

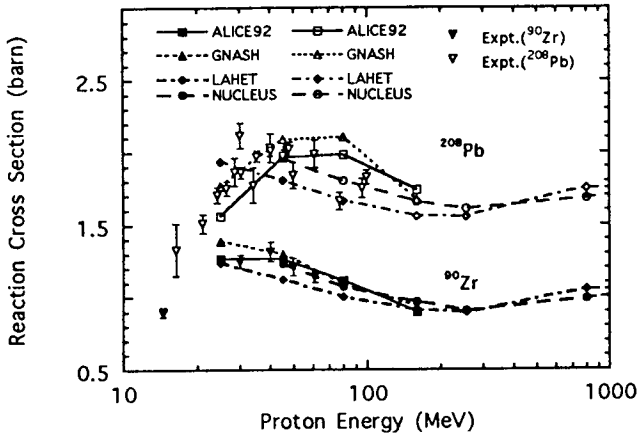

Fig. 1 Total reaction cross sections calculated with the codes ALICE92, GNASH, LAHET and NUCLEUS for proton incidence on ^{90}Zr and ^{208}Pb.

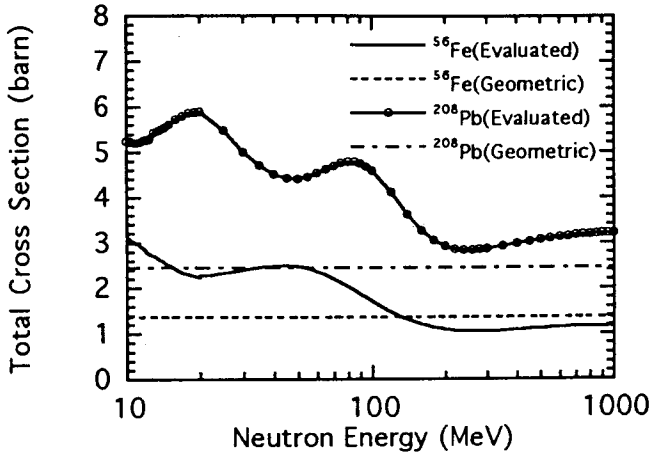

Fig. 2 Total cross sections for neutron incidence on ^{56}Fe and ^{208}Pb. Solid lines represent the values compiled in high energy file. Dotted and dot-dashed lines denote the geometric cross sections.

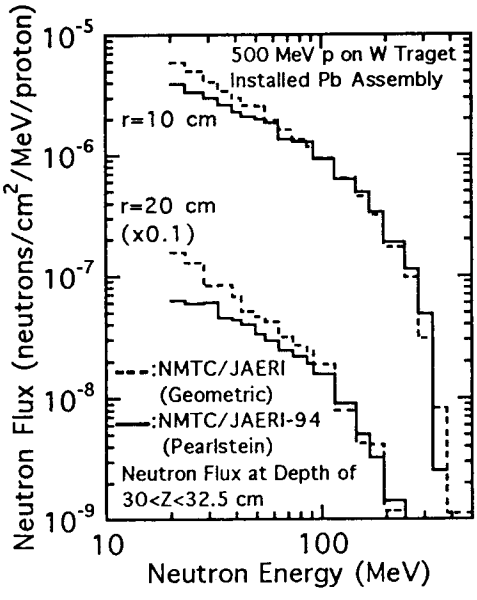

Fig. 3 Calculated neutron energy spectra at the depth between 30 and 32.5 cm in the radial distance of 10 and 20 cm for 500 MeV proton incidence on tungsten target installed lead assembly having the size of 60 cm in diameter and 100 cm in length.

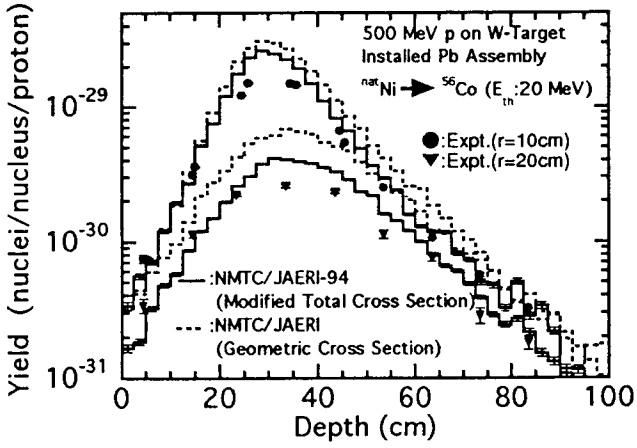

Fig. 4 Experimental and calculated yields of ^{56}Co in ^{nat}Ni samples inserted into tungsten target installed lead assembly for 500 MeV proton bombardment. Solid lines represent the calculated results of NMTC/ JAERI with the total cross section evaluated by Pearlstein. Dashed lines denote the calculated results using geometric cross section.

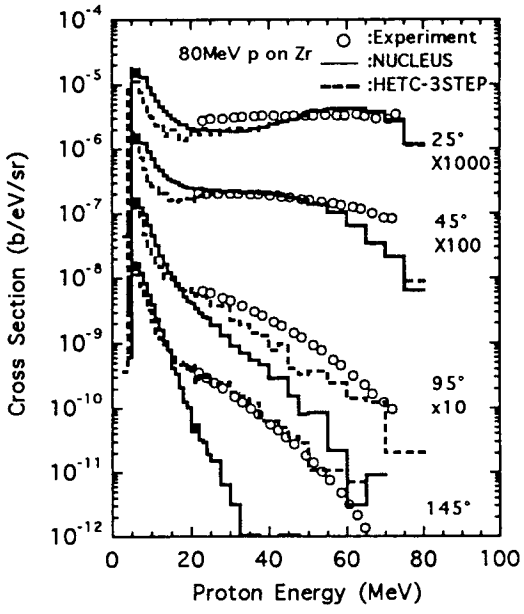

Fig. 5 Experimental and calculated proton differential cross sections of ^{90}Zr for 80 MeV proton incidence. The solid and the dotted lines indicate the results of NUCLEUS and HETC-3STEP, respectively.

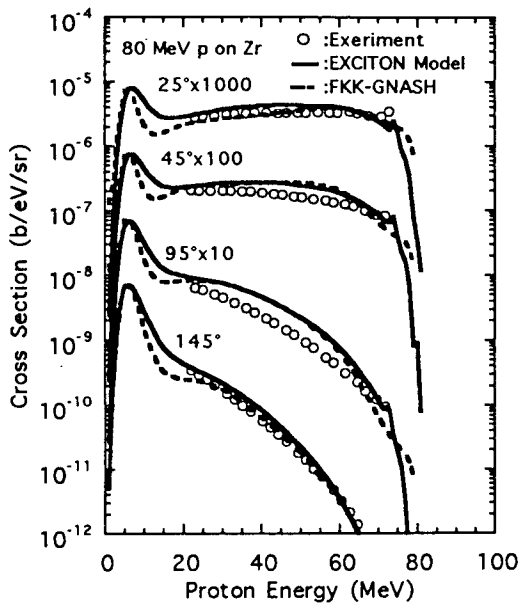

Fig. 6 Experimental and calculated neutron differential cross sections of ^{90}Zr for 80 MeV proton incidence. The solid, the dotted and the dot-dashed lines indicate the results of GNASH and FKK-GNASH, respectively.

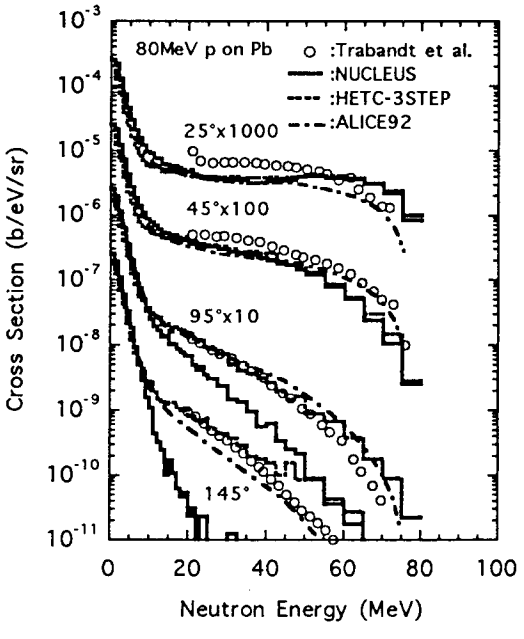

Fig. 7 Experimental and calculated neutron differential cross sections of ^{208}Pb for 80 MeV proton incidence. The solid, the dotted and the dot-dashed lines indicate the results of NUCLEUS, HETC-3STEP and ALICE92, respectively.

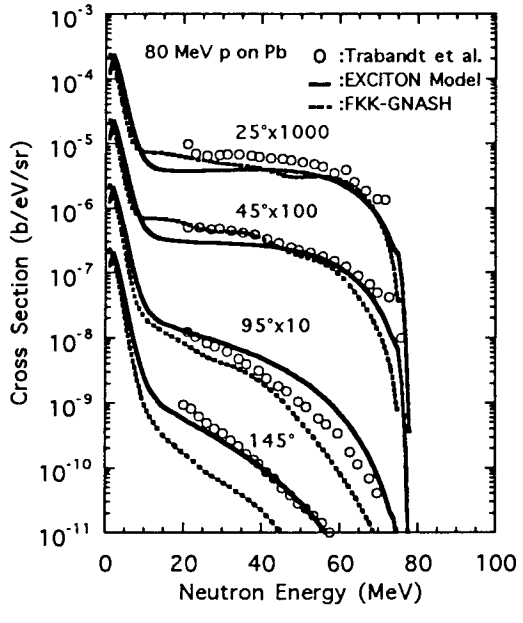

Fig.8 Experimental and calculated neutron differential cross sections of ^{208}Pb for 80 MeV proton incidence. The solid and the dotted lines indicate the results of GNASH and FKK-GNASH, respectively.

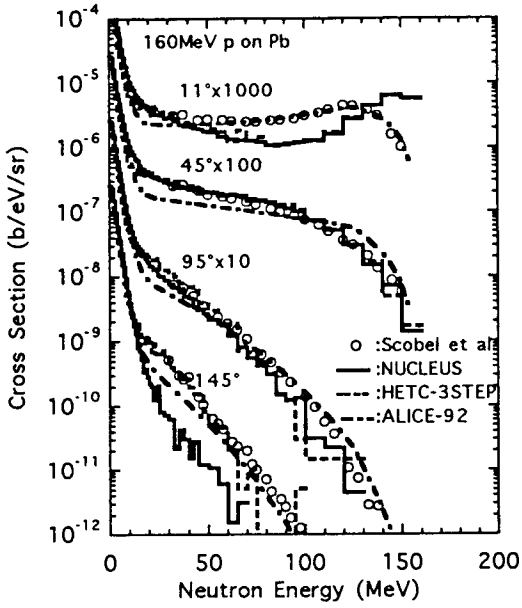

Fig. 9 Experimental and calculated neutron differential cross sections of ^{208}Pb for 160 MeV proton incidence. The solid, the dotted and the dot-dashed lines indicate the results of NUCLEUS, HETC-3STEP and ALICE92, respectively.

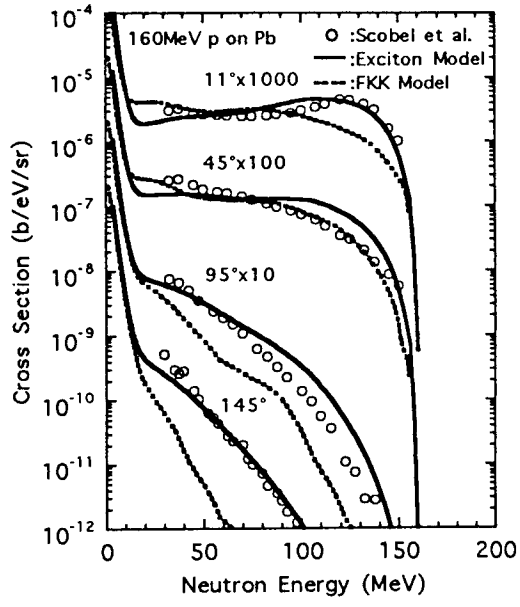

Fig. 10 Experimental and calculated neutron differential cross sections of ^{208}Pb for 160 MeV proton incidence. The solid and the dotted lines indicate the results of GNASH and FKK-GNASH, respectively.

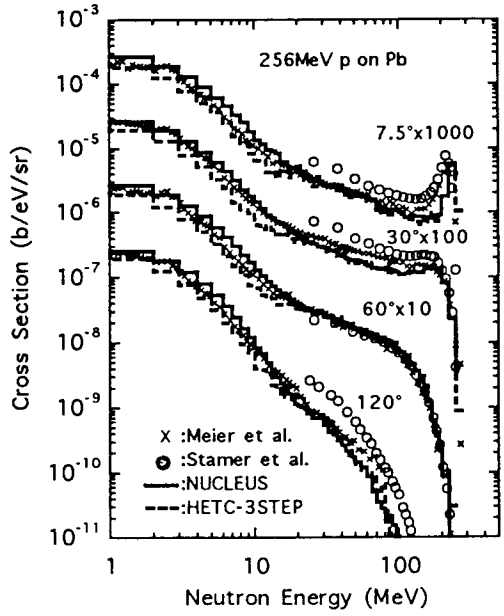

Fig. 11 Experimental and calculated neutron differential cross sections of ^{208}Pb for 256 MeV proton incidence. The solid, and the dotted lines indicate the results of NUCLEUS and HETC-3STEP, respectively.

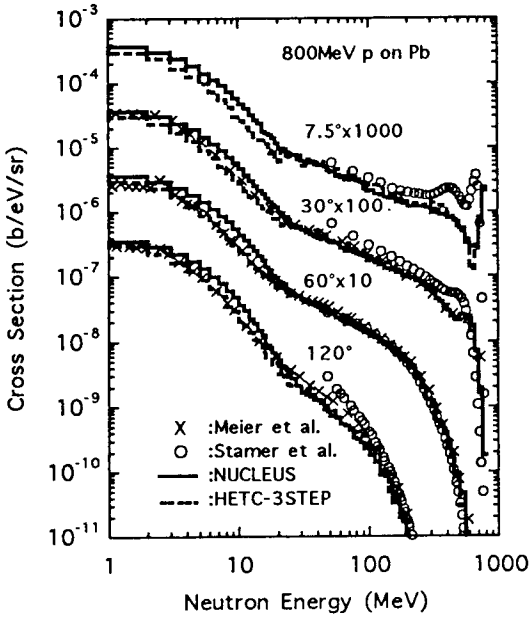

Fig. 12 Experimental and calculated neutron differential cross sections of ^{208}Pb for 800 MeV proton incidence. The solid, and the dotted lines indicate the results of NUCLEUS and HETC-3STEP, respectively.

2. 3 STATUS OF NUCLEAR DATA EVALUATION FOR JENDL HIGH ENERGY FILE

Tokio FUKAHORI and Satoshi CHIBA
Nuclear Data Center, Dept. of Reactor Engineering,
Japan Atomic Energy Research Institute,
Tokai－mura, Naka－gun, Ibaraki－ken, 319－11 Japan

ABSTRACT

The present status of the JENDL High Energy File is reported as well as the code comparison benchmark test and discussion for the file format performed by Japanese Nuclear Data Committee. The PKA/KERMA File and the Photonuclear Data File are also introduced briefly as related topics with the JENDL High Energy File.

I. INTRODUCTION

Nuclear data in the energy range up to a few GeV are necessary to many applications, such as accelerators used for physics research, radiation therapy, medical isotope production and transmutation of radioactive waste. Recently, case studies of intermediate energy nuclear data evaluation have been started. For example, evaluated results for proton- and neutron-induced reactions of ^{12}C, ^{56}Fe, ^{208}Pb and ^{209}Bi up to the GeV region were compiled in the ENDF/B-VI High Energy File[1].

The JAERI Nuclear Data Center has started evaluation work in cooperation with Japanese Nuclear Data Committee (JNDC) to produce the JENDL High Energy File. The evaluation work is separated into two phases. The energy range of the phase-I is up to 50 MeV. The nuclear data in this energy range are needed mainly for the International Fusion Material Irradiation Facility (IFMIF) which is an FMIT-type accelerator facility using Li(d,n) neutron source for a material irradiation test. The neutron spectrum of IFMIF has a high energy tail up to 50 MeV. The energy range for the phase-II is up to a few GeV mainly for an accelerator-driven radioactive waste transmutation system (OMEGA project). The proton- and neutron-induced reactions are considered in the both phases.

In this paper, the present status of the JENDL High Energy File and preliminary results for several nuclides are reported as well as the included physical quantities and their format. The results of benchmark test for isotope production cross sections performed by JNDC[2] are also reviewed. The PKA/KERMA File and the Photonuclear Data File are introduced briefly as related topics with the JENDL High Energy File.

II. SCOPE OF JENDL HIGH ENERGY FILE

The elements included in the JENDL High Energy File are summarized in **Table 1**. The file for the phase-I up to 50 MeV will contain the data for structural materials and other important ones for the above applications. The quantities to be evaluated are the total, elastic scattering, reaction, fission and isotope production cross sections, and double differential

particle and γ−ray emission cross sections of proton− and neutron−induced reactions. The outgoing particles considered are neutron, proton, deuteron, triton, ^{3}He and α−particle. In order to investigate the reliability of model calculations, benchmark calculations[2] were performed for the isotope production cross sections of Mn + n and Fe + p reactions below 50 MeV with the codes of SINCROS−II[3], ALICE−F[4], EXIFON[5], MCEXCITON[6], HETC/3−STEP[7] and NUCLEUS[8]. It was concluded from the benchmark calculations that the codes using the statistical model with correction of the preequilibrium process gave better results than those using the intranuclear cascade model. Therefore, SINCROS−II will be mainly used for the phase−I evaluation, except for light mass nuclei. SCINFUL/DDX[9] code will be used for the phase−I evaluation of light mass nuclei by considering break−up reactions as well as primary knock−on atom spectra (PKA), since any other suitable codes are not available for the light mass region.

For the phase−II up to a few GeV, the fission cross section has to be considered even for intermediate mass nuclides and π−meson production cross sections are also added to the phase−I quantities. The benchmark calculations were also performed for the same quantities produced by proton induced reactions of Al, Fe and Bi up to 1 GeV with the codes of ALICE−F, MCEXCITON and NUCLEUS. It was concluded from this benchmark calculation and NEA/Data Bank International Code Comparison[10] that, in the phase−II evaluation, the ALICE−F and HETC/3−STEP code can be used to evaluation of the isotope production cross sections and of the double differential particle emission cross sections, respectively.

As an advanced method for the evaluation in the intermediate energy region, the application of the quantum molecular dynamics (QMD) theory[11,12] is investigated, which has the merits such as easy treatment of multi−fragmentation to calculate spallation product yields, automatic inclusion of the preequilibrium process, and no requirement of particular assumption on nuclear structures and reaction mechanism.

As a new trial for the compilation of JENDL High Energy Files, "review system" is introduced after evaluation stage. The review is performed with checking physical format by using outputs of file checking code which are FISCON, PSYCHE, CHECKR and DOUBLEP, and concerning by plotting view graphs comparing with experimental data, index list of experimental data, list of produced isotopes, etc. The results of review are shown to evaluators as a feedback, and the evaluator may revise the evaluation if it is necessary.

III. EVALUATION FOR JENDL HIGH ENERGY FILE

Preliminary evaluations have been finished for neutron−induced reactions of ^{1}H, ^{12}C and many structural nuclei up to 50 MeV and for neutron− and proton−induced reactions of ^{1}H (for neutron only), ^{27}Al, Si, Cr, Ni, Cu, Pb and ^{209}Bi up to 1 GeV. Reviews of the results are now in progress. As examples, the evaluated results of ^{1}H and ^{12}C are described below.

The neutron−induced ^{1}H total cross section up to 1 GeV is shown in **Fig. 1**. For this quantity, the evaluation was performed by fitting experimental data below 500 MeV with the least squares method and by calculating from phase−shift data above 500 MeV. The result reproduces the experimental data very well.

Figure 2 shows the evaluated results of double differential proton, deuteron and α−particle emission spectra for ^{12}C at the incident neutron energy of 39.7 MeV and the laboratory angle of 65 deg. The calculation was done by SCINFUL/DDX with considering

break−up reactions. The results are in good agreement with the experimental data.

As the example of evaluated result with ALICE−F for lighter and heavier mass nuclei, the isotope production cross sections for $^{27}Al(p,X)^{24}Na$ and $^{209}Bi(p,x)^{206}Po$ reactions are shown in **Figs. 3 and 4**. The calculated results are almost in good agreement with the experimental data. Hence, other results are expected to reproduce the isotope production cross sections.

IV. PKA/KERMA FILE

The PKA/KERMA file, which contains PKA spectra, displacement per atom (DPA) cross sections and KERMA factors for the estimation of the radiation damage in solid materials, will be produced mainly from the evaluated neutron nuclear data in the JENDL High Energy File up to 50 MeV by using the single particle emission approximation. For light mass nuclei, PKA spectra are evaluated by SCINFUL/DDX, simultaneously with other quantities for JENDL High Energy File. The elements to be included in the file are listed in **Table 2**.

V. PHOTONUCLEAR DATA FILE

For γ−ray induced reaction data up to 140 MeV, the Photonuclear Data File is provided for applications such as electron accelerator shielding and radiation therapy. The photon absorption cross section is evaluated with the giant dipole model and quasideuteron model, and the cross sections of the decaying processes are calculated with the statistical model with preequilibrium correction. For the later purpose, MCPHOT and ALICE−F codes are mainly used. The isotopes shown in **Table 3** are included in the file. The (γ,xn) cross section of ^{98}Mo is shown in **Fig. 5** as an example. The evaluation work has been almost finished, and the file will be released in 1996.

VI. RECOMMENDED FORMAT OF FILES

The major applications of intermediate energy nuclear data need isotope production cross section and double differential light particle, gamma−ray, meson and PKA spectra for neutron−, proton− and photo−induced reactions, fundamentally. Though it is necessary to include individual product nuclides for isotope production cross sections, it seems that composite particle spectra, which are not identified the emitted reaction and summing up the same particle from all the reaction channels, might be enough to use for each application. It is no meaning to separate the energy region in consideration of format.

The physical quantities which are necessary for the files are roughly classified into cross section (MF=3), angular distribution (MF=4), energy spectrum (MF=5) and double differential particle, gamma−ray, meson and PKA emission spectra (MF=6). Since MF=4 and MF=5 can be combined into MF=6 in ENDF−6 format, only MF=6 should be considered in this report. For the cross section, total (neutron−induced reaction only), elastic scattering, total reaction (non−elastic), discrete inelastic scattering (not always) and fission channels should be included, and isotope and particle production cross sections are also important. In the case of combination with existing lower energy evaluated file, neutron capture and (n,z) reaction, where z is light charged particle from proton to alpha, cross sections are might be included as an neutron disappearance cross section. The angular distributions for elastic and discrete

inelastic scattering, and fission neutron spectrum should be considered. The double differential cross sections must be included for neutron, gamma-ray, proton, deuteron, triton, He-3, alpha, pi+, pi0, pi-, (K+, K0, K-). Fission related quantities are also included. Above discussion is summarized in **Table 4.**

For conservation of consistency, some rules should be promised inside the format, for instance, sum rule. The evaluation information and comments are included in MF=1. If fission reaction channel is included, the fission-related quantities, for example, fission neutron spectra (MF=5, MT=18), average prompt neutron number (MF=1, MT=452,455,456), fission product distribution (MF=6, MT=18), etc., should be compiled. For sum rule, 1) (MF=3, MT=1) = (MF=3, MT=2) + (MF=3, MT=3), 2) (MF=3, MT=3) = (MF=3, MT=5) + (MF=3, MT=18), 3) For MF=3, MT=201, 203, 204, 205, 206 and 207, the contributions of elastic scattering, discrete inelastic scattering and fission channels are not included. For the angular distributions of elastic and discrete inelastic scattering channels, it can be compiled both in MF=4 and in MF=6, LAW=2. For fission neutron spectrum, both MF=5 and MF=6 can be used. Other detail of rules for MF=6 are listed below:

MF=6, LAW=0: in the case of only the isotope production ratio (MT=5) to MF=3, MT=5 is included (unknown distribution).
MF=6, LAW=1: for MT=201-213, using Legendre coefficients or Kalbach systematics.
MF=6, LAW=2: for MT=2, 51-90 (discrete two-body scattering), using Legendre coefficients or tabular expression.
MF=6, LAW=5: for MT=2 of charged particle (charged particle elastic scattering).
MF=6, LAW=7: for MT=201-213, using table type format, and MT=5 in the case including the isotope production ratio to MF=3, MT=5, and the PKA spectra.

VII. CONCLUDING REMARKS

The present status of the JENDL High Energy File, PKA/KERMA File and Photonuclear Data File was reviewed, and the preliminary results of evaluation for a few nuclides were shown. These files are compiled in the ENDF-6 format. The review process is newly introduced for compilation of JENDL High Energy File.

In the first step of the JENDL High Energy File, evaluation work will be concentrated to the data below 50 MeV. The research and development of new evaluation method such as QMD will be performed for the data up to few GeV. The PKA/KERMA File will be produced just after the phase-I evaluation work for the JENDL High Energy File is finished. The evaluation work for the Photonuclear Data File has been almost finished, and the file will be released in 1996. The first version of JENDL High Energy File will be released in near future. The release procedure should be considered as soon as possible. The summary of tentative file release schedule is shown in **Table 5.**

ACKNOWLEDGMENTS

The evaluation work for the JENDL High Energy File, PKA/KERMA File and Photonuclear Data File are being produced by members of Japanese Nuclear Data Committee and Nuclear Data Center of JAERI. The authors would like to thank them.

REFERENCES

1) Rose P.F.(ed.): "ENDF−201 ENDF/B−VI Summary Documentation", *BNL−NCS−17541* (1991).
2) Fukahori T., et al.: to be published as JAERI−Code/Data.
3) Yamamuro N.: "A Nuclear Cross Section Calculation System with Simplified Input−Format Version II (SINCROS−II)", *JAERI−M 90−006* (1990).
4) Fukahori T.: "ALICE−F Calculation of Nuclear Data up to 1 GeV", *Proc. Specialists' Meeting on High Energy Nuclear Data*, Tokai, Ibaraki, Oct. 3−4, 1991, JAERI−M 92−039, p.114 (1992).
5) Kalka H.: "Statistical Multistep Reaction Model for Nuclear Data", *Proc. Int. Conf. on Nuclear Data for Science and Technology*, Julich, May 13−17, 1991, p.897, Springer−Verlag, Berlin, Heidelberg (1992).
6) Kishida N., et al.: "On the Validity of the Intranuclear−Cascade and Evaporation Model for High−Energy Proton Induced Reactions", *Proc. Int. Conf. on Nuclear Data for Science and Technology*, Mito, May 30− June 3, 1988, p.1209, Saikon Publishing, Tokyo (1988).
7) Ishibashi K., et al.: "Proton Induced Spallation Reaction Calculation Considering the Intranuclear High−Momentum Nucleons and the Preequilibrium Effect", *Proc. 1989 Seminar on Nuclear Data*, Tokai, Ibaraki, Nov. 16−17, 1989, JAERI−M 90−025, p.362 (1990).
8) Nishida T., et al.: "Development of a Nuclear Spallation Simulation Code and Calculations of Primary Spallation Products", *JAERI−M 86−116* (1986).
9) Kashimoto H., et al.: "Study of the ^{12}C Breakup Process and Carbon Kerma Factor", *Proc. 1992 Symposium on Nuclear Data*, Tokai, Ibaraki, Nov. 26−27, 1992, JAERI−M 93−046, p.287 (1993).
10) Blann M., et al.: "International Code Comparison for Intermediate Energy Nuclear Data", OECD/NEA, Paris (1994).
11) Maruyama T., et al.: "Fragment Mass Distribution in Intermediate Energy Heavy−Ion Collisions and the Reaction Time Scale", *Prog. Theoretical Phys.*, **87**, 1367 (1992).
12) Chiba S., et al.: "Applicability of the Quantum Molecular Dynamics to Nucleon−Nucleus Collisions", *Proc. Int. Conf. on Nuclear Data for Science and Technology*, May 9−13, 1994, Gatlinburg, USA, p.505 (1994).

Table 1 The elements to be included in the JENDL High Energy File.

Phase−I (for neutron, < 50 MeV): 20 elements, 55 isotopes
H, Li, C, N, O, Na, Mg, Al, Si, K, Ca, Ti, V, Cr, Mn, Fe, Ni, Cu, Mo, Pb

Phase−I (for proton, < 50 MeV): 10 elements, 33 isotopes
Li, C, Al, Cr, Fe, Ni, Cu, Mo, W, Ta

Phase−II (for neutron and proton, < a few GeV): 38 elements, 94 isotopes
H, Li, Be, B, C, N, O, F, Na, Mg, Al, Si, Cl, Ar, K, Ca, V, Cr, Mn, Fe, Co, Ni, Cu, Zn, Y, Zr, Nb, Mo, W, Au, Pb, Bi, Th, U, Np, Pu, Am, Cm

Underline: high priority

Table 2 The elements to be included in the PKA/KERMA File.

29 elements, 78 isotopes
H, Li, Be, B, C, N, O, Na, Mg, Al, Si, Cl, K, Ca, Ti, V, Cr, Mn, Fe, Co, Ni, Cu, Zr, Ge, Nb, Mo, W, Pb, Bi

Underline: high priority

Table 3 The nuclei to be included in the Photonuclear Data File.

24 elements, 42 isotopes
^{2}H, ^{12}C, ^{14}N, ^{16}O, ^{23}Na, ^{24,25,26}Mg, ^{27}Al, ^{28,29,30}Si, ^{40,48}Ca, ^{46,48}Ti, ^{52}Cr, ^{55}Mn, ^{54,56}Fe, ^{59}Co, ^{58,60}Ni, ^{63,65}Cu, ^{90}Zr, ^{92,94,96,98,100}Mo, ^{181}Ta, ^{182,184,186}W, ^{197}Au, ^{206,207,208}Pb, ^{209}Bi, ^{235,238}U

Table 4 Physical Quantities and (MF,MT) Numbers in ENDF-6 Format Recommended for JENDL High Energy Files

MT	MF	quantities
1	3	total (only for neutron-induced reaction)
2	3,6	elastic scattering
3	3	total reaction
5	3,6	isotope production by spallation and evaporation processes
18	3,6	fission (FP yield is stored in MF=6, MT=18)
51-91	3,6	discrete inelastic scattering (not always)
102	3,6	capture (only for neutron-induced reaction)
103-107	3,6	(n,z) reactions (only for neutron-induced reaction)
151	2	resonance information (only for neutron-induced reaction)
201	3,6	neutron production
202	3,6	gamma production
203	3,6	proton production
204	3,6	deuteron production
205	3,6	triton production
206	3,6	^{3}He production
207	3,6	α production
208	3,6	π^{+} production (if necessary)
209	3,6	π^{0} production (if necessary)
210	3,6	π^{-} production (if necessary)
211	3,6	K^{+} production (if necessary)
212	3,6	K^{0} production (if necessary)
213	3,6	K^{-} production (if necessary)
451	1	general information
452-458	1	fission-related quantities

Table 5 Tentative Schedule of File Productions

	priority	release
JENDL High Energy File		
Phase-I (< 50 MeV)		
neutron	1	1997
20 elements, 55 isotopes		
proton	2	1998
10 elements, 33 isotopes		
Phase-II (< a few GeV)		
neutron	3	1999
proton	3	1999
38 elements, 94 isotopes		
PKA/KERMA File(< 50 MeV)		
neutron	2	1998
29 elements, 78 isotopes		
Photonuclear Data File(< 140 MeV)		
gamma	1	1996
24 elements, 42 isotopes		

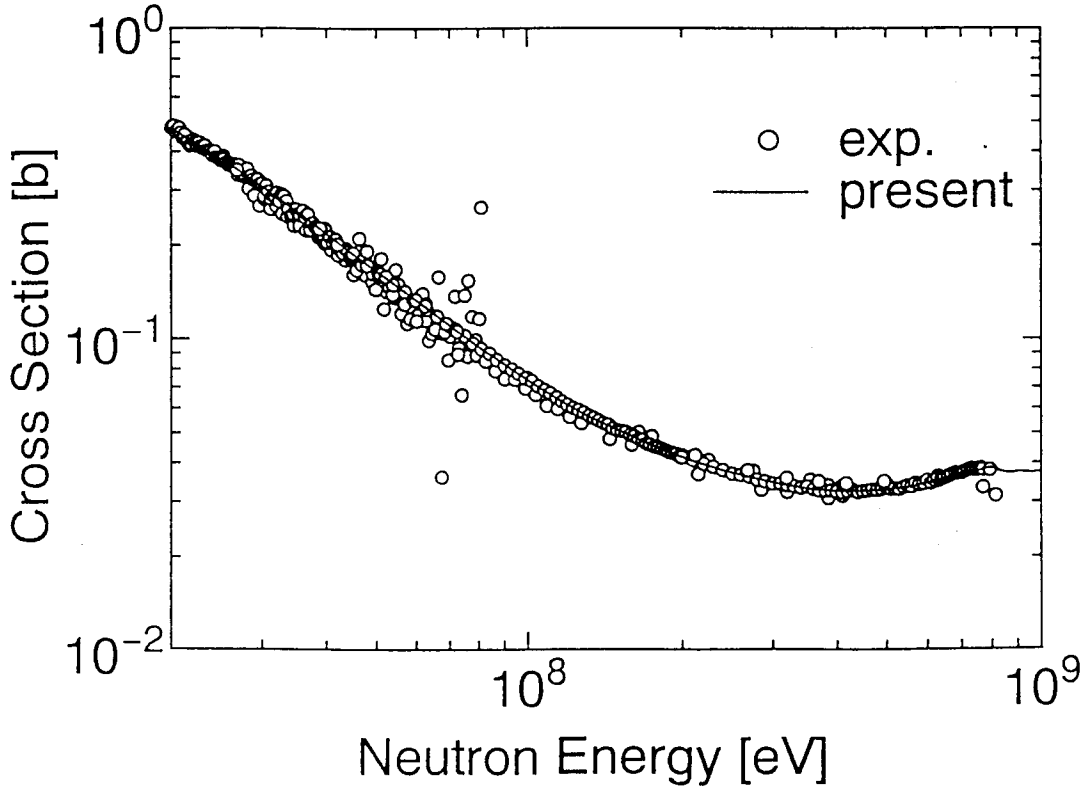

Fig. 1 Neutron-induced ^{1}H Total Cross Section

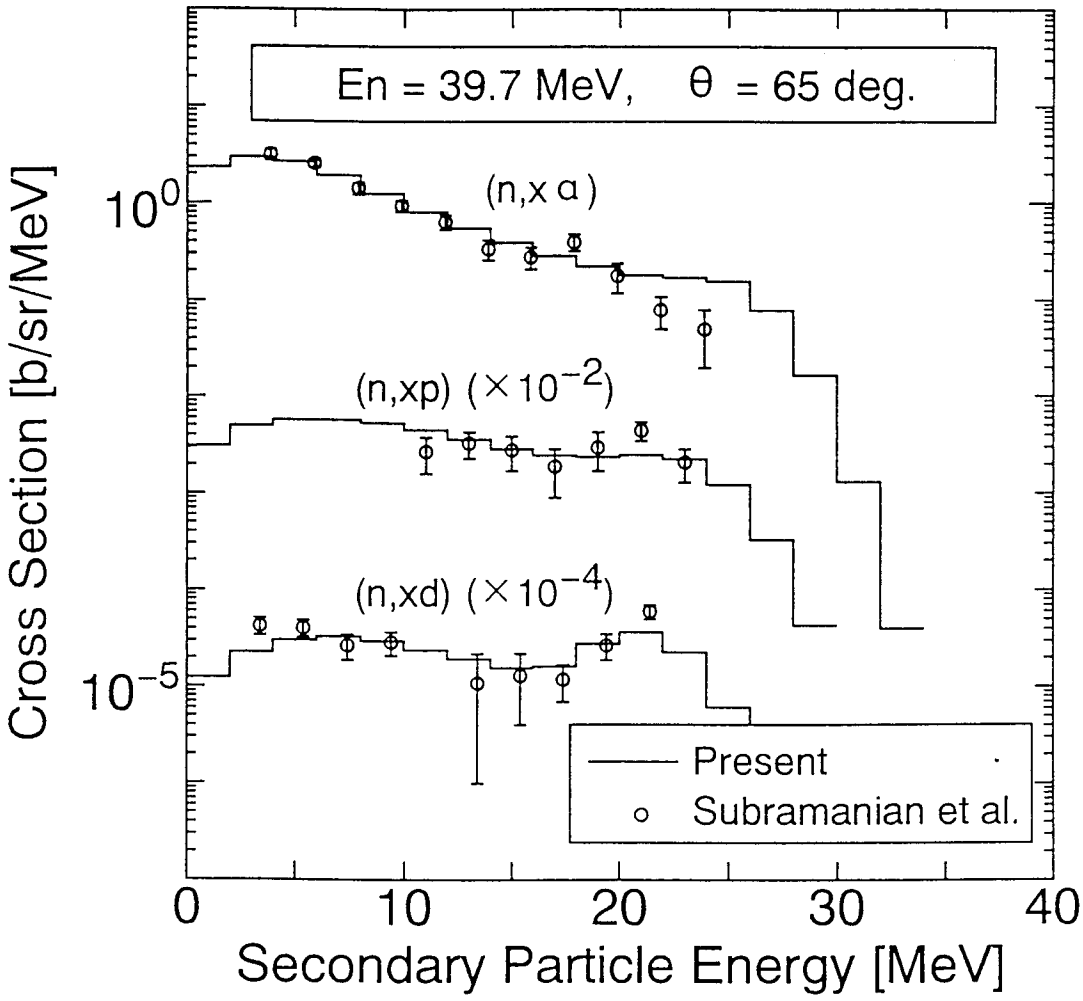

Fig. 2 Double Differential Proton, Deuteron and α-particle Emission Spectra for ^{12}C at the Incident Neutron Energy of 39.7 MeV and the Laboratory Angle of 65 deg

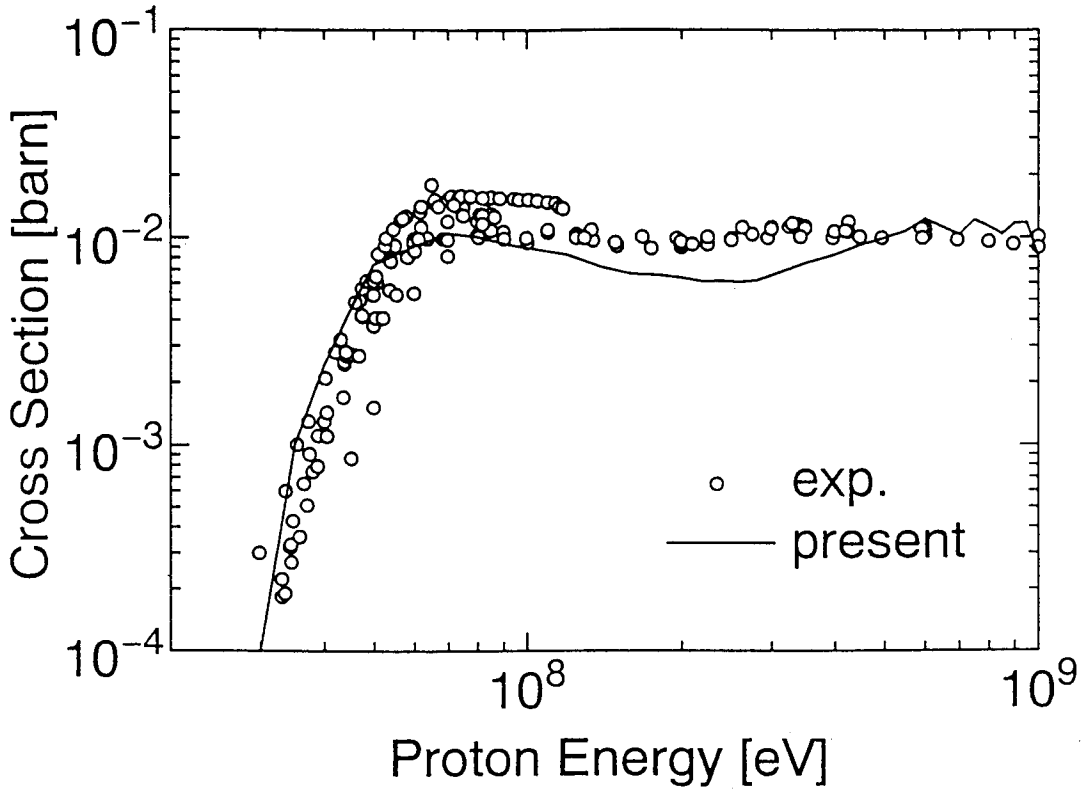

Fig. 3 Isotope Production Cross Section for $^{27}Al(p,X)^{24}Na$ Reaction

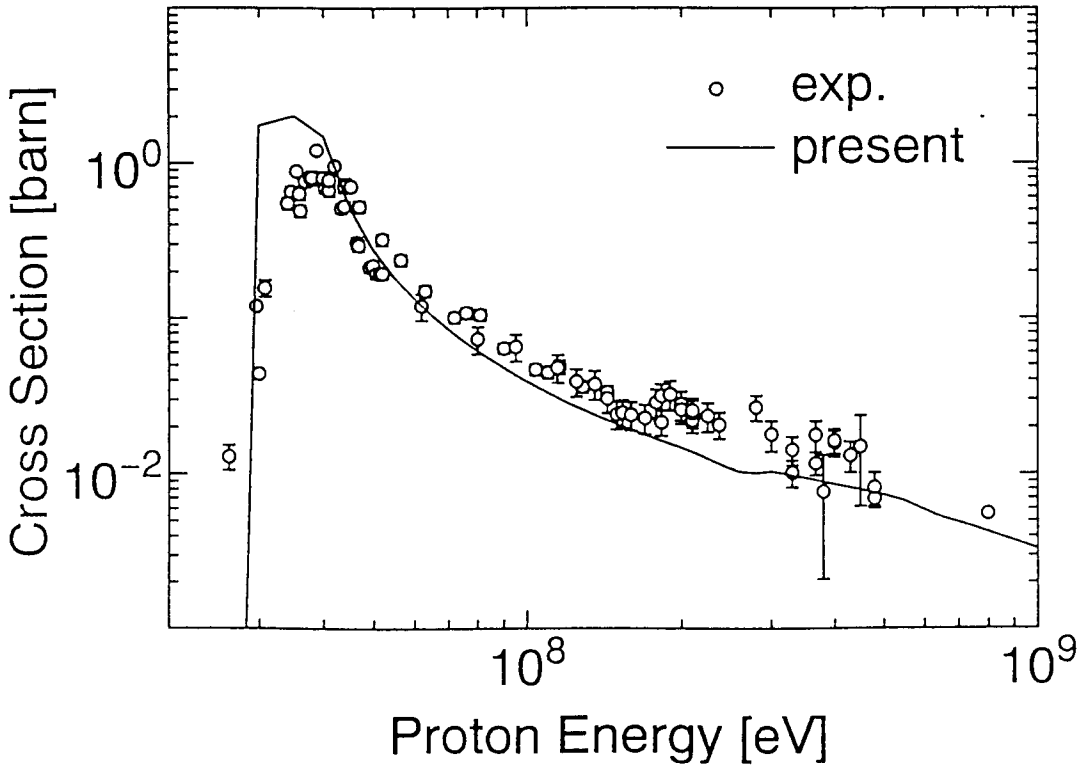

Fig. 4 Isotope Production Cross Section for $^{209}Bi(p,x)^{206}Po$ Reaction

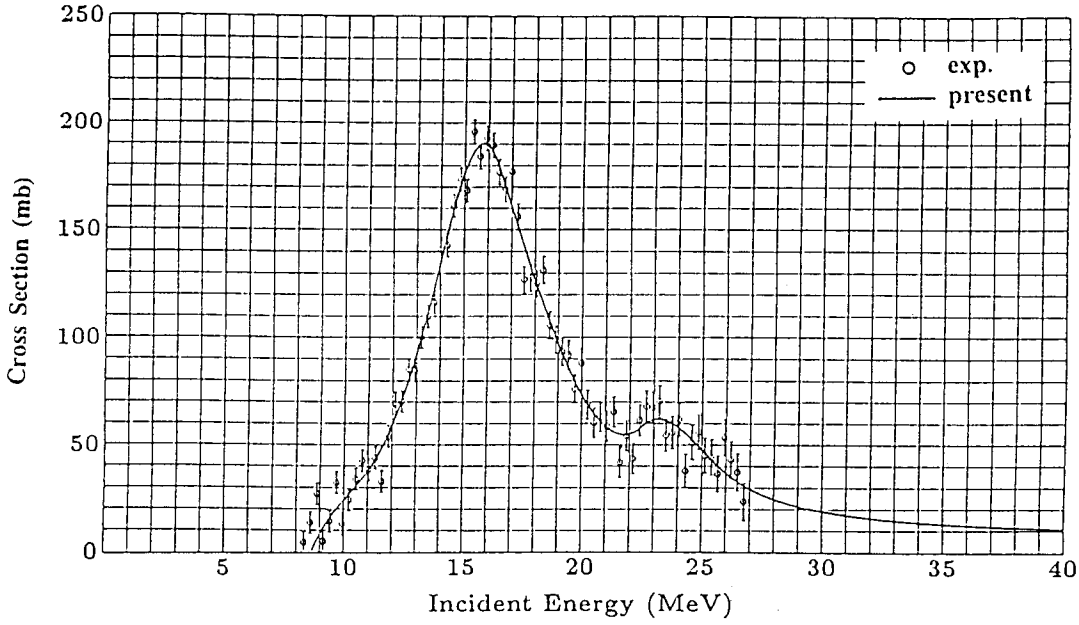

Fig. 5 The (γ,xn) cross section of ^{98}Mo.

2. 4 Calculations of Neutron and Proton Induced Reaction Cross Sections for Actinides in the Energy Region from 10 MeV to 1 GeV

V.A. KONSHIN

Department of Reactor Engineering
Tokai Research Establishment
Japan Atomic Energy Research Institute
Tokai-mura, Naka-gun, Ibaraki-ken

(1995)

Several nuclear model codes were applied to calculations of nuclear data in the energy region from 10 MeV to 1 GeV. At energies up to 100 MeV the nuclear theory code GNASH was used for nuclear data calculation for incident neutrons for ^{238}U, $^{233-236}$U, $^{238-242}$Pu, ^{237}Np, ^{232}Th, $^{241-243}$Am and $^{242-247}$Cm. At energies from 100 MeV to 1 GeV the intranuclear cascade exciton model including the fission process was applied to calculations of protons and neutrons with ^{233}U, ^{235}U, ^{238}U, ^{232}Th, ^{232}Pa, ^{237}Np, ^{238}Np, ^{239}Pu, ^{241}Am, ^{242}Am and $^{242-248}$Cm. Determination of parameter systematics was a major effort in the present work that was aimed at improving the predictive capability of the models used. An emphasis was made on a simultaneous analysis of data for a variety of reaction channels for the nucleus considered, as well as of data that are available for nearby nuclei or other incident particles. Comparison with experimental data available on multiple reaction cross sections, isotope yields, fission cross sections, particle multiplicities, secondary particle spectra, and double differential cross sections indicates that the calculations reproduce the trends, and often the details, of the experimental data.

1. Introduction

Applications such as nuclear waste transmutation, radiation protection for manned space exploration and neutron and charged particle radiotherapy require expanded nuclear data bases [1−3]. The nuclear models play the increased and important role in the provision of nuclear data for such applications.

The previous paper [4] dealt with the actinide nuclear data generation in the energy region from 1 to 20 MeV. The present paper is devoted to the energy region from 10 MeV to 1 GeV.

In this energy region for the majority of actinides experimental data are scarse or nonexistent. For generation of nuclear data the nuclear theory code GNASH [5] and the intranuclear cascade exciton model code CEM [6] were extensively used. An emphasis was made on a simultaneous analysis of data for a variety of reaction channels for the nucleus considered, as well as data that are available for nearby nuclei or other incident particles. Determination of parameter systematics is a major effort in the present work and it is aimed at improving the predictive capability of the models used.

2. Energy Region up to 100 MeV

2.1 Model and Parameters Used in the Energy Region from 10 MeV to 100 MeV

The nuclear theory code GNASH [5], [7] was used in the present work to calculate the fission, (n,xn), ($x \leq 8$) cross sections and composite neutron spectra for 21 nuclides− $^{233-236}$U, ^{238}U, $^{238-242}$Pu, ^{237}Np, ^{232}Th, $^{241-243}$Am and $^{242-247}$Cm in the energy region up to 100 MeV. The code used is the base version [7] and represents statistical plus preequilibrium models with full angular momentum conservation.

For calculation with incident neutrons or protons on nuclei that are strongly deformed such as actinides, the coupled−channel method − the ECIS code developed by Raynal [8] − was used in the present work to obtain transmission coefficients and direct scattering cross−sections. The transmission coefficients are required from low energies up to 100 MeV and they were obtained using relativistic kinematics. In the deformed potential parameters available for actinides [9−11] only a surface absorption term of the imaginary potential was taken into account.

The results of the calculations of $\sigma_t(^{238}U)$ using these parameters show that they reproduce the experimental data for the total cross section quite well up to 18 MeV, but from 20 MeV these parameters lead to too high values of σ_t.

The introduction of the volume absorption term leads to a better agreement with the experimental data for σ_t in the energy region above 20 MeV. The real part of the potential V_R, the surface part of the imaginary potential W_D and the volume absorption term W_V

term W_V for ^{238}U were determined to be the following:

$$V_R = \begin{cases} 45.87 - 0.3E & 0 \le E \le 20 \text{ MeV} \\ 60.84 - 7 \ln E & 20 \le E \le 200 \text{ MeV} \end{cases}$$

$$W_D = \begin{cases} 2.95 + 0.4E & 0 \le E \le 10 \text{ MeV} \\ 6.95 - 0.082(E-10) & 10 \le E \le 90 \text{ MeV} \\ 0.39 & E \ge 90 \text{ MeV} \end{cases} \qquad (1)$$

$$W_V = 8\{1+\exp[-(E-50)/10]\}^{-1}, \quad 0 \le E \le 200 \text{ MeV}$$

V_{SO}=7.5; r_R=1,256; a_R=0.626, r_D=1.260, a_D=0.556, β_2=0.216, β_4=0.080.

2.2 Results of GNASH Calculations

The calculations using the GNASH code were done for ^{238}U, ^{235}U, ^{239}Pu, ^{232}Th, ^{237}Np for which the experimental data for the neutron fission cross sections above 20 MeV exist [12], and for ^{233}U, ^{234}U, ^{236}U, ^{238}Pu, $^{240-242}Pu$, $^{241-243}Am$ and $^{242-247}Cm$ for which there are no experimental data available in the intermediate energy region.

GNASH calculations of the fission cross section of ^{238}U were made with the Ignatyuk et al[13] level density model and with the Gilbert and Cameron level density representation [14] to a neutron energy of 90 MeV (Fig. 1). The Gilbert and Cameron results are seen to be 20 % higher than the experimental data of Lisowski et al [12] and the use of the Ignatyuk et al [13] level density model leads to a better agreement with the experimental data at energies up to 80 MeV. At 90 MeV the present calculated results for ^{238}U with the Ignatyuk et al level density representation have a tendency to underpredict the values of Lisowski et al. At these energies the decay of the 10th and 11th compound nuclei (^{230}U and ^{229}U) should be taken into account (the contribution of ^{230}U to the total fission cross section is about 10 % at 90 MeV). The results of the intranuclear cascade model calculations are also illustrated in Fig. 1. Cascade model results for the fission cross section are too low at energies below 100 MeV.

In Fig. 2 the comparison of the fission cross section of ^{235}U calculated using the GNASH code and the intranuclear cascade model is given. Again, as in the case of ^{238}U, the cascade model gives too low fission cross section values at energies below 100 MeV. The GNASH results are in agreement with experimental data of Lisowski et al [12] up to 100 MeV, even showing the fluctuations of σ_f at 20 and 50 MeV. It should be noted that the fission barrier heights obtained are rather high for the last four compound nuclei $^{228-231}U$ ($E_f^A \approx 6.2$ MeV) compared to the first ones (≈ 5.6 MeV), and E_f^B remains practically constant for A = 228 - 236 ($E_f^B \approx 5.5$ MeV).

The results of calculations of (n,xn) cross sections for ^{235}U are given in Fig. 3. The agreement with experimental data for the (n,3n) cross section by Veeser et al [15] is reasonable.

The results of calculations of the fission and (n,xn) cross sections for ^{239}Pu are given in Figs. 4 and 5. The GNASH results are in good agreement with the experimental data of Lisowski et al [12] for $\sigma_f(^{239}Pu)$ up to 100 MeV (Fig. 4). The decay of nine subsequent compound nuclei was taken into account.

The comparison of the calculations with experimental data available at energies up to 100 MeV generally indicate reasonable agreement. The importance of using realistic optical model parameters and level density models is demonstrated. Unfortunately, experimental data are nonexistent for actinide (n,xn) reaction cross sections which could be of a significant value for validation of the nuclear reaction models used in the 50 - 100 MeV energy range.

3. Energy Region from 100 MeV to 1 GeV

3.1 The Model Used in the Energy Region from 100 MeV to 1 GeV for Actinide Nuclear Data Calculations

In the energy region from 100 MeV to 1 GeV the intranuclear cascade exciton model CEM92 [6,16,17] was used for calculations of proton and neutron induced actinide nuclear data.

The cascade stage of the nuclear reaction is described by the Dubna version of the intranuclear cascade model with the pion production taken into consideration [18]. The emission of n, p, d, t, ^3He and ^4He at both the preequilibrium and the evaporation stages of nuclear reactions are included into the model. The competition between particle emission and fission at the evaporative stage of the reaction is also considered in the model [19].

The approach combines essential features of the exciton and intranuclear cascade models. It was shown by Gudima et al [6] that the experimental data for neutron and proton spectra and neutron double differential cross sections can be reasonably described by the model for Nb, Ni, Fe, Sn for bombarding proton energies below 100 MeV. The model also adequately describes nuclear reactions at higher energies (up to 3 GeV) and is claimed to have a good predictive power [16]. Therefore the model has been chosen for theoretical prediction and systematic investigations of neutron and proton induced fission cross sections and other nuclear characteristics for heavy fissile nuclei. However, it should be noted that this model, although successfully marrying specific features of the cascade model with the exciton pre-equilibrium decay approach, apparently can not be successfully applied to actinides in the energy region below 100 MeV.

3.2. The Sensitivity of the Fission Cross Section Calculated to the Model Parameters

The dependence of actinide fission cross sections on different models for fission barrier height calculations, level density models, ground state shell corrections for fission barriers and the parameter a_f/a_n was investigated here. The aim of the investigation is to find a parameter set which allows all experimental data available for incoming neutrons and protons to be described.

The fission cross section of ^{238}U for proton bombardment for the energy region from 100 MeV to 1 GeV calculated using the CEM92 code is given in Fig. 6. The comparison is made of the experimental data [20–28] and calculations done using different models for fission barrier height calculations [29–35]. It is seen that the phenomenological approach by Barashenkov et al [29],[30] (curves 6,7), as well as the liquid drop model (LDM) with Myers and Swiatecki parameters [31] (curve 5) leads to too low σ_f. Better results can be achieved using the subroutine BARFIT by Sierk [35] which provides the macroscopic fission barrier heights B_f within the framework of the Yukawa–plus–exponential modified LDM, as well as by the approximation by Krappe et al [34]. The most adequate description of macroscopic fission barriers $B_f(A, Z, L)$ for nuclei with Z from 20 to 100 and for the entire range of angular momentum L has been made by Sierk [35].

The change of properties of nuclei with excitation energy increase influences strongly the nuclear fissility leading to the B_f decrease. In the energy region from 100 MeV to 1 GeV this effect is rather small and the $B_f(E^*)$ dependence by Sauer et al [36] was taken into account in final calculations of σ_f(~ 5 % increase in σ_f).

The dependence of the fission barrier height B_f on the rotation of nuclei was calculated using the approximation by Sierk [35] who provides fission barrier heights and saddle point moments of inertia as functions of Z, A and L, where L is the angular momentum transferred to a fission nucleus.

The results of the calculation of the fission cross section of ^{238}U using different level density parameters showed that the dependence of the fission cross section on the different level density systematics presently available [13], [39], [40], [41] is not essential – about 7 % in σ_f at 0.1 – 1 GeV.

3.3. Results of Calculations Using the CEM92 Code

The following set of the parameters was used in the calculations using the CEM92 code: the fission barrier height values by Sierk [35], with $B_f(E^*)$ dependence by Sauer et al [36], with $B_f(L)$ dependence by Cohen et al [38], ground state shell and pairing corrections by Truran et al [42], level density systematics by Iljinov et al [41] (the third set), and a_f/a_n = 1.0. No further adjustments of any parameters was made.

Fig. 7 shows experimental spallation yields by Pate and Poskanzer [43] for ^{238}U, and calculated curves. The comparison is also made with the calculated results of Hahn and Bertini [44] and Barashenkov et al [18]. The better agreement of the present calculated results for the ^{238}U(p,pxn) isotope yields with the experimental data than the calculations [44]

and [18] is seen from Fig. 7 for incoming proton energy of 1.8 GeV. Barashenkov et al [18] have used a constant value of the a-parameter (a = A/15 MeV^{-1}) and Hahn and Bertini [44] employed a rather crude approximation – the energy – independent expression for Γ_n/Γ_f (curve 2, Fig. 7). The use of energy-dependent Γ_n/Γ_f values, on the contrary, in the calculations by Hahn and Bertini [44] gave results which did not follow the experimental data (curve 1).

If the fission process of the excited residual nuclei is neglected and their decay is assumed to be due to the evaporation process, the calculated results are several orders of magnitude higher than the experimental data (curve 5, Fig. 7).

The experimental data for ^{235}U, ^{238}U, ^{239}Pu, ^{232}Th and ^{237}Np for the neutron induced fission cross sections obtained by Lisowski et al [12] in the energy region up to 300 MeV give another possibility to test the model. The calculations of the neutron induced fission cross sections were made with the same parameters as the proton induced fission cross sections.

The results of the neutron induced fission cross section calculations for ^{238}U and $^{245-248}Cm$ are shown in Figs. 8 and 9. A reasonable agreement of calculated results and experimental data by Lisowski et al [12] for ^{238}U is seen.

Neutron angular distributions for ^{238}U for incoming neutron energies 100, 500 and 1000 MeV are illustrated in Fig. 10. Some increase is seen at angles near 180° both for neutrons and protons.

Double differential cross sections for the production of neutrons from 585 MeV proton bombardment of the U target have been measured at emission angles 30°, 90° and 150° by Cierjacks et al [45]. The present calculated results are compared with these experimental data in Figs. 11 and 12. The calculated results obtained using the CEM92 code were corrected for additional neutrons emitted by fission fragments, taking into account the data by Barashenkov and Toneev [46]. The total number of neutrons emitted at 585 MeV is equal to 13, including 1.44 cascade (the mean energy $\bar{E}$ = 77.5 MeV), 1.81 preequilibrium ($\bar{E}$ = 15.5 MeV), 1.80 prefission evaporative neutrons and 8.0 evaporative neutrons emitted from fission fragments ($\bar{E}$ = 2.5 MeV).

The comparison of calculated and experimental results shows that the agreement is reasonable for all three angles in the energy region below 100 MeV. At higher energies (100–300 MeV) a systematic underevaluation of high energy cascade neutrons can be seen which increases with neutron emission angle increase. But the overall agreement is surprisingly good, in particular, if one takes into account a large spread of results obtained by different models [47].

4. Conclusion

The use of two codes – GNASH and CEM92 – with the respective parameter

systematics allows nuclear data to be generated in the energy region from 10 MeV to 1 GeV. For use at energies above 100 MeV GNASH will need some modification, in particular taking into consideration multiple preequilibrium neutron emission [48]. The use of the code CEM92 for the energy region below 100 MeV for actinides leads to unrealistic results. The code CEM92 with the parameter systematics discussed can reliably be used for generation of nuclear data above 100 MeV. Corrections for neutrons emitted by fission fragment have to be introduced into the calculated CEM92 results.

Parameter systematics adopted here allows to improve the predictive capability of the models used. Comparison with experimental data available for multiple reaction cross sections, fission cross section, isotope yields, particle multiplicities, neutron spectra and double differential cross sections both for incoming neutrons and protons indicates that the calculations reproduce the trends, and often the details, of the experimental data.

Acknowledgement

The author is grateful to Dr. Y. Kikuchi and Mr. T. Nakagawa of the Nuclear Data Center, JAERI, for support of the present work, fruitful discussions and for the help in using the computer FACOM-M780.

References

[1] Lisowski P.W., Bowman C.D., Arthur E.D. and Young P.G.: Proc. of the International Conference on Nuclear Data for Science and Technology, Jülich, Germany, 1991, Springer-Verlag, 92 (1992).

[2] Howe S.: Proc. of the International Conference on Nuclear Data for Science and Technology, Jülich, Germany, 1991, Springer-Verlag, 692 (1992).

[3] Wambersie A. and Gregoire V.: Proc. of the International Conference on Nuclear Data for Scinece and Technology, Jülich, Germany, 1991, Springer-Verlag, 579 (1992).

[4] Konshin V.A.: Consistent Calculations of Fast Neutron Induced Fssion, (n,2n) and (n,3n) Cross Sections for 71 Isotopes of Th, Pa, U, Np, Pu, Am, Cm, Bk and Cf, JAERI-Research 95-010 (1995).

[5] Young P.G. and Arthur E.D.: GNASH: A Preequilibrium Statistical Nuclear Model Code for Calculation of Cross Sections and Emission Spectra, LA-6947 (1977).

[6] Gudima K.K., Mashnik S.G. and Toneev V.D.: Nucl. Phys. A401, 329 (1983).

[7] Young P.G., Arthur E.D. and Chadwick M.B.: Proc. of the ICTP Workshop on Computation and Analysis of Nuclear Data Relevant to Nuclear Energy and Safety, Trieste, Italy, 1992, World Scientific, 622 (1993).

[8] Raynal J.: Optical Model and Coupled-Channel Calculations in Nuclear Physics, IAEA

Report SMR-9/8, 281 (1970).
[9] Delaroche I.P., Lagrange Ch. and Salvy I.: Proc. of a Consultants' Meeting on the Uses of Nuclear Theory in Neutron Nuclear Data Evaluation, Vienna, 1976, IAEA, V.1, 251 (1976).
[10] Tamura T.: Rev. Mod. Phys. 37, 679 (1965).
[11] Klepatskij A.B., Konshin V.A., Maslov V.M. and Sukhovitskij E.Sh.: Yadernye Konstanty (Nuclear Constants) 4, 5 (1985), translated INDC(CCP)-336/L, IAEA, Vienna (1991).
[12] Lisowski P.W., Gavron A., Parker W.E., Ullman J.L. Balestrini S.J., Carlson A.D., Wasson O.A. and Hill N.W.: Proc of a Specialists' Meeting on Neutron Cross Section Standards for the Energy Above 20 MeV, Uppsala, Sweden 21-23 May 1991, p.178 (1991).
[13] Ignatyuk A.V., Smirenkin G.N. and Tishin A.S.: Sov. J. Nucl. Phys. 21, 255 (1975).
[14] Gilbert A. and Cameron A.G.W.: Can. J. Phys. 43, 1446 (1965).
[15] Veeser L.R. et al.: Proc. of the Intern. Conference on Nuclear Data for Science and Technoogy, Harwell, 1054 (1978).
[16] Mashnik S.G.: Proc of the Intern. Conf. on Nuclear Data for Science and Technology, Gatlinburg, May 9-13, 1994 p.499 (1994).
[17] Mashnik S.G.: Proc of a Specialists' Meeting on Intermediate Energy Nuclear Data: Models and Codes, Issy-les-Moulineaux, France, p.107 (1994).
[18] Barashenkov V.S., Gereghi F.g., Iljinov A.S. and Toneev V.D.: Nucl. Physics A222, 204 (1974).
[19] Mashnik S.G.: Acta Phys. Slov. 43, 243 (1993)
[20] Fulmer C.B.: Phys. Rev., 116, 418 (1959).
[21] Hyde E., Perlman I. and Seaborg G.: The Nuclear Propetrties of the Heavy Ellments; III Fission phenomena, Englwood Cliffs, N.J. (1964).
[22] DeCarvalho H.G., Cortini G., Muchnik N., Potenza G., Rinzivillo R. and Lock W.O.: Nuovo Cimento 27, 468 (1963).
[23] Bochagov B.A., Bychenkov V.S., Dmitriev V.D., Maltsev S.P., Obukhov A.I., Perfilov N.A., Udod A.V. and Shigaev O.E.: Sov. J. Nucl. Phys. 28 (2), 291 (1978).
[24] Konshin V.A., Matusevich E.S. and Regushevski V.I.: Sov. J. Nucl. Phys. 2, 489 (1966).
[25] Hudis J. and Katcoff S.: Phys. Rev. 180, 1122 (1969).
[26] Hudis J. and Katcoff S.: Phys. Rev. C13, 1961 (1976).
[27] Brandt R., Carbonara F., Cieslak E., Piekarz J. and Zakrzewski J.: The Study of Nuclear Fission Induced by High-Energy Protons, CERN Preprint (1970).
[28] Remy G., Ralarosy J., Stein R., Debeauvais M. and Tripier J.: Nucl. Phys. A163, 583 (1971).
[29] Barashenkov V.S., Iljinov A.S., Toneev V.D. and Gereghi F.G.: Nucl. Phys. A206, 131 (1973).

[30] Barashenkov V.S. and Gereghi F.G.: Preprint JINR 94-10781, Dubna (1977).
[31] Myers W.D. and Swiatecki W.S.: Ark. Fyz. 36, 343 (1967).
[32] Pauli H.C. and Ledergerber T.: Nucl. Phys. A175, 545 (1971).
[33] Krappe H.J. and Nix J.R.: Proc. of the IAEA Symp. on the Physics and Chemistry of Fission, Rochester, New Yourk, 1973, v.1, p.159 (1974).
[34] Krappe H.J., Nix J.R. and Sierk A.J.: Phys. Rev. C20, 992 (1979).
[35] Sierk A.J.: Phys. Rev. C33, 2039 (1986).
[36] Sauer G., Chandra H. and Mosel U.: Nucl. Phys. A264, 221 (1976).
[37] Strutinsky V.M.: Yad. Fiz. 1, 821 (1965).
[38] Cohen S. and Swiatecki W.J.: Ann. Phys. 22, 406 (1963).
[39] Ignatyuk A.V., Itkis M.G., Okolovich V.N., Smirenkin G.N. and Tishin A.S.: Yad. Fiz. 21, 1185 (1975).
[40] Cherepanov E.A. and Iljinov A.S.: Nucleonika 25, 611 (1980).
[41] Iljinov A.S., Mebel M.V., Bianchi N., De Sanctis E., Guaraldo C., Lucherini V., Muccifora V., Polli E., Reolon A.R. and Rossi P.: Nucl. Phys. A543, 517 (1992).
[42] Truran J.W., Cameron A.G.W. and Hilf E.: Proc. of the Conf. on the properties of Nuclei Far From the Region of Beta-Stability, Leysin, Switzerland, v.1, p.275 (1970).
[43] Pate B.D. and Poskanzer A.M.: Phys. Rev. 123, 647 (1961).
[44] Hahn R.K. and Bertini H.W.: Phys. Rev. C6, 660 (1972).
[45] Cierjacks S., Hino Y., Raupp F., Buth L., Filges D., Cloth P. and Armstrong T.W.: Phys. Rev. C36, 1976 (1987).
[46] Barashenkov V.S. and Toneev V.D.: The Interaction of High-Energy Particles and Nuclei with Nuclei, Atomizdat, Moscow (1972).
[47] Nagel P., Rodens J., Blann M. and Gruppelaar H.: Nucl. Sci. Eng. 119, 97 (1995).
[48] Young P.G. and Chadwick M.B.: Proc. of the Intern. Conference on Nuclear Data for Science and Technology, Gatlinburg, May 9-13, 1994, v.1, p.582 (1994).

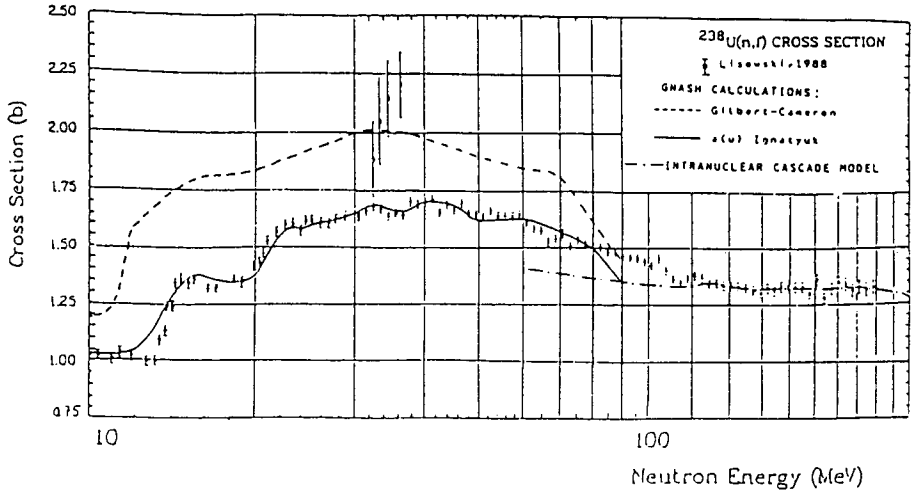

Fig. 1. The fission cross section of ^{238}U.

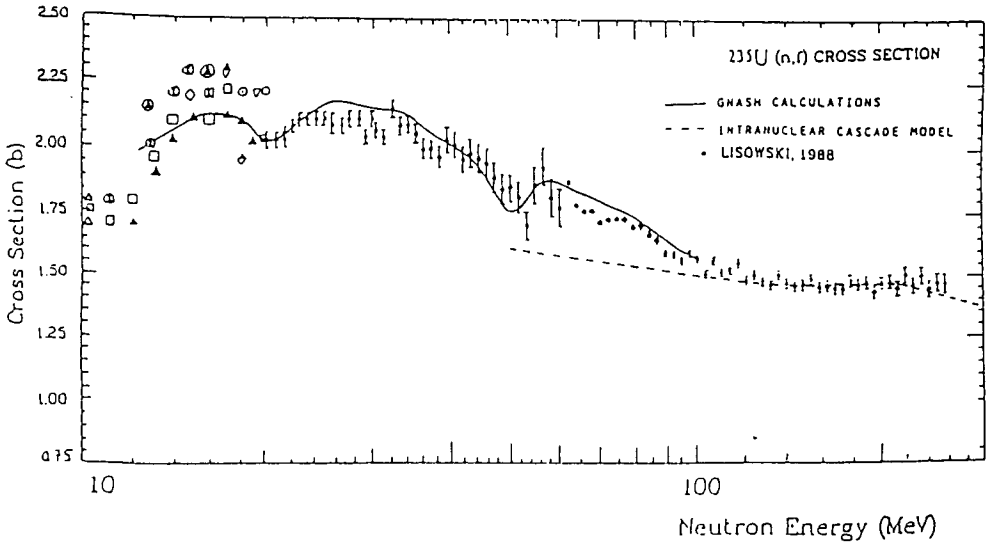

Fig. 2. ^{235}U fission cross section (–GNASH, --- intranuclear cascade model).

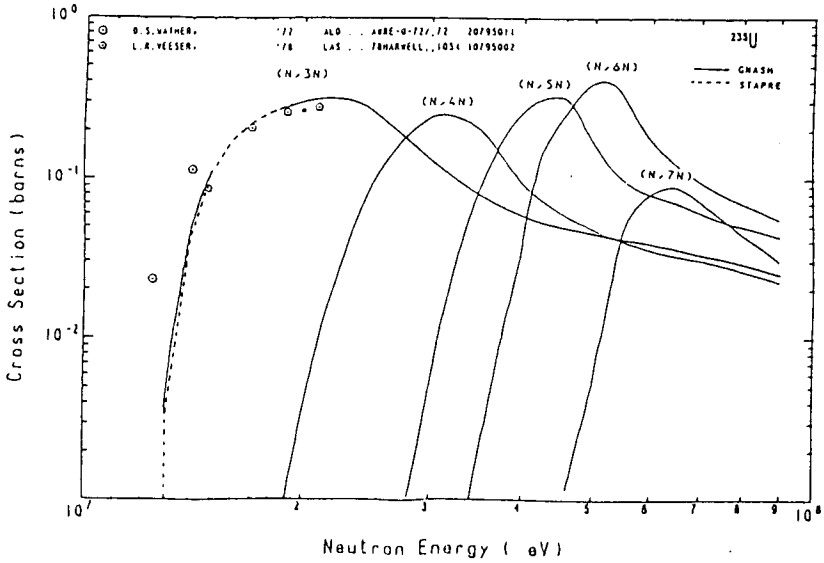

Fig. 3. The (n,xn) reaction cross sections for ^{235}U.

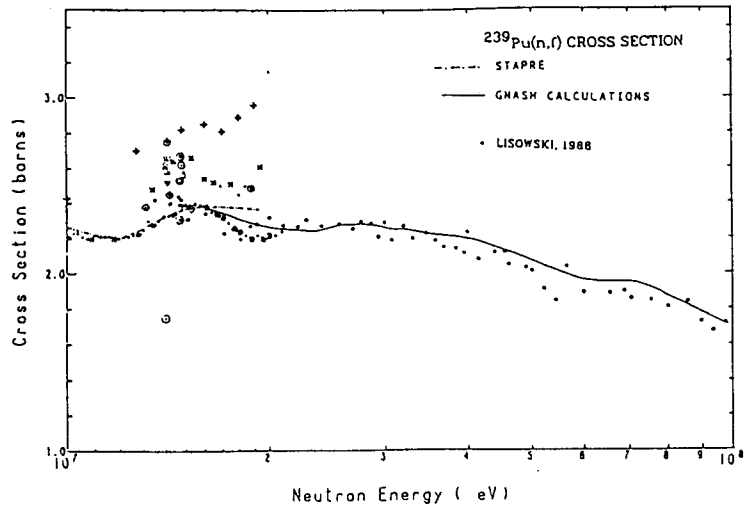

Fig. 4. The ^{239}Pu fission cross section.

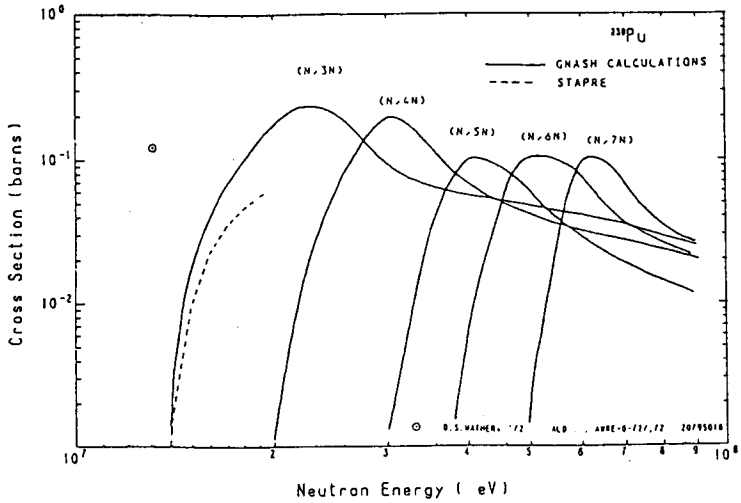

Fig. 5. The ^{239}Pu(n,xn) reaction cross sections.

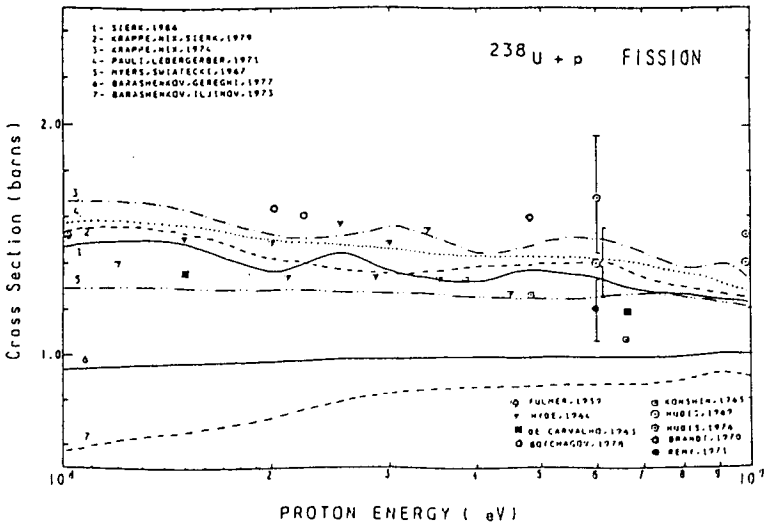

Fig. 6. The ^{238}U proton induced fission cross section dependence on different models for fission barrier height calculations.

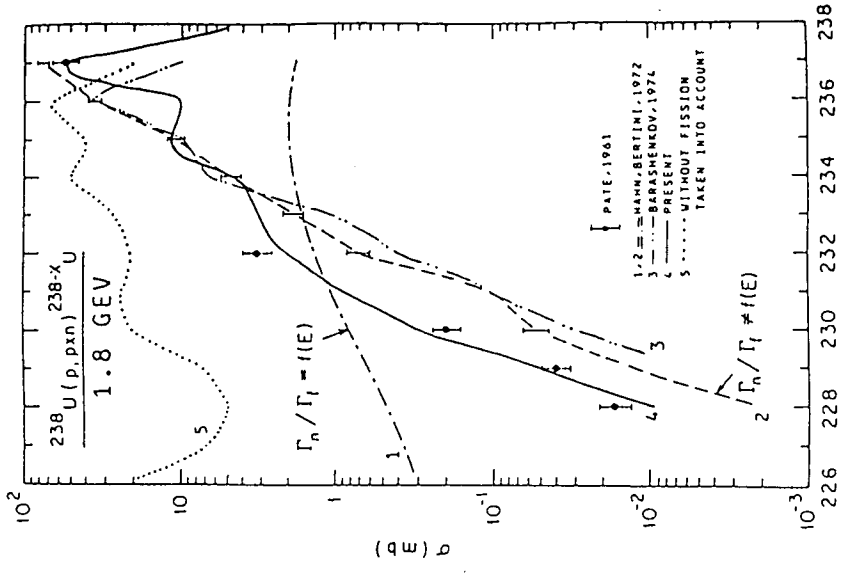

Fig. 7. The yield of uranium isotopes in the reaction $^{238}U(p,pxn)^{238-x}U$ at 1.8 GeV.

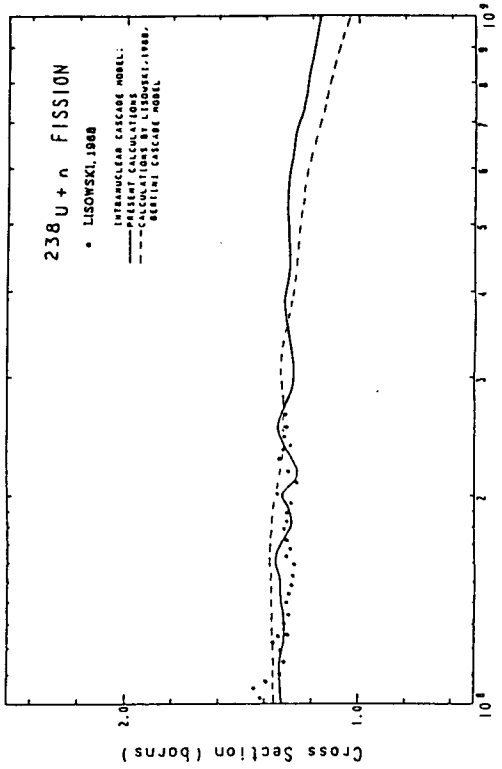

Fig. 8. The neutron induced ^{238}U fission cross section.

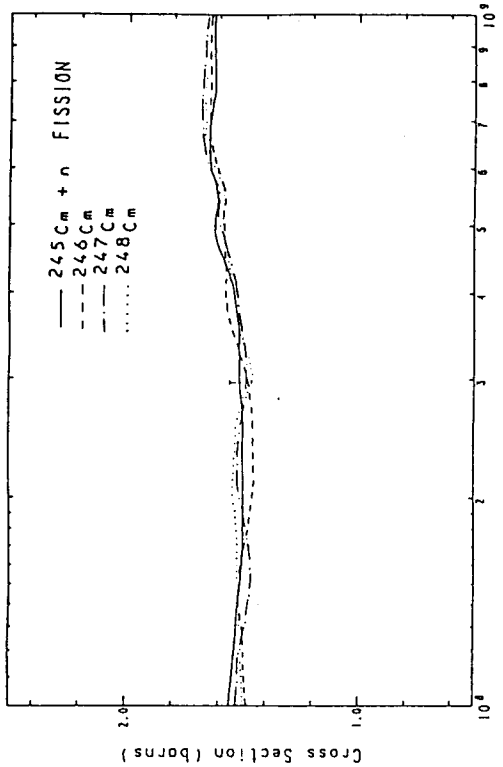

Fig. 9 The neutron induced ^{245}Cm, ^{246}Cm, ^{247}Cm and ^{248}Cm fission cross section.

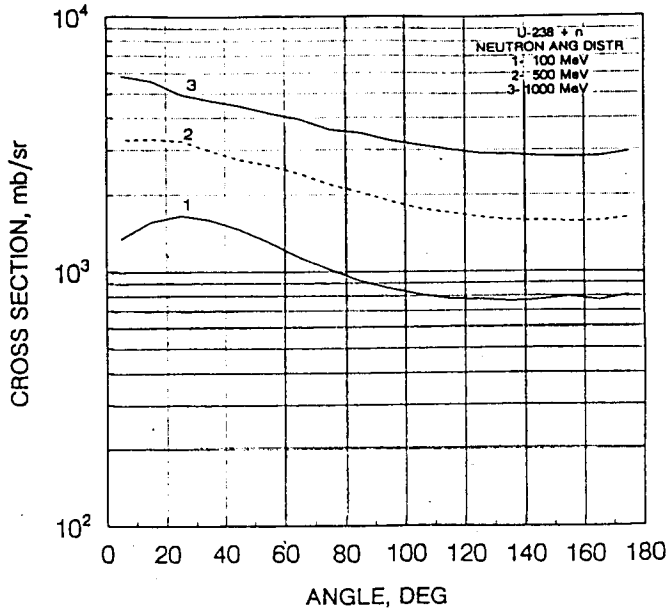

Fig. 10. Neutron angular distributions for ^{238}U neutron bombardment with energies of 100, 500 and 1000 MeV.

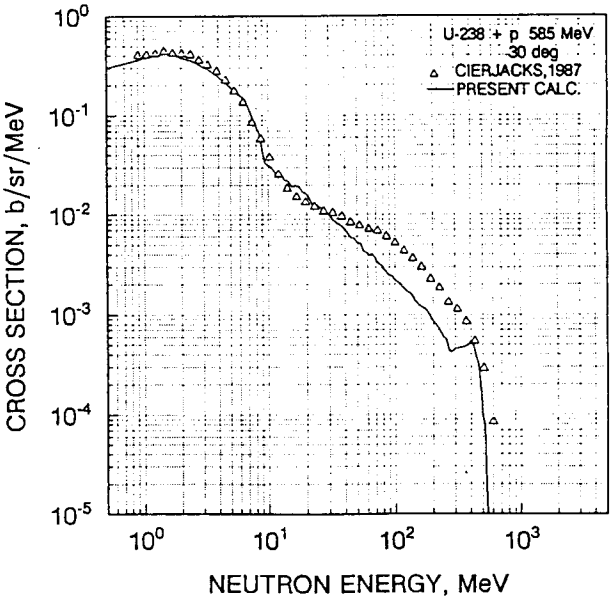

Fig. 11 Comparison of the present calculations of double differential neutron production cross sections for ^{238}U at E_p=585 MeV and 30 deg with experimental data [45].

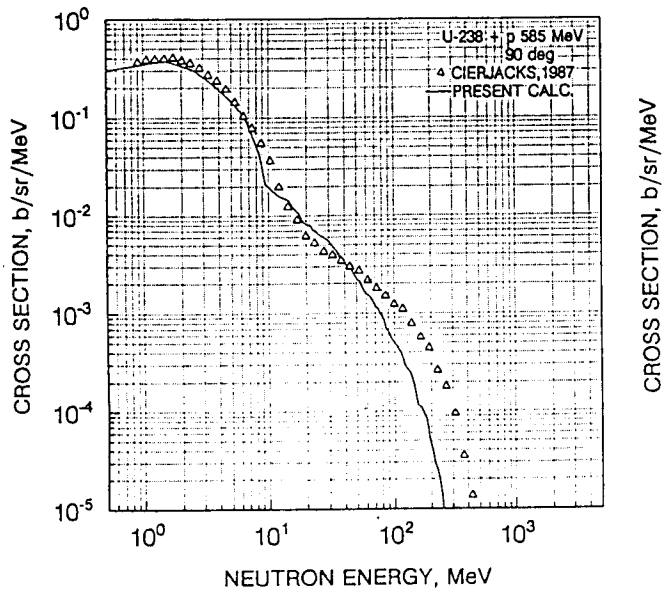

Fig. 12 Comparison of the present calculations of double differential neutron production cross sections for ^{238}U at E_p=585 MeV and 90 deg with experimental data [45].

3. Experiment

3. 1 REVIEW OF RECENT NEUTRON EXPERIMENTS OF ENERGY ABOVE 20 MeV AT CYRIC, TIARA AND RIKEN CYCLOTRON FACILITIES

Takashi Nakamura and Accelerator Shielding Research Group*
Cyclotron and Radioisotope Center, Tohoku University
Aoba, Aramaki, Aoba-ku, Sendai 980, Japan

ABSTRACT

We developed the quasi-monoenergetic neutron fields using $^{7}Li(p,n)$ reaction at three AVF cyclotron facilities; 1) Cyclotron and Radioisotope Center, Tohoku University (CYRIC) for 20 to 40 MeV protons, 2) Takasaki Research Establishment, Japan Atomic Energy Research Institute (TIARA) for 40 to 90 MeV protons, and 3) Institute for Physical and Chemical Research (RIKEN) for 80 to 135 MeV protons. By using these neutron fields, we did the experiments on 1) response functions and efficiencies of neutron detectors, 2) neutron production yield by charged particles, 3) neutron-induced charged particle production cross sections, 4) neutron penetration and streaming through shielding materials, and 5) neutron activation and spallation cross sections.

*Research Group Members:

Masashi Takada, Eunju Kim:
Cyclotron and Radioisotope Center, Tohoku University
Mamoru Baba, Tomohiko Iwasaki, Shigeo Matsuyama, Takehide Kiyosumi:
Department of Nuclear Engineering, Tohoku University
Noriaki Nakao, Tokushi Shibata, Mineo Imamura, Seiichi Shibata:
Institute for Nuclear Study, University of Tokyo
Kazuo Shin:
Department of Nuclear Engineering, Kyoto University
Yoshitomo Uwamino, Noriyoshi Nakanishi:
Institute for Physical and Chemical Research
Shun-ichi Tanaka, Hiroshi Nakashima, Yukio Sakamoto,
Yoshihiro Nakane, Hiroshi Takada, Shinichiro Meigo:
Tokai Research Establishment, Japan Atomic Energy Research Institute
Susumu Tanaka:
Takasaki Research Establishment, Japan Atomic Energy Research Institute

I. INTRODUCTION

Interest to neutron reaction data is world-wide increasing from the viewpoints of intense neutron source of material study, nuclear transmutation of radioactive wastes, induced radioactivity and shielding design of high energy accelerators. Nevertheless, neutron reaction data in the energy range above 20 MeV are still very poor and no evaluated data file exists at present mainly due to very limited number of facilities having

quasi-monoenergetic neutron fields available for neutron reaction cross section and shielding experiments above 20 MeV.

The accelerator shielding research group has been doing as a cooperative project between JAERI and several universities. In this study, we developed the quasi-monoenergetic neutron fields using ^{7}Li(p,n) reaction at three AVF cyclotron facilities; 1) Cyclotron and Radioisotope Center,Tohoku University (CYRIC) for 20 to 40 MeV protons, 2) Takasaki Research Establishment, Japan Atomic Energy Research Institute (TIARA) for 40 to 90 MeV protons and 3) Institute for Physical and Chemical Research (RIKEN) for 80 to 135 MeV protons.

By using these neutron fields, we did the experiments on

1) response functions and efficiencies of neutron detectors
2) neutron production yield by charged particles
3) neutron-induced charged particle production cross sections
4) neutron penetration and streaming through shielding materials
5) neutron activation and spallation cross sections

and so on. These experimental results are quite valuable data in the intermediate neutron energy region, where there exists very poor data. Here, a review will be given on these results.

II. ESTABLISHMENT OF QUASI-MONOENERGETIC NEUTRON FIELD

(1) CYRIC neutron field

The CYRIC neutron field has the 45 m long neutron TOF facility coupled with the beam chopping system and the beam swinger system. The quasi-monoenergetic neutrons of 22.0 and 32.5 MeV having 1.7 and 1.4 MeV FWHM were obtained from 2 mm thick ^{7}Li target bombarded by 25 and 35 MeV protons, respectively, and the proton beam hit the target at 10 deg with the swinger magnet and was fully stopped at the Faraday cup. The neutrons were extracted in the TOF facility through the 50 cm thick iron-polyethylene collimator of 30 cm x 20 cm aperture settled in the 280 cm thick concrete wall of 100 cm x 50 cm aperture. Figure 1 shows the cross-sectional view of the CYRIC neutron field. This neutron field was established as the neutron reference field for detector calibration by determining the absolute neutron fluence with the proton recoil counter telescope (PRT). The 22.0 and 32.5 MeV peak neutron fluences were 1.1×10^{3} and 1.7×10^{3} n cm^{-2} μC^{-1} at the collimator exit behind 8.6 m from the target. The neutron spectra measured with the TOF method using a 12.7-cm-diam by 12.7-cm long BC501A detector are shown in Fig. 2.

(2) TIARA neutron field

The TIARA neutron field was established in the neutron beam line collimated into 10 cm diameter. The 2 to 5 mm thick ^{7}Li target settled in the cyclotron room was bombarded by the proton beam of 20 to 90 MeV at 0 deg and the protons passed through the target were bent down to the beam dump by a clearing magnet, and the neutrons produced at 0 deg were extracted through the 220 cm thick concrete wall. Figure 3 shows the cross-sectional view of the TIARA neutron field.

The absolute fluence of source neutrons was determined with PRT and the neutron fluence during the experiment was monitored simultaneously with the ^{238}U and ^{232}Th fission chambers fixed closely to the target. The FWHM of 40.5 and 64.5 MeV monoenergetic peak and the peak neutron yield have the respective values of 2.0 MeV

and 2.1×10^4 n cm^{-2} μC^{-1}, 2.1 MeV and 3.2×10^4 n $cm^{-2} \mu C^{-1}$, at the collimator exit behind 4 m from the target, for 43 and 67 MeV proton incidence. The neutron spectra measured with the TOF method using BC501A and PRT are shown in Fig.4.

(3) RIKEN neutron field

The RIKEN neutron field is now being established at the E4 experimental room of the separate sector ring cyclotron. The proton beam having energies of 80, 90, 100, 110, 120 and 135 MeV were injected on a 10 mm thick ^{7}Li target through the beam swinger. Protons passed through the target were cleared out by the magnet and absorbed in the spectrograph. Neutrons produced at 0 deg were transported through the iron-concrete collimator of 20 cm by 20 cm aperture and 120 cm length. Figure 5 shows the experimental layout at this field.

The neutron spectra were measured with the TOF method using BC501A and the absolute neutron fluence with the Li activation method using the ^{7}Be activity from the ^{7}Li(p,n)^{7}Be reaction. Figure 6 shows the neutron spectra for 90, 100, 110 and 120 MeV proton incidence.

III. MEASUREMENT OF NEUTRON DETECTOR RESPONSE

By using these quasi-monoenergetic neutron fields, the response functions and detection efficiencies of various neutron detectors have been measured, such as organic liquid scintillator, dose-equivalent counter, track detector, Si diode and TLD. Here, we only describe about the response function measurement of a 12.7-cm diam by 12.7 cm long BC501A scintillator.

These measurements were done under the geometry that the detector was placed at about 12 m away from the target which was thick enough to stop accelerated particles. White-spectral neutrons were generated from the target and the light output distributions of the detector were measured with the TOF method. The TOF spectrum was converted to the energy spectrum. After eliminating gamma-ray pulses by two-dimensional n-γ discrimination technique, we sampled neutron events into neutron energy interval whose width was wider than that of the energy resolution. The interval widths were fixed to be 1, 2, 4, 5 MeV for energy range from 0 to 44, 44 to 70, 70 to 90, 90 to 130 MeV, respectively. We then obtained the response functions of the detector up to 130 MeV neutron energy.

Figure 7 shows some experimental results compared with the Monte Carlo calculations[1-3]. For lower energy neutrons, the measured results show good agreement with the Monte Carlo results, except a small difference in the upper recoil proton edge. With increasing neutron energy, this discrepancy becomes larger and a large discrepancy is especially found in the middle peak of the light output distribution coming from deuteron components of ^{12}C(n,d) reaction. This discrepancy revealed that the calculation model of this reaction is not correct.

IV. NEUTRON PRODUCTION YIELD BY CHARGED PARTICLES

Neutron production yields for several projectile-target combinations were measured with the TOF method using BC501A. Protons of 70 MeV, He ions of 100 MeV and C ions of 220 MeV were transported to the HB beam line in the heavy ion room 1 at TIARA, and were injected into carbon, zirconium, iron and gold targets thick enough to stop injected

particles. The targets were set in a vacuum chamber and the detector was placed at 0, 15, 30, 45, 60, 90 and 120 deg to the beam direction about 5 m behind from the target. The repeated measurements were done with the 40 cm thick iron shadow shield to estimate the room-scattered neutrons. The beam intensity was measured with a target Faraday cup.

Figure 8 shows two examples of differential neutron spectra measured for C and Zr targets bombarded by 220 MeV C ions. The neutron spectra extend up to about 100 MeV energy and become softer with the neutron emission angle. The neutron spectra for C target are harder that those for Zr target.

V. NEUTRON-INDUCED CHARGED PARTICLE PRODUCTION CROSS SECTIONS

The energy spectra of protons and deuterons emitted from thick carbon target which was bombarded by 43 and 67 MeV p-Li quasi-monoenergetic neutrons at TIARA were measured with PRT. Figure 9 shows the experimental arrangement. A carbon sample of 8 cm x 9 cm and 0.3 to 0.5 mm thickness with a 6 cm diam hole was set in the neutron beam. For the measurements at 30 to 120 deg to the beam axis, the PRT was inclined to the beam axis, and at the detection angle less than 25 deg the PRT was set in the beam axis with a blass shadow bar to shut off direct neutron incidence to the PRT. The measurements were repeated with and without carbon sample to estimate background contribution.

Figure 10 exemplifies the proton and deuteron spectra of C(n,px) and C(n,dx) reactions obtained at 12.4 deg for 64.5 MeV neutrons. Two peaks at about 52 and 45 MeV correspond to the ground and first excited states of ^{12}B produced by $^{12}C(n,p)^{12}B$ reaction. Our experimental results for 64.5 MeV neutrons are compared with those at 15 deg for 60.7 MeV neutrons measured at UC Davis[4]. Apart from small difference of incident neutron energy and emission angle, the general tendency of the two spectra is quite similar each other.

VI. NEUTRON PENETRATION AND STREAMING THROUGH SHIELDING MATERIALS

We measured the spectra of neutrons which penetrated concrete and iron shields using BC501A and multi-sphere spectrometer with 40.5 and 64.5 MeV quasi-monoenergetic neutrons at TIARA. The neutron beam were injected into 120 cm by 120 cm concrete slab of 25 to 200 cm thickness or iron slab of 10 to 130 cm thickness, which were fixed in contact with the 10 cm diam collimator exit located at 4 m from the target. The BC501A detector was contacted with the shield surface on the beam axis and also at 20 and 40 cm distances off the beam axis to investigate the surface distribution of scattered neutrons. Multi-sphere spectrometer with four polyethylene moderators of 1.5, 3.0, 5.0 and 9.0 cm thicknesses and without moderator was also used only on the beam axis to get lower energy neutron spectra.

The neutron spectra above 5 MeV were obtained from BC501A with the help of the FERDOU unfolding code[5] and the response functions measured in this study.[6] The neutron spectra below 10 MeV were obtained from multi-sphere spectrometer with the help of the SAND-2 code[7] and the response function given by Uwamino et al.[8] Initial guess spectra in the SAND-2 unfolding was given from the results calculated with the MORSE code[9] and the DLC-119/HILO86 cross section library.[10]

In Figs. 11 and 12, neutron spectra measured on the beam axis behind 70 cm thick iron and behind 100 cm thick concrete for 64.5 MeV neutron source are compared with the

spectra calculated with the MORSE and DOT3.5 codes[11] using the HILO86 group cross section, respectively. The results with DOT3.5 and MORSE are both in good agreement with the measured results within the statistical error. In the figures, the calculation with the HETC code[12] are also compared, in which the effect of elastic scattering cross section is demonstrated. The HETC calculation with elastic scattering gives better results than without it, but still gives overestimation to the measured results.

The experimental data on the streaming through a labyrinth is now in analysis.

VII. NEUTRON ACTIVATION AND SPALLATION CROSS SECTIONS

The neutron reaction cross sections of C, Al, Co, Cu and Bi were measured by irradiating these samples by the p-Li quasi-monoenergetic neutrons at TIARA and RIKEN. The gamma-ray activities of the irradiated samples were counted by using a Ge detector and the reaction rates of identified radioisotopes were obtained after correction of sum-coincidence effect.

By using the neutron energy spectrum $\Phi(E)$ and the reaction rate, A, the activation cross section $\sigma(E)$ can be estimated as follows. The reaction rate, A is divided into two parts; one is induced by the peak energy neutrons and the other by the low energy neutrons, as

$$A = N \int_{E_{th}}^{E_{min}} \sigma(E)\,\Phi(E)\,dE + N\,\sigma(Ep)\,\Phi(Ep)$$

where N : number of target atoms relating to the relevant reaction,

E_{th} : threshold energy,

E_{min}: lowest energy of monoenergetic peak neutrons,

$\sigma(Ep)$: cross section at peak neutron energy,

$\Phi(Ep)$: monoenergetic peak neutron flux.

If the threshold energy E_{th} is higher than E_{min}, the second integration term in the numerator must be zero. Otherwise, this term can be estimated by successive subtraction method using the neutron flux $\Phi(E)$ having lower peak energy. The $\sigma(E)$ values in lower energy region were cited from the evaluated data files, ENDF/B-VI[13], McLane et al.[14] and so on. Some examples of thus-obtained activation cross sections are shown in Figs. 13 and 14. Figure 13 gives the cross section data of $^{12}C(n,2n)$ reaction. Our results are quite different from the ENDF/B-VI high energy file data. Figure 14 gives the cross section data of $^{209}Bi(n,xn)$ reaction, compared with other experimental data and the ENDF/B-VI high energy file data. Our data are generally in good agreement with them, but some discrepancy can be found in high energy region.

References

1. J.K. Dickens, ORNL-6463, Oak Ridge National Laboratory (1988).
2. R.A. Cecil, B.D. Anderson and R. Madey, Nucl. Instrum. Methods, 161, 439 (1979).
3. Y. Uwamino, K. Shin, M. Fujii and T. Nakamura, Nucl. Instrum. Methods, 204, 179 (1982).

4. T.S. Subramanian et al., Phys. Rev. C, 28, 521 (1983).
5. K. Shin, Y. Uwamino and T. Hyodo, Nucl. Technol., 53, 78 (1981).
6. N. Nakao et al., Nucl. Instrum. Methods, in press.
7. W.N. McErloy, S. Berg, T. Crockett and R.G. Hawkins, AFWL-TR-67-41, Vols.1 to 4, Air Force Weapons Laboratory (1967).
8. Y. Uwamino, T. Nakamura and A. Hara, Nucl. Instrum. Methods, A239, 299 (1985).
9. G.R. Straker, P.N. Stevens, D.C. Irving and V.R. Cain, ORNL-4585, Oak Ridge National Laboratory (1970).
10. R.G. Alsmiller, Jr., J.M. Barnes and J.D. Drischler, ORNL/TM-9801, Oak Ridge National Laboratory (1986).
11. W.A. Rhoades and F.R. Mynatt, ORNL/TM-4280, Oak Ridge National Laboratory (1979).
12. P. Cloth et al., Jul-2203, KFA Juelich (1988).
13. National Nuclear Data Center, Brookhaven National Laboratory, "Evaluated Nuclear Data File", ENDF/B-VI (1990).
14. V. McLane, C.L. Dunford and P.F. Rose, "Neutron Cross Sections", Vol.2, Neutron Cross Section Curves, Academic Press Inc., New York (1988).

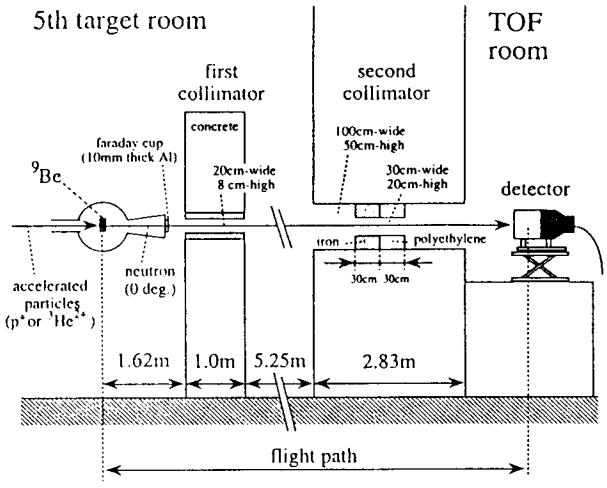

Fig. 1 Cross-sectional view of the CYRIC neutron field

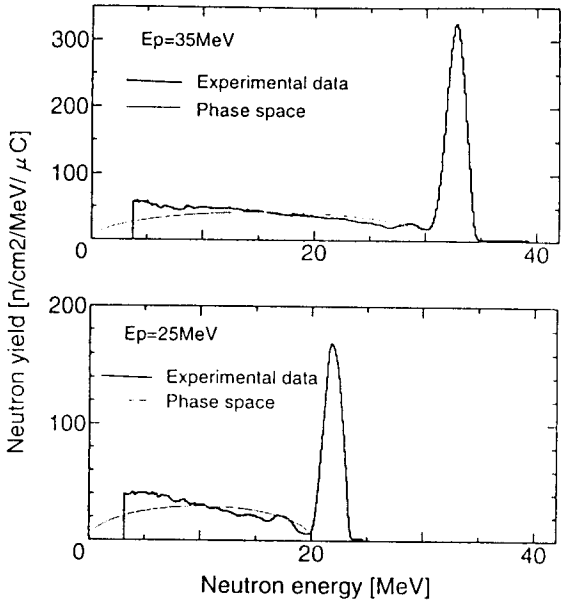

Fig. 2 Neutron spectra of 25 and 35 MeV p-Li reaction at CYRIC

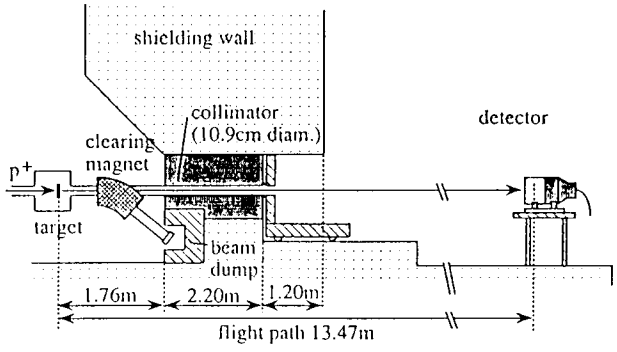

Fig. 3 Cross-sectional view of the TIARA neutron field

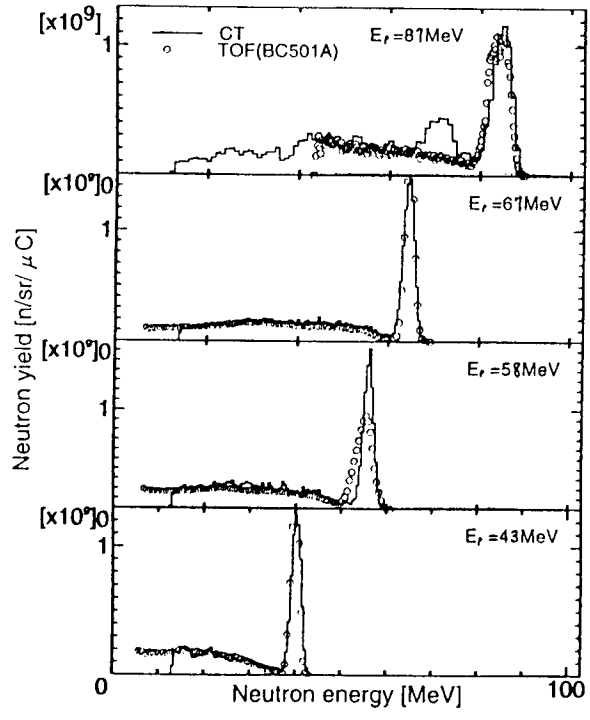

Fig. 4 Neutron spectra of 43, 58, 67 and 87 MeV p-Li reaction at TIARA

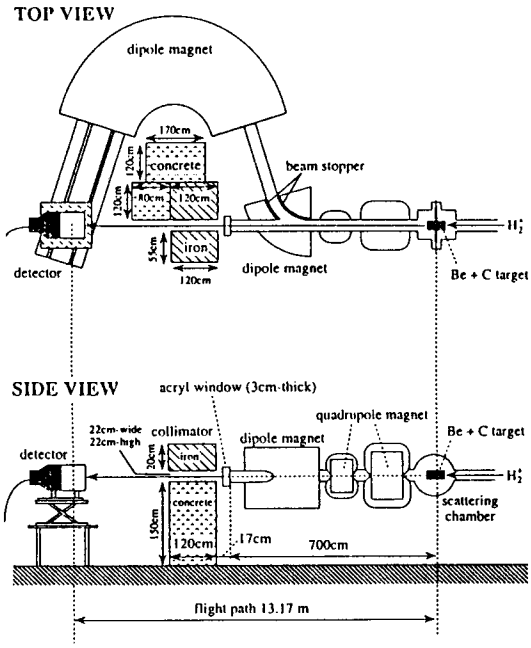

Fig. 5 Cross-sectional view of the RIKEN neutron field

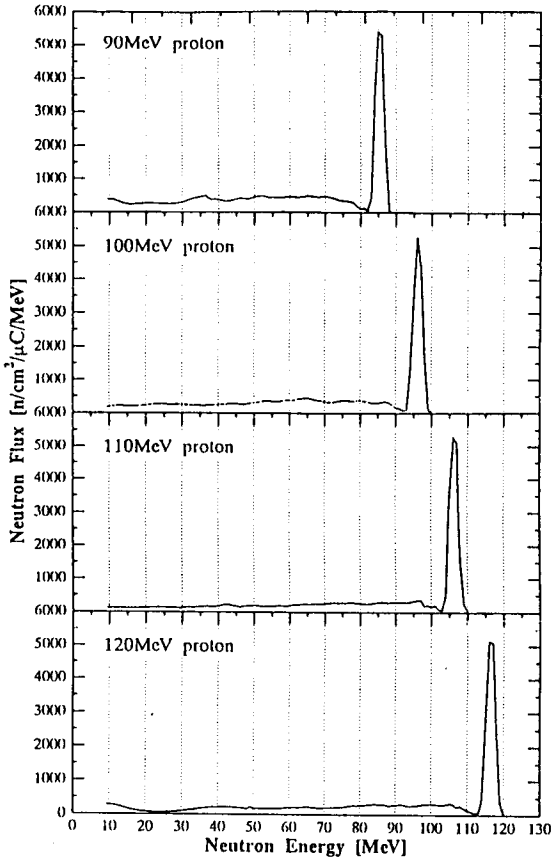

Fig. 6 Neutron spectra of 90, 100, 110 and 120 MeV p-Li reaction at RIKEN

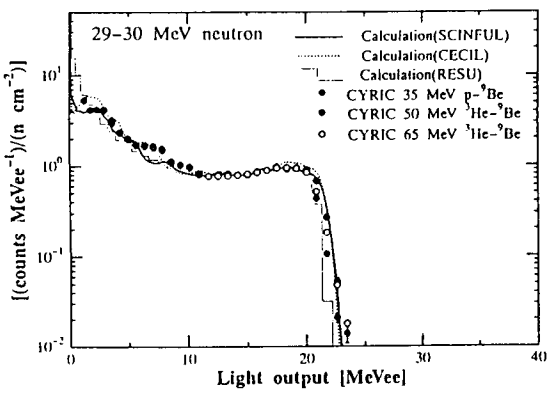

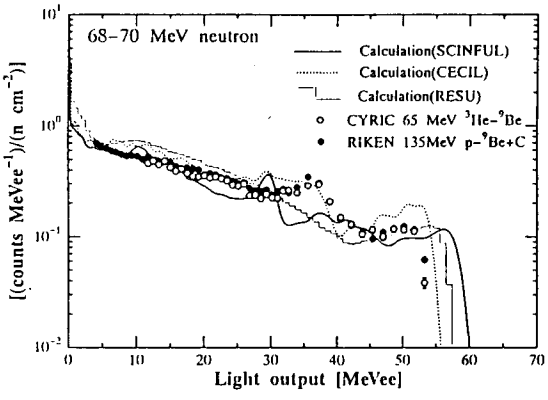

Fig. 7 Measured and calculated response functions of 12.7 cm diam by 12.7 cm long BC501A scintillator for 29 to 30 MeV and 68 to 70 MeV neutrons

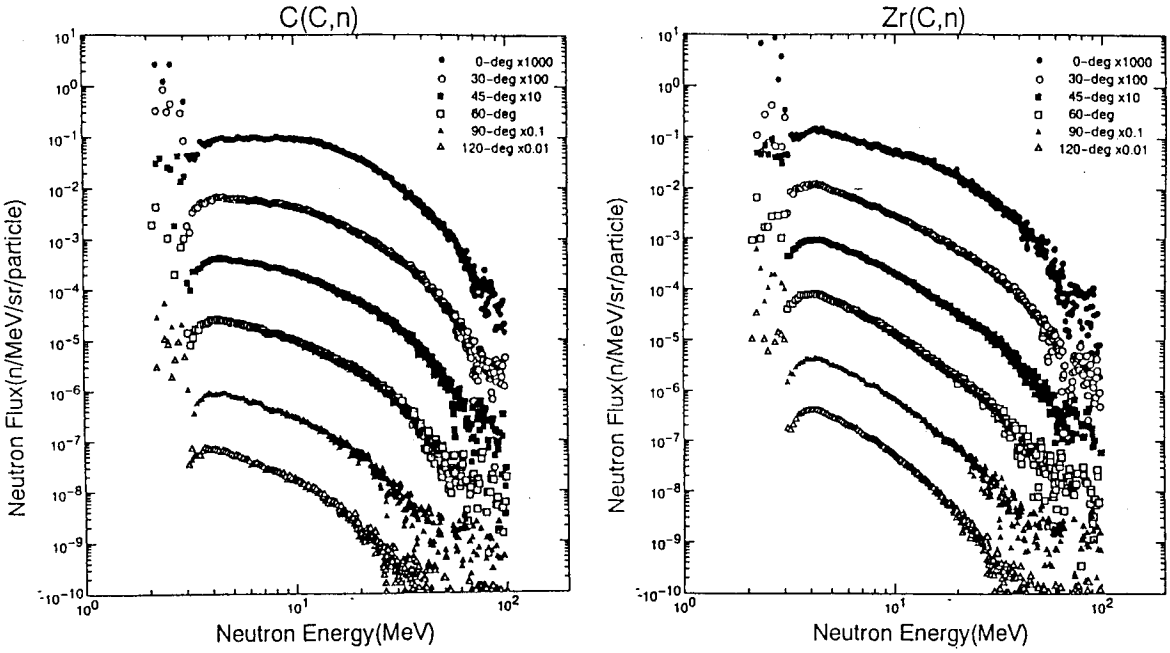

Fig. 8 Differential neutron spectra for C and Zr targets bombarded by 220 MeV C ions

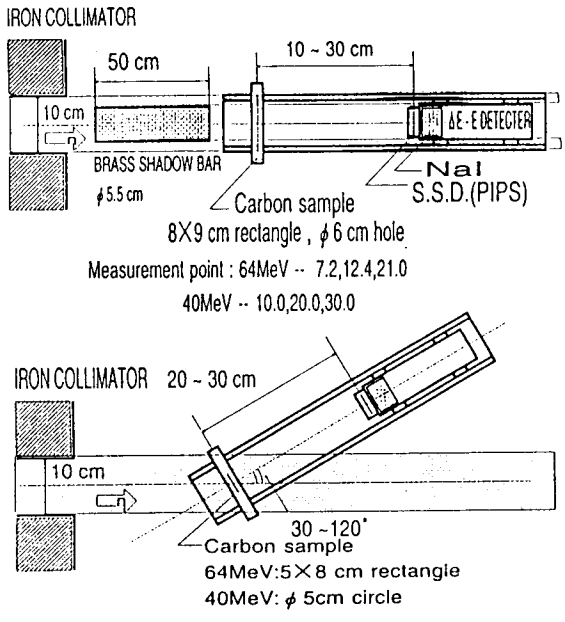

Fig. 9 Experimental arrangement with the proton recoil counter telescope

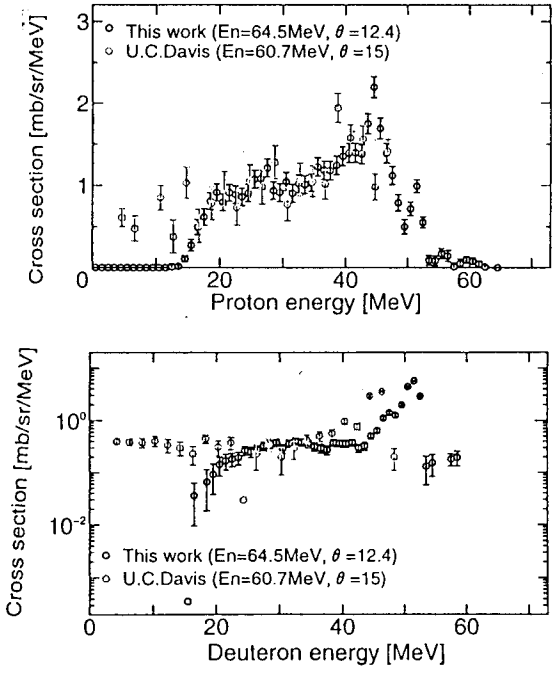

Fig.10 Proton and deuteron spectra of C(n,px) and C(n,dx) reactions at 12.4 deg for 64.5 MeV neutrons, compared with UC Davis data (4)

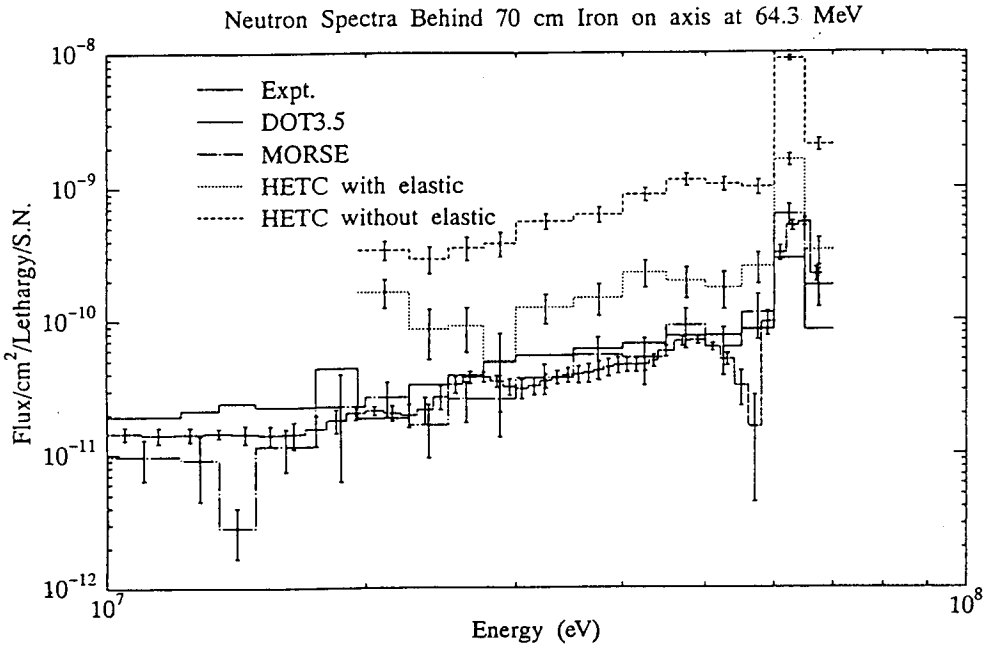

Fig.11 Neutron spectra on beam axis behind 70 cm thick iron for 64.5 MeV neutrons, compared with MORSE, DOT3.5 and HETC calculations

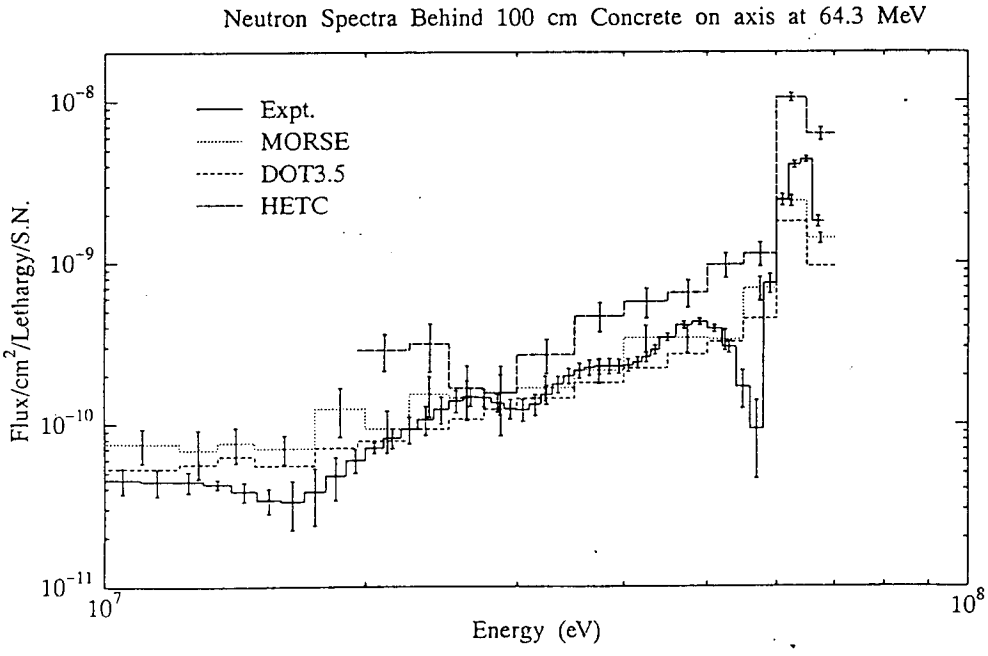

Fig.12 Neutron spectra on beam axis behind 100 cm thick concrete for 64.5 MeV neutrons, compared with MORSE, DOT3.5 and HETC calculations

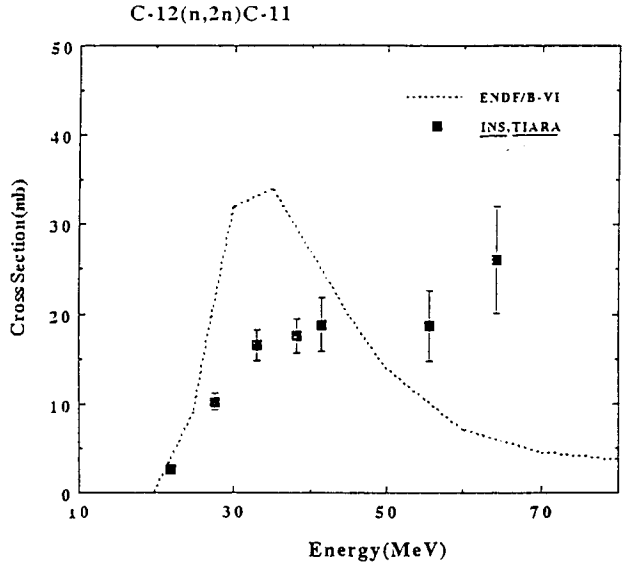

Fig.13 Cross section data of $^{12}C(n,2n)$ reaction compared with ENDF/B-VI

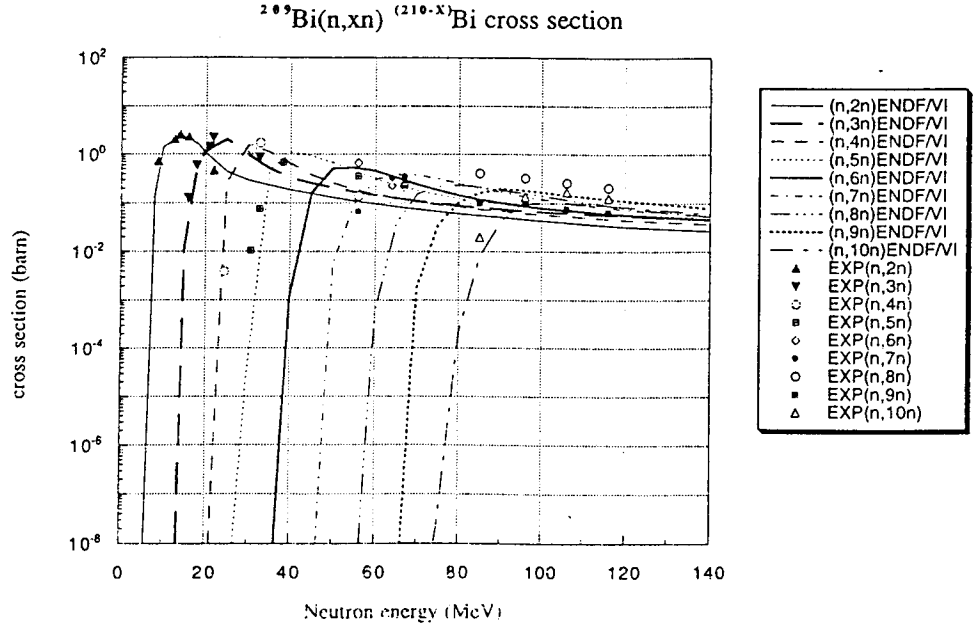

Fig.14 Cross section data of $^{209}Bi(n,xn)$ reaction compared with ENDF/B-VI

3.2 Measurement of Neutron and Gamma-Ray Production Double Differential Cross Section at KEK

Kenji ISHIBASHI
Department of Nuclear Engineering, Kyushu University
Hakozaki, Fukuoka 812-12

ABSTRACT

High energy nuclear radiations were measured for 0.8-3.0 GeV proton induced reactions at KEK. The measurement was carried out to overcome the problems arising from the use of secondary beam line of a quite low incident beam intensity. Digital pulse shape discrimination method was applicable to separation between high energy neutrons and gamma-rays. By the use of a number of scintillators, cross sections were obtained for production of neutrons and gamma-rays.

I. INTRODUCTION

A great number of neutrons are generated by the spallation reaction for incident proton energies around GeV. Design studies have recently been made for such facilities as the spallation neutron sources and the accelerator-driven transmutation systems. It is important to investigate the inclusive cross section for (p,xn) reaction for incident protons of medium energies. The experiments on the neutron production double differential cross section have been made by the time-of-flight (TOF) method at IUCF[1] with incident proton energies of 120 and 160 MeV, at PSI (SIN)[2] with that of 585 MeV, and at LANL[3)-8)] with those of 113 to 800 MeV. At higher energies than these, systematic data covering many targets have not been taken so far. We planned to measure the double differential cross sections on production of the spallation neutrons.

High Energy Transport Code (HETC) based on the intranuclear-cascade evaporation model is used for designing of spallation neutron facilities. Several versions of HETC have been developed and improved at some institutes or laboratories. Among these, HETC-KFA2[9] takes gamma-ray emissions from remnant nucleus into account. However the gamma-ray production cross sections induced by GeV-protons have never been measured, and discussions about the validity of the calculation model have not been made so far. For this reason, we attempted to obtain the gamma-ray production cross sections from experimental data of neutron measurements.

II. EXPERIMENT

The experiment for the neutron and gamma-ray production double differential cross sections was carried out at the $\pi 2$ beam line of KEK. Targets of C, Al, Fe, In and Pb were chosen for incident protons of 0.8, 1.5 and 3.0 GeV. Neutrons and gamma-rays were measured by the TOF method with liquid scintillators. The experimental arrangement is illustrated in Fig. 1. Two different sizes of NE213 liquid scintillator were placed in the directions of 15, 30, 60, 90, 120 and 150 deg. and all of them worked simultaneously. The larger detectors of Φ5"×5" were used for detecting high energy neutrons and gamma-rays with relatively higher efficiency, although the time resolution was slightly poor in the TOF measurement due to the greater size of scintillator and photomultiplier. The smaller detectors of Φ2"×2" were adopted to detect low

energy neutrons, because they exhibited good pulse shape discrimination even in the energy region around 1 MeV. In front of each neutron detectors, NE102A plastic scintillators were mounted as veto detectors to eliminate charged particle events by the anti-coincidence method.

Since incident protons were generated as secondary beam from the internal target mounted on the main ring, they were accompanied with pions with the same momentum. It was necessary to identify incident protons from pions. Hence, another TOF method was adopted for separation between protons and pions by the use of a pair of Pilot U scintillators. The Pilot U scintillators also served to define the size of the proton beam incident on a target, together with two NE102A scintillators. The coincidence of these scintillators was counted to give the number of incident protons. The energy resolution and the measurement efficiency for the neutron measurement were compromised, and the flight path was determined as 1 to 1.5 m for the Φ5"×5" detectors and 0.6 to 0.9 m for the Φ2"×2" ones.

The block diagram of the measurement circuit is shown in Fig. 2 with simplified drawing. When the incident beam came on the target and the coincidence of signals from all beam detectors took place, the pulse with a typical time duration of 150 ns was sent to the next coincidence module. If the signal from neutron detectors reached the coincidence module during the gate time of 150 ns, the start pulses for data taking were sent to the next NIM and CAMAC modules. A μ-VAX computer was used for controlling CAMAC modules. Data collection time was about 20 ms an event. All experimental data were recorded on magnetic tapes and then analyzed by an off-line method.

The two-gate integration method[10] was used for the pulse shape discrimination between neutrons and gamma-rays. The discrimination results are shown in Fig. 3 and are excellent even in the high energy region. The deviation from linearity due to the saturation effect does not deteriorate the discrimination results. The neutron detection efficiencies were obtained from calculation results of SCINFUL code[11] below 80 MeV and from CECIL code[12] above 80 MeV. In addition the neutron detection efficiency were experimentally checked at JAERI at neutron energies of 25, 30 and 64.6 MeV[13]. Discrepancies between experimental and calculated results were within 10 %. We determined the uncertainty of the neutron detection efficiency ranged up to 10 %. The gamma-ray detection efficiencies were obtained from calculation results of EGS4[14]. An experimental check for the gamma-ray detection efficiencies was not performed due to high reliability of EGS4.

The target thicknesses ranged from 15 to 20 g/cm^2. Since the target is not very thin, the multiple scattering and attenuation effects occurred in the target. The effects were checked by the particle transport calculation of HETC for neutrons and by electron and gamma-ray transport calculation of EGS4 for gamma-rays. It was found that the difference between the results of an ideal thin target and the actual thick target was generally within 10 percents. In the case of Pb, however, the correction was exceptionally large and amounted to about 50 percents at neutron energies around a few MeV. The experimental data were corrected on the basis of the transport calculation results.

III. EXPERIMENTAL RESULTS

1. NEUTRON RESULTS

The time resolution for the neutron measurements was typically 0.5 ns for Φ5"×5" detectors after time walk correction, and the energy resolutions in one sigma were 5.7 % at the neutron energy of 10 MeV and 14 % at 300 MeV. The resolutions for the neutron measurements are sufficiently good in the energy range from 1 to 300 MeV.

We compared our experimental data at the incident proton energy of 0.8 GeV with those of LANL[6),(8)]. Figures 4 and 5 show the results at 0.8 GeV for C and Pb, respectively. Present results agree well with the LANL results at energies above 100 MeV in the forward directions. Results on Pb particularly reproduce the LANL results at energies above 10 MeV in the backward directions. A clear disagreement is, however, seen between our data and LANL ones below several MeV. The flight path in present experiment is very short in comparison to the length of 20-40 m at LANL, and our results may have less possibility of being influenced by scattering neutron effects in the low energy region.

Experimental double differential cross section data for C, Fe and Pb at incident proton energy of 1.5 GeV are shown in Figs. 6, 7 and 8, respectively, where calculation results of HETC are drawn by lines. Neutron yields for C are very poor particularly in backward directions above a few hundred MeV. One can see in Fig. 6 that a large discrepancy between measurement and calculation results appears in the all direction from 1 to 20 MeV. This is because the evaporation calculation of HETC does not hold good for the light nucleus C. For Pb the results between measurement and calculation are generally in agreement. The calculation, however, underestimates the experimental data above 20 MeV in backward directions.

2. GAMMA-RAY RESULTS

When monoenergetic gamma-rays are detected by the NE213 liquid scintillator, a pulse charge distribution is continuous due to some gamma-ray interactions such as Compton-scattering. For this reason, the unfolding method was utilized for the data analysis of gamma-ray spectra. Response functions of the NE213 are required for the unfolding analysis at each incident energies of gamma-rays. EGS4 is known as one of the most reliable codes for the response function calculation. FERDOR[15)] is often used for obtaining neutron and/or gamma-ray energy spectra by the unfolding calculation. We adopted them to our analysis.

Figures 9, 10 and 11 shows the double differential cross sections of gamma-ray production induced by 0.8, 1.5 and 3.0 GeV protons on Al target, and Figs. 12, 13 and 14 indicate those on Pb target. Dashed and Solid lines in the figures indicate the calculation results for assumptions that gamma-rays are emitted from continuous levels (model 0) and from realistic discrete levels (model 4), respectively. The experimental cross sections have a considerable magnitude at gamma-ray energies above 10 MeV, and the angular distribution of the higher-energy gamma-ray emission is forward peaked. The HETC calculations reproduce the experiments well in the gamma-ray energy of 4 to 10 MeV, whereas they underestimate the experiments above 10 MeV. This is because the calculation model in HETC allow gamma-rays to be emitted only from exited remnants.

VI. SUMMARY

Differential cross sections for the production of neutrons and gamma-rays were obtained at incident proton energies of 0.8, 1.5 and 3.0 GeV on targets of C, Al, Fe, In and Pb. For the neutron, the acceptable energy resolution was achieved in the neutron energy range from 1 to 300 MeV. The HETC calculations of gamma-ray emissions comparatively agree with the experimental data only in the low energy region. However comparison results of neutrons and gamma-rays between the experiments and the HETC calculations suggest the need for improvement of the calculation model.

REFERENCES

(1) SCOBEL, W., et al.: *Phys. Rev.*, **C41**, 2010-2020 (1990)

(2) CIERJACKS, S., et al.: *Phys. Rev.*, **C36**, 1976-1987 (1987).
(3) MEIER, M., et al.: *Nucl. Sci. Eng.*, **102**, 310-321 (1989)
(4) MEIER, M., et al.: *Nucl. Sci. Eng.*, **110**, 289-298 (1992)
(5) AMIAN, W. B., et al.: *Proc. Nucl. Data for Sci. and Technol.* 696-701 (1991)
(6) AMIAN, W. B., et al.: *Nucl. Sci. Eng.*, **112**, 78-86 (1992)
(7) AMIAN, W. B., et al.: *Nucl. Sci. Eng.*, **115**, 1-12 (1993)
(8) STAMER, S., et al.: *Phys. Rev.*, **C47**, 1647-1658 (1993)
(9) CLOTH, P., et al.: HERMES, High Energy Radiation Monte Carlo Elaborate System, *KFA-IRE-E* **AN/12/88** (1988)
(10) ZUCKER, M. S., et al.: *Nucl. Instr. and Meth.*, **A299**, 281-285 (1990)
(11) DICKENS, J. K.: ORNL-6452 (1988)
(12) CECIL, R. A., et al.: *Nucl. Instr. and Meth.*, **161**, 439-447 (1979)
(13) MEIGO, S., et al.: private communication.
(14) NELSON, W. R. et. al.: SLAC-265 (1985)
(15) BURRUS, R. L. : ORNL-3743 (1965)

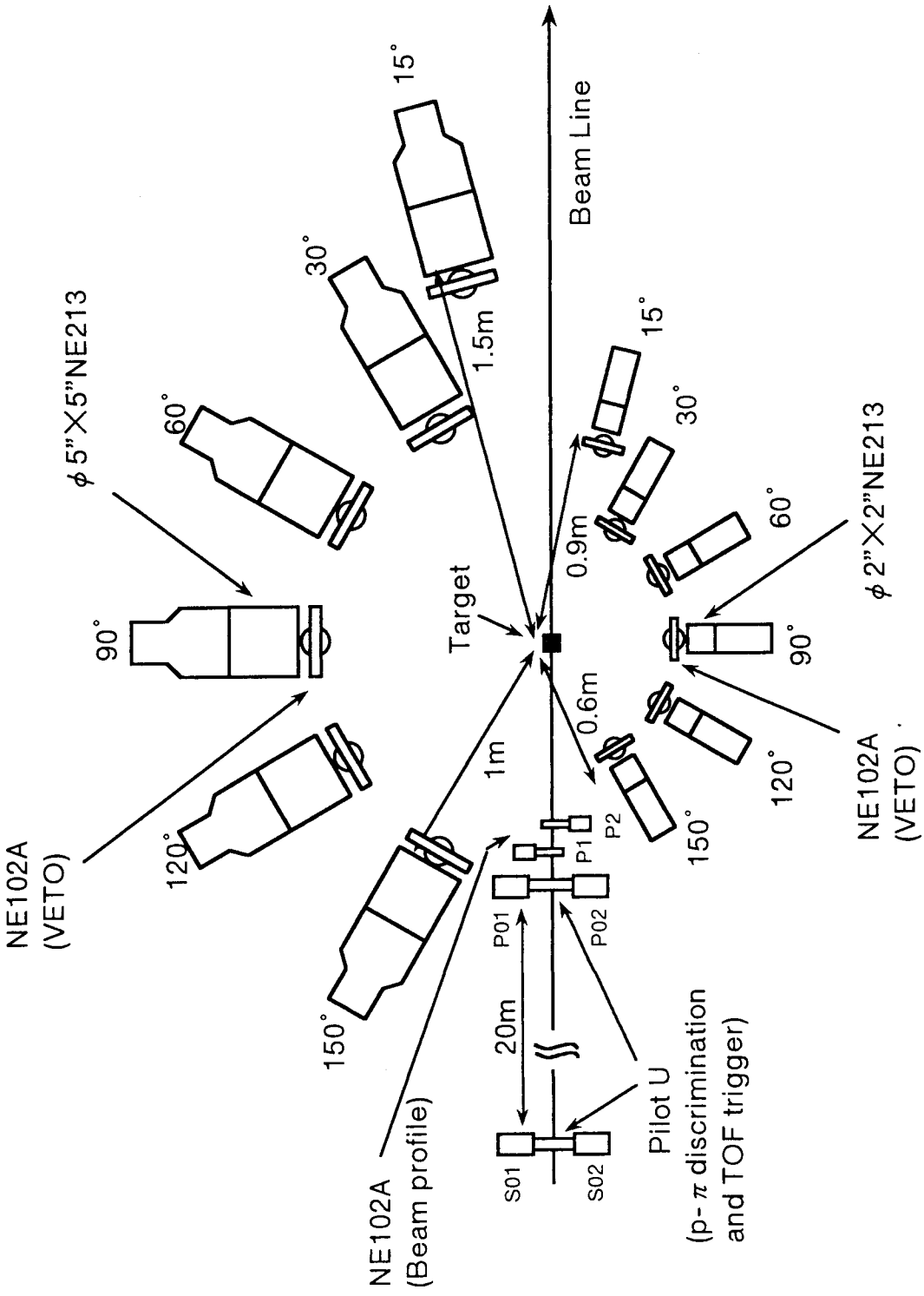

Fig. 1 Illustration of the experimental arrangement.

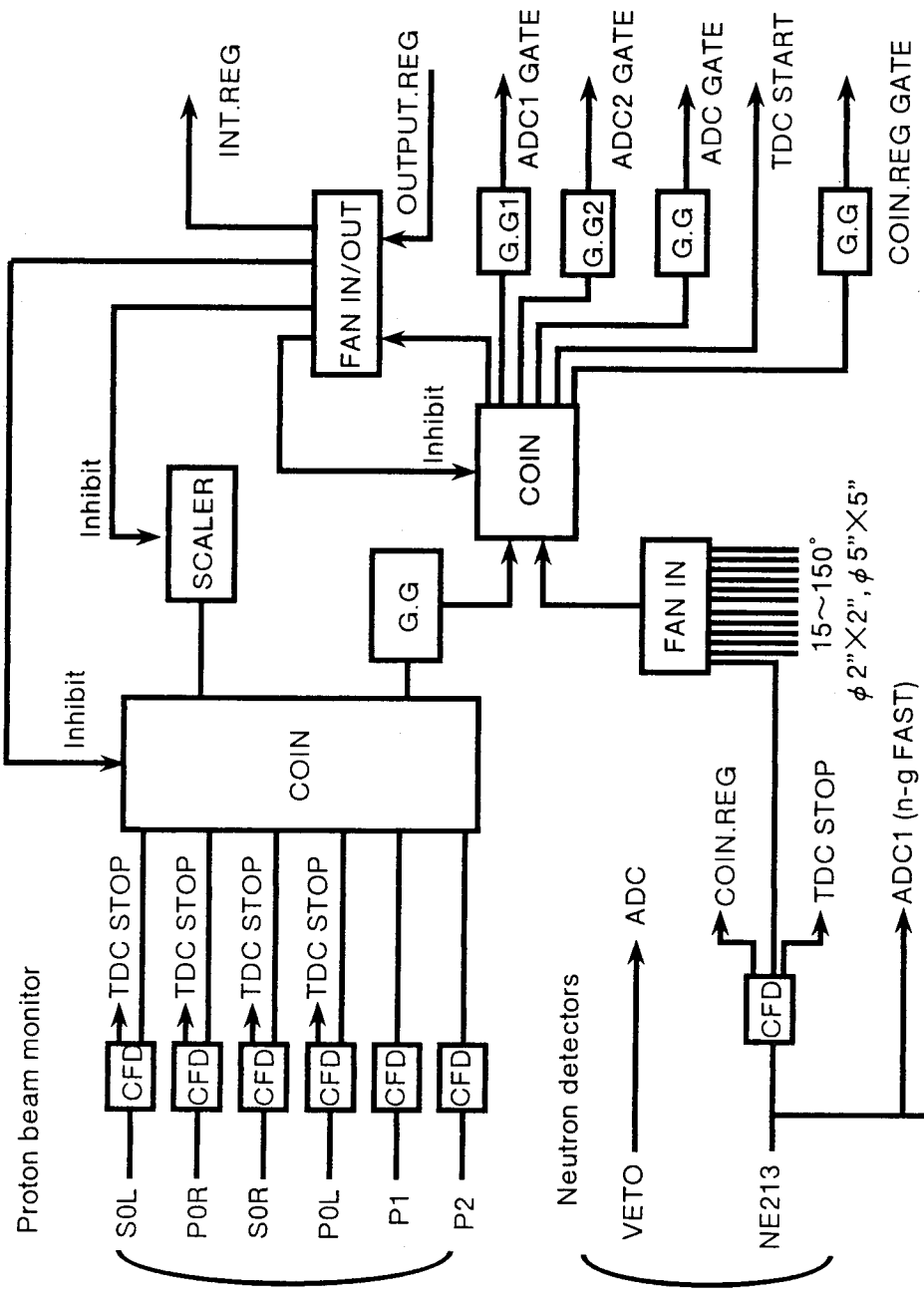

Fig. 2 Block diagram of the measurement circuit with simplified drawing.

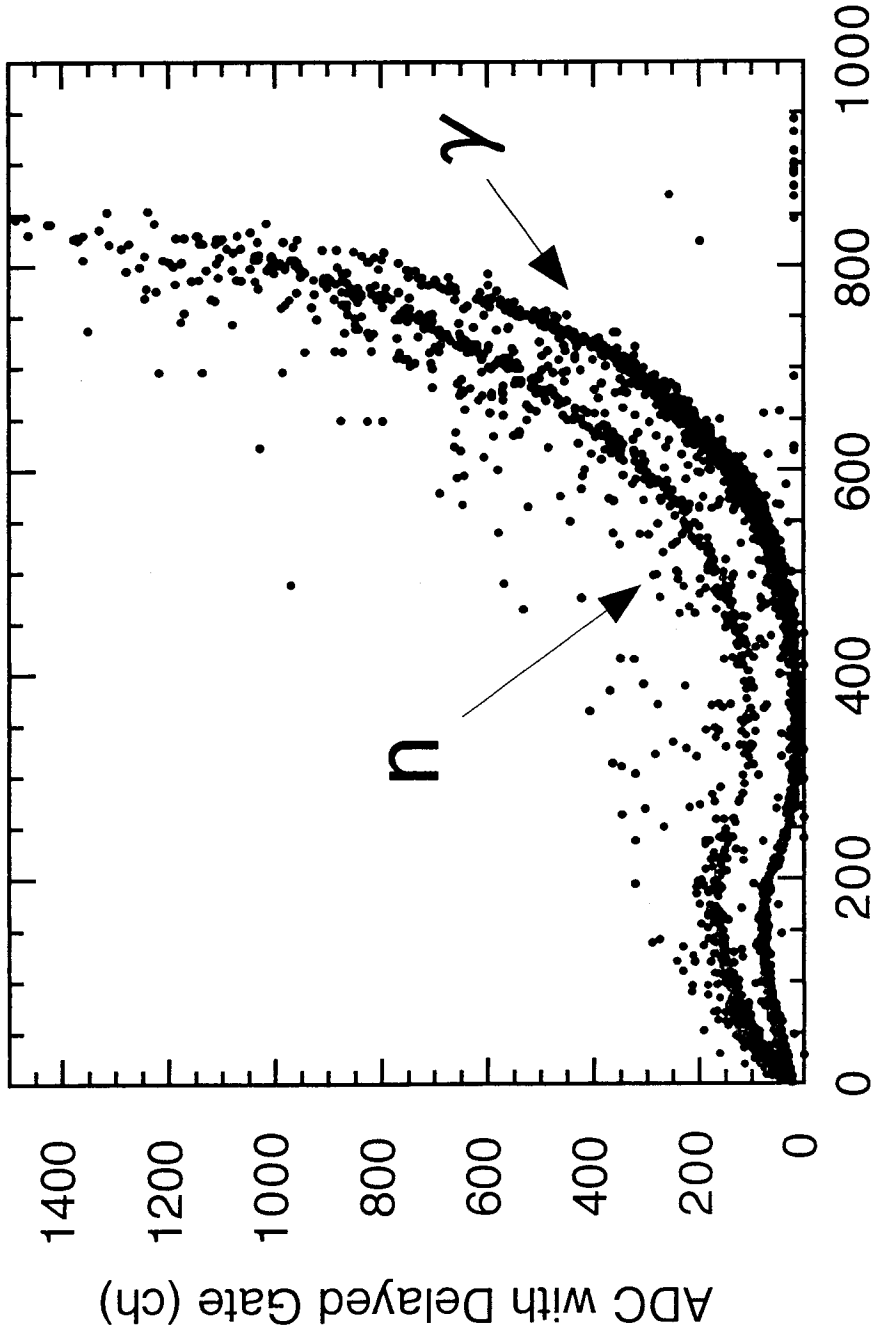

Fig. 3 Neutron and gamma-ray pulse shape discrimination by two-gate integration method.

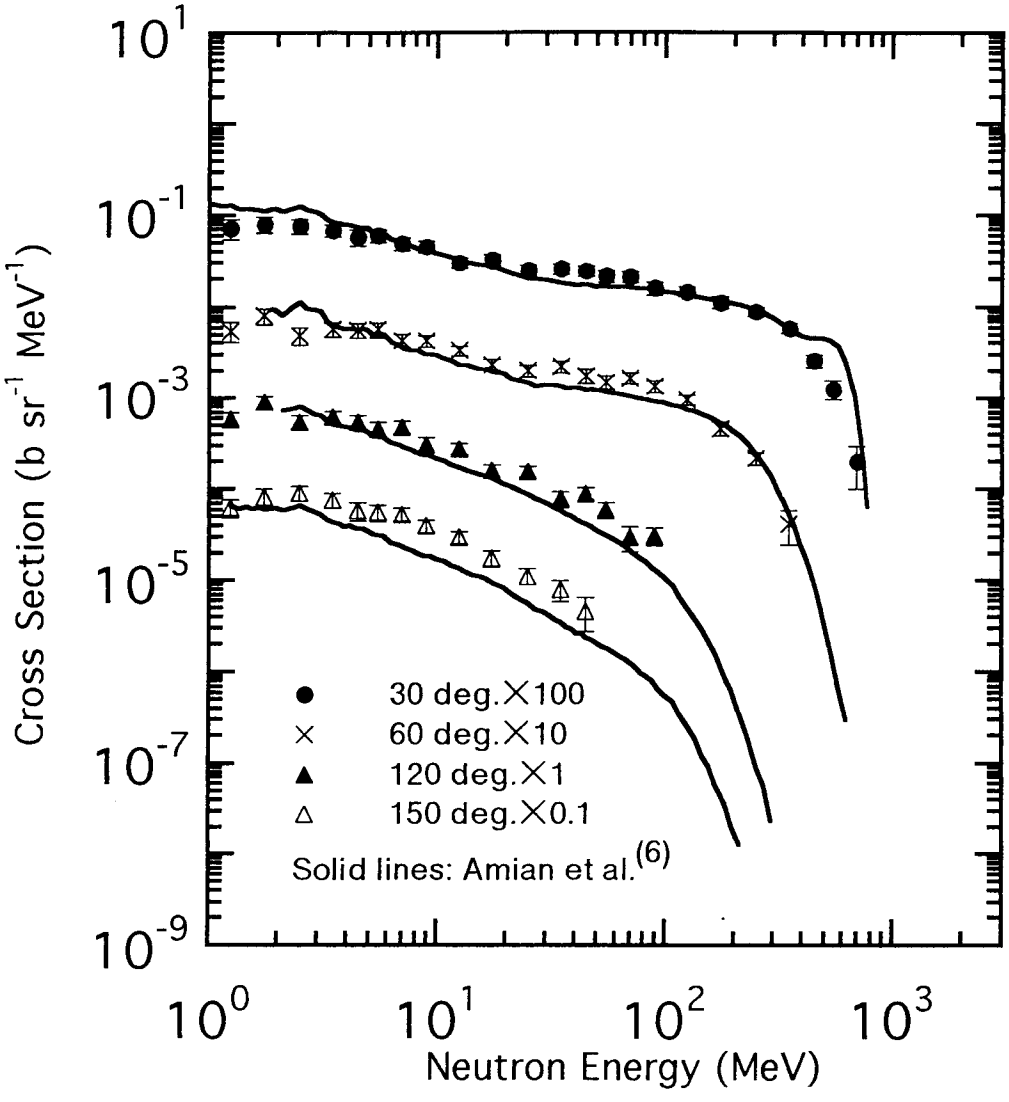

Fig. 4 Neutron produciton double differential cross section for 0.8 GeV p on C.

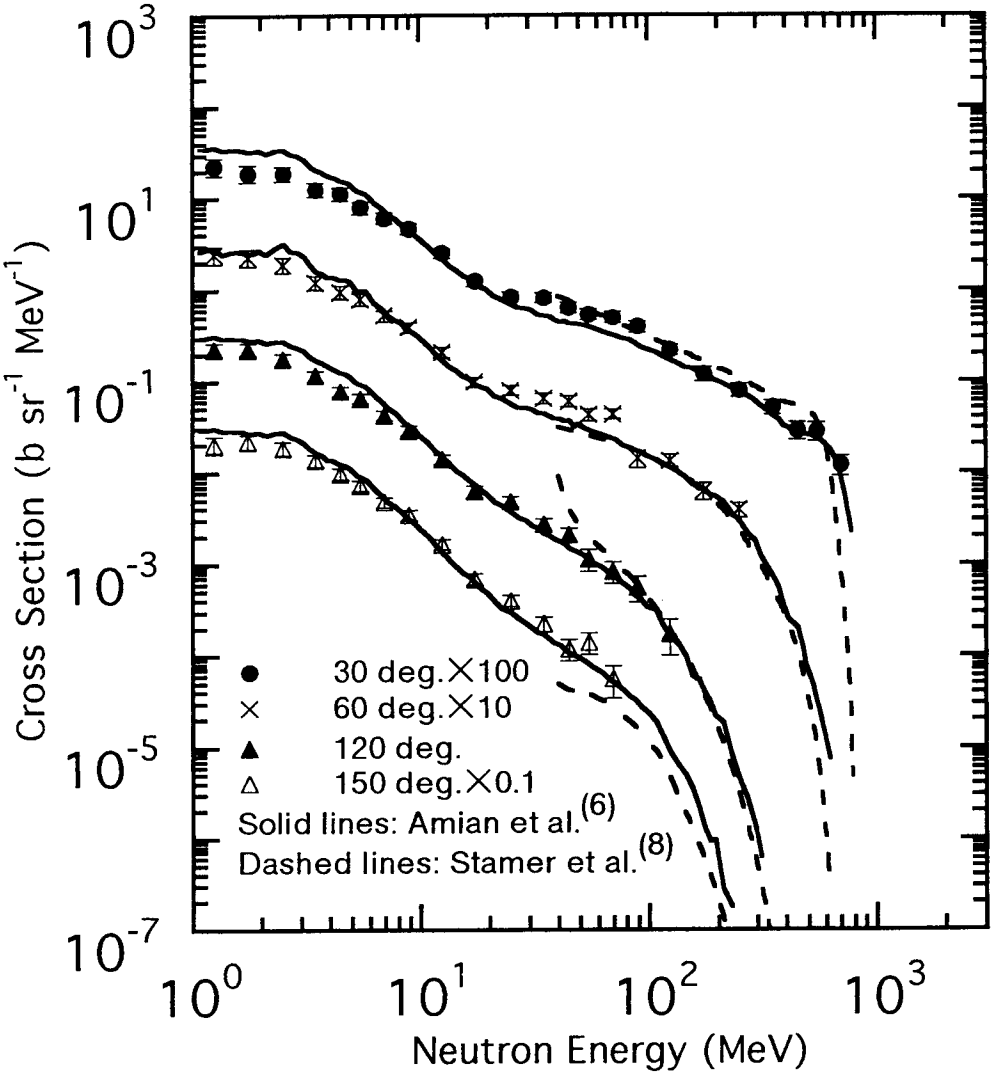

Fig. 5 Neutron produciton double differential cross section for 0.8 GeV p on Pb.

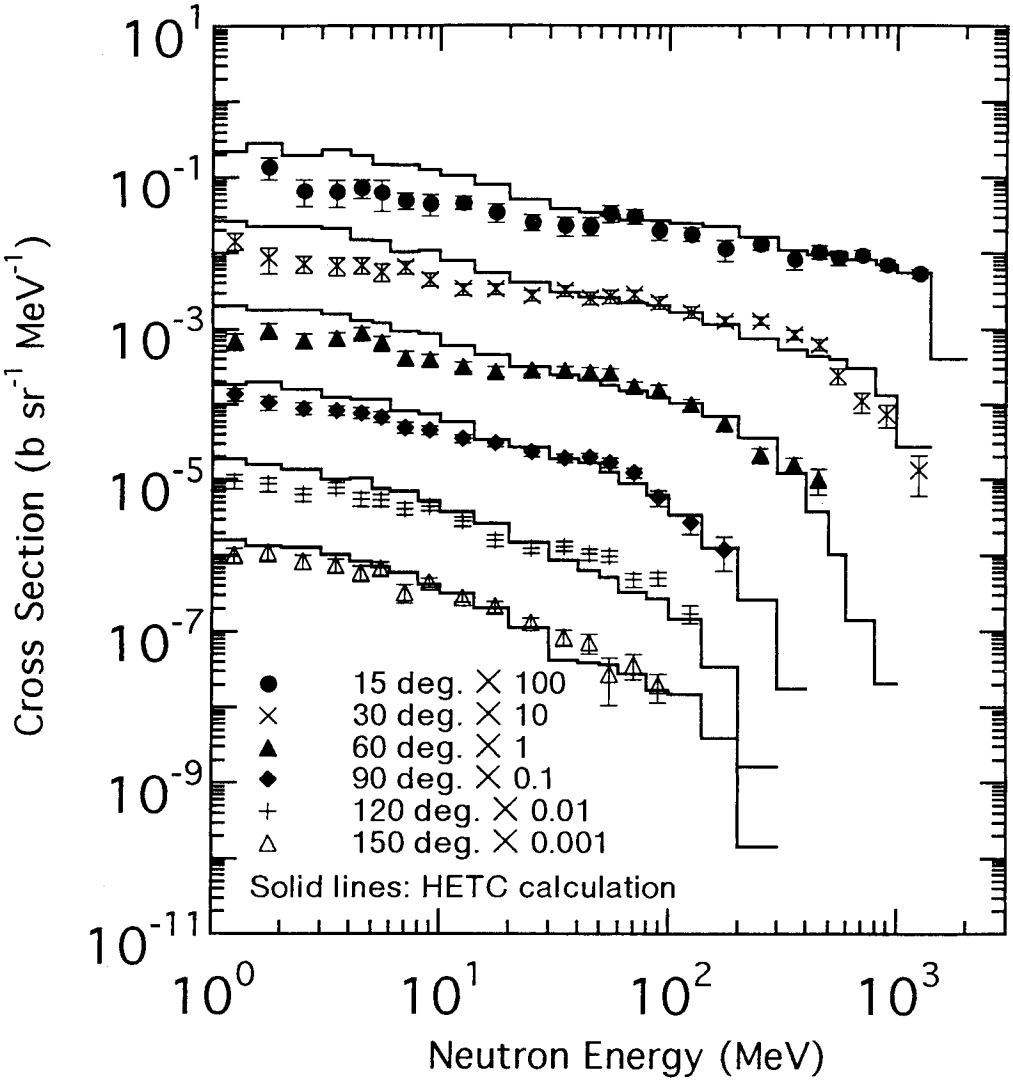

Fig. 6 Neutron production double differential cross section for 1.5 GeV p on C.

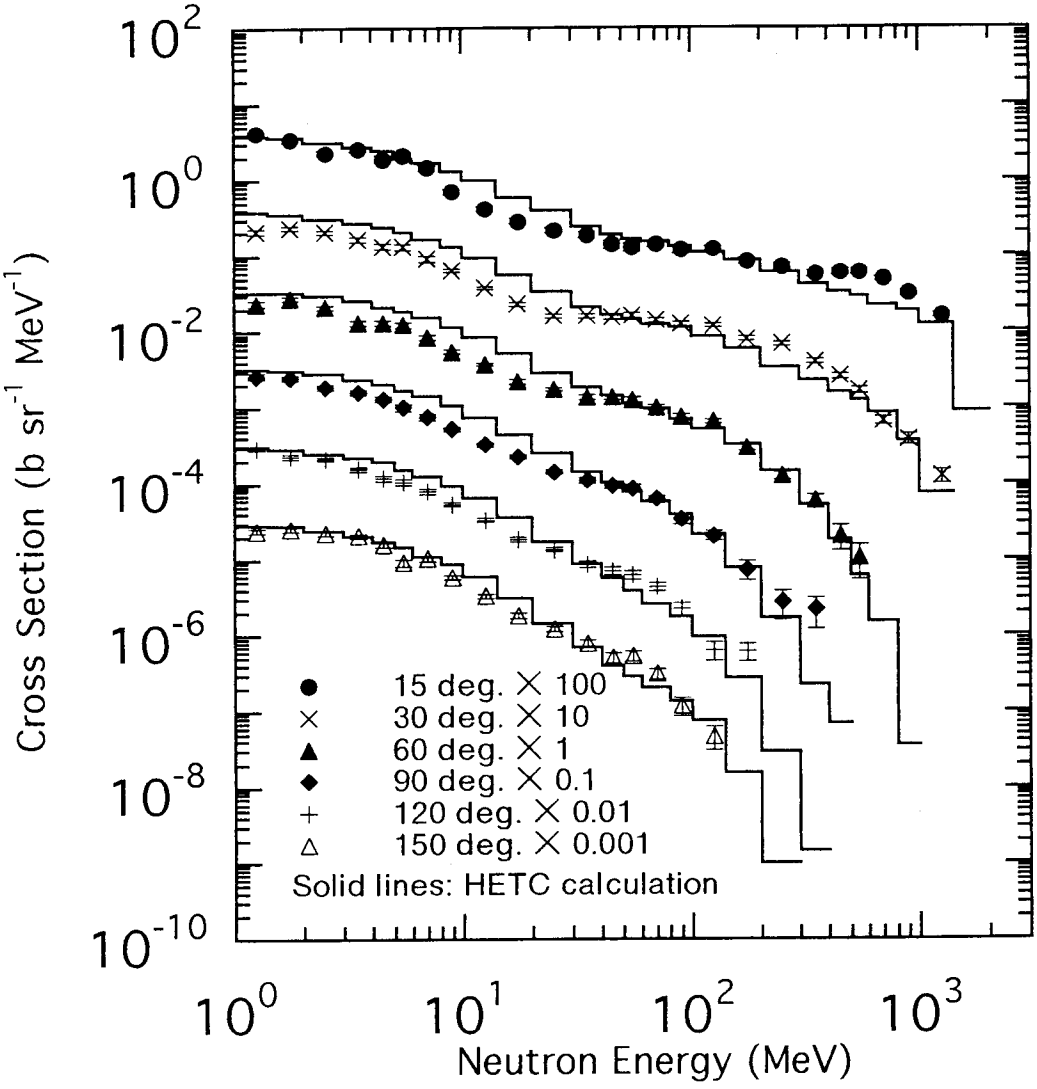

Fig. 7 Neutron production double differential cross section for 1.5 GeV p on Fe.

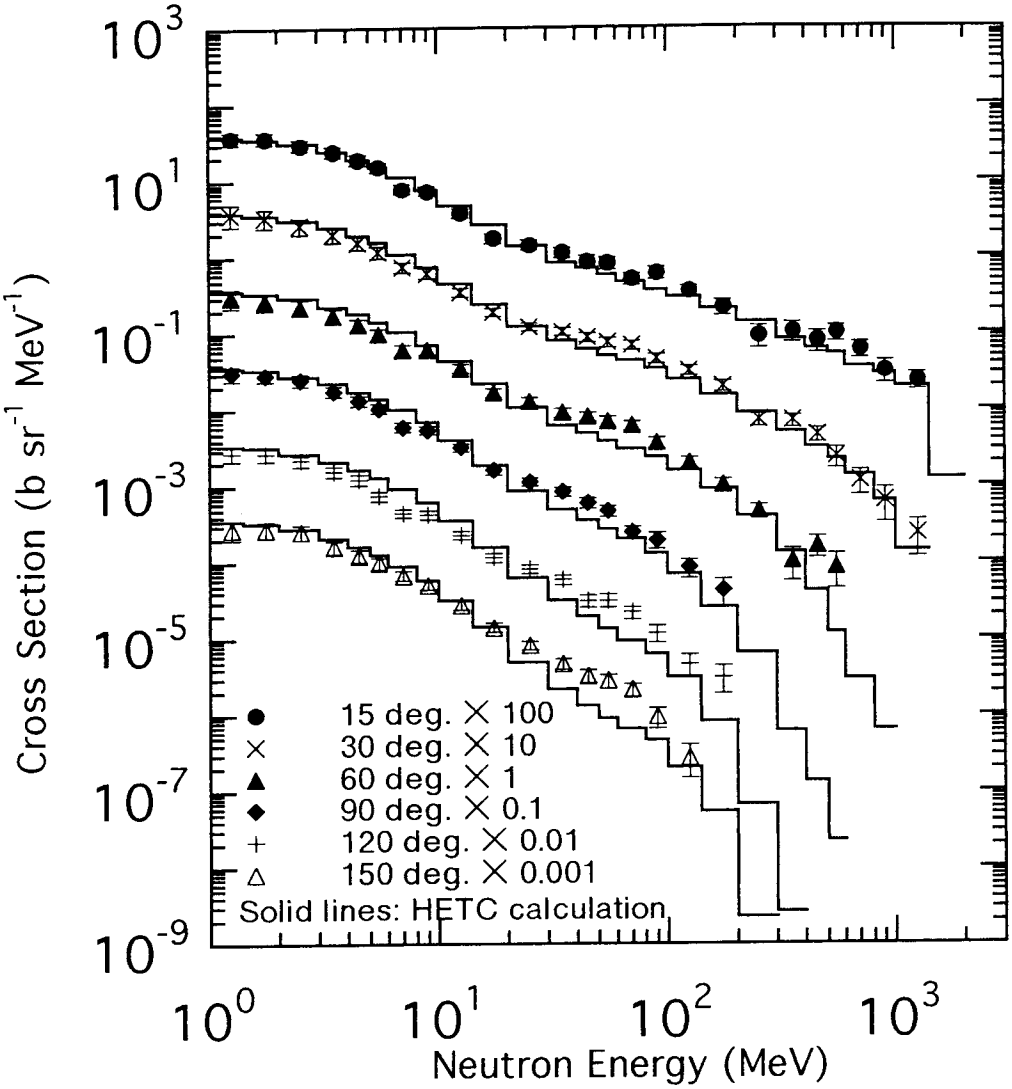

Fig. 8 Neutron production double differential cross section for 1.5 GeV p on Pb.

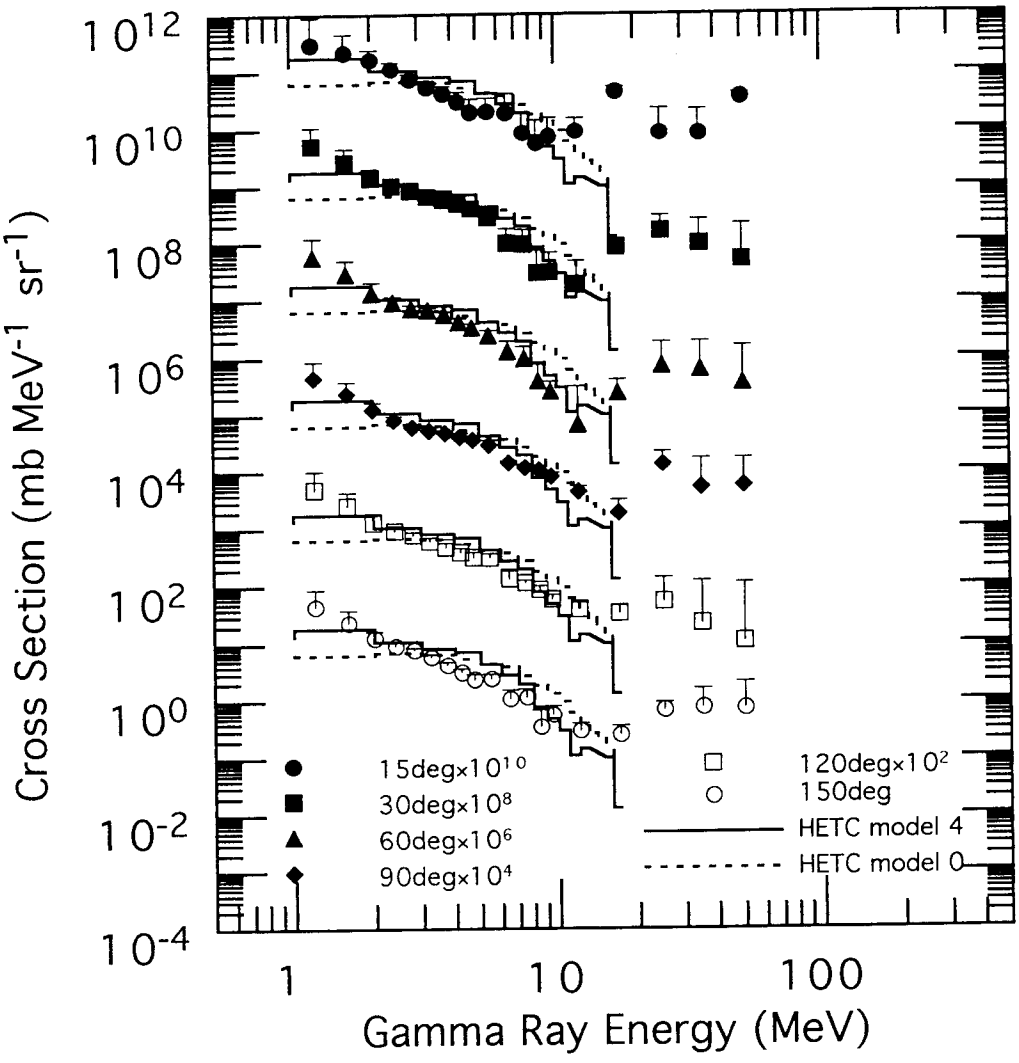

Fig. 9 Gamma ray production double differential cross section for 0.8 GeV p on Al.

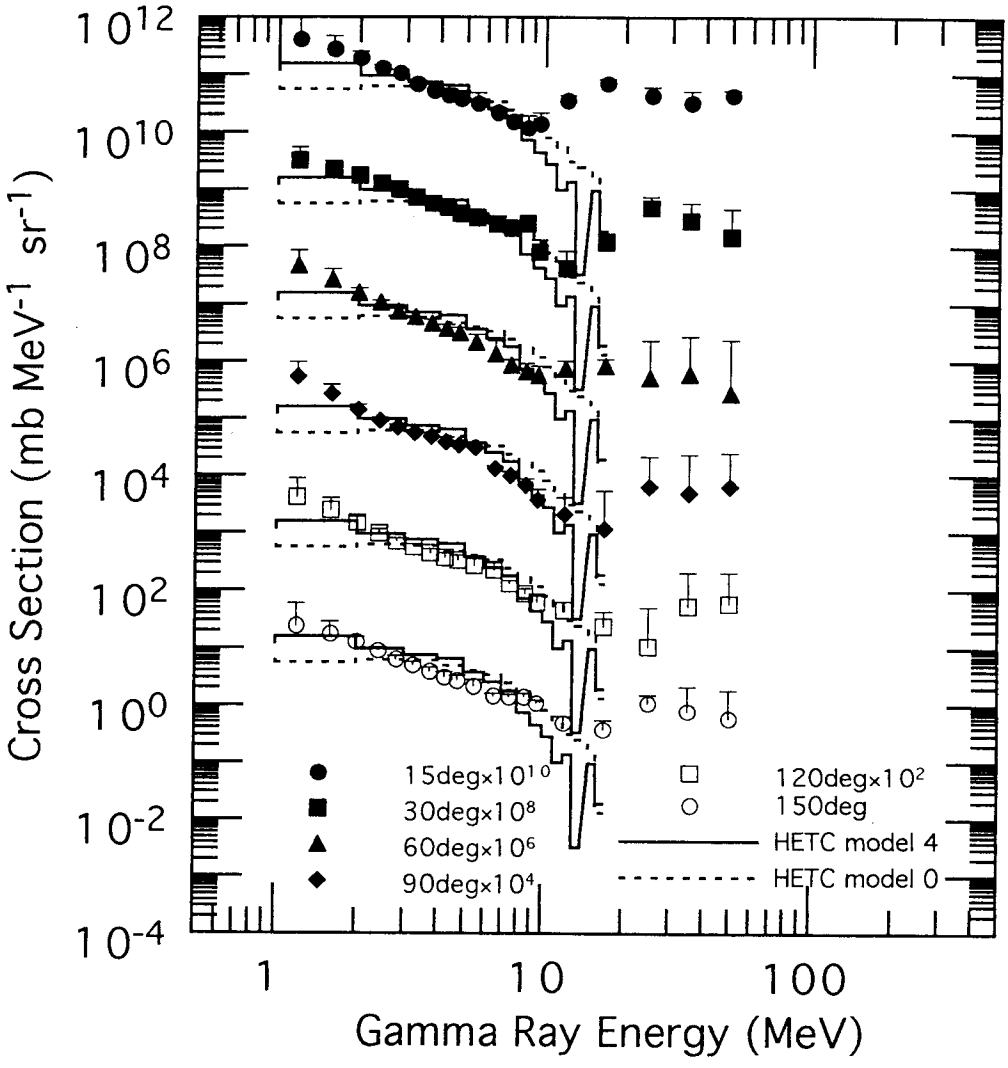

Fig. 10 Gamma ray production double differential cross section for 1.5 GeV p on Al.

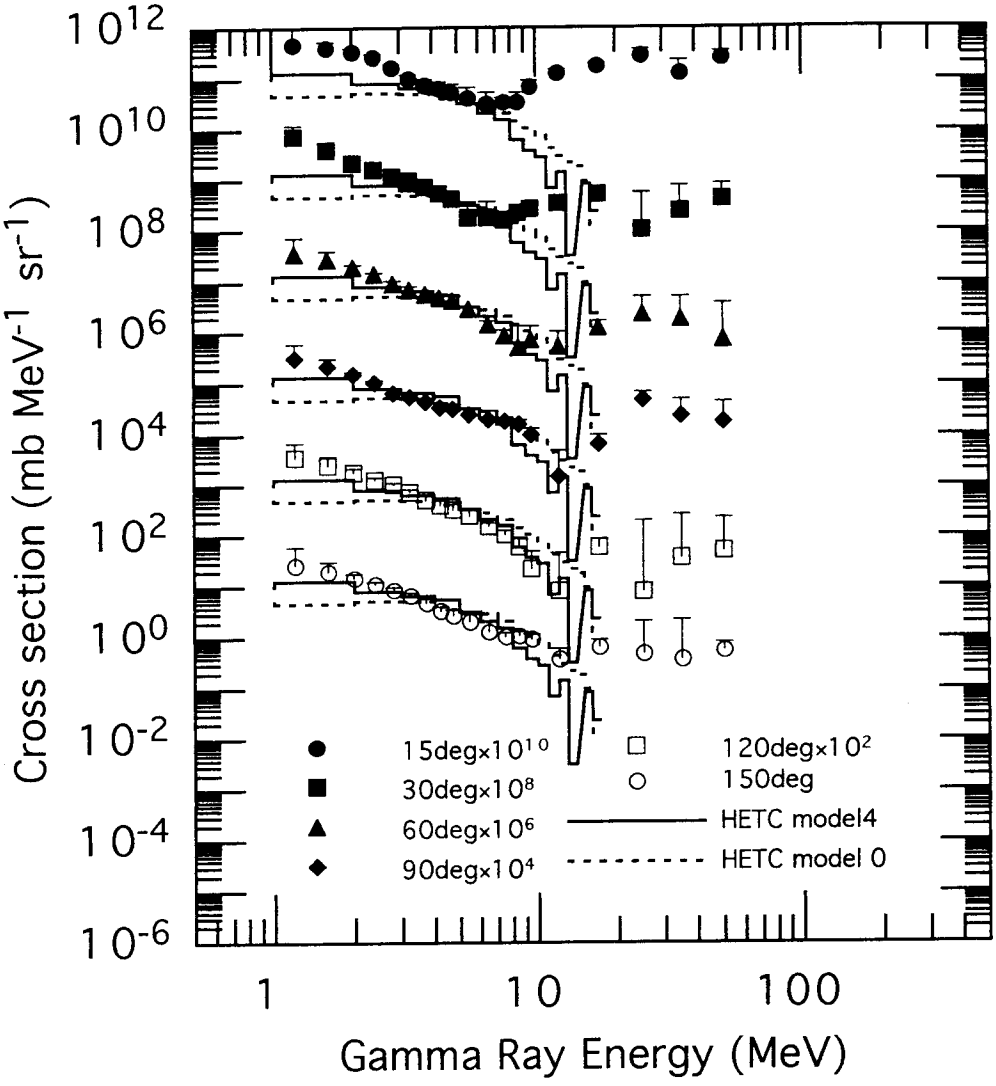

Fig. 11 Gamma ray production double differential cross section for 3.0 GeV p on Al.

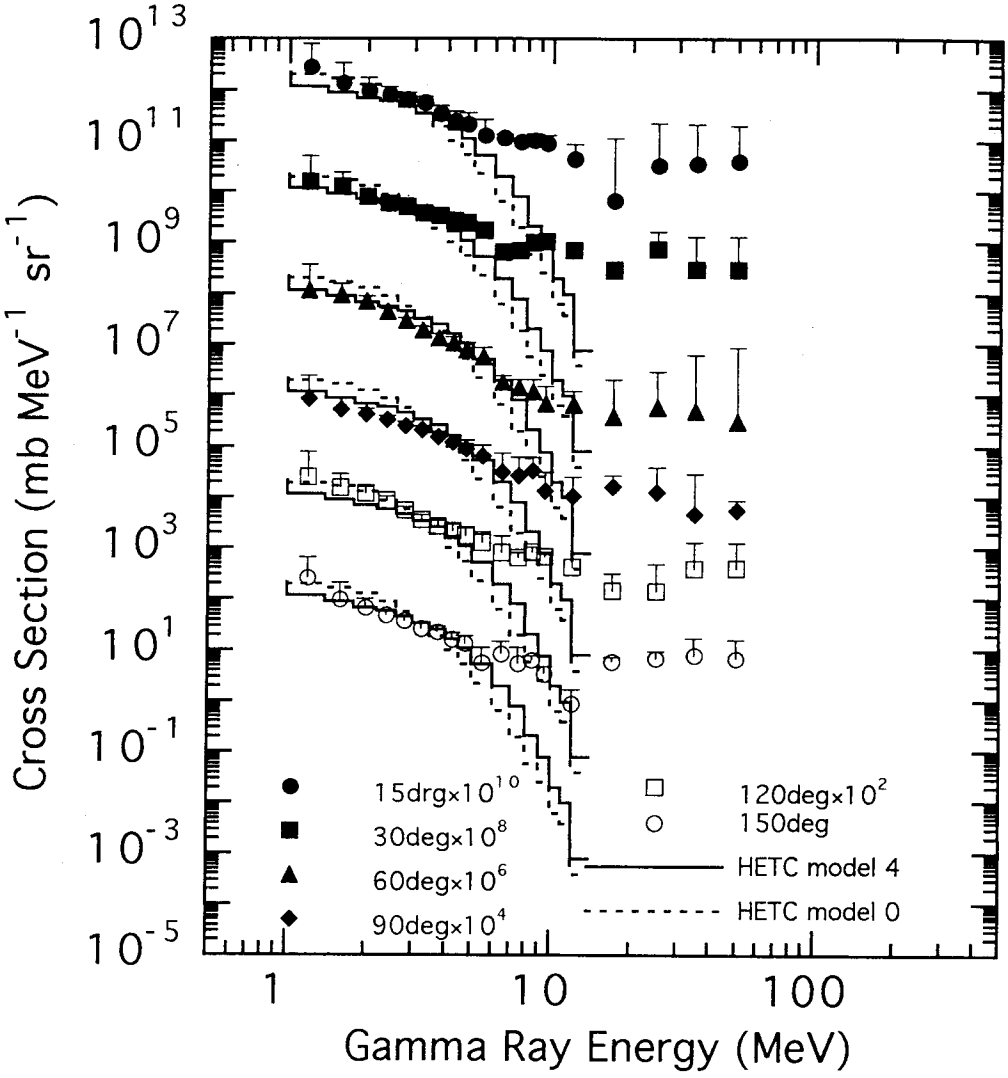

Fig. 12 Gamma ray production double differential cross section for 0.8 GeV p on Pb.

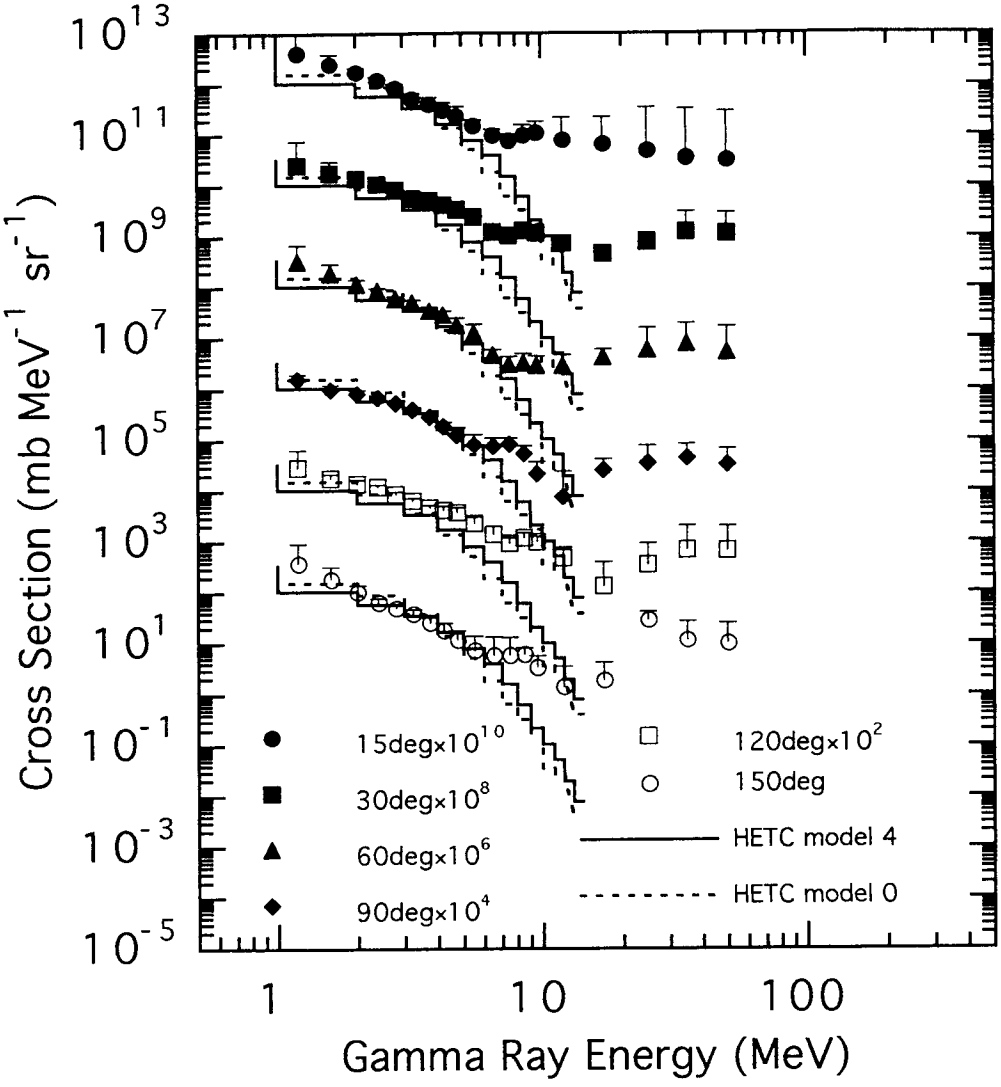

Fig. 13 Gamma ray production double differential cross section for 1.5 GeV p on Pb.

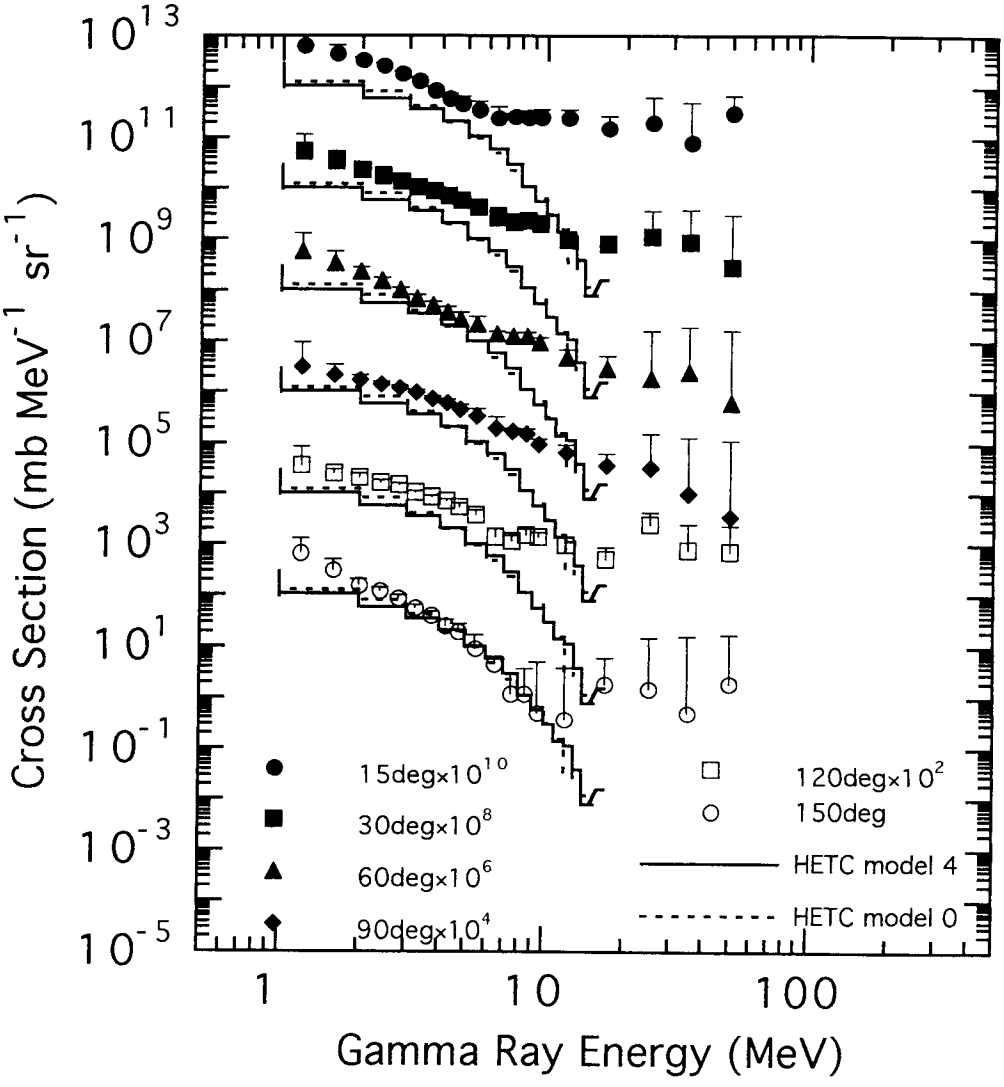

Fig. 14 Gamma ray production double differential cross section for 3.0 GeV p on Pb.

3. 3 Measurements of Neutron Spectra from A Thick Lead Target Bombarded by 0.5 and 1.5 GeV Protons

Shin-ichiro MEIGO[1], Hiroshi TAKADA[1], Satoshi CHIBA[1], Tatsushi NAKAMOTO[2], Kenji ISHIBASHI[2], Naruhiro MATSUFUJI[2], Keisuke MAEHATA[2], Nobuhiro SHIGYO[2], Yoshihisa WAKUTA[2], Yukinobu WATANABE[3] and Masaharu NUMAJIRI[4]

1. Japan Atomic Energy Research Institute, Tokai-mura, Naka-gun 319-11
2. Department of Nuclear Engineering, Kyushu University, Hakozaki, Fukuoka 812
3. Energy Conversion Engineering, Kyushu University, Kasuga-koen, Kasuga 816
4. National Laboratory for High Energy Physics (KEK), Oho, Tsukuba 305

Abstract

Double differential neutron spectra from a thick lead target bombarded by 0.5 and 1.5 GeV protons have been measured. The experiment was carried out at National Laboratory of High Energy Physics (KEK). The neutron spectra were analyzed by the time-of-flight technique and by unfolding analysis. The measured neutron spectra were compared with predictions of NMTC/JAERI and MCNP 4.2 codes. It was found that the calculated values could reproduce the general trend of energy and angular dependence of the measured data. At energies between 10 and 100 MeV, however, the calculated values were lower than the measured one considerably, probably due to a problem in the transport calculation of neutrons in this energy region.

1. Introduction

A great number of neutrons are generated by the spallation reaction at high energies. Recently, engineering utilizations of high energy proton accelerator are proposed for various purposes such as spallation neutron sources and accelerator driven transmutation systems[1]). For the design study of such facilities, it is necessary to use Nucleon-Meson Transport Code which can simulate nuclear reactions and particle transport processes in the energy region up to several GeV as accurately as possible. In order to evaluate the validity of a calculation code system employed in JAERI, the neutron spectra from a thick lead target bombarded with 0.5 and 1.5 GeV protons have been measured 6 angles between 15° and 150° and compared with prediction of NMTC/JAERI and MCNP 4.2.

2. Experimental Procedure

2.1. Incident Protons

The experiment was carried out at π2 beam of National Laboratory for High Energy Physics (KEK) in a series of (p,xn) double differential cross section measurements[2]. The illustration of the experimental arrangement is shown in Fig. 1. At π2 beam line in the East counter hole, the incident proton was supplied as the secondary particle generated by an internal target, which was placed in the accelerator ring of the 12 GeV proton synchrotron. The intensity of incident protons was so weak (<10 fA or 10^5 particles/macro pulse) that incident particles were connected one by one by plastic scintillators. The protons were identified from the pions by time-of-flight (TOF) method with a pair of scintillators (Pilot U) that were located at a separation distance of 20 m. Each Pilot U scintillator was connected with two photo multipliers (Hamamatsu H2431) on opposite sides. The time resolution was 0.25 ns for the incident beam TOF, and protons were well separated from pions in the TOF spectrum. The beam damp was consisted of carbon of 0.5×0.5 m^2 in the area and 1 m in thickness. The carbon was surrounded by sufficiently thick iron blocks except at the beam-incident surface. The distance between the target and the beam dump was 8.5 m.

2.2. Target Configuration

The lead target was consisted of two kinds of rectangular blocks (5×5×5 and 5×10×5 cm^3). These blocks were arranged so that the incident protons did not pass the air gaps between the blocks. A whole shape of the target was 15 cm long, 15 cm wide and 20 cm in thickness. The target had enough thickness to stop the 0.5 GeV protons. Although in the case of 1.5 GeV protons bombarded, the target had thin thickness to stop the incident protons and the average energy loss at the target was 260 MeV.

2.3. Neutron Detector

For the neutron detector, NE-213 scintillators , each having a volume of 12.5 cm ϕ × 12.5 cm thick, were used. The detectors were placed at 30, 60, 90, 120, 150° at a distance of 1 m from the target and at 15° at a distance of 1.5m. The scintillators were optically connected to photo multipliers (Hamamatu R1250) by an optical cement. In order to reject counting the charged particle, NE-102A scintillators (10×10×1 cm^3) were used as veto counters. The veto counters were located in front of the NE-213 scintillators at the separated distance 2 cm.

The pulse height of the neutron detectors was calibrated by measurements of gamma ray sources. The gamma ray energy and light output at the half height of Compton edge, which is described in the unit of electron equivalence (ee), are summarized at Table 1. The

light output at the half height of Compton edge was derived from the empirical formula of Dietze[3]. A good linearity of the pulse height was verified below 4.33 MeVee.

2.4. Electronic Circuit

The diagram of the electronic circuit is show in Fig. 2. When the incident-beam coincidence took place at all the beam scintillators, the pulse with a typical time duration of 150 ns was sent to the next coincidence module. Then, the signal of neutron detectors was accepted for this time duration. The events arising from incident pions were eliminated by tuning a hard ware timing in the beam coincidence. The example of the TOF spectrum from the target is shown in Fig. 3. The prompt gamma rays are seen as a sharp peak in the right hand side. The time resolution of the neutron TOF measurement was typically 1 ns. The TOF and pulse height data were taken event by event by list mode and stored in the magnetic tape (MT) for an off-line analysis. The number of incident proton was counted by the scalar. Since a good discrimination for the incident particle against π was achieved, the uncertainty of the incident proton counting was thought to be less than 2 %.

For the n-γ discrimination, the two-gate integration method[1] was carried out. The conceptual diagram of this method is shown Fig. 4. The anode signal of photo multiplier was branched into two pulses, and they were put into charge ADCs that corrected the charge of pulse during the gate of different time duration. The fast gate on ADC-1 covered the initial peak of photo multiplier signal with time duration of 30 ns. The tail gate for ADC-2 accepted the slow-tail portion during 300 ns after a delay of 130 ns. This method achieved a large dynamic range more than 4000:1. The total gate for ADC-3 was employed to measure the pulse height of the scintillation for the unfolding analysis.

3. Data Analysis

3.1. TOF Technique

The experimental data were analyzed using the FACOM M-780 and Personal Computer (PC-9821Ap). The energy spectra of neutrons were obtained by TOF spectra, at first. The energy spectrum is converted from TOF one by the following expression,

$$\frac{d^2n}{dEd\Omega} = \frac{N_n}{N_p\,\varepsilon\,\Delta\Omega\,\Delta E}, \quad E = m_n c^2\left(1\Big/\sqrt{1-L^2\Big/\left(c\left(t-t_0\right)+L\right)^2}-1\right) \qquad (1),$$

where Nn and Np are counts of neutrons and incident protons, respectively, ε are detection efficiency for the neutron, ΔΩ is solid angle sustained by detector to the center of the target, E and t are observed neutron energy and flight time, respectively , m_n and c are the rest mass of the neutron and the light speed, respectively, L is the distance between the center of the target and detector and t_0 is flight time of the prompt gamma. Here, it should be noted that

the distance between the point at producing and detected is assumed to be L. This assumption, however, is recognized to be correct within 6 % using the code NMTC/JAERI.

In the TOF analysis, the bias of pulse height was set at half height of ^{137}Cs or ^{60}Co Compton edge. For these bias, the detection efficiency up to 80 MeV was calculated using the code SCINFUL[4]. The detection efficiency for the ^{60}Co bias compared with the data of Verbinski[5] and the experimental is shown in Fig. 5. Below the energy 20 MeV, the value of SCINFUL is agreed with the value of Verbinski which is usually used as standard value. Between 20 and 80 MeV, the value of SCINFUL reproduces quite well the experimental data with in 5 %. The uncertainty of the value is determined as 10 % which is derived from the error of experimental data. Neutron spectra determined from the bias at half height of ^{60}Co Compton edge agreed with the ones obtained from ^{137}Cs bias within the statistical errors. Since the statistical accuracy is better in the ^{137}Cs bias set than the one in the ^{60}Co one, the ^{137}Cs bias is employed in the TOF analysis.

The applicable energy range of SCINFUL is up to 80 MeV. In Fig. 5, the calculated result of the code Cecil[6] is also shown; it overestimates uniformly by 20 % the one of SCINFUL. The efficiency above 80 MeV was determined by the calculated result of Cecil which was normalized to the value of SCINFUL at 80 MeV. The efficiency of BC−418 measured at IUCF[7] is shown in Fig. 6 and is compared with the present efficiency which is normalized by the thickness of the detector. Above 80 MeV, the normalized value of the Cecil reproduces the one measured at IUCF within 4 %. The uncertainty of the value is determined as 15 % which is derived from the error of IUCF data.

3.2. Unfolding Analysis

Secondary, for the low energy neutron spectrum, the multiple scattering in the target made spectra softer than real spectrum. In order to verify this effect, the neutron spectra were obtained by unfolding analysis which could deduce spectrum independent on the time of flight. In the unfolding analysis, the FORIST[8] code was employed and the response matrix was calculated by SCINFUL code. Since a saturation of the pulse height was observed above 20 MeV neutron, the unfolding analysis was employed only for the neutrons below 14 MeV.

In Fig. 7, the neutron spectrum at 30° obtained by unfolding analysis is compared with the one by the TOF technique for 500 MeV proton incidence. In the region below 3 MeV, a difference of more than 50 % is seen in the comparison between the two methods. This difference is thought to be caused by ambiguity of the efficiency around the ^{137}Cs bias, which is used in the TOF technique. Therefore, it was found that the neutron spectra reduced by the unfolding analysis was more reliable than ones obtained by the TOF technique below 3 MeV. In the energy region between 3 and 14 MeV, however, the results of unfolding

analysis agree with one of TOF quite well. It is concluded from these results that the neutron scattering effect is negligibly small above 3 MeV. Therefore, the overall spectrum was obtained by unfolding and by TOF methods in the region below 3 MeV and above 3 MeV, respectively.

4. Calculation

The calculation of the particle transport and nuclear reaction was performed with the code NMTC/JAERI[9] in the energy region above 20 MeV. The code NMTC/JAERI employs Baba's level density parameter and nucleon−nucleus elastic scattering into account. The total and the elastic cross section of nucleon−nucleus reactions, which was used geometrical cross sections originally in NMTC/JAERI, were replaced by Pearlstein Systematics[10]. For the neutron transport calculation below 20 MeV, MCNP 4.2[11] was employed. The neutron cross−section library was deduced from the evaluated nuclear data file JENDL−3.1[12].

5. Result

5.1 Energy Resolution

At Table 2, origins of the error of neutron spectra and the resolution of neutron energy are summarized. The error of the neutron yield is mainly produced by the statistical error and the uncertainty of the detection efficiency. The energy resolution was derived from the uncertainty of the time and the length. The time uncertainty is concerned the time resolution of the detector and time of flight for the incident protons in the target. The resolution of the detector, which is derived from the thin target measurements[2], is decided 0.7 ns. In the target, the time of flight for the 0.5 and 1.5 GeV incident protons is 0.6 and 0.3 ns[13], respectively. The length uncertainty is found to be 6.0 cm using a Monte−Carlo method which is assumed that the neutrons are produced and detected uniformly at the target and at the detector, respectively.

5.2 Energy Spectra

In Fig. 8 and 9, the measured neutron spectra are compared with the calculated results for the 0.5 and 1.5 GeV proton incidence, respectively. For both incident energies, the calculated results are in good agreement with the measured ones at various emission angles, although they underestimate the measured data in several tens of MeV region. In order to concern the effects of the energy resolution, the neutron spectra are calculated with the smeared the energy resolution and are shown as the dash line in Fig. 8 and 9. The difference between the calculated spectra with and without smeared the energy resolution is not shown

in the energy region below 100 MeV. In the energy region above 100 MeV, the calculated spectra with smeared the energy resolution are more flat than without one.

In order to verify the shape of the present experimental data, the data is compared with the result of JINR[14], which was carried out by using 20×20×15 cm^3 lead target and bombarded by 2.5 GeV protons. In the Fig. 10, the comparison of the experimental result between present and measured at JINR is given , showing that the shape of each data agrees quite well. The calculated spectrum, obtained by using the code SITHA[15] is also shown in Fig. 10. The calculated data using SITHA also underestimate the measured one in several tens of MeV region.

5. Discussion

To investigate the underestimation of calculation result in the energy region between 20 and 100 MeV, a neutron spectrum from thin target was calculated. The calculation results compared with the KEK[1] and LANL[16] data, which is normalized by target thickness, and are shown in Fig. 11 and 12. The calculated result is in good agreement with experimental data. The overestimation is found to be small than 20 %. In the case of thick target for 1.5 GeV incident protons, the average energy of the incident protons after transported the target is 1.26 GeV, so it is found that this underestimation is not mainly caused by the neutron spectrum produced by the (p,xn) reaction for the incident protons.

From the calculation results, the number of collision is found to be smaller than 3 in the process between the incident protons bombarded and the neutron leaked from the target. It is found that this underestimation is not caused by the error multiplication for the particle in the energy region above 1.26 GeV. The result of calculation for the target with small cross-section (4×4 cm^2) is compared with present results in Fig 13. In the energy region between 20 and 100 MeV, the neutron yields of the calculation result for the small target is larger by two times than the present results. This result shows large effect of the transport of neutron in the lead target, which might be the origin of the discrepancy between the experimental and calculated values in the energy region between 20 and 100 MeV.

6. Conclusion

In order to evaluated recognize the validity of the Nucleon−Meson Transport Code−calculation code, the neutron spectra from a thick lead target bombarded by 0.5 and 1.5 GeV protons have been measured at 6 angles between 15° and 150°. The experimental neutron spectra were obtained by TOF and unfolding method. The shape of the present spectrum shows a good agreement with experimental data carried out at JINR.

The calculated result using NMTC/JAERI and MCNP-4.2 shows agreement, although underestimates the experimental data in the region of several tens MeV. Importance of the transport effects in the neutron spectra were shown, which might be the origin of this underestimation.

References

1) T. Takizuka, et al., Proc. of OECD/NEA Mtg., Argonne 398 (1993)
2) K. Ishibashi, et al., Proc. Int. Conf, Gatlinburg, (1994).
3) G. Dietze and H. Klein, Nucl. Instrum. Meth., 193, 529 (1982).
4) J.K.Dickens, ORNL-6436 (1988).
5) V.V. Verbinski, et al., ORNL-P-993 (1965).
6) R.A. Cecil, et al., Nucl. Instrum. Meth., 161, 439 (1979).
7) R.H. Johnson and B.W. Wehring, ORNL/RSIC-40 p.33(1976).
8) W.B. Amian, et al., Nucl. Instrum. Meth., A281, 353 (1989)
9) Y. Nakahara and T. Tsutsui, JAERI-M 82-198 (1982).
10) S. Pearlstein, J. Atrophies. , 346 ,1049 (1989).
11) J.F. Briesmeister, et al., LA-12625 (1993).
12) K. Shibata, et al., JAERI-1319, (1990).
13) J.F Janny, Atom. Data and Nucl. Data Tables, 27, 147 (1982).
14) A.D. Kirillov, et al., JINR-R-13-90-193 (1990).
15) A.V. Daniel, V.Yu. Perov and E.A. Sokol, JINR-R-3-91-320 (1991).
16) M.M. Meier, et al., Radiation Effects, 96 ,73 (1986).

Table 1. Pulse height at the half height of Compton edge for the gamma ray sources.

Gamma Ray Source	E_γ(MeV)	Pc1/2(MeVee)*1
^{137}Cs	0.662	0.493
^{60}Co	1.173,1.333	1.074*2
Am－Be	4.439	4.331

*1 : Pulse height at the half height of Compton edge. This unit is electron equivalence, 1 MeVee shows the light output given 1 MeV electron.

*2 : Only one Compton edge is observed, because NE－213 has worse resolution to distinguish 2 Compton edge. This light output is calculated from 1.25 MeV which is mean of the 2 gamma rays.

Table 2. Errors and energy resolution of the present experimental data.

Neutron Energy (MeV)	Statistical Error*3 (%)	Detection Efficiency Error(%)	Neutron Yield Error*3 (%)	Energy Resolution*3 (%)
10	4.1	3	5.4	10.9
10	4.9	3	6.0	11.6
15	5.5	3	6.6	12.0
20	5.5	10	11.6	12.4
50	8.4	10	13.2	14.8
100	7.7	15	16.9	18.4
200	10.5	15	18.4	25.0
500	37.7	15	40.6	44.8

*3 : In the case of bombarded 1.5 GeV protons and measured at 30°

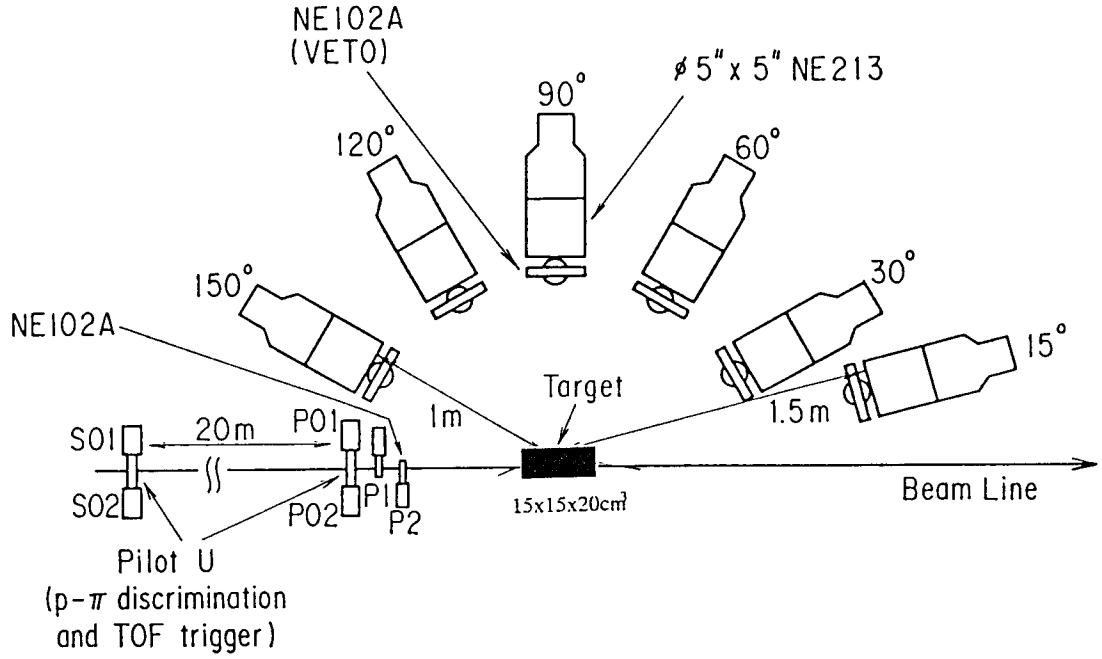

Fig. 1 Illustration of the experimental arrangement.

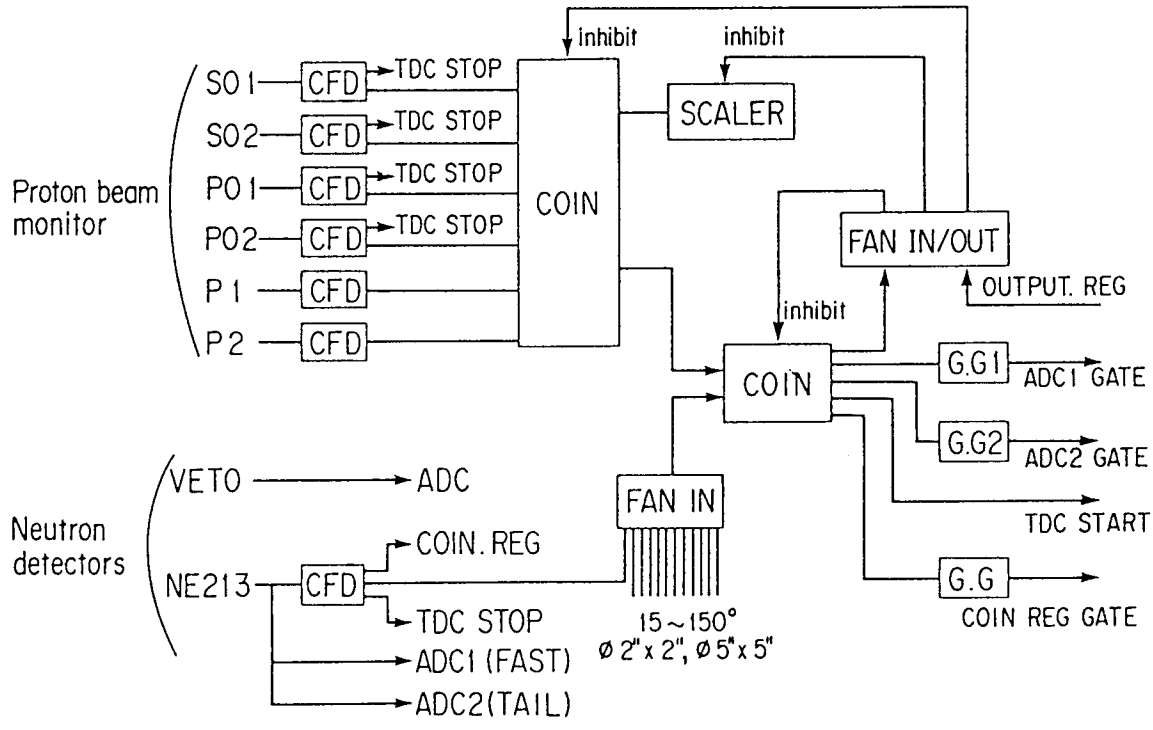

Fig. 2 Diagram of the electronic circuit used in the present experiment.

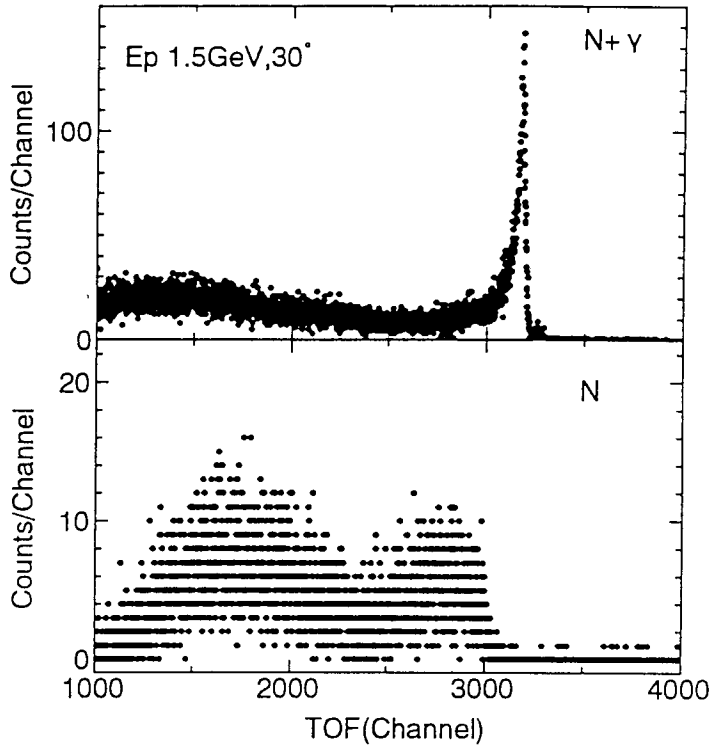

Fig. 3 Time-of-flight (TOF) spectrum measured at 30° bombarded by 1.5 GeV protons (above; for the neutron and the gamma ray, below; only for the neutron). Width of the TOF bin is 28 ns.

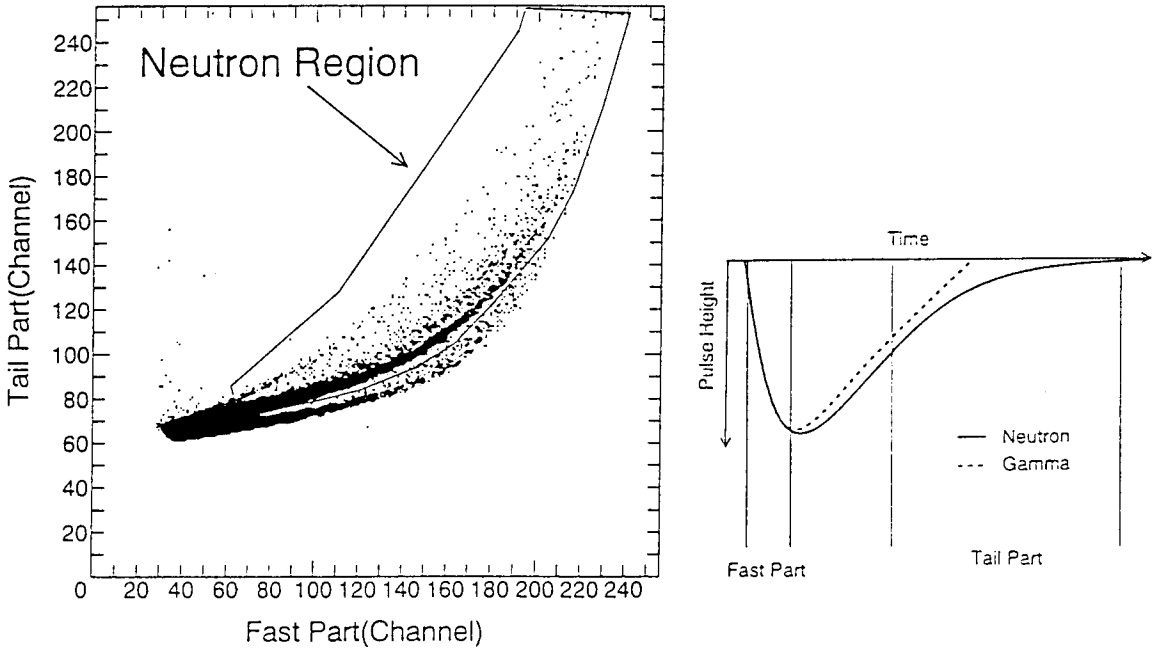

Fig. 4 Conceptual diagram of the two-gate integration method of neutron-gamma discrimination.

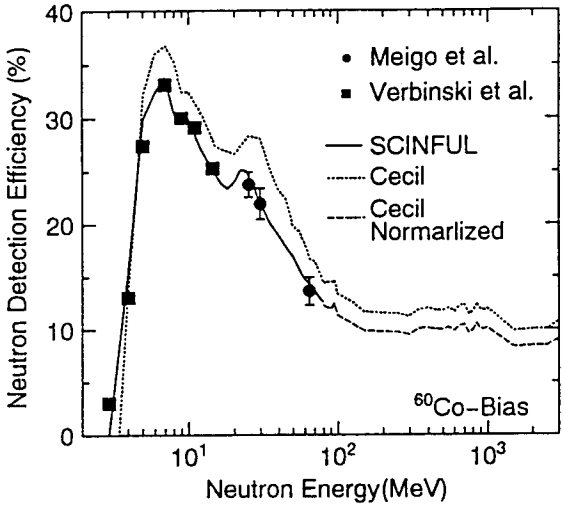

Fig. 5 Calculated and experimental neutron detection efficiency of the NE-213 12.7 cm ϕ × 12.7 cm t.

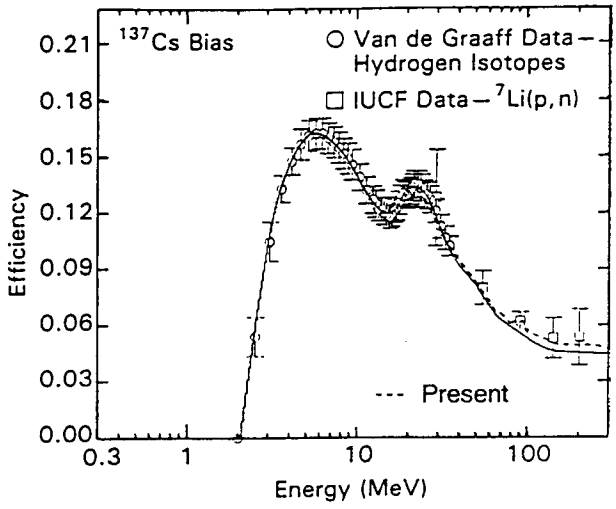

Fig. 6 Neutron detection efficiency used in the TOF technique compared with the values measured at IUCF.

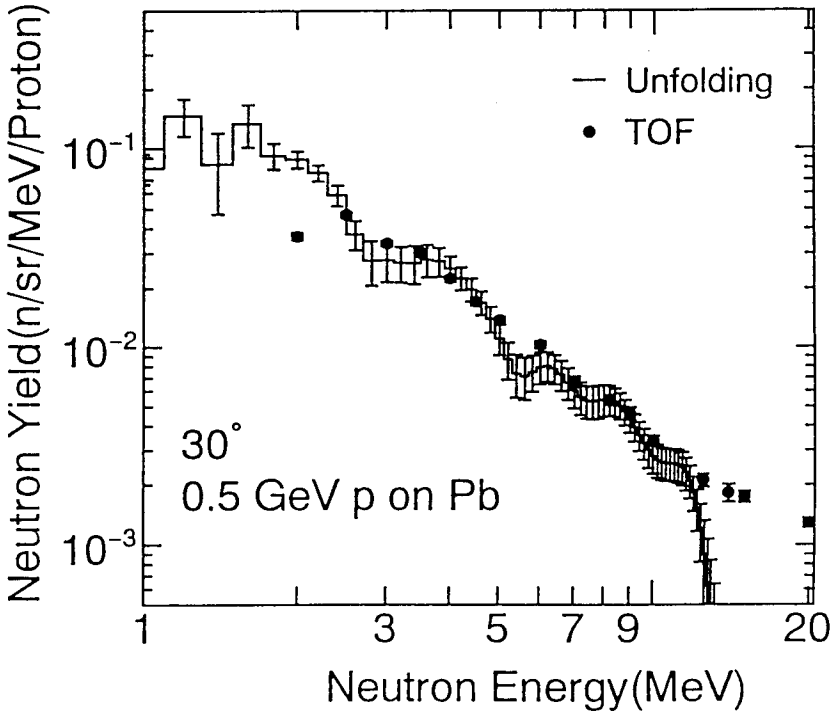

Fig. 7 Comparison of neutron spectra obtained by TOF and unfolding methods for 0.5 GeV proton incidence on thick lead target at 30°.

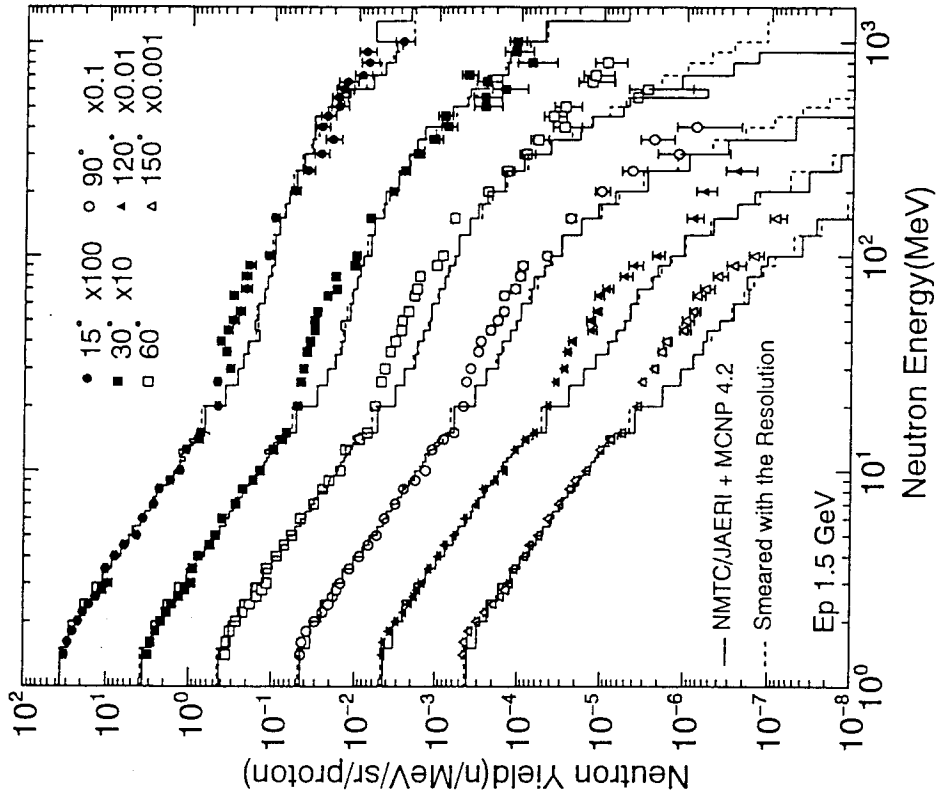

Fig. 8 Neutron spectra for 0.5 GeV proton incidence on thick lead target. Solid lines and dash lines show results of NMTC/JAERI and MCNP-4.2. calculation with and without including the uncertainty of the energy resolution for the neutron, respectively.

Fig. 9 Neutron spectra for 1.5 GeV proton incidence on thick lead target. Solid lines and dash lines show results of NMTC/JAERI and MCNP-4.2. calculation with and without including the uncertainty of the energy resolution for the neutron, respectively.

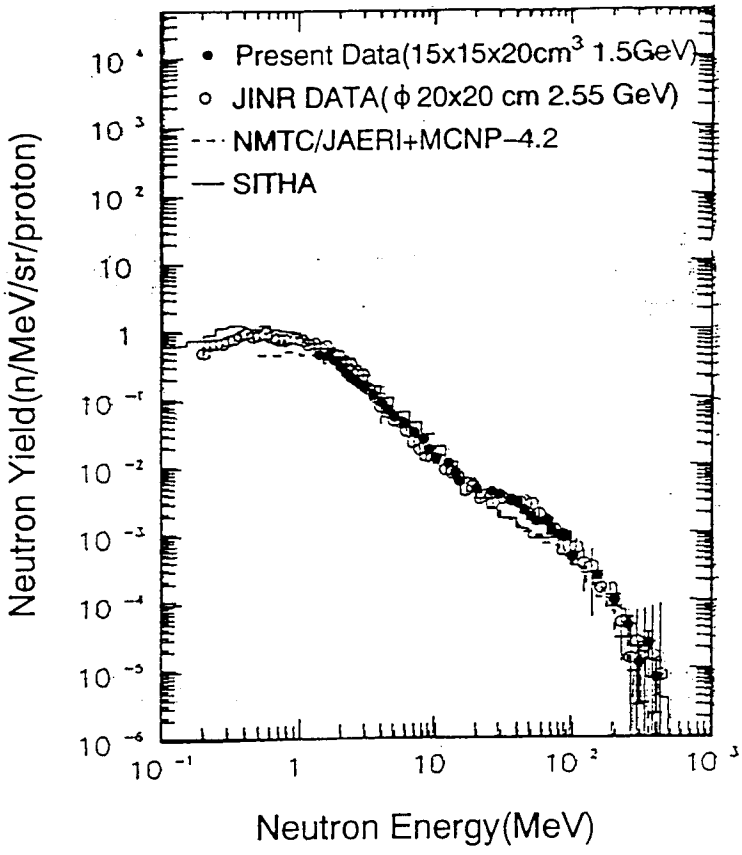

Fig. 10 Comparison of the experimental data between present and measured at JINR. Dash and solid line shows the result of NMTC/JAERI and SITHA, respectively.

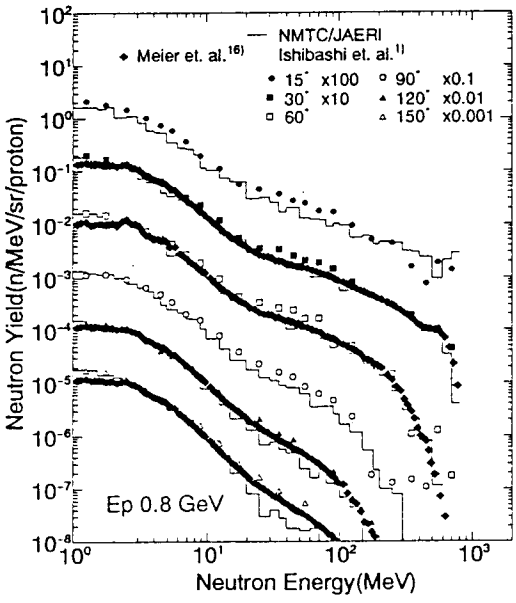

Fig. 11 Neutron spectra of experimental and the result of NMTC/JAERI from a thin lead target (4×4×1.2 cm^3) bombarded by 0.8 GeV protons.

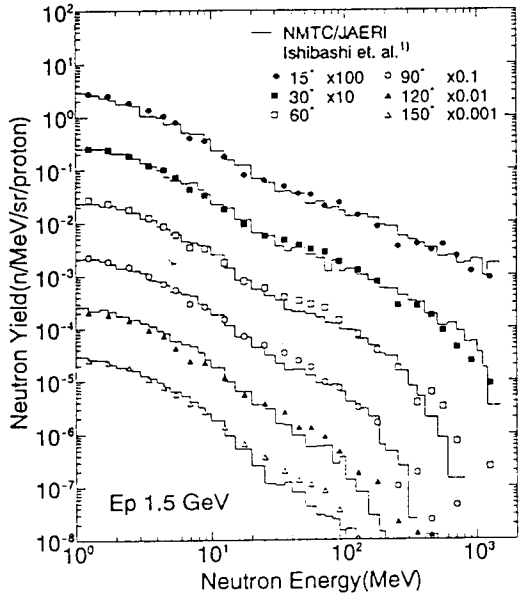

Fig. 12 Neutron spectra of experimental and the result of NMTC/JAERI from a thin lead target (4×4×1.2 cm^3) bombarded by 1.5 GeV protons.

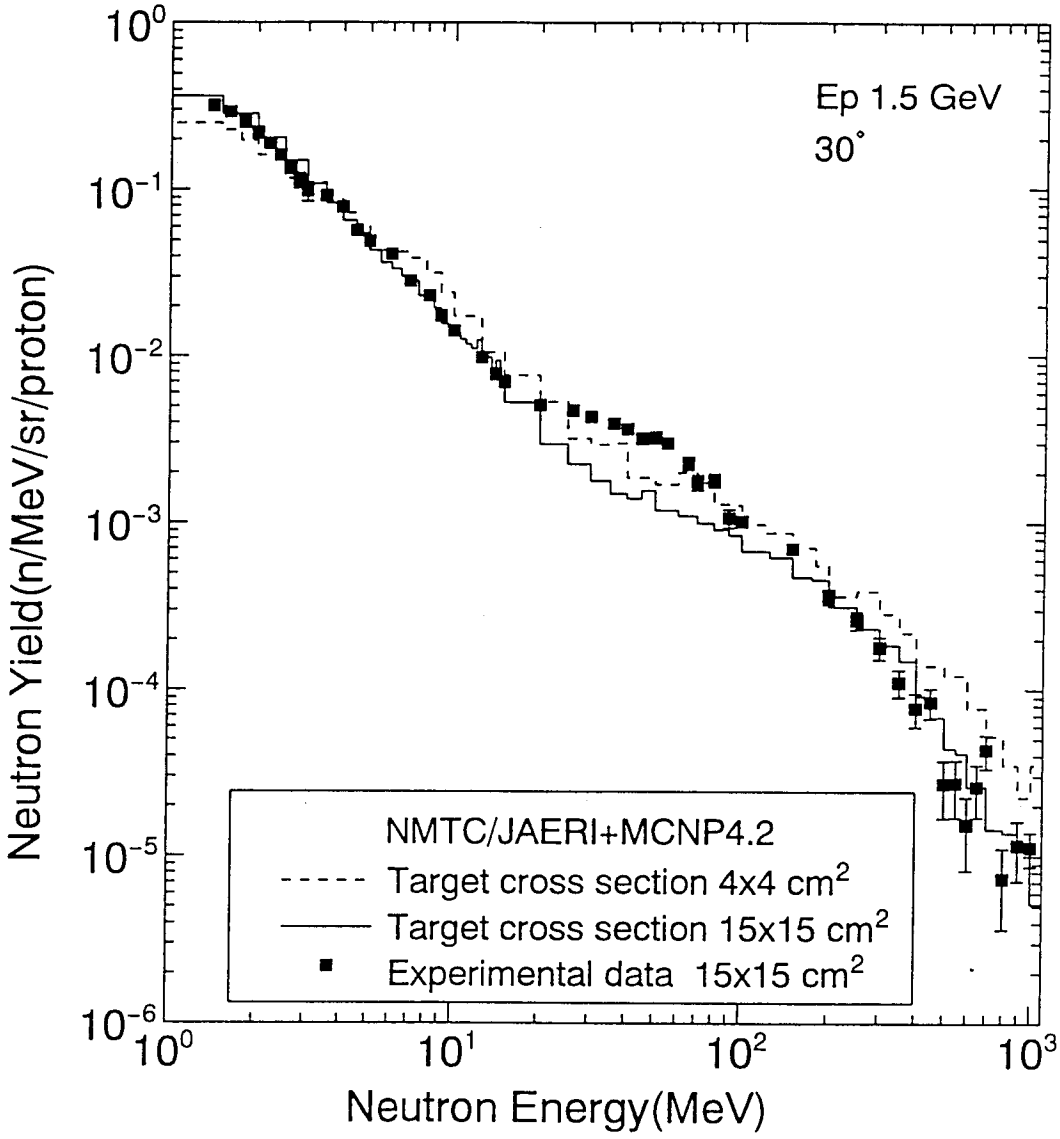

Fig. 13 Calculation result of neutron spectra from small target (4×4×20 cm^2) and present target compared with the experimental data.

4. Application

4.1 HIGH INTENSITY PROTON ACCELERATOR AND ITS APPLICATION (PROTON ENGINEERING CENTER)

Shun-ichi TANAKA
Japan Atomic Energy Research Institute, Tokai Research Establishment

A plan called PROTON ENGINEERING CENTER has been proposed in JAERI. The center is a complex composed of research facilities and a beam shape & storage ring based on a proton linac with an energy of 1.5 GeV and an average current of 10 mA. The research facilities planned are OMEGA・Nuclear Energy Development Facility, Neutron Facility for Material Irradiation, Nuclear Data Experiment Facility, Neutron Factory, Meson Factory, Spallation Radioisotope Beam Facilty, and Medium Energy Experiment Facility, where high intensity proton beam and secondary particle beams such as neutrons, π-mesons, muons, and unstable isotopes originated from the protons are available for promoting the innovative research of nuclear energy and basic science and technology.

1. BACKGROUND

In '80s, a few of dawnlike activities have been made for high intensity proton accelerators to apply it to the nuclear fuel breeding and the incineration of high level radioactive waste.[1,2] After the partitioning and transmutation R&D program OMEGA was proposed by the Atomic Energy Agency(AEC) of Japan in 1988, JAERI has made an intensive work of the OMEGA program to study a transmutation system of minor actinides(MAs) with a proton accelerator as an option, and proposed the development of the high intensity proton linac, called Engineering Test Accelerator(ETA) with an energy of 1.5 GeV and an average current of 10mA.[3] In the course of the ETA development, since 1991, Research & Development(R&D) has been continued concerning the initial stage components; high brightness ion source, radio-frequency quadrupole linac(RFQ), drift-tube linac(DTL), and radio-frequency source(RF), as well as the conceptual design of the ETA collaborating with the LANL in USA.[4,5]

Besides, the potential possibility for applying the ETA to development of new nuclear energy production system and basic sciences has been discussed in addtion to the transmutation of MAs,[6] and recently an idea of Proton Engineering Center was proposed to apply the ETA for versatile purposes.[7]

2. OUTLINE OF THE PROTON ENGINEERING CENTER

Fig. 1 is a bird-eye figure based on a preconceptual layout of the PROTON ENGINEERING CENTER, which is composed of the ETA, a beam shape & storage ring, and seven research facilities as the following;

A. OMEGA・Nuclear Energy Development Facility,
B. Neutron Facility for Material Irradiation,

C. Nuclear Data Experiment Facility,
D. Neutron Factory,
E. Meson Factory,
F. Spallation Radioisotope Beam Facilty,
G. Medium Energy Experiment Facility.

Positive hydrogen of an average current of 10 mA and negative one of about a few mA are accelerated up to 1.5 GeV by the linear acelerator(ETA) with a length of about 1200 m. Positive ion beam of 1.5 GeV is mainly used in the OMEGA/Nuclear Energy Development Facility, and also that of 0.6 GeV extracted on the way for the Neutron Facility for Material Irradiation and the Medium Energy Experiment Facility. On the other hand, a part of negative hydrogen beam of 1.5 GeV is used for the Spallation Radioisotope Beam Facilty, while positive one is guided into the beam shape & storage ring to supply such a pulsed beam with various time structure as to meet various experimental requirements in the Nuclear Data Experiment Facility, Neutron Factory, and Meson Factory.

Beam sharing in the Proton Engineering Center and typical researches in the facilities are demonstrated in Fig.2. The beam intensity of the ETA is almost enough to supply it required from the facilities so that all of the experiments at each facility and each beam line are realized simultaneously.

3. ENGINEERING TEST ACCELERATOR(ETA)

The ETA is a proton linear accelerator, and consists of a high brightness ion source, an RFQ linac, a DTL and a high β linac as demonstrated in Fig.3. The principle parameters are given in Table 1.

Table 1 Principle Parameters of the ETA

Energy	1500 MeV
Average current(H^+,H^-)	10 mA
Peak current	100 mA
Repetiton rate	50 Hz
Duty	10 %
Pulse width	1.0 ms

4. EXPERIMENTAL FACILITY

Table 2 represents a preliminary plan of the main parameters and experimental equipments of the facilities.

4.1 OMEGA and Nuclear Energy Technology Development Facility

A typical PWR of 3000 MWt produces about 25−30 kg of MAs having a long half-life per year.[8] Several concepts have been proposed for proton accelerator-based transmutation system of MAs by JAERI and others,[9] of which the examples are shown

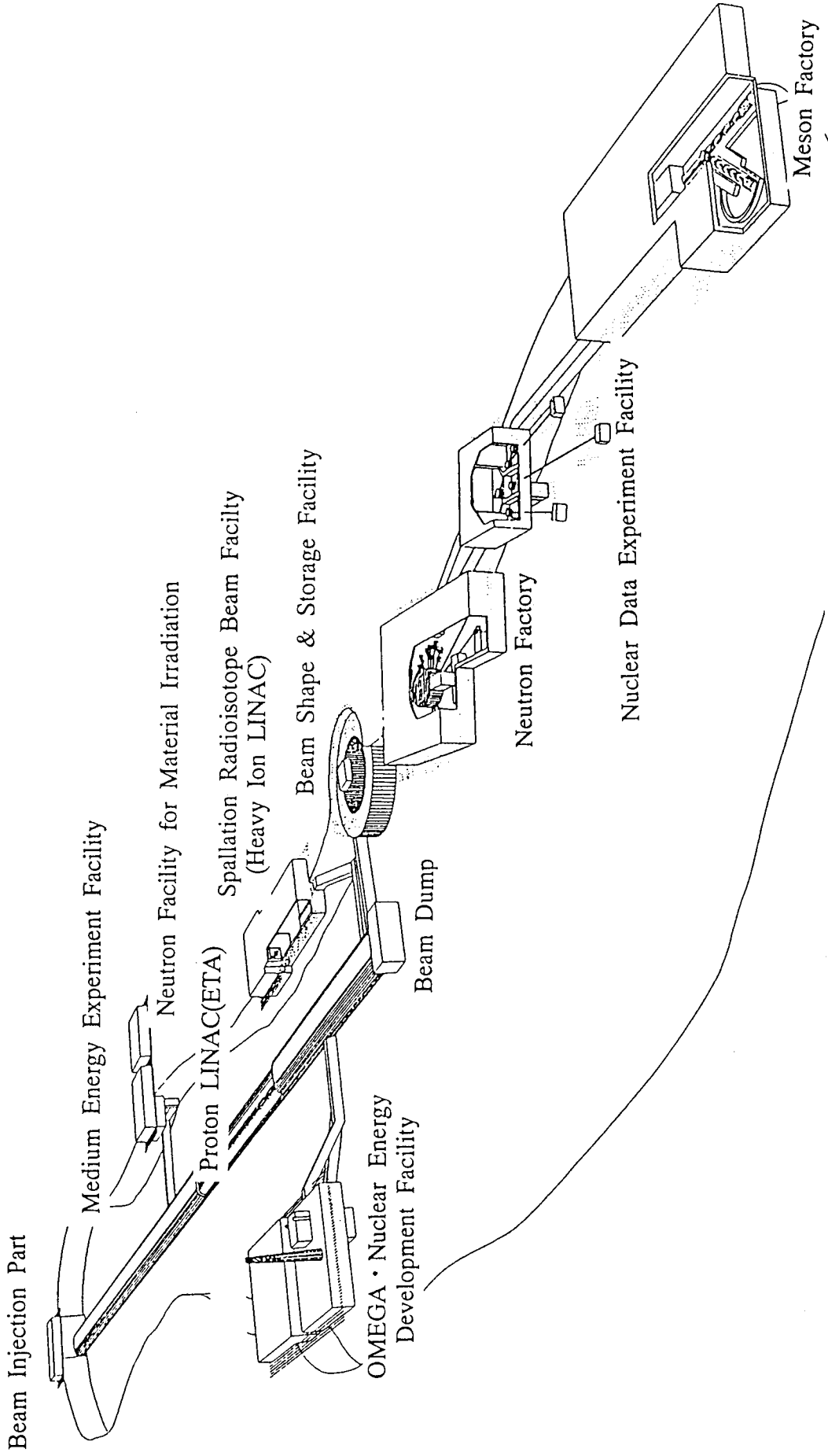

Fig.1 A Bird-Eye Figure of ETA and Research Facilities

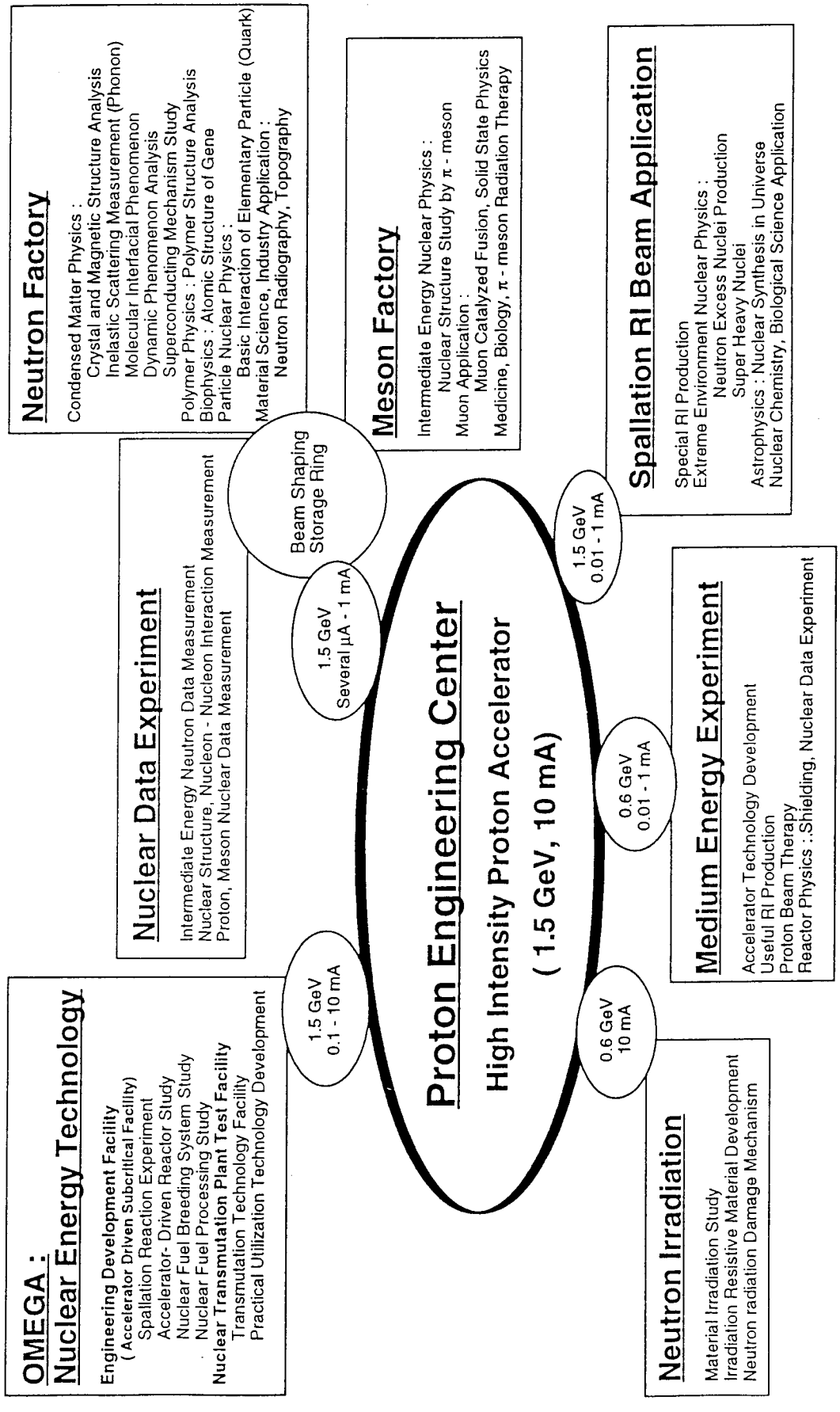

Fig.2 Facilities in Proton Engineering Center & Main Research Items

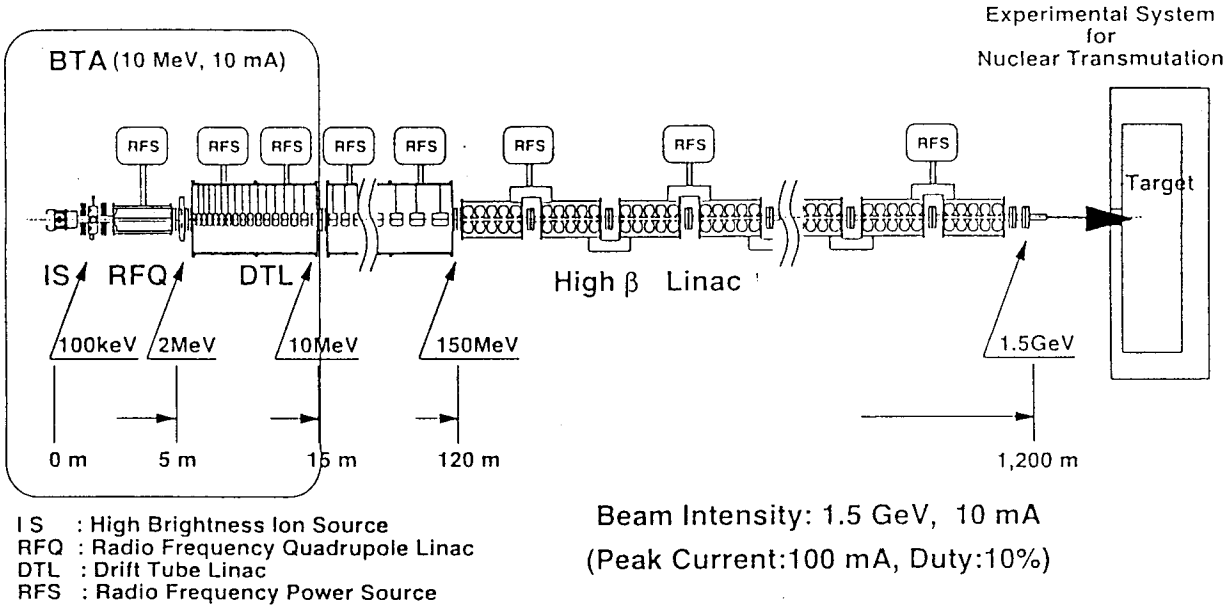

Fig.3 A Conceptual Layout of ETA(Engineering Test Accelerator)

in Figs.4, 5, and Tables 3, 4.[10)]

In this facility, two main experimental facilities; Enginnering Development Facility and Nuclear Transmutation Plant Test Facility, are expected to be consructed for the R&D for the OMEGA program aiming at transmutation of MAs and for the demonstration test of the transmutation plant. In the Enginnering Development Facility, various experiments are made to verify the design base of reactor physics and shielding of accelerator-driven

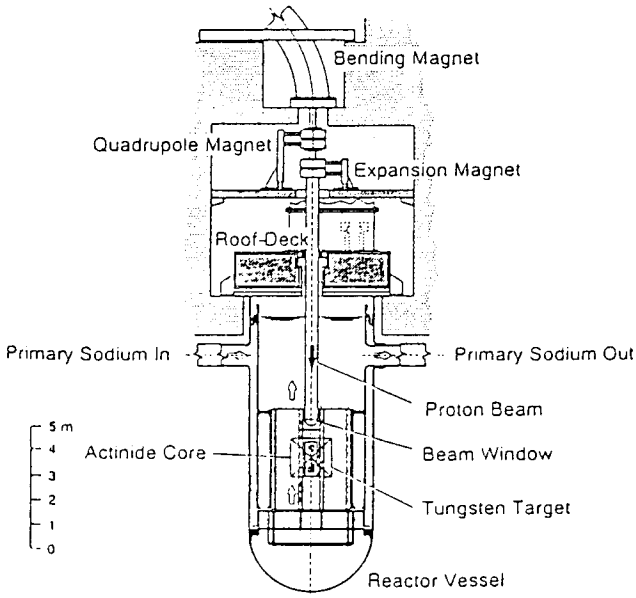

Fig.4 Solid Target/Core System

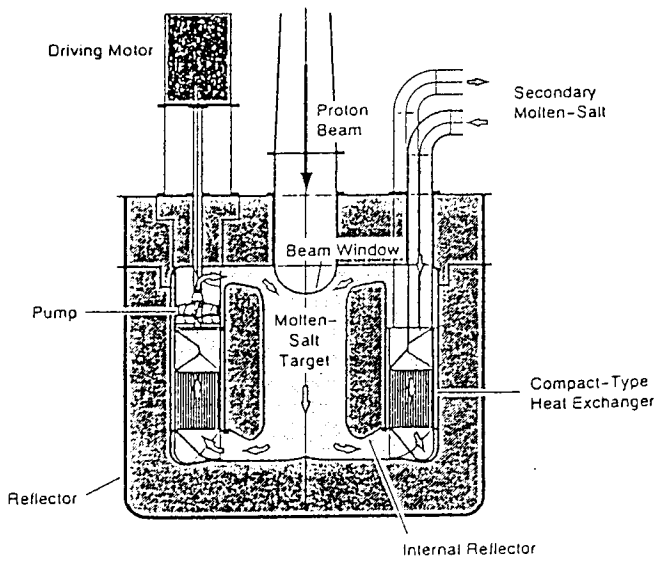

Fig.5 Molten Salt Target/Core System

Table 2 Features of Facilities in Proton Engineering Center

OMEGA・Nuclear Energy Development Facility

MAIN FACILITY	PRINCIPAL PARAMETERS	
Engineering Development Facility	Proton energy	1.5 GeV, 0.1 - 10 mA
	Apparatus	Accelerator driven subcritical assembly Spallation reaction experiment facility Fuel processing test facility Elementary technology development facility
	Floor plan	100 x 80 m^2
Nuclear Transmutation Plant Test Facility	Proton energy	1.5 GeV, 10 mA
	Experimental apparatus	Transmutation plant demonstration facility
	Floor plan	80 x 80 m^2

Neutron Facility for Material Irradiation

MAIN FACILITY	PRINCIPAL PARAMETERS	
Neutron Irradiation Facility	Proton energy	0.6 GeV, 10 mA
	Maximum flux	$2x10^{16}$ n/cm^2s
	Volume	1 - 2 litre (>100 dpa/y for SUS)
	Post Irradiation Experimental Facility	Neutron & muon probes
	Floor plan	50 x 50 m^2

Nuclear Data Experiment Facility

MAIN FACILITY	PRINCIPAL PARAMETERS	
Nuclear Data Measurement Facility	Proton energy	1.5 GeV, several μA - 1 mA
	Secondary radiations	neutrons, π
	Time of flight	50 - 100m(3 flights) 20 - 50m(3 flights)
	Pulse width	~ns
	Floor plan	50 x 50 m^2

Neutron Factory

MAIN FACILITY	PRINCIPAL PARAMETERS	
Slow Neutron Facility	Proton energy	1.5 GeV, 0.1 - 1 mA
	Beam channel	20
	Neutron energy	10^{-7} - 10 eV
	Pulse width	<200 ns
	Peak flux	10^{17} n/cm^2s
	Floor plan	100 x 100 m^2 20 x 20 m^2

Table 2(continued)

Meson Factory

MAIN FACILITY	PRINCIPAL PARAMETERS	
μ Facility	Proton energy	1.5 GeV, 0.1 - 1 mA
	Beam channel	28
	μ energy	10 keV - several 10 MeV
	Pulse width	50 - 20 ns
	Beam intensity	10^7 - 10^9 /s
π -meson Facility	Beam channel	3
	π -meson energy	0.5 - 1 GeV/c
ν Facility	Beam channel	1
	Floor plan	150 x 60 m^2 (μ)
		50 x 80 m^2 (π)
		30 x 50 m^2 (ν)

Spallation Radioisotope Beam Facilty

MAIN FACILITY	PRINCIPAL PARAMETERS	
Spallation RI Production Facility	Proton energy	1.5 GeV, 0.01 - 1 mA
	Target/Ion source	300 kV
Heavy Ion Linac	Energy	10MeV/u
	Accelerated ion	proton - Uranium
	Beam intensity	1 ppA - 1 μpA
	Floor plan	100 x 40 m^2 (Linac)
		50 x 50 m^2 (Experiment)

Medium Energy Experiment Facility

MAIN FACILITY	PRINCIPAL PARAMETERS	
Experiment Facility	Proton energy	0.6 GeV, 0.01 - 1 mA
	Beam channel	RI production
		Multi-purpose
	Floor plan	50 x 60 m^2

Beam Shape & Storage Ring

MAIN FACILITY	PRINCIPAL PARAMETERS	
Shaping - Storage Ring	Proton energy	1.5 GeV, 0.1 - 1 mA
	Ring length	200 m
	Pulse width	<20 ns for meson
		<200 ns for neutron
	Floor plan	100 x 80 m^2

subcritical system, and further for developing the spallation target system and the beam window and so forth which are essential technology for making the transmuation system realized. Besides, this facility is also expected to be used for the R&D of hybrid energy production and fuel breeding reactor system using proton accelerators.

The Nuclear Transmutation Plant Test Facility should be constructed for demonstrating the total enginnering system based on the results in the Engineering Dvelopment Facility.

Table 3 Design Parameters and Operating Condition for Solid Target/Core System

Fuel	Metal Alloy Np-15Pu-30Zr AmCm-36Pu-10Y
Target	Soild Tungsten
Primary coolant	Liquid sodium
Actinide inventory	3160 kg
Multiplication factor(k_{eff})	0.89
Spallation neutrons(z)	40 n/p
Proton beam	1.5 GeV - 39 mA
Thermal power(W)	820 MW
Burnup	250 kg/y(8.0% per year)
Power density	930 MW/m^3 (Max.) 400 MW/m^3 (Avg.)
Temperature, Core Inlet/Outlet	330/430 °C
Coolant maximum velocity	8 m/s

Table 4 Design Parameters and Operating Condition for Molten Salt Target/Core)

Fuel	Chloride salt 64NaCl-5$PuCl_3$-31$MACl_3$ (MA: Np, Am, Cm)
Target	Chloride salt
Primary coolant	Chloride salt
Actinide inventory	5430 kg
Multiplication factor(k_{eff})	0.92
Spallation neutrons(z)	38 n/p
Proton beam	1.5 GeV - 25 mA
Thermal power(W)	800 MW
Burnup	250 kg/y(4.6% per year)
Power density	1660 MW/m^3 (Max.) 310 MW/m^3 (Avg.)
Temperature, Core Inlet/Outlet	650/750 °C
Coolant maximum velocity	3.6 m/s

4.2 Neutron Facility for Material Irradiation

To confirm the integrity of materials for fast neutron irradiation is very important to endorse the life and safety of nuclear plants. In this context, fast neutron irradiation facility for materials is an essential one for developing fission and fusion reactors, and several fission reactors have been constructed for material irradiation testing. However, no accelerator-based fast neutron irradiation facility, so far, has been constructed, although a couple of ideas have been proposed using d-Li reaction neutrons[11] and spallation neutrons[12,13] from deutron and proton accelerators.

A comparison of neutron flux and corresponding irradiation volume is demonstrated among typical existing and planned neutron irradiation facilities in Table 5. As an intensity of average 10 mA of 0.6 GeV protons is available in the present facility as shown in Fig.3, the neutron intensity above 0.4 MeV is about $5x10^{14}$ n/cm^{2}s at 10 cm and $5x10^{15}$ n/cm^{2}s at 1 cm estimated from the EURAC's design for Pb target, which is about one-order higher than that of IFMIF in the ratio of flux-volume.[14]

The present facility is expected to be used for material researches as a powerful pulsed neutron source to complement ion-beam accelerators and fission reactors for material irradiation and researches.

Table 5 Typical Existing and Planned Neutron Irradiation Facilities

Reactor		
	JMTR(JAERI)	ϕ=4 x10^{14} n/cm^2 s
	HIFR(ORNL)	ϕ=1.4x10^{15} n/cm^2 s (30dpa/y for SUS)
	HIFR-RB(ORNL)	ϕ=7 x10^{14} n/cm^2 s (10dpa/y for SUS)
	ORR(ORNL)	ϕ=3.0x10^{14} n/cm^2 s (4dpa/y for SUS)
	ANS(ORNL)	ϕ>1.4x10^{15} n/cm^2 s (planned)
Accerelator		
	IFMIF	Li target
		E_d=35MeV, Beam current=250mA
		Continuous operation(CW)
		ϕ=1.5x10^{14} n/cm^2 s
		V = about 1 litre
	EURAC(ISPRA)	Spallation target(Pb)
		E_p=0.6GeV, Beam current=6mA
		Quasi-pulse operation
		2x10^{16} n/cm^2 s (max 320dpa/y for SUS)
		V = 1-2 litre(>100dpa/y for SUS)
	ETA	Spallation target(Pb)
		E_p=0.6GeV, Beam current=10mA
		Pulse operation
		2x10^{16} n/cm^2 s (maximum)
		V > 1-2 litre(>100dpa/y for SUS)

ϕ:neutron flux, V:irradiation volume

4.3 Nuclear Data Experiment Facility

In this facility, versatile experimental data are measured to verify theoretical models and directly for special purposes with respect to protons and neutrons from 20 to 1500 MeV, π－meson, and various secondary particles produced by protons and neutrons. For example, Koning[15] summarizes the data requirements for accelerator-based transmutation as Table 6.

The necessity for intermediate-energy nuclear data libraries up to a few GeV is increasing not only for accelerator-based transmutation, but also in medical field, fusion material research, space exploration research, and fundamental nuclear science. Nevertheless, the present status of intermediate-energy nuclear data is far from the level required in the quality and quantity, furthermore, the experimental facilities are completely insufficient worlwidely.

The Nuclear Data Experiment Facility is expected to become an international center of excellence in nuclear data research, in addition to the production of qualified nuclear data.

Table 6 Requirements for Evaluated Nuclear Data File for Accelerator-Based Transmutation

Energy range covered	
a data library from 0 to about 100 MeV	
a reference data library from 20 to 1500 MeV	
an activation/transmutation library from 0 to 100 MeV	
Materials	
Targets	:Ta, W, Pb, Bi
Actinides	:^{238}U, ^{237}Np, ^{238}Pu, ^{241}Am, ^{243}Am, ^{244}Cm, ^{245}Cm
Shielding & Reactor	:H, C, N, O, Na, Mg, Al, Ar, K, Ca, Cr, Mn, Fe, Co, Ni, Cu Zn, Zr
Projectile	
Neutron, Proton	
Data for neutrons and protons	
(n,xn),(n,xγ) double differential cross section	
Neutron and photon yields	
Products yields as a function of energy	
(n,fission) cross section	

4.4 Neutron Factory

This facility is proposed to use slow neutrons for condensed matter physics, polymer physics, biophysics, particle nuclear physics, and other applications. The proton beam firstly is introduced into the beam shape & storage ring from the ETA to produce the pulsed beam having various time structure required in the Neutron Factory, and after that the pulsed proton beam with an enegy of 1.5 GeV and the maximum current of 1 mA bombards neutron targets to generate pulsed neutrons from 10^{-7} to 10 eV. The proton

beam of 1.5 MW, which is a little bit greater than that of the SINQ(Swiss Intense Neutron Source "Quelle") under construction and smaller than 5 MW of the ESS(European Spallation Source) planned, could generate a peak neutron flux of about 10^{17} n/cm^{2}s−eV which is several hundreds times higher than that of JRR−3M, and the intense neutrons are expected to be available for developing new scientific fields such as time−dependent behavior in biology and material sciences.

In this facility, various experimetal researches can be performed simultaneously using more than 20 beam lines, which looks like a research factory using neutrons.

4.5 Meson Factory

This facility is composed of muon channels, π−meson channnels and a beam dump for neutrino experiment. A model of the meson factory is the Meson Arena in the JHP(Japan Hadron Project)[16]. Muon beams from about 10 keV to several 10 MeV are produced by thin targets using pulsed proton beam from the beam shape & storage ring, and are provided for various experiments through the beam lines equipped around the targets. The muon intensity is 2−3 orders stronger than those in the exsisting muon facilities of LAMPF, TRIUMF, and ISIS. The intense muon beam is powerful not only for the μCF(muon−catelyzed fusion) and as a probe of the μSR(muon spin resonance), but it is expected that a new field of muon science is developed as a meson factory.

4.6 Spallation Radioisotope Beam Application Facilty

Various radioisotopes will be produced via spallation process by bombading a target with proton beam of 1.5 GeV. In this facility, the produced radioisotopes are seperated using an ISOL(Isotope Seperator on Line), and then accelerated up to 10 MeV/nucleon by a heavy ion linac, which is the same concept with the Exotic Nuclei Arena in the JHP.

It is thought that the present facilty develop a new frontier in nuclear structure investigation with respect to super−heavy elements and astrophysics based on the advanced research at the Tandem−Booster[17] of JAERI.

4.7 Medium Energy Experiment Facility

Proton beam of 0.6 GeV is guided to the facility to do complemental experiments for proton beam of 1.5 GeV and to develop the technology of proton beam applications for medicine and industry. Specially, it is expected that the intense proton beam is powerful for massive−production of radioisotopes tabulated in Table 7 which are useful for therapy, diagonosis, and industrial applications.

ACKNOWLEDGEMENTS

I would like to appreciate deeply M. Mizumoto for his great suggestions for the present report, and to note that a lot of data and figures are owing to T. Takizuka, K. Noda and M. Tanase.

Table 7 Useful Radioisotopes Produced by Proton Accelerator

$^{68}Zn(p,2n)^{67}Ga$	:Diagonosis of tumor
$^{203}Tl(p,3n)^{201}Pb \rightarrow {}^{201}Tl$	:Diagonosis(Sacnning) of myocardium
$^{111}Cd(p,n)^{111I}n$	:Scintigraphy of brain
$^{127}I(p,5n)^{123}Xe \rightarrow {}^{123}I$	:Therapy of thyroid
$^{16}O(p,\alpha)^{13}N$	:Positron tomography(PET)
$^{14}N(p,\alpha)^{11}C$	:Positron tomography(PET)
$^{58}Ni(p,pn)^{57}Ni \rightarrow {}^{57}Co$	:Calibration source, Mossbauer

REFERENCES

1) "Spallation Neutron Engineering", Ed. by the Research Committee on Neutron Target System, Atomic Energy Society of Japan(1984). (in Japanease)
2) Proc. of the 2nd International Symposium on Advanced Nuclear Research−Evolution by Accelerators−, Organized by JAERI, Jan. 24−26 (1990).
3) M. Mizumoto et al.:"Development of Proton Linear Accelerator and Transmutation system," Global '93, Seattle (1993).
4) M. Mizumoto:"Development of High Intensity Proton Accelerator," Proc. on Workshop on the JHP, p67 (1994).(in Japanease)
5) K. Hasegawa et al.:"First Beam Test of the JAERI 2 MeV RFQ for the BTA," 17th Intern. Linac Conf., Tsukuba, Japan (1994).
6) Y. Kaneko et al.:"High Intensity Proton Accelerator Program," JAERI−M 91−095 (1991).(in Japanease)
7) S. Tanaka et al."Engineering Application of High Intensity Proton Accelerator," Proc. on Workshop on the JHP, p75 (1994).(in Japanease)
8) "Present Status of Transmutation R&D," Ed. by the Research Committee on Transmutation, Atomic Energy Society of Japan (1994).(in Japanease)
9) "Overview of Physics Aspects of Different Transmutation Concepts," OECD Nuclear Energy Agency, NEA/NSC/DOC(94)11 (1994).
10) T. Takizuka et al.:"A Conceptual Design Study of an Accelerator−based Actinide Transmutation Plant with Sodium Cooled Solid Target/Core", 2nd OECD/NEA Information Exchange Meeting on Partitioning and Transmutation of Actinide and Fission Products, ANL, Argone (1992).
11) G. L. Varsamis et al., Nucl. Sci. Eng., 106, 160 (1990).
12) W.Kley et al.:"EURAC:The JRC Proposal for a European Fusion Reactor Material Test and Development Facility", Nucl. Instr. Meth., A255, 384 (1987).
13) D.G.Doran:"Report of the LASREF Evaluation Committee", PNL−SA−18584 (1990).
14) Y. Oyama, K. Noda: Private communication.
15) A.J.Koning:"Requirements for an Evaluated Nuclear Data File for Accelerator−Based Transmutation", NEA/NSC/DOC(93)6, NEA/P&T Report No.6 (1993).
16) A Draft Proposal for Japanese Hadron Project, Institute of Nuclear Study of The University of Tokyo (1987). (in Japanese)
17) C. Kobayashi, H. Ikezoi:"JAERI Tandem−Booster Accelerator," J. Atomic Energy Society of Japan, Vol.36, No.12, 1111 (1994). (in Japanese)

4. 2 ISSUES IN SPACE RADIATION SHIELDING FOR LUNAR BASE

Koji Oishi

Space Project Office, Shimizu Corporation
Seavance South, 1-2-3 Shibaura, Minato-ku 105-07, Tokyo
Phone:(03)5441-8951
Fax:(03)5441-8955
E-mail:oishi@spo.shmz.co.jp

ABSTRACT

Precise estimation of production of secondary neutrons from space radiation particles in the thick shield is very important to define dose rate inside the lunar base. NASA has developed one-dimensional baryon transport code BRYNTRN, which requires only a very small fraction of computer resources. However, for neutrons, backward production and scattering are not modeled in BRYNTRN. Comparisons of the calculated secondary particle spectra in lunar concrete and regolith at the depth of 10, 50,100, and 200g/cm^2 between BRYNTRN and Monte-Carlo calculation code system HETC-MCNP were performed. From the comparison, large underestimation of the calculated result of BRYNTRN in the lower neutron energy region, En<10MeV, were observed. Verification of nuclear data used in MCNP calculation for low energy neutrons were performed, and good agreement between experiment and calculation was obtained. It is concluded that careful consideration for the lower energy neutrons will be required by using BRYNTRN transport code system.

I. INTRODUCTION

On the 20th anniversary of the lunar landing mission, President Bush outlined a program to return to the Moon to stay and to land humans on Mars, Space Exploration Initiative (SEI) program.[1] To accomplish this program, lunar base where astronauts stay for long duration is indispensable. Although this program has been postponed, lunar base will be necessary for the future programs, such as lunar exploration, lunar based observation, and development of energy resources to Earth.

Proper lunar base shielding design to reduce exposure to astronauts is one of the most important issues to be solved as the first step. Several parametric studies for selecting materials, obtaining the optimum arrangement of the shield, and so forth will be necessary to accomplish this task. Usually, accelerator shielding calculations in such high energy protons have been performed by using Monte Carlo calculation codes which need enormous

computational requirements. For various systematic studies of optimizing shielding design in the space program, such a calculational method is not appropriate.

NASA has developed a transport calculation code named BRYNTRN[2], which is one-dimensional and makes some simplifying approximations to improve execution speed. Some verifications on the code have been performed by using Monte Carlo calculation codes and experiments with mono energy proton sources.[3,4] However, from the practical point of view, verification by using continuous proton spectra like Galactic Cosmic Ray (GCR) is very important. In this study, comparisons of the calculated proton and neutron spectra by BRYNTRN and those by HETC[5]-MCNP[6] three dimensional Monte Carlo calculational code have been performed in order to confirm the validity of BRYNTRN in the practical radiation field.

II. RADIATION ENVIRONMENT ON THE MOON

There are several types of particle radiations in space shown in Fig. 1. As far as the radiation shielding for the lunar base is concerned, galactic cosmic rays and solar particle events contribute as radiation sources.

II.A. Galactic Cosmic Ray

Galactic Cosmic Ray (GCR), which irradiates the moon constantly, originates from outside the solar system. The principle components of GCR are hydrogen (87%), helium (12%), and heavy ions. The energies of these particles are up to several thousand GeV. The differential energy spectra, from hydrogen to iron with electron, are shown in Fig. 2.

The intensity of GCR varies in response to solar activity. Since the solar wind moderates the GCR intensity, it is minimum when the solar activity is maximum.

II.B. Solar Particle Event

Solar Particle Event (SPE) is induced by solar flares and energy of particles varies 1~100 MeV. The main component is proton, and it also contains alpha particles of about 3 ~ 20%. There exists continuous plasma flow from the Sun called solar wind, but its energy is too low to be a source for radiation shielding. The SPE changes in frequency during 11 year cycle, reaching a maximum during the periods before and after sunspot maximum. Energy spectra from two large historical SPE, those of February 1956 and August 1972, are shown in Fig. 3.

III. NASA's CALCULATION FOR LUNAR BASE SHIELDING

NASA Langley Research Center has developed baryon transport code system BRYNTRN. This code solves the fundamental Boltzmann transport equation in the one dimensional form (straight ahead approximation):

$$\left[\frac{\partial}{\partial x}-\frac{\partial}{\partial E}S_j(E)+\sigma_j(E)\right]\phi_j(x,E)=\sum_{k>j}\int_E^{\infty}\sigma_{jk}(E,E')\phi_k(x,E')dE'$$

where ϕ_j : quantity to be evaluated, type j with having energy E at spatial location x,
S_j : stopping power in various media,
σ_j : macroscopic total nuclear cross section,
σ_{jk} : differential nuclear interaction cross section, the production of type j particles with energy E by type k particles of energies E' (>E).

The solution methodology in detail, as a combined analytical-numerical technique, is found in reference 2.

John E. Nealy et al.[7] have calculated penetration spectra of GCR through lunar regolith by using BRYNTRN. The composition of lunar regolith is SiO_2, MgO Al_2O_3, and FeO. The relative atomic densities for O, Al, Mg, Si, and Fe are 61.5, 7.5, 5.5, 19.3, and 6.1%, respectively. The cosmic ray environment used is for solar minimum, shown in Fig. 4. Figure 5 shows a calculated spectrum at 50 cm depth in regolith. In the depth, it is notable that the population of the secondary neutrons, which were produced by the interaction between induced particles and nuclei of regolith components, became very large especially in the lower neutron energy region. Figure 6 shows the variation of the total flux of several particles resulting from incident GCR vs. regolith thickness. Alphas and heavy ions decrease rapidly as the depth of regolith increases. On the contrary, secondary neutron component became evident, and for layers thicker than about 25 cm, the neutron flux exceed that for protons. They have also calculated the dose rate and blood forming organ (BFO) dose equivalent at 5cm depth from the calculated spectra. The result of BFO dose vs. regolith thickness is shown in Fig. 7. From the result it is concluded that, in the depth of the shield, secondary neutrons and protons contribute over 90 % to the total dose equivalent.

IV. COMPARISON OF CALCULATED SPECTRA BETWEEN BRYNTRN AND HETC-MCNP

From the result mentioned in section III, the accuracy to obtain the flux of secondary neutrons and protons is very important to estimate the proper shield thickness of lunar base. In

this section, the verification of BRYNTRN transport code by HETC-MCNP Monte Carlo calculation code was performed.

IV.A. Source and Shielding Materials

The incident proton spectrum, shown in Fig. 8, is GCR solar minimum, with energy range 1 x 10^1~6 x 10^5 MeV. The shielding materials of lunar base examined were lunar regolith and concrete. The densities of regolith and concrete were 1.3 g/cm^3 and 2.3 g/cm^3, respectively. The compositions (atomic densities) of these materials are shown in Table I.

IV.B. Calculational Conditions for HETC-MCNP

The geometry used for HETC-MCNP calculation was a rectangular prism with 10 m x 10 m and a thickness of t m. The thickness t of the shield was 10, 50, 100, 200 g/cm^2. For obtaining accurate lower energy neutron spectra (En<15 MeV), MCNP Monte Carlo calculation code with its related library based on ENDF/B-IV was also applied. The input neutron spectra for MCNP calculations were obtained from the results of HETC.

The histories of the calculation were varied from 10,000 to 100,000, according to enough statistics for each calculated position. Calculation period was up to 1 hour by using CRAY XMP, though a typical problem for BRYNTRN can be solved within 2 or 3 minutes on a VAX 8800.

IV.C. Results

Calculated Spectrum

The calculated proton and neutron spectra of lunar concrete for 10 and 200 g/cm^2 cases are shown in Figure 9 and 10. Energy spectra 10^1 ~ 10^5 MeV and 10^{-1} ~ 10^5 MeV were obtained for protons and secondary neutrons, respectively.

The statistics of the HETC calculated results were not enough in the proton energy range Ep < 10^2 MeV, but above 10^2 MeV, statistical errors were less than 20%. The shape of the proton spectra at the back of the shield did not differ from that of the incident proton spectrum. However, calculated spectrum by BRYNTRN became softer in the lower energy region Ep<200MeV, even in the case of 10g/cm^2. The peak of the proton spectra shifted from 500 MeV to 100 MeV. For neutrons, energy spectra above 10^{-1}MeV were obtained by both BRYNTRN and HETC-MCNP calculations. Statistical errors for neutrons were less than 10%, except at the higher energy region En>10GeV. Note that the population of the lower energy neutrons increased as the thickness of the shield increased. The same results were also obtained in the case of regolith.

Comparison of the calculated results between the two codes

Figure 11 shows the ratio of integrated spectra calculated by BRYNTRN to those by HETC-MCNP (B/H) in several energy regions.

For protons, a good agreement from -20% to +20%, within HETC's statistical errors, between these two codes for both regolith and concrete was obtained, except proton energy range Ep < 200 MeV. The BRYNTRN's results overestimated HETC's ones in this energy region, but the HETC's results are not reliable because of its very low statistics.

For neutrons, B/H values varied from 0.3 to 3.0 for the shield thickness t <50 g/cm^2, however for the thicker case, t >80 g/cm^2, large underestimation of the BRYNTRN's results to those of HETC were observed for all energy regions. In the neutron energy range En <10MeV, all the calculated results by BRYNTRN underestimated those by HETC.

V. DISCUSSION

From the shielding point of view, underestimation by BRYNTRN for lower energy neutrons is important to be investigated, because the population of these neutrons became larger abruptly as the shield thickness increased. The main difference between BRYNTRN and HETC-MCNP calculations for obtaining lower energy neutrons, En<15.85 MeV, is that the ENDF-B/IV nuclear data library was applied in the case of HETC-MCNP calculation.

Measurement of neutron spectra in a concrete assembly was performed in order to verify nuclear data library used for calculation by using Fusion Neutronics Source at the Japan Atomic Energy Research Institute[8]. The source neutron was produced by deuterium- tritium reaction and the energy was 15MeV.

The calculated results by using ENDF-B/IV library, which was applied for the HETC-MCNP calculation, were compared to the experimental results. Figure 12 shows the calculational to experimental ratios (C/E) in the several neutron energy region. Very good agreement between experiment and calculation was obtained within 20%. From the comparison between experiment and calculation, the nuclear data library used by the HETC-MCNP calculation was verified for the lower energy neutron transport calculation, En<15MeV, through concrete assembly.

To improve the BRYNTRN's results, reevaluation of the approximation of the transport cross sections for lower energy neutrons will be needed. However, from the practical point of view, it is very useful to prepare the adjustment factor to the HETC results, which will be obtained from a parametric study of the B/H values vs. thickness of the shielding materials.

VI. CONCLUDING REMARKS

Verification of a baryon transport code BRYNTRN was performed by using Monte Carlo calculation code HETC-MCNP for the lunar regolith and concrete shielding materials in a practical radiation field. In the present calculational conditions, BRYNTRN overestimated HETC-MCNP for proton spectra, Ep<200MeV, and underestimated neutron spectra En<10MeV and En>500MeV.

The reason of the underestimation for the neutron spectra, En<10 MeV, calculated by BRYNTRN was clarified through the investigations of the concrete shielding experimental results. It was concluded that the BRYNTRN is very effective for the basic study of the lunar base shielding which needs enormous computation time, provided that these underestimations are carefully treated.

ACKNOWLEDGMENTS

The author wishes to express his sincere thanks to S.L.Huston of McDonnell Douglas Space System Company who performed shielding calculation by using BRYNTRN.

REFERENCES

1."America at the Threshold," U.S. Government Printing Office, Washington D.C. (1991)

2.J.W.WILSON,L.W.TOWNSEND,J.E.NEALY,S.Y.CHUNB.S.HONG,S.L.LAMKIN,B.D.GANAPOL, F.KHAN and F.A.CUCINOTTA, "BRYNTRN: A Baryon Transport Model," NASA Technical Paper, 2887 (1989)

3.J.W.WILSON,L.W.TOWNSEND,B.GANAPOL,S.Y.CHUN and W.W.BUCK, "Charged-Particle Transport in One Dimensional," Nucl. Sci. and Eng., 99, 285 (1988)

4.J.W.WILSON,L.W.TOWNSEND,B.D.GANAPOL,S.L.LAMKIN, "Methods for High-Energy Hadronic Beam Transport," Trans. Ame. Nucl. Soc., 56,271 (1988)

5.K.C.Chandlerh and T.W.ARMSTRONG, "Operating Instructions for the High-Energy Nucleon-Meson Transport code HETC," ORNL-4744, Oak Ridge National Laboratory (1972)

6."MCNP;Monte Carlo Neutron and Photon Transport Code," CCC-200, RSIC, Oak Ridge National Laboratory (1983)

7.J.E.NEALY, J.W.WILSON and W.TOWNSEND,"Preliminary Analyses of Space Radiation Protection for Lunar Base Surface System," SAE Technical Paper Series, 891487 (1989)

8.K.OISHI,Y.IKEDA,H.MAEKAWA and T.NAKAMURA,"Experiment and Analysis of Neutron Spectra in A Concrete Assembly Bombarded by 14 MeV Neutrons," Nucl. Sci. and Eng.,103, 46 (1989)

TABLE I

Compositions of the Shielding Materials Used for Calculations

Element	Regolith	Concrete
H	1.93E+21*	---------
O	1.75E+22	1.74E+22
Mg	---------	7.73E+20
Al	4.02E+21	3.54E+21
Si	4.01E+21	4.74E+21
Ca	2.47E+21	1.91E+21

* Read as 1.93×10^{21}

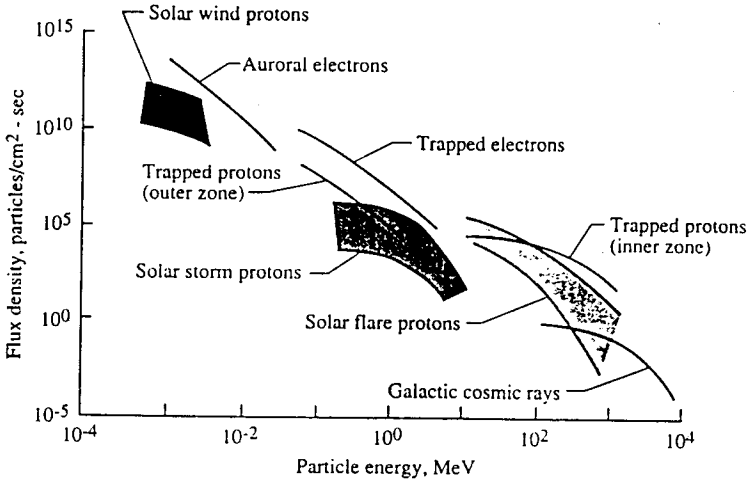

Fig.1 Space-radiation environment.

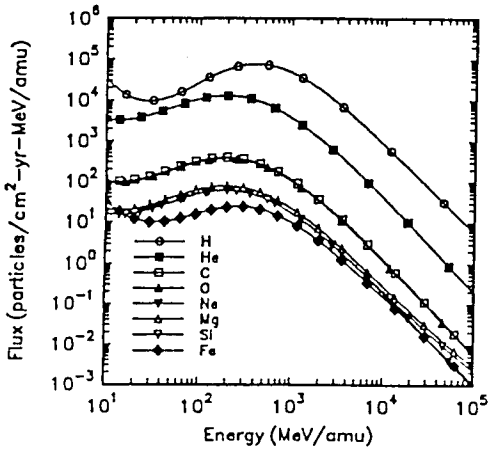

Fig.2 Differential flux spectra for galactic cosmic rays at solar minimum.

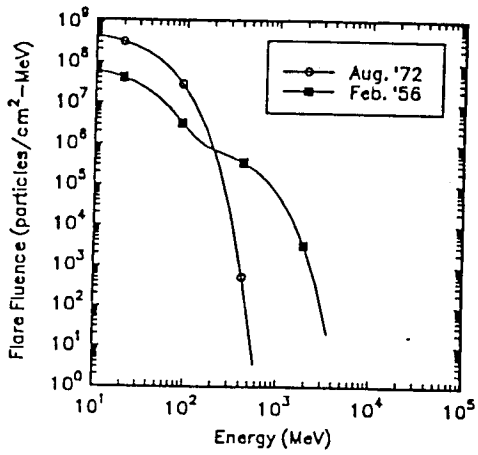

Fig.3 Event-integrated proton fluence spectra for the February 1956 and August 1972 solar proton events.

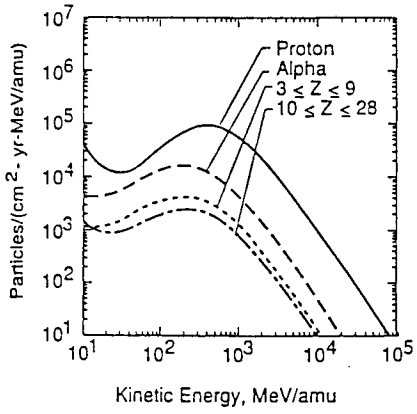

Fig.4 Annual flux for constituents of the interplanetary galactic cosmic ray.

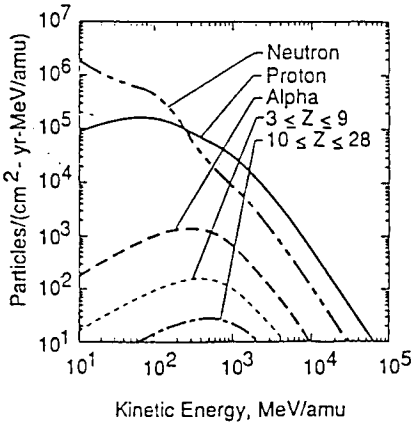

Fig.5 Annual flux variation with energy for particles at 10 cm depth in regolith.

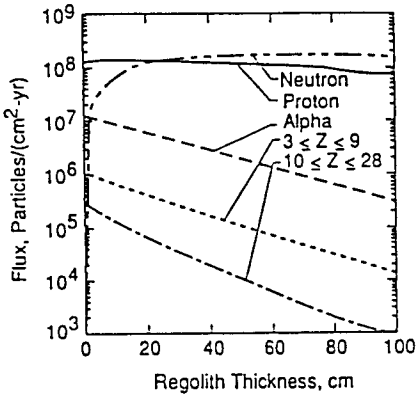

Fig.6 Annual variation of energy integrated particle flux as a function of thickness.

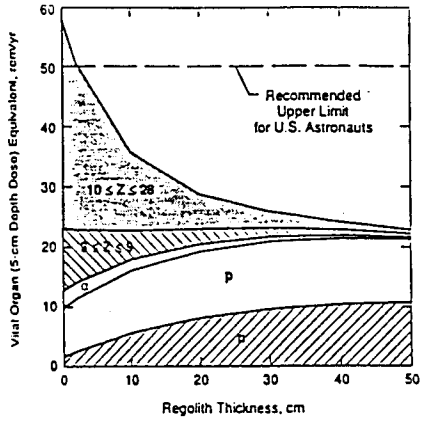

Fig.7 BFO annual dose equivalent as a function of regolith thickness.

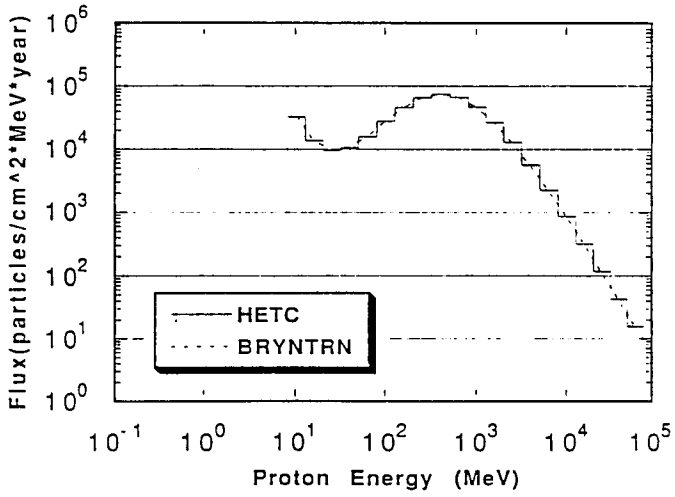

Fig.8 Incident proton spectra.

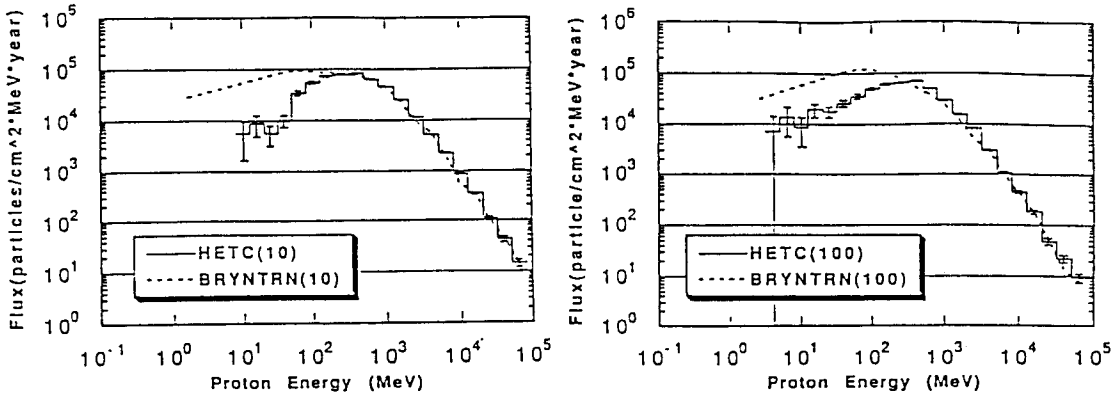

t = 10 g/cm²　　t = 100 g/cm²

Fig.9 Calculated proton spectra by BRYNTRN and HETC-MCNP.

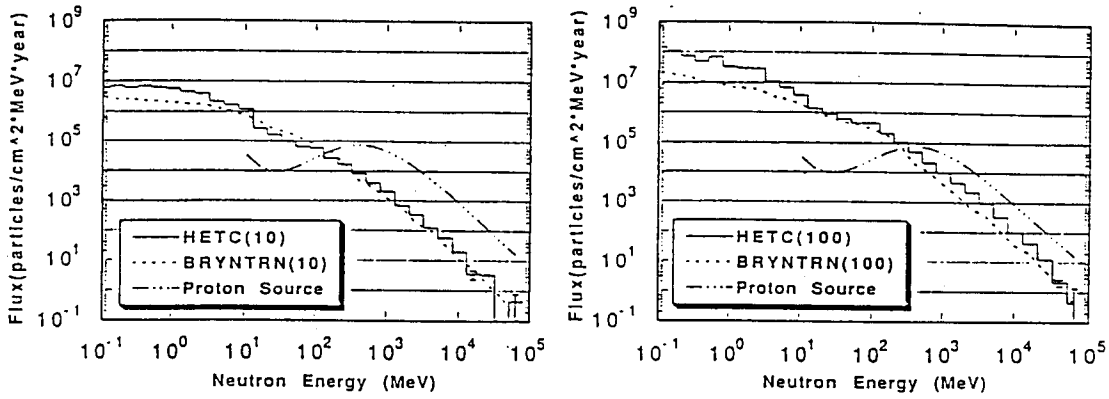

t = 10 g/cm² t = 100 g/cm²

Fig.10 Calculated neutron spectra by BRYNTRN and HETC-MCNP.

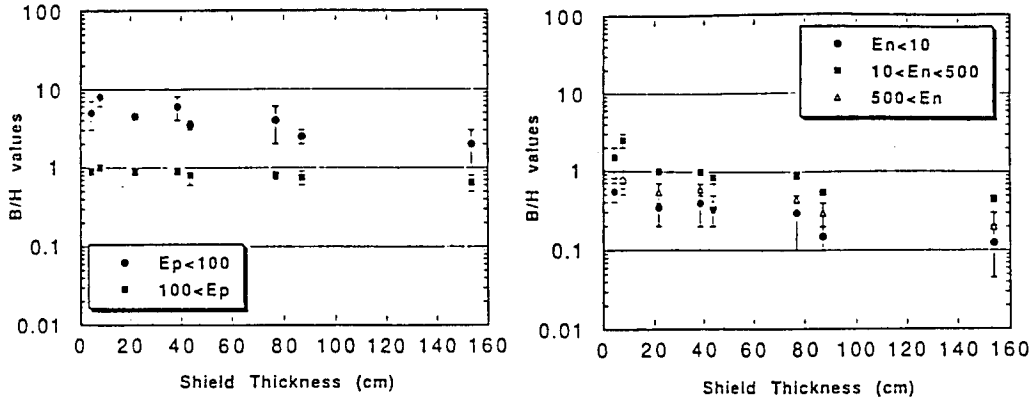

(i) proton (ii) neutron

Fig.11 Ratios of BRYNTRN to HETC-MCNP values vs. shield thickness.

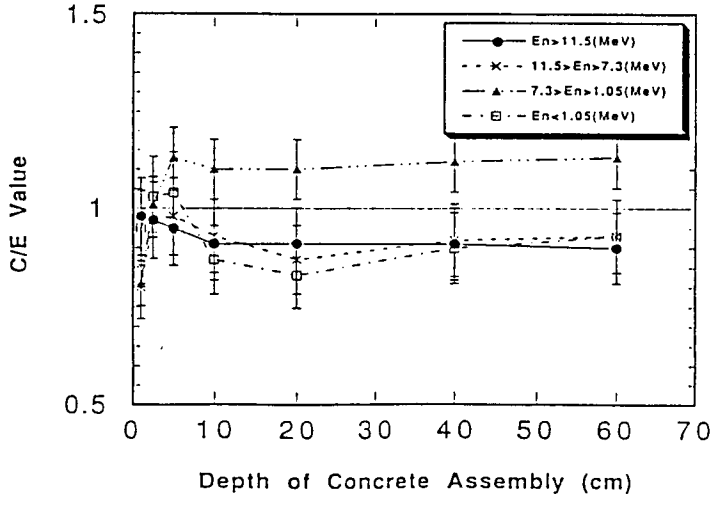

Fig.12 Ratios of calculated results to experimental.

4.3 Radiation therapy using high-energy heavy-ion

Tatsuaki Kanai
National Institute of Radiological Sciences,
4-9-1, Anagawa, Inage-ku, Chiba-shi, CHIBA 263 JAPAN

ABSTRACT

The clinical trial of the heavy-ion radiotherapy was started at June 1994 after pre-clinical experiments using 290 MeV/u carbon beam. In this paper, an irradiation system for the heavy-ion radiotherapy installed at HIMAC and the physical characteristics of the therapeutic beam were discussed.

1. INTRODUCTION

Heavy-ion radiotherapy is expected to improve results of the radiation therapy because of its excellent dose localization and high LET effects of the biological responses. HIMAC (Heavy Ion Medical Accelerator in Chiba) was commissioned for pre-clinical experiments at the end of February in 1994. After three and half months of the pre-clinical experiments, the clinical trial of the heavy-ion therapy was started at June 24, 1994. For the pre-clinical experiments just before the clinical trial using HIMAC beam, we ascertained the feasibility of the irradiation system and the bio-physical properties of the heavy-ion beams. In the radiation therapy, it is important to know LET distributions of the radiation fields besides the dose distribution because of LET dependence of biological responses of the heavy ion beam. The depth dose distribution of the 290 MeV/u carbon beam was measured and compared with calculation results. LET of the carbon beams were calculated including contributions from the secondaries and tertiaries which were produced by nuclear interactions of the carbon ion with water material.

In this paper, the irradiation system for the heavy-ion radiation therapy and physical characteristics of the beam were described.

2. IRRADIATION SYSTEM

Figure 1 illustrates an irradiation system of the HIMAC facility. The irradiation system comprises wobbler magnets, a scatterer, beam monitors, a range shifter, a ridge filter, collimators, patient positioning devices and a patient couch. In order to make a uniform irradiation field, we used a pair of wobbler magnets and the scatterer. The range shifter is used for adjusting the peak position in the patient. The ridge filter is used for spreading out Bragg peak.

The accelerated beam is focused on the iso-center of the irradiation course. The focused beam draw a circular trace at the iso-center with the wobbler magnets. Then, the wobbled beam is scattered to make a uniform field at the iso-center. Large irradiation fields of diameters over 16 cm were obtained so that the difference between the intensities at the central part and the peripheral highest part was less than 2 % of the average intensity by this method.

A papient is fixed on the irradiation coach so that a target of the paient is aliened in the beam line. The target is positioned accurately using images obtained by X-rays and image intensifiers.

3. CALCULATION OF DEPTH DOSE DISTRIBUTIONS OF CARBON BEAM

Fig. 2 shows the results of the depth dose distribution in water of carbon 290 MeV/u beam. Open circle and closed triangles in the figure are the relative ionization in water and in Lucite, respectively. The thickness of the Lucite is converted to water equivalent thickness. Solid line in the figure shows the result of a depth dose calculation, in which secondary and tertiary particle contributions are taken into consideration[1,2,3]. The calculated results agreed very well with the experimental results measured by the ionization chamber.

In order to apply this heavy-ion beam to radiation therapy, we have to extend the sharp Bragg peak according to the target thickness, that is Spread-Out Bragg Peak. And in the radiation therapy, it is important that cells in the target volume should be sterilized uniformly. Biological effects of the heavy-ion beam, the ability of sterilization of the cells, generally varies with the LET of the radiation. Especially in the LET regions of 10 - 500 keV/μm, the biological effects depends largely on LET of the beam. In case of 290 MeV/u carbon beam in water, LET at the entrance is about 13 keV/μm and LET near the Bragg peak is over 200 keV/μm. Then, we have to know the detail LET or energy distribution of the beam in the water in order to design the SOBP.

As penetrating in the water or tissues of the human body, the incident nuclei experiences nuclear reaction with the target nuclei, hydrogen, carbon, nitrogen, oxygen and other elements. In the many types of the nuclear reactions, projectile fragmentation is the most important nuclear reaction which contributes the depth dose distribution. Sihver et al[1] developed the empirical equations for the production cross section of the fragmented nuclei. The cross section reproduce experimental cross sections measured at LBL or at GSI. Using the equation, a computer code to calculate the depth dose distribution of the heavy-ion beam in any target material was also developed[3]. In the code, fluence of the projectile carbon beam reduces at the rate calculated from the total nuclear rection cross

section. Secondaries are produced at the rate calculated by the projectile fragmentation cross section. The secondaries are assumed to be the same speed with the projectile when they are produced. The secondaries are also penetrate in water material. The production of tertiaries from the secondaries during traveling in the water is also took into acount in the calculation code. The fourth and more higher order fragmentations are neglected in the calculation.

As shown in Fig. 2, the resultant depth dose distribution agree with the depth dose distributions measured by an ionization chamber except near the Bragg peak. W-value of the air of the heavy-ion depends largely on the carbon energy below around several MeV/u, that is near the Bragg peak. This may be the reason the measured ionization curve was below the calculated Bragg curve near the Bragg peak. LET distribution of the 290 MeV/u carbon beam in water was also calculated by this code. Fig. 3 shows the calculated LET distribution of the 290 MeV/u carbon beam in water material. Strictly speaking, the biological effects of the different particles are slightly different even if the LET of the particle are the same. However, at this stage, we don't know the established data on the LET dependence of individual fragmented nuclei, we calculated dose averaged LET of the projectile and the fragmented nuclei of the carbon beam in water material. And LET-RBE relationship of the HSG cells on carbon beam was used to estimate the biological response of the 290 MeV/u carbon beam.

4. BIOLOGICAL DEPTH DOSE DISTRIBUTION OF THE SPREAD-OUT BRAGG PEAK

Using not only the calculated depth dose distribution and LET distribution but also the biological responses of the carbon beams on HSG cells, the spread-out Bragg peak were designed as described in references[4,5]. Figure 4. shows the LET-RBE relation of the HSG cells for the carbon beam, which was obtained by the experiments using 135 MeV/u carbon beam. The spread-out Bragg peak were made by putting a bar ridge filter in the beam course. Spacing of the each ridge is 5 mm, and it does not move during the irradiation. Due to multiple scattering in the ridge filter and the angular distributions of the wobbled beam, shade of the bar ridge filter was smeared out. Depth dose distributions of the spread-out Bragg peak are shown in Fig. 5. The depth dose distributions were taken by changing Lucite thickness placed in front of the parallel plate ionization chamber. The Lucite thickness was again converted to water equivalent thickness. A calculated biological depth dose distribution is shown in Fig. 6. The biological dose is defined as physical dose multiplied by RBE. In the ridge filter design, biological dose in the spread-out Bragg peak were planned to be flat. Figure 7. shows survival distribution of HSG cells in water exposed by the ridge filtered beam. The cell survivals in the spread-out Bragg peak were satisfactorily flat as expected.

5. CONCLUSION

A heavy-ion irradiation system was designed and constructed at HIMAC facility for the clinical trials of heavy-ion therapy. For the first clinical trial of the heavy-ion radiotherapy with HIMAC beams, we have selected to use a beam of carbon 290 MeV/u and to start with an irradiation schedule of neutron therapy. Spread-out Bragg peaks were designed for the carbon beam to have uniform biological responses in the peak. The physical dose distributions of the beam agreed very well with the predicted depth dose distributions, and also the biological responses were satisfactorily flat in the spread-out Bragg peak. The heavy-ion dosimetry was checked by three different methods. The results of the dosimetries were coincided each other within 5 %. From these feasibility studies of the irradiation system and bio-physical studies of the carbon beam, the clinical trial of the heavy-ion radiation therapy has been safely started at the HIMAC facility.

References

[1] L.Sihver et al., "Total reaction and partial cross section calculations in proton-nucleus and nucleus-nucleus reactions", Phys. Rev. C47, 1225, 1993

[2] C.H.Tsao, et al., "Scaling algorithm to calculate heavy-ion spallation cross sections", Phys.Rev.C47,1257,1993.

[3] L.Sihver et al., "Depth-dose and fluence distributions when using heavy ion beams", The proceedings of NIRS International Seminar on Application of Heavy Ion Accelerator on Radiation Therapy of Cancer in connection with XXI PTCOG Meeting., NIRS, Chiba, 14-16 Nov. 1994., HIMAC report, NIRS-M-103/HIMAC-008.

[4] T.Kanai et al., "Biological and physical proposals for a heavy-ion clinical trial.", Proceedings of Third Workshop on Physical and Biological Research with Heavy ions, (Edited by K.Ando and T.Kanai), HIMAC report (NIRS Publication), HIMAC-003,1-3, 1993.

[5] T.Kanai et al., "Preparatory studies for heavy-ion therapy.", Proceedings of the fifth Japan-China Joint Symposium on Accelerators for Nuclear Science and Their Applications, Oct.,1993, Osaka, Japan.

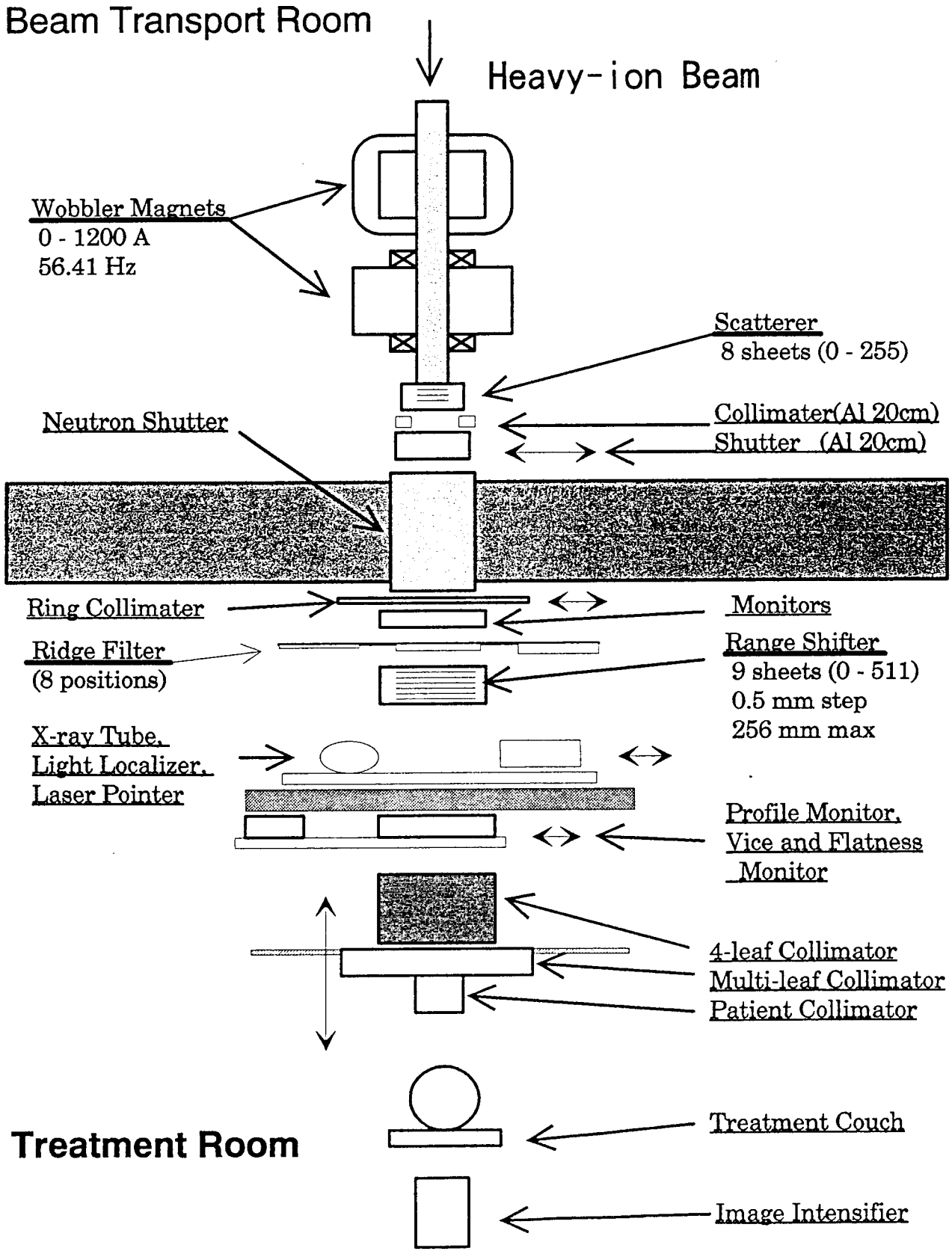

Fig. 1 an irradiation system of the HIMAC facility.

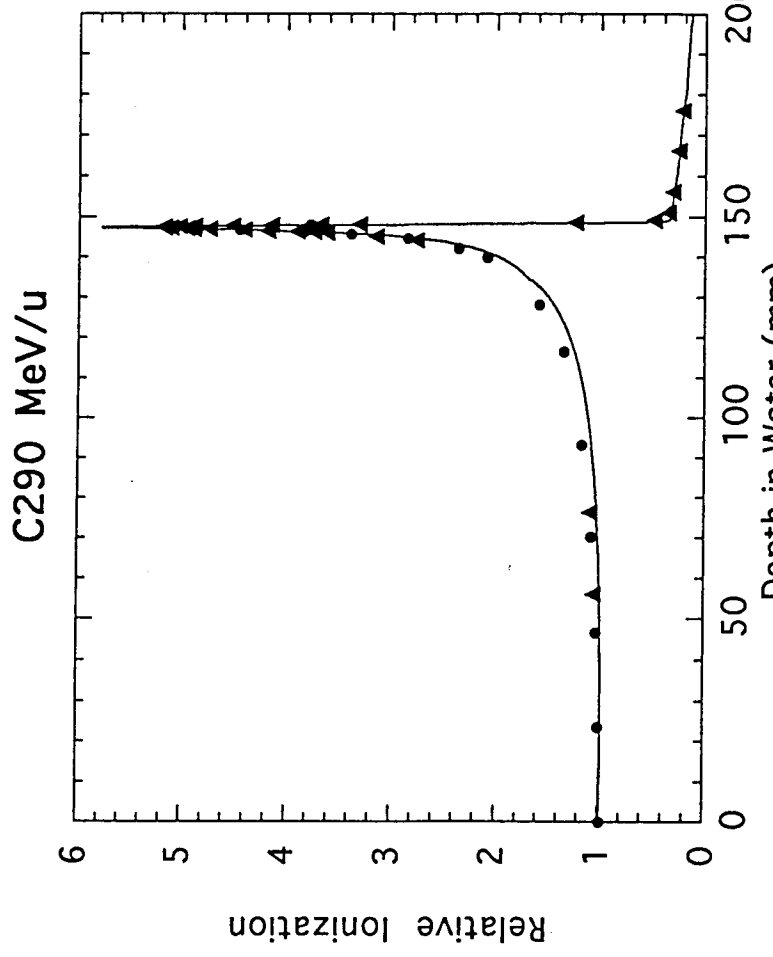

Fig. 2 the results of the depth dose distribution in water of carbon 290 MeV/u beam. Open circle and closed triangles in the figure are the relative ionization in water and in Lucite, respectively. The thickness of the Lucite is converted to water equivalent thickness. Solid line in the figure shows the result of a depth dose calculation, in which secondary and tertiary particle contributions are taken into consideration[1,2,3].

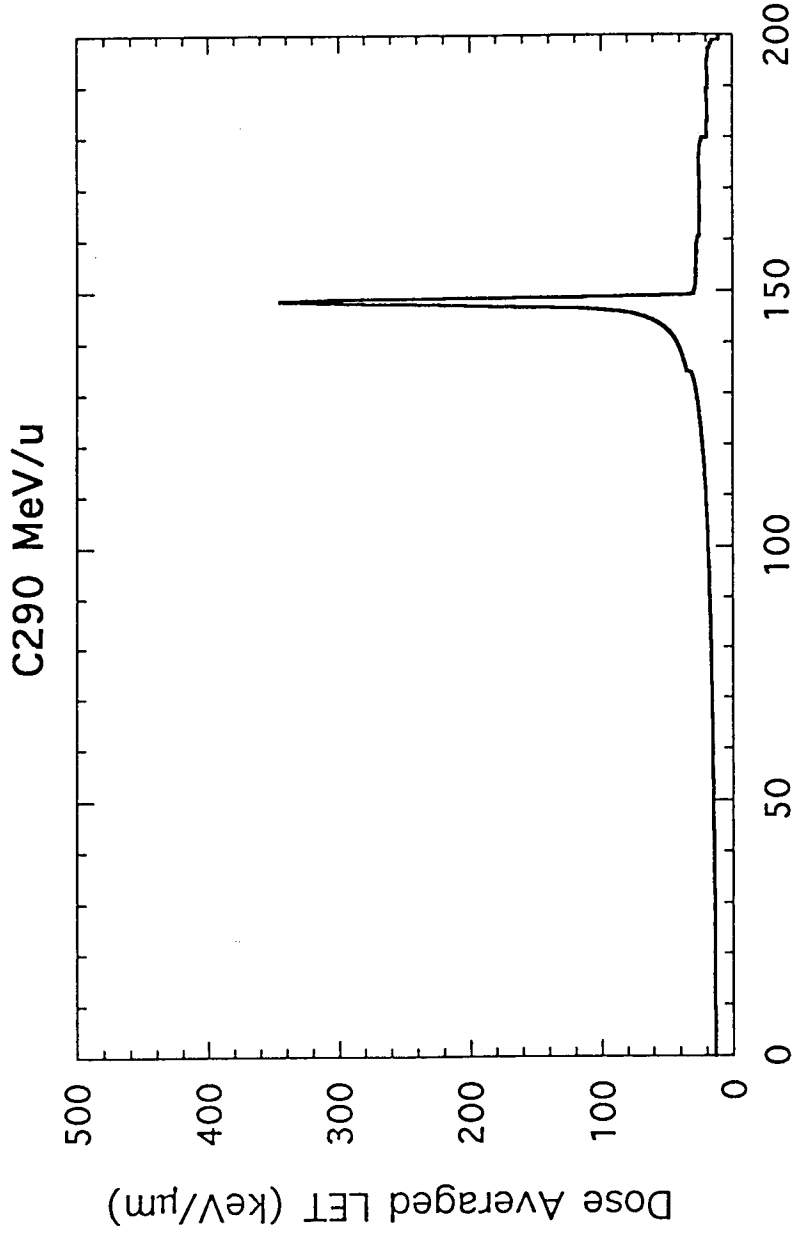

Fig. 3 the calculated LET distribution of the 290 MeV/u carbon beam in water material.

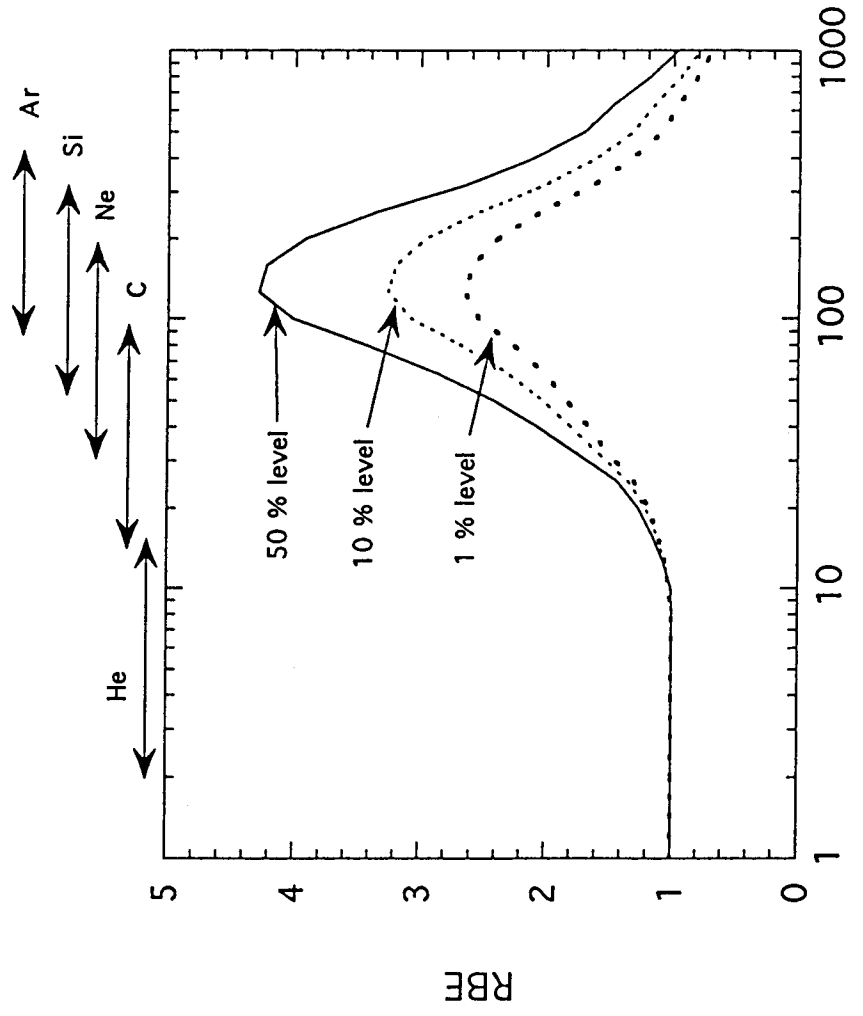

Fig. 4 the LET-RBE relation of the HSG cells for the carbon beam, which was obtained by the experiments using 135 MeV/u carbon beam.

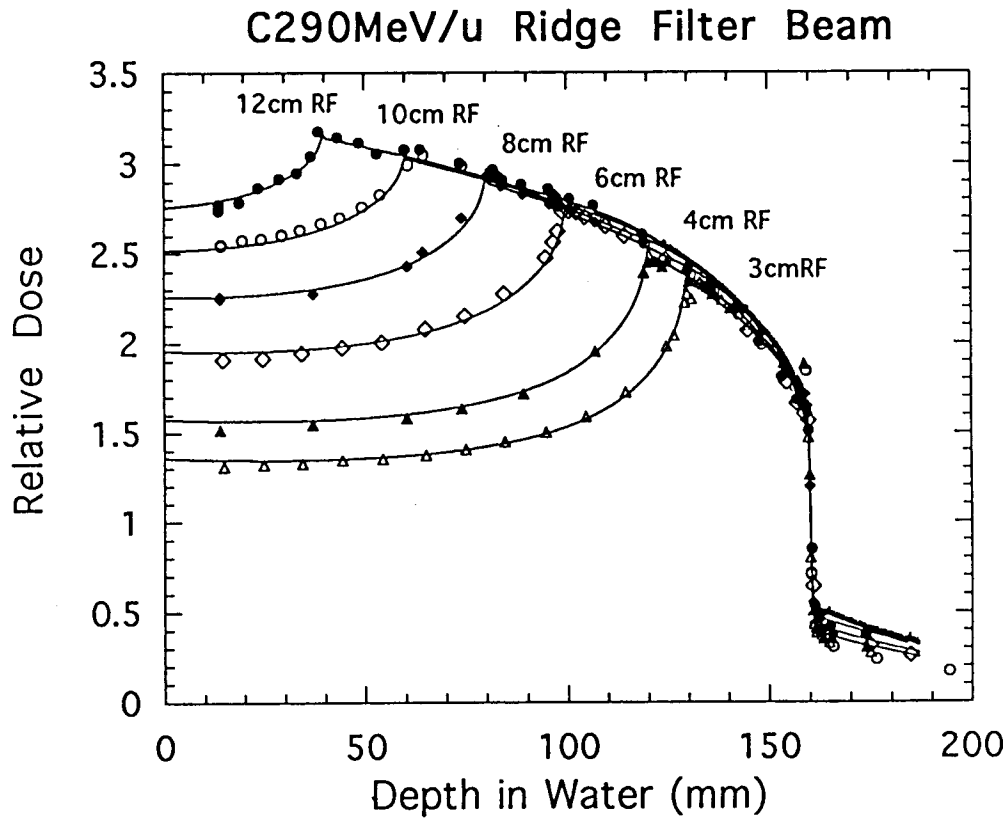

Fig. 5 Depth dose distributions of the spread-out Bragg peak

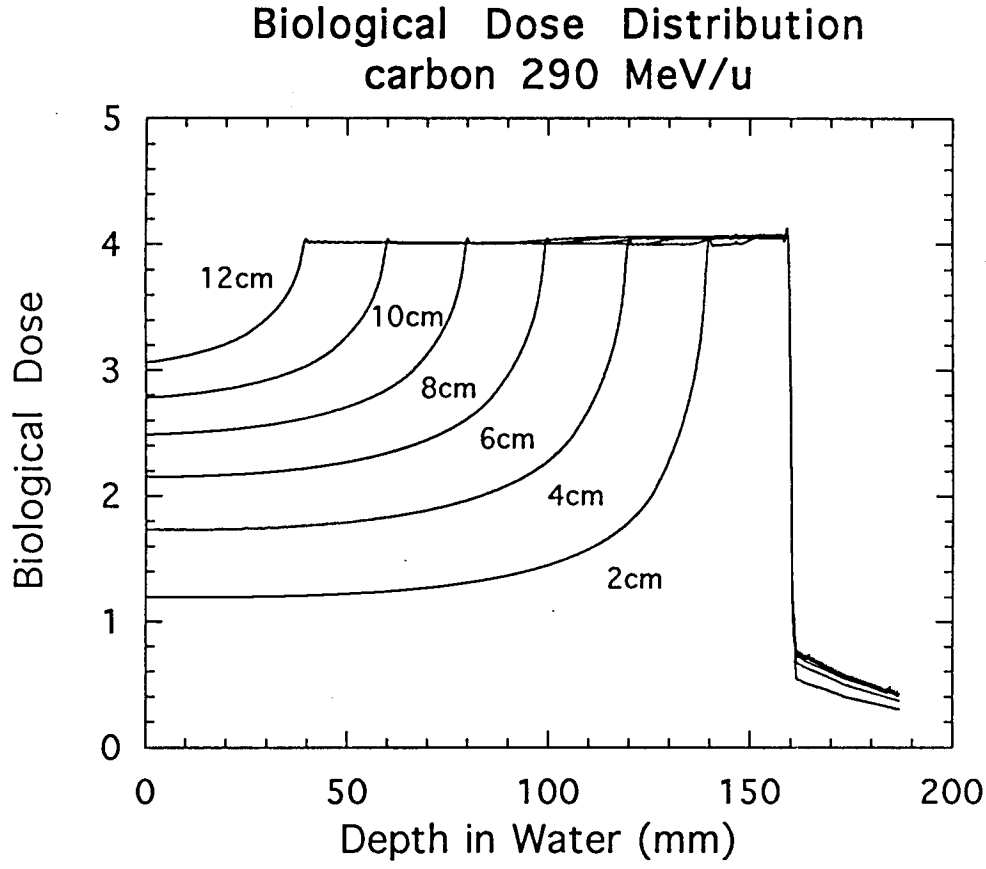

Fig. 6 A calculated biological depth dose distribution

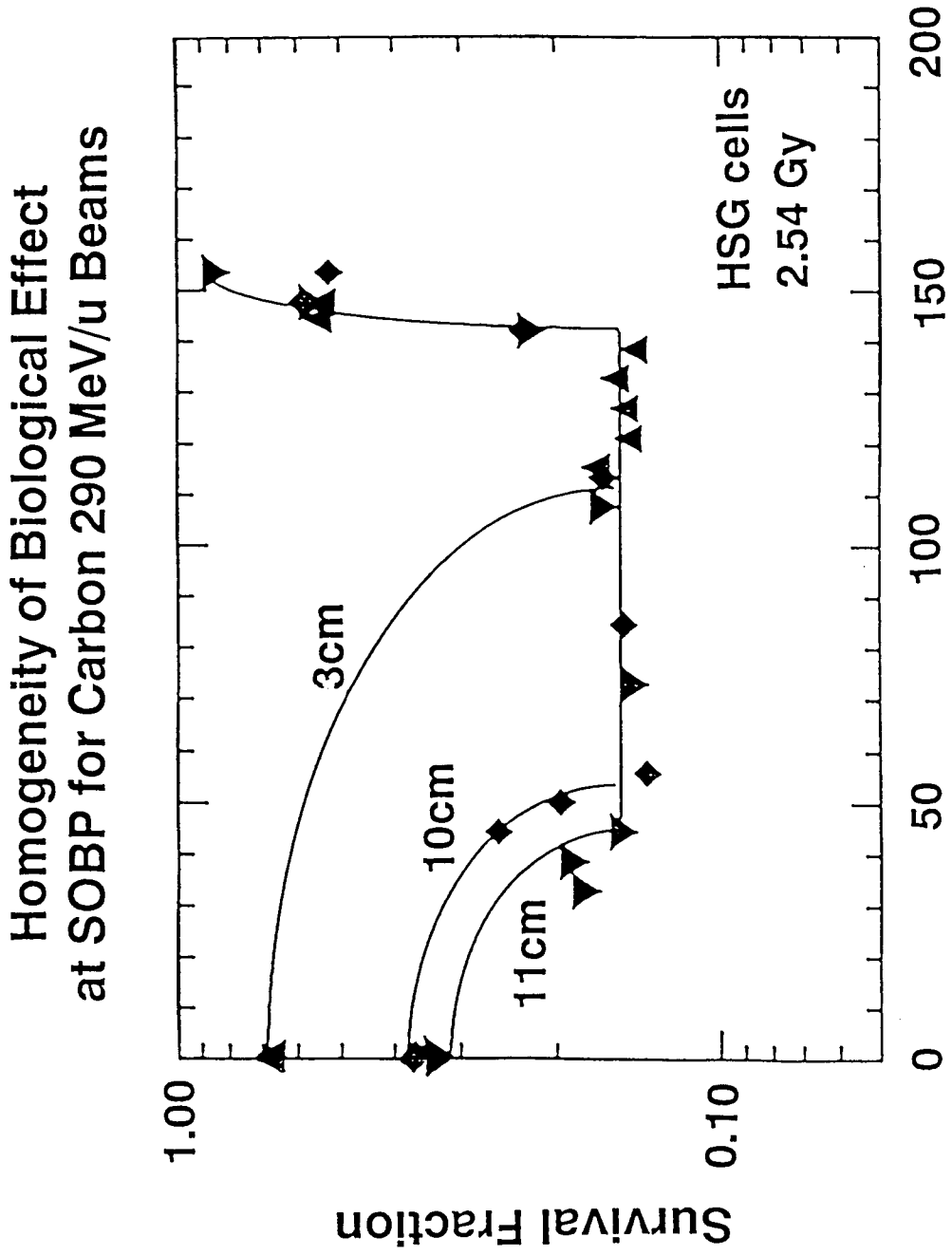

Fig. 7 survival distribution of HSG cells in water exposed by the ridge filtered beam.

Appendix I Program of the Second Specialists' Meeting on High Energy Nuclear Data

Jan. 26 (Thu.)

9:55 - 10:00 Opening Address H. Yoshida (JAERI)

10:00 - 12:00 1. Theory (Chairman: N. Kishida (CRC))

1.1 A Semiclassical Approach to Statistical Multistep Direct Reactions
- Recent Progress in Semiclassical Distorted Wave Model -
Y. Watanabe (Kyushu Univ.)

1.2 Progress in Quantum Molecular Dynamics
T. Maruyama (JAERI)

12:00 - 13:00 Lunch

13:00 - 15:00 2. Evaluation (1) (Chairman: K. Ishibashi (Kyushu Univ.))

2.1 Discussion on the Computer Simulation Scheme for the Intermediate Energy Hadron Nucleus Interactions
Y. Nakahara (JAERI)

2.2 NEANSC International Code Comparison for Intermediate Energy Nuclear Data
H. Takada (JAERI)

15:00 - 15:30 Coffee Break

15:30 - 17:30 3. Evaluation (2) (Chairman: Y. Watanabe (Kyushu Univ.))

3.1 Status of Nuclear Data Evaluation for JENDL High Energy File
T. Fukahori (JAERI)

3.2 Calculation of Neutron and Proton Induced Reaction Cross Sections for Actinides in the Energy Region from 10 MeV to 1 GeV
V.A. Konshin (JAERI)

18:00 - 20:00 Reception

Jan. 27 (Fri.)

9:00 - 12:00 4. Experiment (Chairman: M. Baba (Tohoku Univ.))

4.1 Review of Recent Neutron Experiments of Energy above 20 MeV at CYRIC, TIARA and RIKEN Cyclotron Facilities

T. Nakamura (Tohoku Univ.)

4.2 Measurement of Neutron and Gamma-ray Production Double Differential Cross Section at KEK

K. Ishibashi (Kyushu Univ.)

4.3 Measurements of Neutron Spectra from a Thick Lead Target Bombarded by 0.5 and 1.5 Gev Protons

S. Meigo (JAERI)

12:00 - 13:00 Lunch

13:00 - 15:00 5. Application (1) (Chairman: S. Chiba (JAERI))

5.1 High Intensity Proton Accelerator and its Application (Proton Engineering Center)

S. Tanaka (JAERI)

5.2 Issues in Space Radiation Shielding for Lunar Base

K. Oishi (Shimizu Co.)

15:00 - 15:15 Coffee Break

15:15 - 16:15 6. Application (2) (Chairman: Y. Uwamino (RIKEN))

6.1 Radiation Therapy Using High-energy Heavy-ion

T. Kanai (NIRS)

16:15 - 16:20 Summary Talk Y. Kikuchi (JAERI)

Appendix II List of Participants for the Second Specialists' Meeting on High Energy Nuclear Data

Participant	Affiliation
ASAI, Kiyoshi	Japan Atomic Energy Research Institute
ASAMI, Tesuo	Data Engineering Inc.
BABA, Mamoru	Tohoku University
CHIBA, Satoshi	Japan Atomic Energy Research Institute
ENDO, Akira	Japan Atomic Energy Research Institute
FUKAHORI, Tokio	Japan Atomic Energy Research Institute
FUKETA, Toyojirou	Nuclear Energy Data Center
HACHIYA, Masanori	Data Engineering Inc.
HARIMA, Yoshiko	CRC Research Institute Inc.
IDENO, Kazumi	Japan Atomic Energy Research Institute
IGASHIRA, Masayuki	Tokyo Institute of Technology
IGUCHI, Tetsuo	University of Tokyo
ISHIBASHI, Kenji	Kyushu University
IWAMOTO, Akira	Japan Atomic Energy Research Institute
IWASAKI, Shin	Tohoku University
KANAI, Tatsuaki	National Institute of Radiological Sciences
KAWAI, Masayoshi	Japan Atomic Energy Research Institute
KIKUCHI, Yasuyuki	Japan Atomic Energy Research Institute
KISHIDA, Norio	CRC Research Institute Inc.
KONSHIN, Valentin A.	Japan Atomic Energy Research Institute
KOTEGAWA, Hiroshi	Japan Atomic Energy Research Institute
MAEKAWA, Fujio	Japan Atomic Energy Research Institute
MARUYAMA, Tomoyuki	Japan Atomic Energy Research Institute
MARUYAMA, Toshiki	Japan Atomic Energy Research Institute
MATSUFUJI, Naruhiro	National Institute of Radiological Sciences
MATSUNOBU, Hiroyuki	Sumitomo Atomic Energy Industries Ltd.

Participant	Affiliation
MEIGO, Shin-ichiro	Japan Atomic Energy Research Institute
MIZUMOTO, Motoharu	Japan Atomic Energy Research Institute
MORI, Masataka	Japan Atomic Energy Research Institute
MURATA, Toru	Nuclear Fuel Development Co. Ltd.
NAKAGAWA, Masayuki	Japan Atomic Energy Research Institute
NAKAGAWA, Tsuneo	Japan Atomic Energy Research Institute
NAKAHARA, Yasuaki	Japan Atomic Energy Research Institute
NAKAJIMA, Yutaka	Japan Atomic Energy Research Institute
NAKAMURA, Takashi	Tohoku University
NAKANE, Yoshihiro	Japan Atomic Energy Research Institute
NAKAO, Noriaki	Tohoku University
NAKASHIMA, Hiroshi	Japan Atomic Energy Research Institute
NARITA, Tsutomu	Japan Atomic Energy Research Institute
NISHIDA, Takahiko	Japan Atomic Energy Research Institute
ODANO, Naomitsu	Ship Research Institute
OHKUBO, Makio	Japan Atomic Energy Research Institute
OISHI, Koji	Shimizu Co.
OTAKE, Iwao	Data Engineering Inc.
OYAMA, Yukio	Japan Atomic Energy Research Institute
SASA, Toshinobu	Japan Atomic Energy Research Institute
SHIBATA, Keiichi	Japan Atomic Energy Research Institute
SIEGLER, Peter	Japan Atomic Energy Research Institute
SU, He	Tokyo Institute of Technology
TAKADA, Hiroshi	Japan Atomic Energy Research Institute
TAKANO, Hideki	Japan Atomic Energy Research Institute
TANAKA, Shun-ichi	Japan Atomic Energy Research Institute
TOMURA, Hiromi	National Institute of Radiological Sciences
TOYAMA, Mitsuru	Kyorin University
UNO, Yoshitomo	Japan Atomic Energy Research Institute
UWAMINO, Yoshitomo	The Institute of Physical and Chemical Research

Participant	Affiliation
WATANABE, Takashi	Kawasaki Heavy Industries Co. Ltd.
WATANABE, Yukinobu	Kyushu University
YAMAGUCHI, Yasuhiro	Japan Atomic Energy Research Institute
YAMANO, Naoki	Sumitomo Atomic Energy Industries Ltd.
YOSHIDA, Hiroyuki	Japan Atomic Energy Research Institute
YOSHIZAWA, Nobuaki	Mitsubishi Research Institute Inc.